PhD Thesis

Atherosclerosis susceptibility of mice deficient in enzymes involved in lipolysis and lipogenesis

submitted by

Nemanja VUJIĆ

for the Academic Degree of

Doctor of Philosophy

(PhD)

at the

Medical University of Graz

Institute of Molecular Biology and Biochemistry

under the supervision of

Ao. Univ. Prof. Mag. Dr. rer. nat. Dagmar KRATKY

2015

Declaration

I hereby declare that this thesis is my own original work and that I have fully acknowledged by name all of those individuals and organizations that have contributed to the research for this thesis. Due acknowledgement has been made in the text to all other material used.
Throughout this thesis and in all related publications I followed the guidelines of “Good Scientific Practice“.

Graz, September 2015

Nemanja Vujić

Acknowledgements

I would like to express my deepest gratitude to Dagmar Kratky for giving me the opportunity to do my PhD under her supervision. Thank you for your unconditional support and encouragement, for excellent guidance, and fruitful discussions. Thank you for believing in me and for always being there for me when I was seeking for an advice.

I am very grateful to Branislav Radović for his friendship, support, all the knowledge he shared with me, and for making my first steps in science much easier. Many thanks to our current and former lab members, especially Silvia Rainer and Anton Ibovnik for their friendship and tremendous technical support. Special thanks to Madeleine Göritzer and Stefanie Schlager for being great colleagues and friends. I could always count on you when I needed a helping hand in the lab. Thanks to Sascha Obrowsky, Prakash Doddapattar, Martin Wegscheider, Julia Reindl, Jay Patankar, Melanie Korbelius, Christina Leopold, Sabrina Rexeis, Vinay Sachdev, and Madalina-Cristina Duta-Mare for your support and friendship. Thanks to Isabella Hindler for excellent mice care.

Moreover, I would like to thank our collaborators Wolfgang Graier, Achim Lass, Albert Wölfler, Thomas Eichmann, Silvia Schauer, Clemens Diwoky, Corina Madreiter-Sokolowski, and Ulrike Taschler as well as my thesis committee members Robert Zimmermann, Gerald Höfler, and Günter Hämmerle for their help, support, and fruitful discussions. I also would like to thank Suneil Koliwad for welcoming me at UCSF and guiding me through the work on DGAT1 project. Thanks to his lab members Martin Valdearcos, Jess Porter Abate and Megan Robblee for their friendship.

I am very grateful to my colleagues and friends in Austria who supported me during my PhD studies: Jelena Đurđević, Jelena Belić, Lada Brkić, Bojana Borjan, Dragana Marković, Alen Ašćerić, and many others.

Finally, I would like to express my enormous gratitude to my family and Jovana for their unconditional encouragement and support. Thank you for being there for me during difficult times, you made all this possible.

Table of contents

Zusammenfassung

Von Makrophagen abgeleitete, fetthaltige Schaumzellen stellen einen signifikanten Anteil in atherosklerotischen Läsionen dar und sind maßgeblich an der Bildung von Atherosklerose involviert. Die Beteiligung von lipidstoffwechsel-regulierenden Enzymen in diesem Zusammenhang wurde bisher wenig ausreichend untersucht, obwohl man davon ausgeht, dass diese Enzyme an der Regulierung von Makrophagenfunktion, sowie an der Entstehung von Atherosklerose beteiligt sind.

Im ersten Teil meiner Dissertation habe ich die Rolle der Monoazylglyzeridlipase (MGL), welches das letzte Enzym in der Lipolyse darstellt, hinsichtlich Makrophagenfunktion, Lipid- und Kohlenhydratstoffwechsel, sowie Atherogenese untersucht. Aus diesem Grund generierte ich ein atherosklerotisches MGL/Apolipoprotein E -/- Mausmodell (DKO). Aufgrund der Fähigkeit von MGL das Endocannabinoid 2-Arachidonylglyzerol (2-AG) zu spalten, reguliert dieses Enzym eine Vielzahl von Vorgängen, wie z.B. Lipidstoffwechselprozesse und Entzündungsreaktionen. In DKO Mäusen zeigten sich systemisch, sowie auch lokal in der Aorta und Leber erhöhte 2-AG Konzentrationen. Ferner waren in DKO Mäusen verminderte systemische Entzündungserscheinungen, verzögerte Chylomikronensynthese, verminderte Lebersteatose, verminderte Cholesterinausscheidung über den Stuhl und eine Verbesserung im Kohlenhydratstoffwechsel zu beobachten. Anhand dieser Veränderungen erwartete ich eine Auswirkung des Fehlens von MGL auf die Entstehung von Atherosklerose. Interessanterweise entwickelten DKO Mäuse vermehrt atherosklerotische Plaques mit einem allerdings vermindert entzündlichem Erscheinungsbild, charakterisiert durch einen reduzierten Makrophagen- und Lipidgehalt, verminderter Nekrose und einem erhöhtem Gehalt an Kollagen, welcher als präventiv gegen Plaqueruptur wirkt. Zusammengefasst betrachtet konnte ich anhand einer Vielzahl von Stoffwechsel- und Entzündungsparametern, eingeschlossen der Auswirkung auf Atherogenese, zeigen, dass MGL Defizienz zu einem verbesserten Erscheinungsbild führt. Somit würde eine pharmakologische Inhibierung von MGL ein Ansatzpunkt für die Behandlung von Stoffwechselerkrankungen darstellen.

Im zweiten Teil meiner Dissertation untersuchte ich die Auswirkung von DGAT1 Defizienz auf hämatopoetische Zellen und in weiterer Folge auf die Entwicklung von Atherosklerose. Bisherigen Untersuchungen zufolge zeigten DGAT1/ApoE-DKO

Mäuse eine verminderte Entstehung von Atherosklerose. Ursächlich für diese verminderte Plaqueentwicklung können entweder eine reduzierte Schaumzellbildung gemeinsam mit einer verbesserten Entzündungsantwort von Makrophagen oder eine verminderte intestinale Cholesterinaufnahme und –absorption einhergehend mit verminderten Plasma Lipidkonzentrationen sein. Um die Beteiligung von Makrophagen an dieser Beobachtung zu untersuchen, wurden „low density lipoprotein receptor“ KO Mäusen Knochenmark von Wildtyp oder DGAT1-KO Mäusen transplantiert. Wir beobachteten eine vergleichbare Plaquebildung in beiden Genotypen, wobei in DGAT1-KO transplantierten Mäusen ein instabile Läsion, charakterisiert durch erhöhten Makrophagen- und verringerten Kollagengehalt, vorlag. Aus diesen Ergebnissen schließen wir, dass DGAT1 Defizienz in hämatopoetischen Zellen nicht die zugrundeliegende Ursache für die beobachtete verminderte Atherosklerose ist, sondern dass dies womöglich auf einen veränderten Cholesterinstoffwechsel zurückzuführen ist.

Abstract

Macrophage-derived foam cells represent the main core of the atherosclerotic plaque and thus largely contribute to lesion dynamics. Enzymes regulating lipid metabolism in macrophages have been poorly investigated in the past. However, they strongly regulate macrophage function and concomitantly affect the process of atherogenesis.

In the first part of this thesis, I investigated the role of monoglyceride lipase (MGL) as the final enzyme in lipolysis on macrophage function, lipid and carbohydrate metabolism, and atherosclerosis development. Therefore, I generated atherosclerotic MGL/Apolipoprotein E double knockout (DKO) mice. Since MGL cleaves 2-arachidonoylglycerol (2-AG), the main endocannabinoid in mammals, it also affects a wide range of functions involved in lipid metabolism and inflammatory responses. I found systemically elevated 2-AG levels as well as increased aortic and hepatic 2-AG concentrations in DKO mice. Additionally, DKO mice had reduced systemic inflammation, delayed chylomicron secretion, decreased hepatic steatosis, increased cholesterol elimination via stool, and improved carbohydrate metabolism, which all may affect atherosclerosis progression. Interestingly, DKO animals developed increased atherosclerotic plaques, but these lesions were anti-inflammatory with reduced macrophage and lipid accumulation, decreased necrotic core size, and enlarged collagen-rich fibrous cap, which protects the lesion and prevents its rupture. The results obtained from DKO mice clearly demonstrate a range of metabolic and inflammatory parameters, including the atherosclerotic phenotype, which are improved due to MGL deficiency. Thus, pharmacological inhibition of MGL emerges as a potential target for treatment of metabolic disorders.

In the second part of my thesis, I investigated the relative contribution of DGAT1 deficiency in hematopoietic cells and the concomitant effect on atherosclerosis development. Previous research showed that DGAT1/ApoE-DKO mice have reduced atherosclerotic plaque formation. The reduction in plaque size can be attributed either to reduced foam cell formation and ameliorated macrophage response to inflammation or to reduced intestinal cholesterol uptake and absorption, which resulted in reduced plasma lipid concentrations. To determine solely macrophage contribution to the observed effect, we transplanted low-density lipoprotein receptor-KO mice with the bone marrow from wild-type or DGAT1-KO

mice. We found comparable plaque formation in both genotypes with the development of unfavorable, destabilizing lesion profile in DGAT1-/- transplanted mice, due to increased plaque macrophage and reduced collagen content. These data clearly indicate that hematopoietic DGAT1 deficiency does not cause the improved atherosclerosis observed in DGAT1/ApoE-DKO mice, arguing in favor of decreased plaque formation due to altered cholesterol lipid metabolism in these animals.

PART I: Consequences of MGL deficiency on atherosclerosis development

1. Introduction

1.1. Atherosclerosis – the plague of the 21st century

Atherosclerosis is a chronic, progressive, inflammatory disease of the vascular wall, associated with an imbalance in lipid metabolism (1). Macrophage lipid accumulation, formation of foam cells, their subendothelial retention within the large-to-medium sized arteries, and subsequent apoptosis and/or necrosis are the hallmarks of atherogenesis. The first evidence of atherosclerosis in humans dates as far back as the ancient Egypt. Recently performed computerized tomography scanning of the Egyptian mummies from the period of 1580-1550 BC identified atherosclerotic calcifications in the arterial vessel walls (2). Nowadays, cardiovascular diseases (CVDs) as a consequence of atherosclerosis represent a global health issue, comprising up to 29.6 % of all death causes World-wide in 2010 (3), and as many as 46 % of all death causes in the European region in 2014 (4). Although the mortality rates have shown slight decline in Western European countries and Australia during the last two decades, trends have been opposite in the large portion of the world, including Central and Eastern Europe, and in particular the developing countries (3, 4).

1.1.1. The pathogenesis of atherosclerosis – from lipids to inflammation – causes and consequences

Current knowledge of atherosclerotic pathogenesis favors the response-to-injury model, although, due to its complexity, the true etiology of atherosclerosis still remains unclear.

Endothelial dysfunction is considered to be the initial step in the development of atherosclerosis. In homeostatic conditions, endothelial cells provide a non-adherent surface for circulating leukocytes. However, certain physical conditions such as hypertension and low shear stress, or chemical stressors like hyperlipidemia, hyperglycemia, elevated plasma homocysteine levels, tobacco smoking, and recurrent infections, can cause endothelial dysfunction (5). Arterial branches and curvatures are especially prone to the disturbances in blood flow, which can affect endothelial cell function, and therefore present the predicted sites for early atherogenic lesions (6).

A dysfunctional endothelial layer has increased permeability, allowing lipoprotein particles to reach intimal layers more easily. Apolipoprotein B-100 (ApoB-100)-containing lipoproteins, such as low-density lipoprotein (LDL), accumulate in the subendothelial layers due to interactions between negatively charged ApoB-100 and positively charged proteoglycans in the intimal region (7). Although LDL is protected from modifications in the circulation, LDL particles within the intimal space are exposed to various modifications including oxidation, acetylation or glycation, and become immunogens (8). These modified particles also affect endothelial cells, changing their phenotype into proliferative, pro-coagulatory and pro-inflammatory states with high expression of leukocyte adhesion molecules on their surface.

Leukocyte adhesion on the endothelial surface is a multistep process, which involves capture, selectin-dependent rolling, slow rolling and activation by endothelial chemokines, firm adhesion mediated by integrins, and subendothelial migration (9). Activated endothelium expresses P-, E- and L-selectins and leukocyte adhesion to these selectins is mediated mainly via its ligand P-selectin glycoprotein ligand 1 (PSGL-1) and possibly other ligands as well. Further on, firm adhesion and arrest are formed through the interaction of the adhesion molecules on the endothelial cells, vascular cell adhesion molecule 1 (VCAM-1) and intracellular adhesion molecule 1 (ICAM-1), with their integrin ligands, very late antigen 4 (VLA-4) and leukocyte function-associated antigen 1 (LFA-1), respectively, expressed on leukocytes (10). Finally, the trafficking of leukocytes into subendothelial regions, the process known as diapedesis, is mediated by various chemokines and their receptors (Figure 1).

Among leukocyte populations, circulating monocytes represent the most important cells in the pathogenesis of atherosclerosis. Within the subendothelial regions, these cells are differentiating into macrophages, which are the most dominant cell species in the atherosclerotic plaque (11) (Figure 2B). Monocyte diapedesis is dependent on several chemokines among which the most important one is macrophage chemoattractant protein 1 (MCP-1), which is secreted by activated endothelial and smooth muscle cells (SMCs). MCP-1 interacts with chemokine CC motif receptor (CCR) 2 on the monocyte surface leading to directed cellular chemotaxis towards the chemokine gradient. Moreover, interleukin (IL) 8, macrophage inflammatory protein (MIP) 1α and 1β as well as RANTES are capable to interact with CXCR2 and CCR5, respectively, contributing to subendothelial migration. Once reaching atherosclerotic lesions, monocytes differentiate into macrophages in a process driven by macrophage-colony stimulating factor (M-CSF) and possibly other lymphocyte- and endothelial cell-derived cytokines (12).

Within intimal regions, macrophages are exposed to a large amount of lipids and ApoB-containing lipoproteins in modified state, which are then subjected to uptake, lysosomal degradation and re-esterification, and storage within lipid droplets (LDs). This process leads to foam cell formation and represents the key step in the intimal cholesterol accumulation. In addition to ubiquitously present mechanisms of cholesterol homeostasis regulated by LDL receptor (LDLR), macrophages also possess scavenger receptors (SRs) responsible for the internalization of modified lipids and lipoproteins (Figure 1). The expression of these SRs is not regulated by intracellular cholesterol concentrations, allowing macrophages to take up and accumulate the excessive amounts of cholesterol and become foam cells (13). There are 8 different classes of SRs among which SR-AI/II and cluster of differentiation 36 (CD36) carry most of the cholesterol internalizing capacity. Additionally, SR-BI can traffic lipids bidirectionally, depending on the cell type, and in macrophages even causes cholesterol efflux towards high-density lipoprotein (HDL) (14).

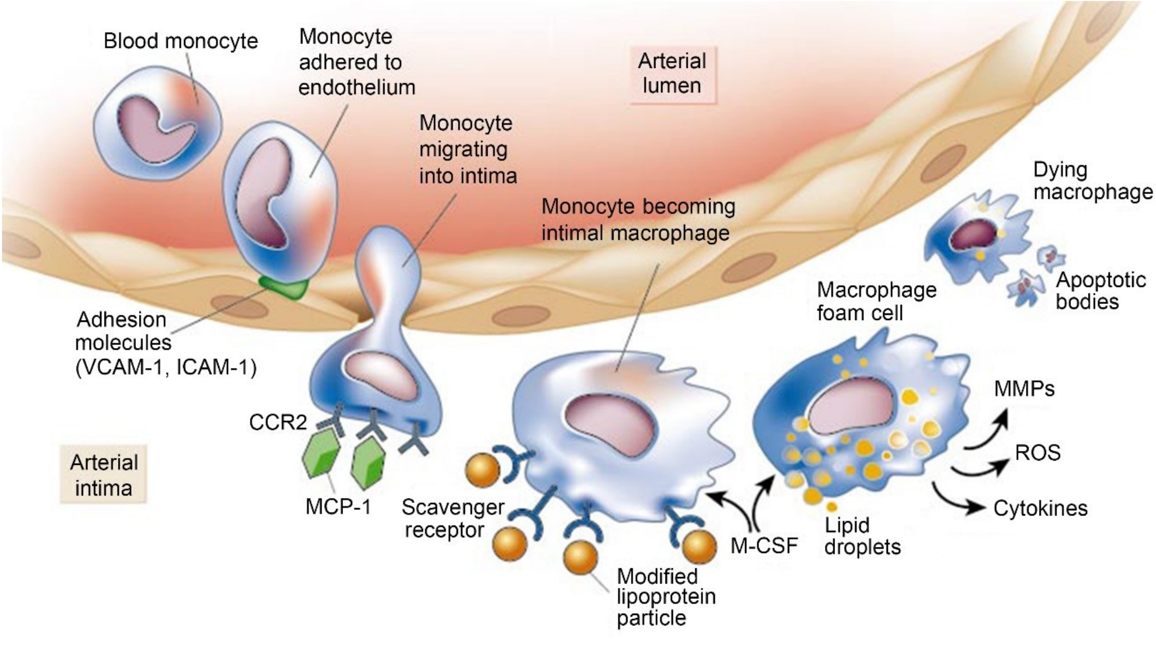

Figure 1. Mononuclear phagocytes in the pathogenesis of atherosclerosis. Monocyte interaction with the surface of activated endothelium involves capture, selectin-dependent rolling, slow rolling and activation by endothelial chemokines (VCAM-1 and ICAM-1), firm adhesion mediated by integrins and subendothelial migration (mediated by MCP-1), and differentiation into macrophages (mediated by M-CSF). Within subendothelial regions, macrophages are exposed to modified lipoprotein particles, which are taken up by scavenger receptors in an uncontrolled manner, leading to foam cell formation. Foam cells have pronounced inflammatory propensity and produce increased amounts of matrix metalloproteinases (MMPs), reactive oxygen species (ROS), and cytokines, resulting in further infiltration of inflammatory cells and plaque destabilization. Finally, these cells can undergo apoptosis and secondary necrosis, causing buildup of a destabilizing necrotic core. Adapted from Libby P., Inflammation in atherosclerosis (15).

Further fate of these lesional macrophages transformed into foam cells can take multiple pathways. There is evidence that lesional macrophages can egress, at least from regressive plaques, removing the lipids from the site of inflammation and reducing the plaque size, cellularity, and inflammatory propensity (16). Lesional macrophages are also involved in reverse cholesterol transport, a process which allows cells to transfer internalized cholesterol via ATP-binding cassette A1 (ABCA1), ABCG1 and SR-BI transporters to external acceptors such as ApoA-I or HDL particles, respectively (17). Lastly, foam cells within the plaque can also undergo apoptotic cell death. These apoptotic cells can either be subjected to further phagocytic removal by newly invading macrophages in a process known as efferocytosis (18) or can undergo secondary necrosis with the release of its intracellular content and generate a necrotic core within the lesion consisting of cholesterol crystals, accumulated lipids, and cellular debris (19) (Figure 2C).

During atherosclerosis development, macrophages also secrete numerous cytokines and chemokines, which modulate cellular homeostasis in an autocrine and paracrine manner and contribute to lesion remodeling. Vascular smooth muscle cells (VSMCs) are especially influenced by this process. In homeostatic conditions, these cells reside in *tunica media* of the arterial wall in the quiescent, contractile state, where they control the arterial vascular tone (Figure 2A). However, VSMCs can undergo a phenotypic switch mediated by platelet derived growth factor (PDGF), changing to synthetic, proliferative, migratory phenotypes (20). These cells then reach intimal regions and produce a variety of extracellular matrices, mainly collagen and elastin, which give structural support and scaffold for the atherosclerotic plaque, thereby causing its stabilization (21). However, the process of collagen production and lesion stabilization is opposed by the production and activity of matrix-degrading enzymes, MMPs. These enzymes are mostly produced by plaque-invading inflammatory cells and their activity is directed towards thinning of the fibrous cap. Consequent plaque rupture and sudden intraluminal thrombosis are the major processes in the pathophysiology of acute occlusive vascular events, namely heart attack and stroke (Figure 2D). Therefore, the fate of advanced lesion is mostly determined by a net effect of the two processes, matrix production and degradation (22).

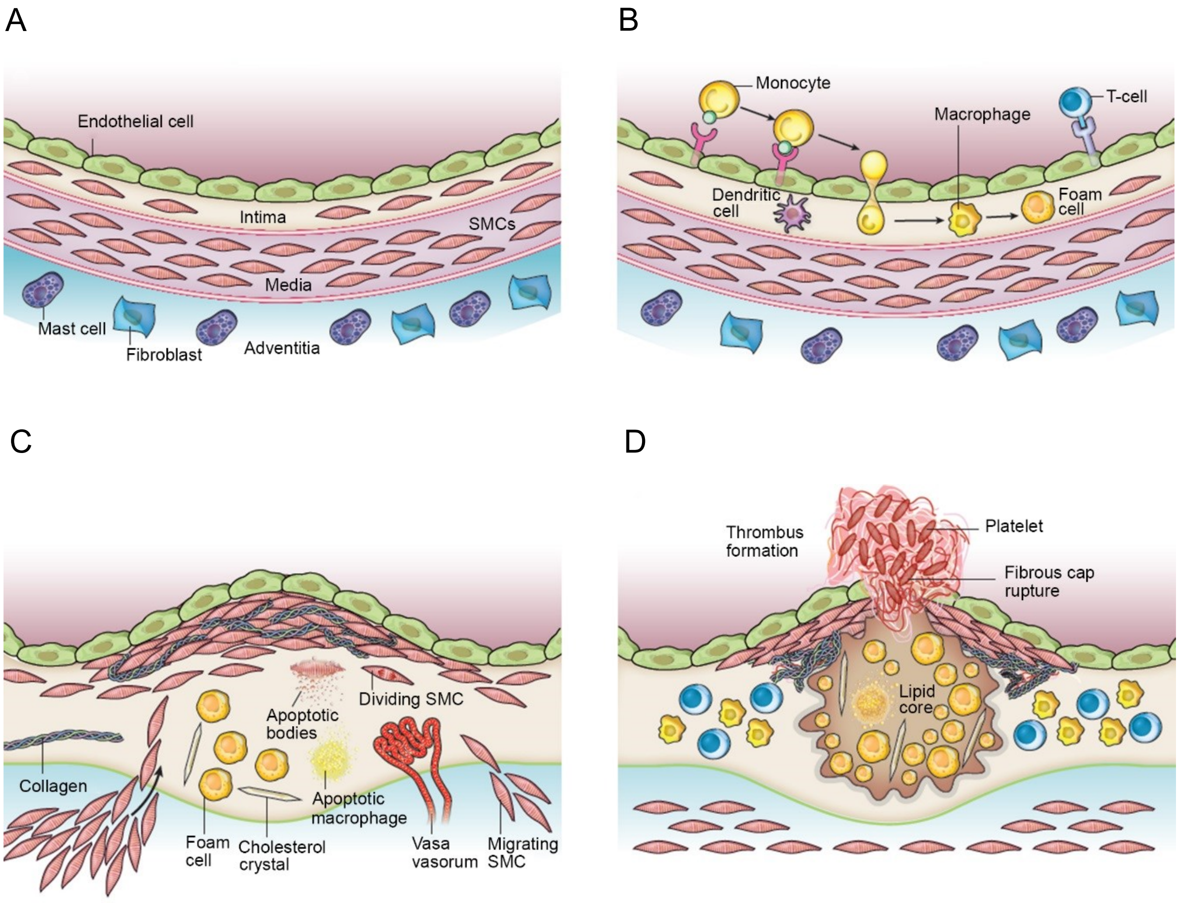

Figure 2. The pathogenesis of atherosclerosis. (A) Healthy arteries consist of three layers: endothelial cell-lining *intima* which contains small numbers of resident VSMCs. *Tunica media* consists mostly of VSMCs in a complex extracellular matrix which gives structure and contractile capacity to the vessel wall. The outer layer *tunica adventitia* contains mast cells, nerve endings, and microvessels. (B) Early lesions represent “fatty streaks” which consist mostly of inflammatory cells. Activated endothelial cells express adhesion molecules leading to T lymphocyte and monocyte adhesion and subendothelial transmigration. Within intimal regions, monocytes differentiate into macrophages which take up modified lipoproteins and generate foam cells. (C) Advanced lesions have complex structure. VSMCs migrate from the *media*, proliferate and produce extracellular matrices which give a scaffolding structure to the lesion, and prevent plaque rupture. Foam cells undergo apoptosis and

increase inflammatory propensity of the lesion by attracting newly invading leukocytes and generating a lipid-rich atherosclerotic pool which contributes to the buildup of the necrotic core. (D) Intravascular thrombosis as a terminal stage of atherosclerosis. Thinning fibrous cap fails to prevent contact between circulating blood cells (leukocytes and platelets), and intraplaque necrotic core (consisting of extracellular lipids and cellular debris). Upon plaque rupture, a series of sudden intravascular events consequently leads to thrombus formation which fully occludes the artery or breaks off and causes a downstream ischemic stroke in the affected tissue. Adapted from Libby P. *et al*, Progress and challenges in translating the biology of atherosclerosis (23).

1.1.2. Neutrophils – inflammatory scouts and advanced lesion destabilizers

Neutrophils represent the first cellular members of the innate immunity to reach the pathogens and initiate the inflammatory response upon rapid mobilization from the bone marrow (BM). These cells are short-lived, with circulating half-life of only 18 hours (24), after which they undergo apoptosis and are rapidly cleared by other phagocytes (25). Thus, their detection and identification within the atherosclerotic lesions has been largely hindered for a long time. Recent data, however, demonstrate the role of neutrophils in both early atherogenesis and advanced atherosclerotic lesions. Within the early lesions, neutrophils contribute to intraplaque inflammation and buildup of the early atherogenic core (26). In advanced lesions, neutrophil abundance is high in vulnerable shoulder regions of the atheroma, where they cause degradation of matrix collagen and fibrous cap thinning (27, 28). Elastase, proteinase 3, and MMP-2, -8 and -9 as the most prominent and potent members of the large family of MMPs, are readily produced by neutrophils and can affect lesion stability via matrix degradation. In addition, neutrophils produce a wide range of enzymes involved in immune processes. For example, myeloperoxidase (MPO) is responsible for the production of ROS and in the context of atherosclerosis, aggravation of endothelial dysfunction and lipoprotein modification (29). Among cytokines and chemokines, neutrophils are known to produce azorucidin, cathepsin G, and α-defensins, which all boost immune responses and trigger secondary infiltration of monocytes and other members of the innate immunity into the lesions, thereby affecting inflammatory responses (7) (Figure 3).

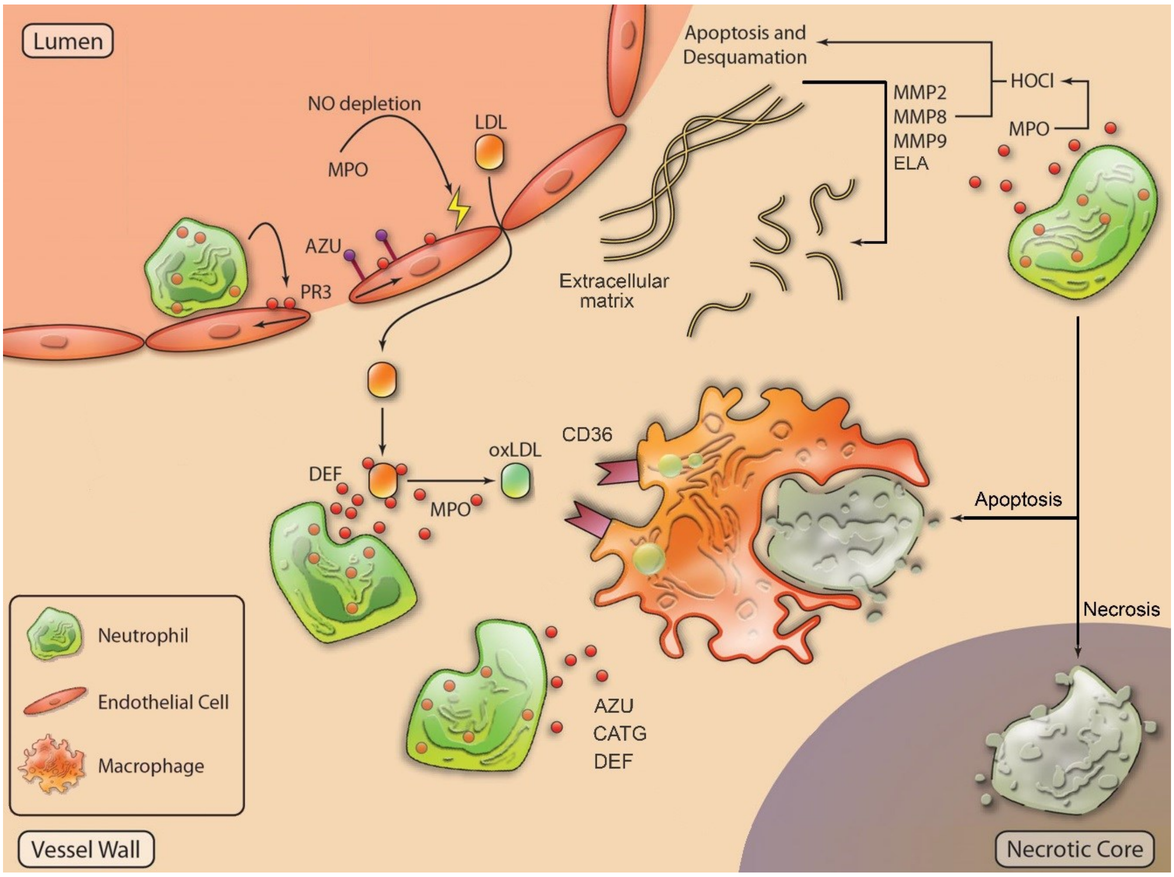

Figure 3. Neutrophil dynamics in atherosclerotic lesions. Neutrophil accumulation is characteristic for shoulder regions of atherosclerotic plaque. Sustained secretion of MPO causes production of ROS, aggravates endothelial dysfunction and causes lipoprotein modification. Neutrophils stimulate other immune cells by producing large amount of pro-inflammatory cytokines: azorucidin (AZO), cathepsin G (CATG), α-defensin (DEF). In addition, neutrophils largely contribute to plaque destabilization by producing elastase, proteinase 3 (PR3), and MMP-3, -8 and -9 which are responsible for degradation of the extracellular matrix and fibrous cap thinning, rendering advanced lesions prone to rupture. Finally, due to their short half-life, neutrophils quickly undergo apoptosis and are efferocytosed by invading macrophages, stimulating the inflammatory propensity event more, or are subjected to secondary necrosis which contributes to the necrotic core build up. Adapted from Soehnlein O., Multiple roles of neutrophils in atherosclerosis (29).

1.1.3. Monocytes – the infantry

Monocytes are considered to be the most important circulating white blood cells involved in the pathogenesis of atherosclerosis, particularly because they give rise to lesional macrophages and are continuously accumulating in atheromas or predicted sites for atherosclerotic lesion formation (30). There are two main subsets of monocytes, characterized by their surface markers. Pro-inflammatory $Ly6C^{high}$ monocytes are characterized by $CCR2^{+}CX_{3}CR1^{low}$ antigen expression pattern in mice and CD14^{high} or CD14^{+}CD16^{+} in humans. They represent the main monocyte subset involved in the inflammatory response caused by microbial infections. These cells also give rise to the classically activated, pro-inflammatory M1-like macrophage subset. On the other hand, CCR2^{low}CX$_{3}$CR1^{high} cells in mice or CD14^{dim} in humans are resident Ly6C^{low} monocytes, which patrol blood vessels even in homeostatic conditions and are responsible for the resolution of inflammatory response. This subset of monocytes gives rise to alternatively activated, anti-inflammatory M2-like macrophages (31). The importance of specific monocyte subsets in atherogenesis has been previously documented. Numbers of Ly6C^{high} monocytes significantly increase during hypercholesterolemia due to increased cellular production and survival, whereas Ly6C^{low} population remains unaffected (32). Moreover, Ly6C^{high} cells represent the dominant class of monocytes capable to infiltrate atherosclerotic lesions and increase their cellularity and size (33). It is therefore plausible to believe that the change in a Ly6C^{high} to Ly6C^{low} monocyte ratio within the circulation significantly determines the fate of lesion progression.

1.1.4. Macrophages and foam cells – the cavalry

Macrophage subtypes are divided into classically activated pro-inflammatory M1 and alternatively activated anti-inflammatory M2 macrophages. However, the whole range of macrophage phenotypes is much wider and can be found between these two main subtypes. The differentiation pattern of macrophages largely depends on cytokines to which monocytes are exposed. It is generally considered that M-CSF mediated monocytic differentiation *in vitro* leads to an M0 phenotype (9). However, occurrence of different circulating cytokines *in vivo*, particularly in the complex setting of an atherosclerotic lesion, can lead to selective differentiation of specific monocyte subsets to a certain macrophage phenotype.

Cytokines generated by T-helper (T$_{H}$) 1 lymphocytes such as interferon-γ (IFN-γ), IL-2 and tumor necrosis factor-α (TNF-α) as well as bacterial lipopolysaccharides (LPS) lead to M1 macrophage polarization (34). This process consequently generates lesional macrophages which produce pro-inflammatory cytokines (TNF-α, IL-1β, IL-6, IL-12, and IL-23) largely responsible for potentiation of inflammatory response and finally lesion destabilization. Indeed, in human atherosclerotic plaques, destabilized lesional shoulders are enriched in M1 macrophages (35, 36) (Figure 4A).

Likewise, T_H2-lymphocyte derived cytokines such as IL-4, -10, and -13 lead to M2 macrophages (34). M2 macrophages are considered as anti-inflammatory since they produce high levels of inflammation-resolving cytokines such as IL-4, IL-10, and TGF-β. This type of macrophages is mostly associated with the resolution of acute inflammatory responses, and in the chronic state like in atherosclerosis, can reduce inflammatory propensity within the lesion, leading to its stabilization. Thus, it was not surprising to find that stabilized parts of atherosclerotic lesions contain significant numbers of M2-polarized macrophages (35, 36). To date, *in vitro* experimentation lead to division of M2 macrophages in four different sub-populations: M2a, M2b, M2c, and M2d. M2a macrophages express high levels of manose receptor and secrete pro-fibrotic cytokines. M2b cells produce high amounts of both pro-inflammatory (IL-1β, TNF-α, IL-6) cytokines and anti-inflammatory cytokine IL-10. M2c macrophages seem to be professional efferocytes, due to high expression of Mer receptor tyrosine kinase (Mer-TK) responsible for removal of apopototic cells. Finally, M2d cells have low manose receptor expression and produce high levels of IL-10 and vascular endothelial growth factor (37).

Moreover, at least four additional macrophage phenotypes were identified in human atherosclerotic plaques. M(Hb) macrophages are found in the hemorrhagic zones of human atherosclerotic plaques and are responsible for hemoglobin clearance. These cells show anti-inflammatory properties by increased IL-10 secretion, resistance to lipid accumulation due to induced cholesterol efflux, and reduced ROS production. Mhem macrophages differentiate upon exposure to heme and (similarly to M(Hb) macrophages) demonstrate reduced levels of oxidative stress and lipid accumulation. Mox macrophages develop upon exposure to oxidized phospholipids and have reduced phagocytic and chemotactic capacities. These cells, although anti-inflammatory by nature, produce some inflammatory cytokines like IL-1β and COX-2 (Figure 4B). Finally, M4 macrophages are formed upon exposure to CXCL4. Unlike all other macrophage phenotypes, they are differentiated terminally and cannot undergo a phenotypic switch. These cells completely lack phagocytic capacities and show a pro-inflammatory phenotype similar to M1 macrophages (38) (Figure 4C).

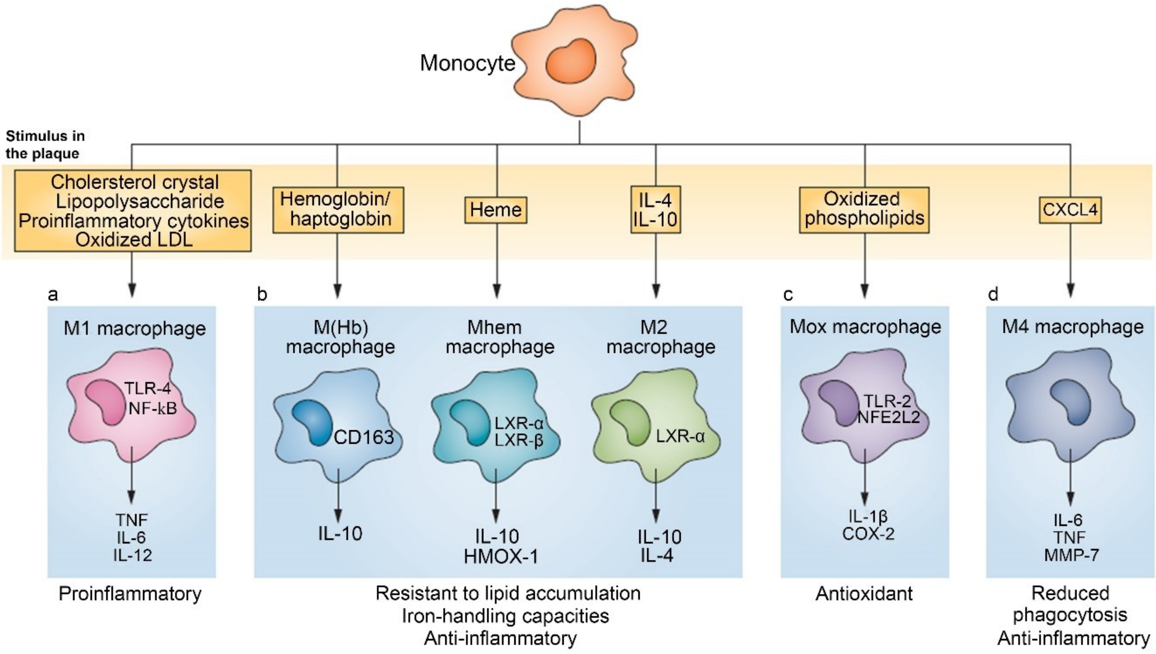

Figure 4. Spectrum of macrophage phenotypes. Monocytes differentiate to a range of macrophage phenotypes depending on the stimulus in the plaque. (A) M1 macrophages differentiate in response to T_H1 stimulus, lipid loading or LPS and secrete pro-inflammatory cytokines. (B) M(Hb), Mhem and M2 macrophages develop upon stimulation with hemoglobin, heme or T_H2 cytokines, respectively, and secrete anti-inflammatory cytokines. (C) Mox macrophages are formed as a consequence to oxidized phospholipid exposure and are able to produce both pro- and anti-inflammatory cytokines. (D) M4 macrophages differentiate in response to CXCL4, have reduced phagocytic capacity and show a phenotype similar to M1 macrophages. Adapted from Chinetti-Gbaguidi G. *et al*, Macrophage subsets in atherosclerosis (38).

1.1.5. T lymphocytes – gray eminences of intraplaque dynamics

T lymphocytes are the second most abundant hematopoietic cells within the lesions and can be detected already in fatty streaks, although at much lower frequencies compared to macrophages (39). Even though T lymphocytes do not phagocyte modified lipoproteins or accumulate LDs, they actively produce a plethora of cytokines and chemokines, thereby indirectly modulating macrophage behavior and atherogenesis (40). T_H1 $CD4^+$ lymphocytes are the most dominant T-lymphocyte subpopulation present in human atheromas (41). As mentioned before, these cells produce a large number of IFN-γ and TNF-α and thus stimulate M1 macrophage polarization, which consequently promotes further macrophage plaque infiltration and increases lesion cellularity and plaque destabilization (Figure 5). In contrast, T_H2 cells are present in human plaques with much lower frequency (42) and cytokines secreted by these cells stimulates M2 macrophage polarization (Figure 5). Finally, regulatory T lymphocytes (T_{regs}) are important in the resolution of the inflammatory response and thereby affect plaque development by reducing plaque burden (43). Recent data show that the ratio of T_{reg}s critically influences atherogenesis and high ratios can even be associated with atherosclerotic plaque regression (44).

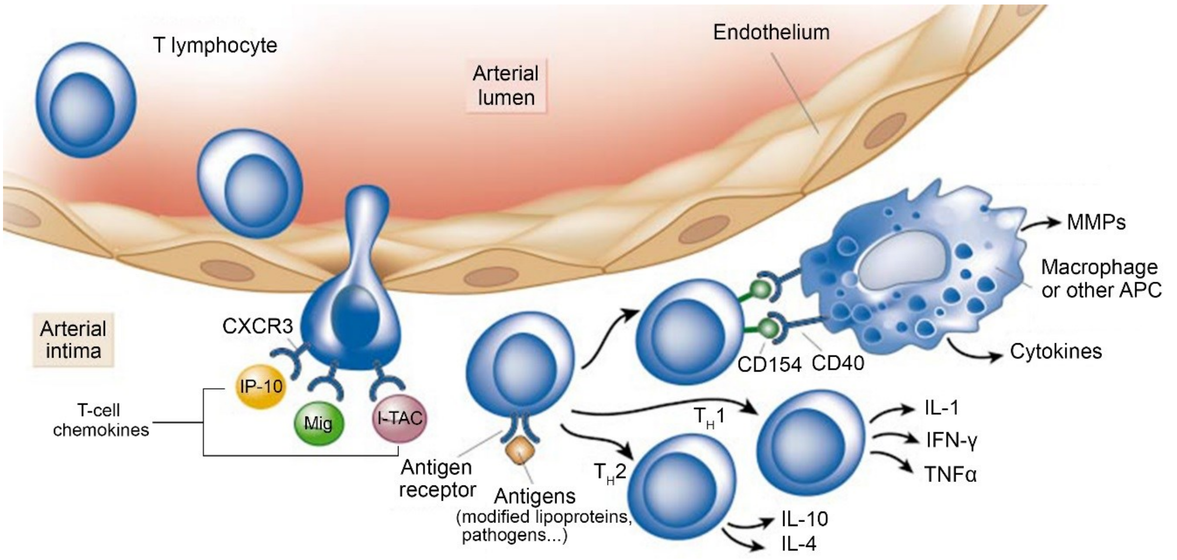

Figure 5. Role of T lymphocytes in the pathogenesis of atherosclerosis. T lymphocytes adhere to the activated endothelium, where they undergo diapedesis and subendothelial homing in a CXCR3-dependent process. T lymphocytes are exposed to modified lipoproteins and other immunogens, which drive lymphocyte differentiation to T_H1, T_H2 or T_{reg} phenotypes. Differentiated lymphocytes as members of the adaptive immunity secrete a wide range of cytokines and chemokines, thus influencing cellular members of innate immunity and largely affecting intravascular inflammation. Adapted from Libby P., Inflammation in atherosclerosis (15).

1.2. Lipolysis

Triglycerides (TGs) are the main energy depot in mammals, predominantly stored in white adipose tissue (WAT). In times of increased energy demands or upon fasting, TGs are efficiently mobilized from their storage pools during lipolysis. Lipolysis represents a multistep process of intracellular TG hydrolysis, which requires the consecutive activity of at least three enzymes: adipose triglyceride lipase (ATGL), hormone sensitive lipase (HSL), and monoglyceride lipase (MGL). End products of lipolysis are free fatty acids (FFAs) and glycerol, which mainly serve as substrates for adenosine triphosphate (ATP) production in the process of β-oxidation and gluconeogenesis, respectively. FFAs are also involved in signaling pathways and regulation of gene transcription (reviewed in (45)).

1.2.1. ATGL – the first but the youngest

ATGL is the first and rate limiting enzyme in TG hydrolysis (46). The enzyme belongs to the family of patatin-like phospholipase domain containing proteins (PNPLAs) and shows substrate specificity towards TGs (47) and, to a much lesser extent, phospholipids (48). Its activity is induced by fasting, glucocorticoids, peroxisome proliferator-activated receptor (PPAR) agonists, adenosine monophosphate-activated protein kinase α (AMPK) activation and decreased by feeding and insulin (45). By far the strongest regulation of ATGL activity is carried out by comparative gene identification-58 (CGI-58) (47) as its co-activator, and G0/G1 switch gene 2 (G0S2) as its inhibitor (49). In the basal state, ATGL is located on the LD surface and in the cytosol (49), whereas CGI-58 is associated with the LD membrane protein perilipin-1. Upon β-adrenergic stimulation, ATGL does not undergo direct phosphorylation and activation via protein kinase A (PKA), but instead PKA phosphorylates perilipin-1, which allows CGI-58 to dissociate from perilipin-1 and bind to ATGL, resulting in ATGL activation and translocation of cytosolic ATGL to the LD (Figure 6) (45).

ATGL knockout (-/-) mice are is characterized by massive TG accumulation in several tissues. Severe ectopic TG accumulation in cardiomyocytes leads to cardiac dysfunction and premature death of these mice. In addition, they exhibit reduced plasma TG, FFA, and insulin concentrations but despite ectopic fat accumulation, increased glucose tolerance and insulin sensitivity (50).

ATGL mutations in humans are named neutral lipid storage disease and are characterized by Jordans' anomaly (fat-filled leukocytes), skeletal muscle and cardiomyopathy, and occasionally hepatomegaly (51, 52). The disorder shares a similar phenotype with Chanarin-Dorfmann syndrome (mutation of CGI-58), which is additionally associated with severe ichthyosis but no cardiomyopathy (53).

1.2.2. HSL – the middle and the promiscuous one

HSL belongs to the α/β-hydrolase family of enzymes (54). Although it shows broad range of substrate specificities, being able to cleave TGs, monoglycerides (MGs), cholesterol esters (CEs), and retinyl esters, HSL is the rate-limiting for the catabolism of diglycerides (DGs) (55, 56). HSL activity is strongly regulated by hormones. Under basal conditions, HSL is localized in the cytosol. In adipose tissue, β-adrenergic stimulation causes perilipin-1 phosphorylation and HSL translocation to the LD surface. In addition, HSL gets phosphorylated and activated in a PKA-dependent manner (Figure 6). Other kinases, such as AMPK, extracellular signal-regulated kinase (ERK) and glycogen synthase kinase 4 are also capable to activate HSL, whereas insulin reduces HSL activity (45).

Mice genetically deficient in HSL are characterized by a lean phenotype, resistance to diet-induced obesity, and DG (57) and CE (58) accumulation in different tissues. Knockout mice have improved glucose tolerance and show reduced diet-induced insulin resistance (59, 60). Male knockout mice are infertile due to severe oligospermia (61).

Recently, a mutation of human HSL has been reported, characterized by reduced WAT storage and increased inflammation, ectopic hepatic fat accumulation, dyslipidemia, and early onset of type 2 diabetes (T2M) (62).

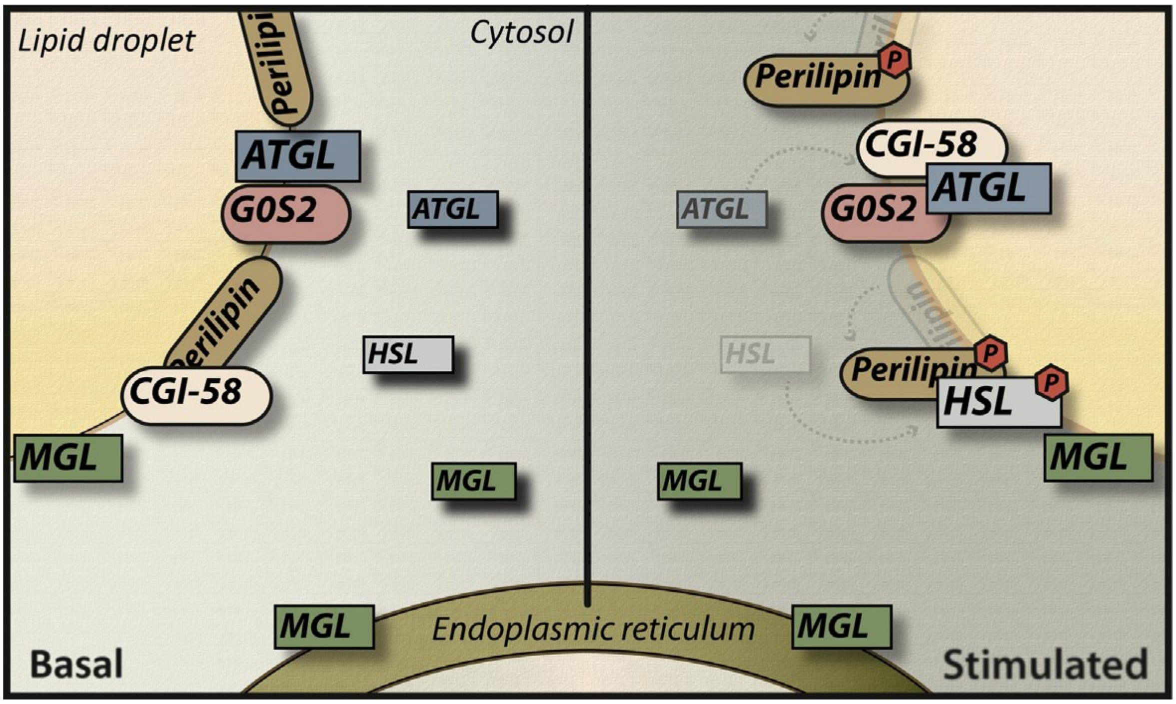

Figure 6. Lipases in lipolysis in basal and stimulated states. (A) In the basal state, CGI-58 is bound to perilipin-1 and thus cannot bind and activate ATGL. HSL is located in the cytosol, whereas MGL localizes to the surface of the LD, cytosol, and endoplasmic reticulum (ER). (B) Upon β-adrenergic stimulation, perilipin-1 gets phosphorylated, allowing CGI-58 to recruit cytosolic ATGL, bind ATGL and cause its activation to cleave TGs to DGs. Moreover, perilipin-1 and HSL phosphorylations lead

to HSL translocation to the LD surface and degradation of DGs to MGs. Finally, MGL hydrolyzes MGs to glycerol and FFA. Adapted from Schweiger M. et al, Measurement of lipolysis (63).

1.2.3. MGL – last but not the least

The first evidence of MG hydrolase activity in rat and rabbit adipose tissue homogenates was reported by Vaughan *et al.* (64) in 1964. Soon afterwards, MGL was purified from rat adipose tissue and partially characterized (65). Finally, cloning of the murine gene sequence encoding for MGL was carried out in 1997 (66). Within the mouse genome, MGL gene is located on chromosome 6 and consists of 7 exons (67). The enzyme is a 303 amino acids long protein with 33 kDa mass and belongs (similar to HSL) to the α/β-hydrolase superfamily (68). MGL contains a catalytic triad consisting of Ser122, Asp239 and His269, as confirmed by point mutation studies (66). X-ray diffraction was used to solve the 3D structure of human MGL and the enzyme crystallized as a dimer (69, 70).

The optimal pH for the enzymatic activity of MGL is 8.0, with a *Km* of approximately 0.3 μM for oleoylglycerol. MGL seems to be strictly responsible for MG cleavage since it does not show any hydrolytic activities towards TGs, DGs, CEs, lysophosphatidylcholine, and only very low activity towards prostaglandin glycerol esters (71-74). The enzyme is not regioselective and hydrolyzes 2-oleoylglycerol and 1(3)-oleoylglycerol with equal rates (71). Within MG species, MGL does not show selectivity towards acyl chain length, (65) however, MGs containing unsaturated FAs are preferential substrates for its activity (75, 76).

Within the mammalian system, MGL is ubiquitously expressed with highest mRNA transcript levels found in white and brown adipose tissue, kidney, testis, adrenal gland, brain, heart, lung, skeletal muscle, liver, ovary, and spleen, with descending abundance of order (66). Within the cell, MGL has been identified within the cytosol and on the plasma membrane (77-79), endoplasmic reticulum (ER) (80), and on surface of LDs (65, 66, 71).

In contrast to ATGL and HSL, there is no evidence that MGL requires hormonal activation or mediation of co-activators for its hydrolytic activity. However, it cannot be excluded that other forms of regulation, such as alternative splicing or posttranslational modifications, can occur. This is plausible since, depending on the tissue, MGL exists in different variants. Western blot analyses revealed that in addition to a 33 kDa large murine MGL in adipose tissue, liver, lung, heart, kidney, spleen, and adrenals, in brain and testis a second 2 kDa larger MGL band can be identified, whereas in skeletal muscle MGL is a 40 kDa large protein (67, 77, 81, 82). Moreover, recent results have shown that MGL can be upregulated on the transcriptional level by PPARα activation (83).

To date, there is no case report of MGL mutation in humans. Mice genetically deficient in MGL have been generated only recently (84-86). These animals are characterized by a significant increase in MG species in virtually all tissues. Importantly, 2-arachidonoylglycerol (2-AG), the main endocannabinoid in the mammalian system, is inactivated by the hydrolytic activity of MGL. Although 2-AG concentrations in the brain of these mice were elevated 10-60 fold, animals showed lack of cannabimimetic effects on peripheral inflammatory and neuropathic pain stimuli, locomotor activity and food intake. In contrast, they remained resistant to the effects caused by exogenous cannabinoid receptor (CBR) agonist treatment. These observations are explained by cannabinoid 1 receptor (CB1R) desensitization in brain regions, as a consequence of elevated 2-AG concentrations and concomitant CB1R downregulation and dampening of signaling mediated by this receptor (84-86).

However, little is known regarding metabolic adaptations in mice genetically lacking MGL. Current knowledge is limited on the effects of MGL in lipolysis, reduced fasting plasma TG concentrations, reduced hepatic TG content and very low-density lipoprotein (VLDL) secretion, as well as improved glucose tolerance after high-fat diet treatment (86). Recently, consequences of MGL deficiency on intestinal functions have been described. MGL-/- mice on low-fat diet showed reduced body weight, similar energy expenditure to wild-type (WT) animals but increased food intake. High-fat diet-fed MGL-/- mice had similar weights and food intake to controls but reduced energy expenditure. Moreover, circulating TG concentrations and chylomicron secretion were reduced in both low and high-fat diet-fed MGL-/- mice (87).

Therefore, MGL-/- mice are a powerful tool to phenocopy and investigate direct consequences of chronic MGL inhibition and indirect effects of endocannabinoid signaling on whole body metabolism. Pharmacological inhibition of MGL arises as a future possibility for pharmacological treatment, as the small molecule inhibitor JZL 184, which selectively inhibits MGL (88).

1.3. Endocannabinoid (EC) system

For centuries, marijuana has been used throughout the world as traditional medicine and a psychoactive drug. The main active component of *Cannabis sativa* is Δ^9-tetrahydrocannabinol (Δ^9-THC) (89), which exhibits a plethora of pharmacological effects in humans and laboratory animals, ranging from hallucinations, euphoria, impairment of short-term memory, hyperphagia, analgesia, and locomotor hypomotility to suppression of immune response (90). During the 1990s, CB1R (91) and CB2R (92) were identified and THC postulated as their natural ligand. However, it is uncommon in nature that an organism produces highly expressed receptors, at least in brain tissue, for an exogenous ligand. This notion prompted the search for the endogenous ligands of the CBRs and the first one identified was N-arachidonoylethanolamine, named anandamide (93). Soon after, 2-arachidonoylglycerol (2-AG) was identified as a second CBR ligand (94, 95). Thus, lipid molecules were identified as mediators of EC signaling. Among the enzymes involved in biosynthesis and degradation of ECs, MGL emerged as an enzyme at the crossroad of TG hydrolysis and 2-AG inactivation by directly affecting lipolysis and indirectly EC signaling.

1.3.1. CBRs

Both CBRs belong to the seven transmembrane Gi/Go protein-coupled receptor family and are thus negatively coupled to adenylyl cyclase and positively to mitogen-activated protein kinase (MAPK) (96).

Human CB1R is a 472 amino acids long protein, which gene is located on the 6q14-15 chromosome. CB2R consists of 360 amino acids and its gene is located on the 1p36 chromosome. The receptors share approximately 44% of sequence homology (90). CB1R has the highest expression in central nervous system (CNS) and in primates is mostly found in substantia nigra, cerebellum, hippocampus, and cortex (97). Lower CB1 receptor densities are found in peripheral tissues such as liver, pancreas, skeletal muscle, adipocytes, adrenals, and testis (98). CB2R is abundantly expressed in human immune cells, with declining expression levels from B lymphocytes, natural killer (NK) cells, monocytes, neutrophils to T lymphocytes (99). It is important to mention, however, that CBR distribution is biphasic but not dichotomic. This means that most of the tissues express both receptors but the receptor abundance is shifted towards one of the extremes, with CB1R in the CNS and CB2R in immune cells, respectively.

1.3.2. CB1R

After identification of CBRs and extensive investigation of the cannabinoid system by using pharmacological interventions, CB1R-/- mice were generated in 1999 (100). The animals are viable and fertile but have a reduced life span (101). Surprisingly, these mice show a series of cannabimimetic effects (101), despite the absence of the main CBR, but remain resistant to agonist-induced potentiating of cannabinoid signaling (100). In addition, these mice are lean, resistant to diet-induced obesity, protected from insulin and leptin resistance (102) as well as from hepatic steatosis HFD treatment (103).

However, only few studies investigated the implication of CB1R on atherosclerosis. Most of the work so far is limited to pharmacological inhibition of CB1R-mediated signaling by the inverse CB1R agonist rimonabant (SR141716-A). In apolipoprotein E (ApoE) -/- mice, rimonabant had no direct effect on atherogenesis but significantly improved endothelial dysfunction and reduced ROS production (104). In LDLR-/- mice, rimonabant treatment dramatically reduced atherosclerotic plaque formation, macrophage inflammatory propensity, and thioglycolate-induced recruitment (105). Multiple beneficial effects of CB1R inhibition on cardio-metabolic parameters and energy homeostasis led to a series of randomized, double-blind clinical trials investigating rimonabant in obesity. Beneficial effects were proven on weight reduction and CVD risks (106, 107), dyslipidemia (108), and glycemic control (109, 110), resulting in the European approval of the use of rimonabant for obesity treatment in 2006. However, a meta-analysis of randomized trials found a significant increase in psychiatric adverse effects of rimonabant-treated patients (111). Reduced compliance to the therapy due to increased anxiety and depression as well as two suicidal cases among rimonabant-treated patients led to withdrawal of the drug from the European market in 2009 (112).

1.3.3. CB2R

The first CB2R-/- mice were generated in 2000. They are viable, fertile, and without gross morphological characteristics (113). However, these animals are deficient in splenic B and memory CD4$^+$ T lymphocytes, peritoneal B1a lymphocytes, and intestinal NK cells (114). They also show pronounced age-related bone loss, due to proliferation of osteoclast precursors (115), increased fibrosis, and hepatic damage in liver injury models (116, 117).

The role of CB2R in atherosclerosis has been investigated as well. Low doses of Δ^9-THC attenuated atherogenesis in ApoE-/- mice by reducing macrophage migratory capacity, which resulted in decreased macrophage lesion infiltration, diminishing proliferation capacity of T_H1 lymphocytes with a shift in T_H1/T_H2 balance, and decreasing IFN-γ secretion. However, the beneficial effects of Δ^9-THC treatment were abolished when mice were treated with a specific CB2R antagonist, suggesting that CB2R but not CB1R signaling is crucial for the anti-atherosclerotic effect of Δ^9-THC (118). Moreover, pharmacological activation of the cannabinoid system with the CB1R/CB2R agonist Win55212-2 caused a similar plaque phenotype in a CB2R-dependent manner (119). When crossed to ApoE-/- background, CB2R-/- mice showed more pronounced atherogenesis with increased plaque macrophage infiltration, ROS production, and endothelial dysfunction. The phenotype was independent from CB2R expression in hematopoietic cells, as shown by BM transplantation. Interestingly, the same study showed that CB2R deficiency caused alterations in EC signaling compared to WT mice, with the reduction in aortic, but not plasma 2-AG concentrations and diminished expression of MGL and diacylglycerol lipase (DAGL) (120). Other studies showed that whole body (121) or hematopoietic CB2R deficiency mildly aggravates atherogenesis in LDLR-/- mice (122). These data indicate that CBR signaling has a strong influence on lipid and carbohydrate metabolism, inflammatory response, and concomitantly, on atherogenesis.

1.3.4. Anandamide – the first to be discovered

N-arachidonoylethanolamine (anandamide) was the first EC molecule isolated from porcine brain. It binds CB1R with great affinity (Ki = 52 nM) and upon administration causes cannabimimetic effects in mice (123). It is, however, still a matter of debate whether anandamide is a true endogenous cannabinoid. Receptor activation studies showed that anandamide acts only as partial agonist on CBR, even being able to antagonize the agonist-mediated receptor activation (124-127). It is extremely uncommon that the true endogenous receptor ligand possesses only partial agonistic activity. Moreover, structure-activity relationship studies suggested that 2-

AG rather than anandamide is the true natural ligand for both CB1R and CB2R (128, 129). On the other hand, anandamide has been proposed as a true endogenous ligand for the transient receptor potential cation channel subfamily V member 1 (TRPV1) (130-132). Although multiple biosynthesis pathways for anandamide have been proposed, knockout mice for these proposed genes lack anandamide accumulation, arguing for an alternative, yet undiscovered biosynthesis pathway.

The main enzyme responsible for anandamide degradation is fatty acid amide hydrolase (FAAH). Indeed, FAAH-/- mice demonstrate 15-fold increased concentrations of anandamide in the brain, but except for hypoalgesia, fail to show any other cannabimimetic effects. In contrast to WT animals, these mice are highly sensitive to exogenous application of anandamide, producing profound cannabimimetic effects (133). Another study, however, found increased body weight and adiposity in FAAH-/- mice on both chow and HFD, increased plasma FFA, TG, and glucose concentrations, ectopic TG deposition, and insulin resistance (134).

After crossing on the ApoE-/- background and feeding with HFD, FAAH-/- mice developed smaller but destabilized atherosclerotic plaques. These lesions were characterized by comparable amount of intraplaque macrophages, but reduced T lymphocyte and VSMC content, increased neutrophil infiltration, and increased circulating concentrations of T_H1 cytokines. Important to mention, this study also showed unchanged 2-AG concentrations in ApoE-/-FAAH-/- mice during HFD feeding, whereas 2-AG levels were constantly increasing during nutritional challenge of ApoE-/- mice (135). The same authors published later the opposite effect of anandamide on SMCs in the model of neointima formation triggered by ballooning injury in ApoE-/-FAAH-/- animals (136).

1.3.5. 2-AG – the true and the right one

Soon after anandamide, 2-AG was postulated as a potential EC with strong binding affinity to rat synaptosome membranes (94). 2-AG from the canine gut binds to CB1R and mimics a Δ^9-THC-provoked tetrad consisting of hypomotility, hypothermia, antinociception and catalepsy when administered to mice (137). Although 2-AG binds CB1Rs with reduced affinity compared to anandamide (Ki = 15 μM), in the mammalian system it is present at much higher, nmol/g tissue concentrations, compared to pmol/g tissue range of anandamide (90). Further studies defined 2-AG as the only endogenous CBR ligand which acts as full agonist on both CB1R and CB2R (127-129, 138).

2-AG biosynthesis can take several different pathways. Most of the cellular 2-AG is generated after hydrolysis of membrane phosphatidylinositol (PI) with arachidonic acid at the *sn*-2 position by phospholipase (PL) C to DG, with the subsequent DG cleavage by DAGLα or β to 2-AG (139). This is probably the most dominant pathway in 2-AG biosynthesis. Alternatively, 2-AG can be generated by PLA_1 mediated hydrolysis of PI, generating lyso-PI, which is further cleaved by PLC to 2-AG (140). Finally, lysophospathidic acid can be esterified with arachidonoyl-CoA to generate phosphatidic acid, which is subsequently hydrolyzed by PA phosphohydrolase to generate DG, which is hydrolyzed by DAGL to 2-AG (141) (Figure 7).

Since there is no evidence of vesicular transport of 2-AG, particularly due to its high lipophilic properties, it is considered that the molecule is produced “on-demand” when physiologically required by cleavage of membrane phospholipids, after which it exerts its effects and is rapidly degraded and inactivated (142, 143).

Degradation of 2-AG can be performed through the action of at least 5 different enzymes: MGL, HSL, FAAH, and recently discovered α/β hydrolase domain containing protein (ABHD) 6 and ABHD12 (Figure 7). The first overexpressing (77) and silencing experiments (78) undoubtedly demonstrated the capability of MGL to degrade 2-AG. The data were reconfirmed by pharmacological inhibition of MGL activity towards 2-AG hydrolysis (144-146). Functional proteomic analysis revealed that, at least in rat brain, MGL accounts for as much as 85 % of total 2-AG hydrolysis, with ABHD12, ABHD6, and FAAH accounting for the remaining 9, 4, and 1 %, respectively (81). FAAH is also capable to directly cleave 2-AG *in vitro* (147). In addition, HSL was identified as a contributing factor in the hydrolysis of WAT-derived MGs, being able to partially compensate for the lack of MGL in the knockout model (86). It is, however, important to mention that besides MGL and HSL, there is no evidence that other lipases, although possessing MGL hydrolase activity, have any physiological relevance to 2-AG homeostasis and EC signaling, since FAAH deficiency (148, 149) and ABHD6-anti sense oligonucleotide (ASO) treatment (150) did not alter 2-AG concentrations in the respective animal models. Further generation and analysis of 2-AG levels in ABHD6 and -12-/- mice should help to unveil the contribution of these two enzymes to 2-AG homeostasis.

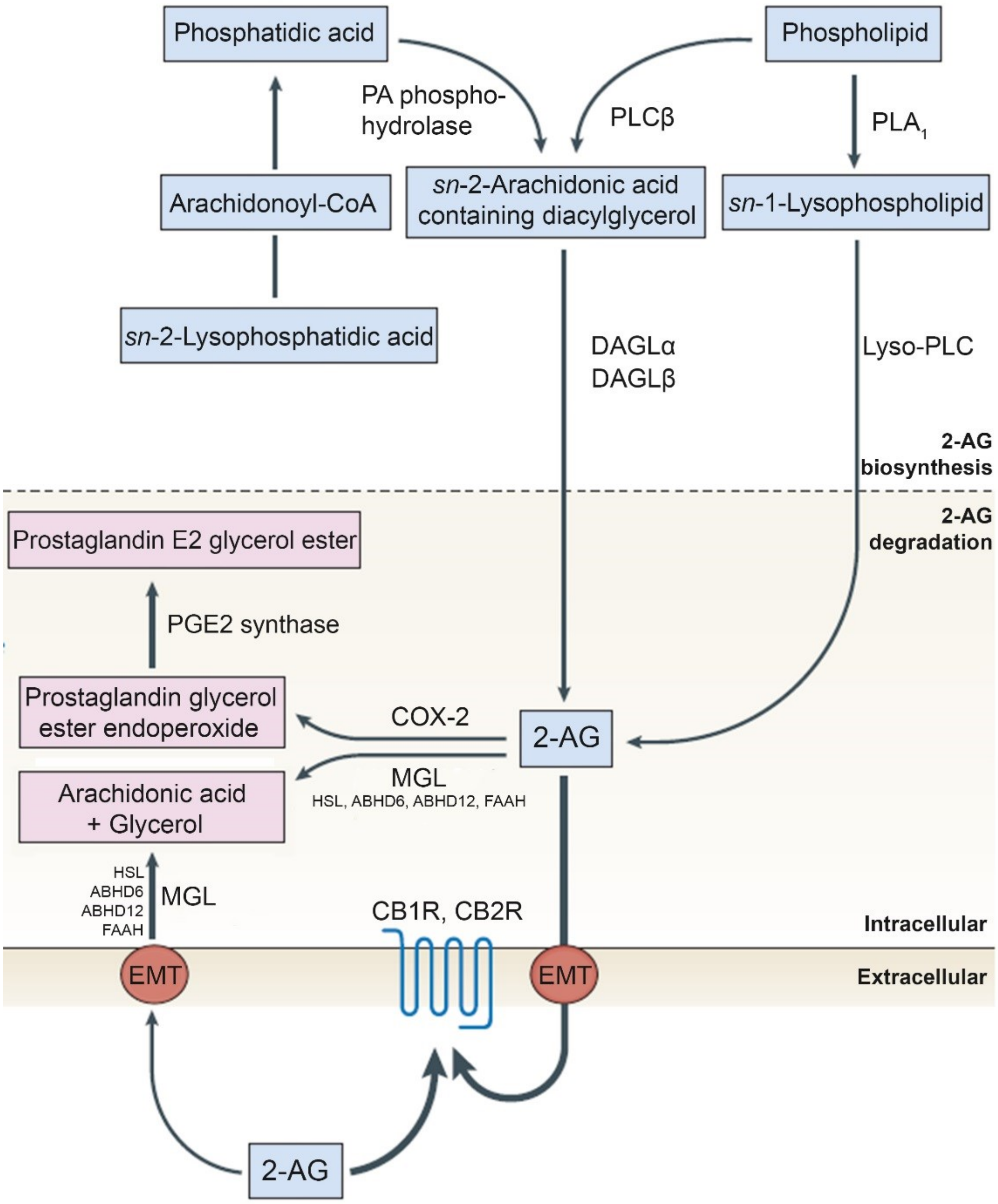

Figure 7. Biosynthesis and degradation of 2-AG. Biosynthesis of 2-AG can take three different pathways: lysophosphatidic acid (LPA) can be re-esterified with arachidonoyl-CoA to phosphatidic acid (PA), which is then cleaved by PA phosphohydrolase to DG. DAGLα or β hydrolyze DG to 2-AG. Alternatively, phosphatidylinositol (PI) is either cleaved by PLC to DG and concomitantly by DAGLs to 2-AG, or it gets hydrolyzed by PLA_1 to lyso-PI, which is then subjected to PLC-mediated degradation to 2-AG. Degradation and inactivation of 2-AG is mediated mainly by MGL, although HSL, ABHD6, ABHD12, and FAAH showed hydrolytic activity towards 2-AG, at least *in vitro*. 2-AG can be also cleaved by COX-2 and PGE_2 synthase to prostaglandin E2 glycerol ester. Adapted from Di Marzo V., Targeting the endocannabinoid system: to enhance or reduce? (151)

1.3.6. CB1R in (patho)physiology

The majority of cannabimimetic effects are found in the CNS, which expresses the highest density of CB1R. These effects are mostly associated with modulation of signal transduction, memory and learning, regulation of food intake, pain sensations, and locomotor activity. Initial experiments revealed that in neurons, 2-AG suppresses depolarization-induced rapid elevation of intracellular free Ca^{2+} concentrations, essential for neurotransmitter release. This led to the theory that the EC system functions in the retrograde manner and modulates neural plasticity. Indeed, further investigations showed that increased synaptic transmission in postsynaptic neurons stimulates 2-AG production from membrane phospholipids. This newly produced 2-AG then diffuses through the cell membrane towards presynaptic neurons where it binds CBRs. Upon binding and via Gi/o stimulation, voltage Ca^{2+} channels on the presynaptic neurons are inhibited, which leads to the reduction in intracellular Ca^{2+} levels and reduced release of vesicle-stored neurotransmitters from presynaptic neurons, namely γ-aminobutyric acid (GABA) and glutamine (90). Since GABA has inhibitory and glutamine excitatory functions in the CNS, EC signaling is thereby capable to inhibit both of these processes through depolarization-induced suppression of inhibition and depolarization-induced suppression of excitation. Concomitantly, high CB1R densities are found in the brain regions characterized by high synaptic activity responsible for learning and memory, where the EC system modulates the CNS plasticity and signal transduction. Thus, 2-AG can mediate the suppressive effects of cellular hyperexcitability and also prevent epileptiform seizures through neuroprotection (152).

In addition, 2-AG-mediated neuroprotection was documented in close-head injury (153), hypoxia (154), and multiple sclerosis models (155). Pain sensations are modulated by EC activation with increased analgesia after direct 2-AG administration (137) or the increase of 2-AG levels in brain upon administration of MGL inhibitors (156, 157). A mouse restraint-induced anxiety model shows inverse correlation in terms of stress induction and brain 2-AG levels (158). Limited data are available regarding emesis, but it seems that 2-AG, similarly to THC, reduces vomiting (159). Food intake is also strongly regulated by EC signaling, since brain 2-AG levels inversely correlate with satiety and 2-AG administration induces hyperphagia (160). Increased hypothalamic EC levels are found in genetically obese mouse and rat models with dysregulated leptin signaling, and leptin administration reduces elevated hypothalamic 2-AG levels, arguing for a strong link between leptin signaling and the EC system (161).

CB1R is present in peripheral tissues, where it regulates specific metabolic pathways associated with lipid and carbohydrate metabolism. In adipocytes, CB1R expression increases during adipogenesis. Activation of adipose EC stimulates PPARγ signaling (162), *de novo* lipogenesis (through increased activation of sterol regulatory element-binding protein 1c (SREBP-1c) and its downstream targets acetyl-CoA carboxylase 1 (ACC1) and fatty acid synthase (FAS) (103)), increases glucose uptake (163), and potentiates lipid uptake through upregulation of lipoprotein lipase (LPL) (164). In addition, 2-AG concentrations were increased in epididymal but reduced in subcutaneous WAT of mice fed HFD (165).

Similarly, visceral but not subcutaneous adipose tissue of obese humans contains higher 2-AG levels, indicating alterations in adipose EC signaling during obesity (162). Although adipocytes were considered as an inert energy storage depot for a long time, numerous data show the importance of adipose tissue as an endocrine organ through adipokine production, cell signaling, and concomitantly energy homeostasis. However, data regarding regulation of adipokine production by EC are limited and controversial. While some studies showed that CB1R activation in adipocytes causes reduced production of adiponectin (162), which is reversed with rimonabant treatment (166), others failed to reproduce the effect of EC on regulation of adiponectin production (163, 167, 168).

Liver is another organ which is strongly involved in energy homeostasis and which can be influenced by the EC system in physiological and pathological states. CB1Rs are found at very low levels in hepatic tissue and their activation potentiate fibrosis (169, 170). However, 2-AG itself has antifibrinogenic effects via a CB1R-independent mechanism (171). In contrast, CB2R activation has a protective role in liver fibrosis, since CB2R agonist treatment of rats with cirrhotic livers ameliorated (172) and genetic CB2R deficiency in mice aggravated the state of hepatic fibrosis (116). Evidence of an EC involvement in hepatic metabolism came with the notion that CB1R densities increase in liver during HFD feeding, whereas receptor blockade attenuated *de novo* lipogenesis caused by SREBP1-c activation and upregulation of its downstream targets ACC1 and FAS (103, 173). Moreover, hepatic FA β-oxidation is reduced with potentiated CB1R activation, which is a contributing factor for lipid accumulation and steatohepatitis (174). However, it still remains elusive whether these effects of the EC system are caused solely due to CB1R activation in hepatocytes or other tissues. In fact, liver-specific CB1R deficiency only partially reduces hepatic steatosis (174), whereas selective transgenic overexpression of CB1R in hepatocytes of CB1R-/- mice shows the same profound reduction in hepatic steatosis as in CB1R -/- mice (175). A recent study from Ruby *et al.* also shows that acute MGL inhibition with concomitant 2-AG increase regulates the lipoprotein metabolism by reducing the ApoE-mediated clearance of ApoB-rich lipoprotein particles, even though VLDL output remained unchanged and LPL activity increased (176).

Effects of EC signaling on glucose metabolism have been described as well. The increase in CB1R densities in skeletal muscle has been found in mice fed HFD (98) as well as increased EC levels in sera of overweight patients with T2M (162). Human skeletal muscle cells treated with EC-containing conditioned media from obese patient adipocytes showed reduced insulin-stimulated glucose uptake, which could be reversed by CB1R blockade (177). Conversely, blockade of CB1R-mediated signaling improved glucose uptake and oxygen consumption in soleus muscle preparations of genetically obese *ob/ob* mice (167). *In vivo* studies in rats confirmed improved insulin sensitivity and glucose uptake after chronic CB1R blockade (178, 179), whereas mice treated with the inhibitor of EC degrading enzymes showed strongly induced glucose intolerance (180). On the other hand, involvement of pancreatic EC in insulin secretion and pancreatic β-cell function has been elusive. Interestingly, recent evidence point out that infiltrating macrophages have an important role in β-cell survival and function since macrophage CB1R activation triggers the inflammasome pathway and increases production of pro-inflammatory cytokines which cause β-cell failure (181).

1.3.7. CB2R in (patho)physiology

The EC system also largely affects immune functions and inflammatory responses, predominantly via CB2R-mediated signaling. Currently, it is widely accepted that Δ^9-THC-mediated effects on CB2R suppress immune responses, in human and animal models. The effects are associated with reduced T-lymphocyte mitogenic responses (182-185), Ca^{2+} flux (186) and cAMP levels (187, 188), cytolysis (189, 190), antibody production (191-193), macrophage phagocytosis, spreading (194, 195), and oxidative burst (196). In addition, CB2R activation inhibited antigen presentation

(113, 197), leukocyte migration (118, 198), cytokine production (199), and induced leukocyte apoptosis (200, 201). It is important to mention that not all of the effects of Δ^9-THC on the immune system were phenocopied in the models with 2-AG treatment or elevation. The reason for this should not be surprising, though it is often neglected during data interpretation. In 1996, Bayewitch *et al.* elegantly demonstrated that Δ^9-THC, although acting as full agonist on CB1R, exerts very low agonistic activity on CB2R and, in addition, is capable to antagonize the agonist-induced CB2R activation (202). Thus, in the presence of (patho)physiologically elevated 2-AG levels, Δ^9-THC is able to antagonize intrinsic cannabimimetic 2-AG activity, thereby reducing CB2R activation.

Interestingly, the type of biological system also seems to be relevant for the data interpretation, since there seems to be a difference in CBR expression between human and murine monocyte/macrophage cells. Human monocytes express high amount of CB2R, whereas CB1R expression is 17-fold lower. However, cellular stimulation and differentiation to macrophages reduces CB2R and increases CB1R expression in monocytes to a final ratio of 3:1. In mice, however, macrophage activation in the thioglycolate model of aseptic peritonitis causes almost complete depletion of CB1R (203).

Current data addressing 2-AG effects on the immune system are limited, scarce, and often contradictory. It has been shown that 2-AG exerts anti-inflammatory effects by suppressing IL-2 gene expression in murine T lymphocytes (204) and production of TNF-α (205), IFN-γ (206), and IL-6 (207) in murine splenocytes, LPS-stimulated macrophages, and J774 macrophage-like cells, respectively. However, 2-AG also induced production of IL-8 and MCP-1 in HL-60 cells (208). Moreover, 2-AG enhanced the migratory capacity of murine B lymphocytes (209), macrophages (210), microglia (211), and eosinophils (212), and human NK-cells (213), monocytes (214), and eosinophils (215), all leading to the potentiation of the immune response. An additional effect mediating inflammatory response is increased adhesion of human peripheral blood monocytes, which was enhanced by 2-AG (216). Important to mention, however, is that 2-AG may exert some of its effects independently from CBRs, since it was shown that ERK activation by 2-AG is independent of adenylyl cyclase inhibition (217). Thus, some of these effects may possibly be mediated by 2-AG metabolites or degradation products. Namely, arachidonic acid represents a crucial substrate for prostaglandin biosynthesis and therefore could contribute to the mentioned effects on the immune response. Accordingly, in MGL-/- mice where the classical 2-AG degradation pathway is defective, prostaglandin biosynthesis in the ischemia/reperfusion model is attenuated and thereby limits the inflammation (218). Macrophage functions are clearly modulated by 2-AG effects as well. It has been shown that 2-AG treatment enhances phagocytosis of opsonized zymosan particles by HL-60 cells (219). Moreover, lipid uptake and foam cell formation are modulated by the EC system, since 2-AG reduces CD36 expression in human macrophages in a CB2R-dependent manner and thereby limits modified-LDL uptake, lipid accumulation, and macrophage differentiation to foam cells (220). All these data unequivocally demonstrate the importance of the EC system in whole body energy homeostasis, lipid and carbohydrate metabolism as well as immune response and inflammation. More importantly, immune cells are capable to produce EC and secrete them, thereby activating CBRs in autocrine and paracrine manners, causing the potentiation of cannabimimetic effects and inflammatory response modulation.

2. Aim and hypothesis

In the present study, we investigated the role of MGL on atherosclerosis development. We therefore generated an atherosclerotic mouse model deficient in MGL by crossing MGL-/- mice with ApoE-/- animals. Due to the tight association of lipid and carbohydrate metabolism with atherogenesis, we also investigated the effects of MGL deficiency on regulation of lipid and carbohydrate homeostasis. Since MGL catalyzes the final step of TG hydrolysis, we hypothesized that its deficiency limits FFAs release, their availability, and cytotoxicity and in turn potentiates carbohydrate metabolism as a compensatory mechanism in the energy homeostasis. Moreover, since MGL deactivates 2-AG, we hypothesized that the accumulation of this EC leads to desensitization and blunting of EC signaling mediated by CB1R as it was previously shown with MGL-/- mice. However, the effect of chronic elevation of 2-AG on CB2R-dependent functions is still largely elusive and thus we expected that accumulated 2-AG affects macrophages and/or other immune cells, modulates inflammatory response, and contributes to alterations in atherogenesis.

3. Materials and methods

3.1. 3 % Thioglycolate medium

700 mg agar, 0.25 g L-cysteine, 6 g glucose, 3 g peptone 110, 17 g peptone 140, 2.5 g NaCl, 0.1 g Na_2SO_3, 0.5 g Na-thioglycolate were dissolved and boiled in 1000 ml double distilled water (ddH_2O). The solution was allowed to cool down at room temperature (RT) and stored in 15 or 50 ml aliquots at -20°C.

3.2. Ammonium-Chloride-Potassium (ACK) lysis buffer

1 g $KHCO_3$, 8.29 g NH_4Cl and 37.2 mg disodium ethylenediaminetetraacetate (EDTA) were dissolved in 800 ml dH_2O after which pH was adjusted to 7.2 – 7.4 with HCl. dd H_2O was added until 1000 ml volume and solution was sterilized by filtration through a 0.2 µm pore filter.

3.3. Diethyl pyrocarbonate water

400 µl diethyl pyrocarbonate (DEPC) were mixed with 400 ml ddH_2O and thereafter kept under the hood overnight and autoclaved.

3.4. Lysis buffer pH 7

2.72 g KH_2PO_4 (100 mM), 17.12 g sucrose (250 mM), 72 mg EDTA (1 mM) were mixed with 200 ml ddH_2O. 1 mM dithiothreitol, 20 µg/ml leupeptin, 2 µg/ml antipain, and 1 µg/ml pepstatin were added ex tempore to the lysis buffer.

3.5. Oil red O (ORO) stock solution

ORO (0.5 g) was mixed with 100 ml isopropanol under constant stirring for 24 h. The working solution (30 ml of filtered stock and 20 ml ddH_2O, mixed for 10 min, filtered) was freshly prepared before use.

3.6. Protein quantification

Protein concentration was determined by a modified Lowry assay. Cells for protein estimation were dissolved in 1 ml 0.3 M NaOH for 2-4 h with continuous shaking or lysed with lysis buffer (pH7) or RIPA buffer (50 mM Tris-HCl, 150 mM NaCl, 1 % Triton X-100, 0.5 % deoxychelate) and sonicated on ice for 3x, 15 seconds each. Tissues were digested in 1 M NaOH by incubating overnight at 65°C or lysed in lysis buffer (pH7) or RIPA buffer and sonicated on ice for 3x, 15 seconds each. NaOH-digested tissues were diluted with ddH_2O to final concentration of NaOH ≤ 0.3 M. Two to 5 µl of sample were used for protein estimation with DC™ Protein assay (BioRad) according to manufacturer's protocol. BSA (1 mg/ml) was used as protein standard.

3.7. Western blot buffers and reagents

3.7.1. Acrylamide

30 g acrylamide and 0.8 g bisacrylamide were dissolved in 100 ml ddH_2O.

3.7.2. 10 x SDS running buffer

150.1 g glycine, 10 g SDS, and 30.3 g Tris were dissolved in 1000 ml ddH_2O.

3.7.3. Separating gel buffer

4 ml of 10 % SDS, 18.2 g Tris and 80 ml ddH_2O were mixed and pH 8.8 was adjusted with HCl. The final volume was adjusted to 100 ml with ddH_2O.

3.7.4. Stacking gel buffer

6 g Tris was dissolved in 90 ml ddH_2O, pH 6.8 was adjusted with HCl, and the volume was adjusted to 100 ml with ddH_2O.

3.7.5. SDS sample buffer

2.15 g SDS, 0.76 g Tris, and 45 ml ddH_2O were mixed and pH 6.8 was adjusted with HCl. Thereafter, 10 ml glycerol (80 %) and a small quantity of bromphenol blue were added.

3.7.6. SDS running buffer

30.3 g Tris, 150.1 g glycine, and 10 g SDS were dissolved in 1000 ml H_2O.

3.7.7. 10 x Blot buffer

1 mg/ml EDTA, 30 g glycine and 12.1 g Tris were mixed in 1000 ml ddH_2O.

3.7.8. 10 x Blot washing buffer

90 g NaCl, 5 g Tween 20, 100 ml of 1 M Tris-HCl (pH 7.4) were mixed in 1000 ml ddH_2O.

3.7.9. Stacking gel

Stock solutions	Volume
Acrylamide	350 µl
Stacking gel buffer	385 µl
50 % Glycerol	885 µl
Tetramethylethylenediamine (TEMED)	3.8 µl
10 % w/v Ammonium persulphate (APS)	38 µl

3.7.10. Separating gel (10 %)

Stock solutions	Volume
Acrylamide	4.3 ml
Separating gel buffer	2.17 ml
ddH2O	2.13 ml
Tetramethylethylenediamine (TEMED)	4.4 µl
10 % w/v Ammonium persulphate (APS)	76 µl

3.8. Gelatin zymography buffers and solutions

3.8.1. Zymography loading buffer

Tris (757.13 mg) was dissolved in 20 ml of ddH_2O and pH was adjusted with HCl to 6.8, after which 4 g of SDS were dissolved and ddH_2O added to the final volume of 25 ml. Then, 25 g of glycerol and 10 mg of bromphenol blue were added to the final concentrations Tris-HCl 125mM, 50% glycerol, 8% SDS, and 0.02% bromphenol blue. One part of zymography loading buffer was mixed with two parts of the sample.

3.8.2. Gelatin solution

100 mg gelatin and 0.5 ml 10 % SDS were mixed in 4.5 ml ddH_2O.

3.8.3. Stacking gel

Stock solutions	Volume
Acrylamide	0.65 ml
Stacking gel buffer	1.25 ml
ddH_2O	3.05 ml
10% w/v SDS	50 µl
10% w/v ammonium persulfate (APS)	25 µl
Tetramethylethylenediamine (TEMED)	8 µl

3.8.4. Running gel (10 %)

Stock solutions	Volume
Acrylamide	4.0 ml
Separating gel buffer	3.75 ml
ddH_2O	5.75 ml
Gelatin solution (20 mg/ml, 1 % w/v SDS)	1.5 ml
10% w/v ammonium persulfate (APS)	50 µl
Tetramethylethylenediamine (TEMED)	10 µl

3.8.5. Running buffer

28.83 g glycine, 6 g Tris, and 2 g SDS were dissolved in 2000 ml ddH_2O (final concentrations: 25 mM Tris, 192 mM glycine, 0.1% SDS, pH 8.3).

3.8.6. Renaturation buffer

25 g of Triton X-100 was dissolved in 975 ml of ddH_2O (final concentration 2.5 %).

3.8.7. Incubation buffer

8.766 g NaCl, 1.47 g $CaCl_2x2H_2O$, 6.057 g Tris, and 0.5 g NaN_3 were dissolved in 1000 ml ddH_2O (final concentrations: 50 mM Tris HCl, 150 mM NaCl, 10 mM $CaCl_2$).

3.8.8. Coomassie Brilliant Blue solution

250 mg Coomassie brilliant blue, was added to 125 ml methanol, 50 ml glacial acetic acid, and 325 ml ddH_2O.

3.8.9. Destaining solution

40 ml methanol and 80 ml glacial acetic acid were mixed with 880 ml ddH_2O.

3.9. Animals and diets

All experimental protocols were approved by the Austrian Federal Ministry of Science and Research, Division of Genetic Engineering and Animal Experiments, Vienna, Austria. (BMWF-66.010/0057-II/3b/2011; BMWF-66.010/0159-II/3b/2012; BMWF-66.010/0085-II/3b/2013).

ApoE-/- mice were obtained from the Jackson Laboratory, Bar Harbor, ME. MGL-/- and WT littermate breeding pairs were kindly provided by Dr. Robert Zimmermann, University of Graz. DKO mice were generated by crossing ApoE-/- with MGL-/- mice. Animals were maintained in a clean environment with unlimited accesses to chow diet (4 % fat and 19 % protein; Altromin Spezialfutter GmbH & Co, Lage, Germany) and water, in a regular light-dark cycle (12 h light, 12 h dark). At the age of 6 to 8 weeks, mice were challenged with Western-type diet (WTD, 21 % fat, 0.2 % cholesterol; Ssniff Spezialdiaeten GmbH, Soest, Germany) for 9 to 16 weeks. Fed state body weight was measured weekly during the first 8 weeks of WTD feeding.

3.10. Genotyping

Genotyping was performed after weaning at the age of 4 weeks. DNA was isolated by digesting tail tips in 140 µl Direct PCR-tail lysis reagent and 10 µl proteinase K (10 mg/ml) for 2 h at 56°C and vigorous shaking. To deactivate proteinase K, samples were incubated at 85°C for 45 min. For ApoE genotyping, the following primers were used:

ApoE-forward: 5’-GCCTAGCCGAGGGAGAGCCG-3´;
ApoE-reverse: 5’-TGTGACTTGGGAGCTCTGCAGC-3´;
ApoE-ko forward-: 5’-GCCGCCCCGACTGCATCT-3´.

The reaction mix contained ~100-200 ng of template DNA, 2.5 mM $MgCl_2$, 0.4 mM of each dNTP, 0.1 µM of each primer, 1 U FIREPol DNA Polymerase I (Solis Biodyne, Riia, Estonia), and DyNAzyme™ DNA Polymerase (Finnzymes, Espoo, Finland).

For the MGL genotyping, the following primers were used:

MGL-forward: 5’-TTGCAGCTGGAGTCT GTGTC-3´;
MGL-reverse: 5’-GTCAGTCGAGGCTGGAAGAG-3´;

MGL-ko forward-: 5’-GAGAGTAGAGGCAGCACTGACAA–3´.

In addition to the substances mentioned above for ApoE genotyping, the reaction mix contained 4 % DMSO.

The following cycle conditions were used for the amplification of the specific DNA products:

	ApoE		MGL	
Initial denaturation	95°C – 15 min		95°C – 15 min	
Denaturation	95°C – 30 sec	40 x	95°C – 30 sec	35 x
Annealing	65°C – 1 min		66°C – 1 min	
Elongation	72°C – 1 min		72°C – 1 min	
Final elongation	72°C – 10 min		72°C – 10 min	
Cool down	4°C – ∞		4°C – ∞	

3.11. Fecal production

Fecal production was determined for single-housed animals during 3 consecutive days. Mice were kept on a fasting grid, fecal pellets were collected daily. Samples of 3 days from the same animals were pooled and lyophilized for 24 h. Dry fecal weight production was determined as an average fecal production during 3 days.

3.12. *In vivo* magnetic resonance imaging (MRI) of body fat

MRI of anesthetized mice were acquired at 3T MRI system (Siemens Tim-Trio, Erlangen, Germany) with an eight-channel multipurpose coil (Noras MRI products, Hoechenberg, Germany) to maximize signal-to-noise ratio.

3.13. Energy metabolism *in vivo*

Assesment of energy intake and energy expenditure were performed by indirect calorimetry (TSE PhenoMaster, Tse Systems, Bad Homburg, Germany). Following 48 h acclimatization O2 consumption and CO2 production, locomotor activity, food and water consumption were measured every 15 min during 4 consecutive days.

3.14. Plasma parameters

Mice were fasted for 12 h before 100 µl blood were drawn from *v. facialis.* Plasma was separated by centrifugation at 7000 rpm for 7 min at 4°C and triglyceride (TG), total cholesterol (TC), free cholesterol (FC), glycerol, and non-esterified fatty acid concentrations were measured using enzymatic test kits (Triglycerides FS, Cholesterol FS, Free Cholesterol; DiaSys, Holzheim, Germany; Free Glycerol: Sigma-Aldrich, St. Louis, MO; NEFA-HR: Wako Chemicals; Neuss, Germany) according to manufacturers' instructions.

3.15. Enzyme linked immunosorbent assay (ELISA)

Plasma concentrations of insulin (Mercodia, Uppsala, Sweden), IL-6 (Enzo Life Sciences, Lausane, Switzerland), MCP-1 (R&D Systems, Minneapolis, MN), leptin, and adiponectin (both from EMD Millipore, Billerica, MA) were measured using ELISA kits, according to manufacturers' instructions.

3.16. Fast protein liquid chromatography

Plasma from 5 mice per genotype was pooled and diluted with PBS (1:4). Two hundred µl of each plasma pool was injected onto a Superose 6 column (Amersham Biosciences, Piscataway, NJ) and separated by fast protein liquid chromatography (FPLC) (Pfizer Pharma, Karlsruhe, Germany). The lipoproteins were eluted with 10 mM Tris-HCl, 1 mM EDTA, 0.9% NaCl, and 0.02% NaN_3 (pH 7.4). Forty eight fractions of 0.5 ml each were collected, and TG and TC concentrations were assayed enzymatically. To enhance sensitivity, reaction buffers were supplemented with sodium 3,5-dichloro-2-hydroxy-benzenesulfonate.

3.17. Quantification of 2-AG in tissues and plasma

Tissues and macrophages were homogenized in 800 µl dH_2O. Two hundred µl plasma were mixed with 800 µl dH_2O. Lipids were extracted twice with 4 ml $CHCl_3$/MeOH/H_2O (2:1:0.6, v:v:v) containing 2 µg C17:0 MG (Avanti Lipids, Alabaster, AL) as internal standard. The lipid-containing organic phase was dried and MGs were isolated by solid phase extraction using a self-packed silica gel column. Fractions were obtained by eluting lipids with 99/1 and 90/10 $CHCl_3$/MeOH (v/v) consecutively. 2-AG concentrations were quantitated in the latter fraction using an AQUITY-UPLC (Waters, Manchester, UK) equipped with a BEH-C18-column

(2.1x150 mm, 1.7 µm; Waters) coupled to a SYNAPT™ G1 qTOF HD mass spectrometer (Waters) equipped with an ESI source (221).

3.18. Lipoprotein lipase activity assay

Mice were fasted for 12 h after which animals were injected intraperitoneally with sodium-heparin in PBS (1 IU/kg body weight). Blood was taken from *v. facialis* and immediately stored on ice. Plasma was isolated by centrifugation at 3,500 rpm for 5 min at 4°C. Samples were stored at -80°C until use.

For substrate preparation per sample, 1 µCi of [^{3}H]triolein and 920 ng trioleate (200 mg/ml in chloroform) were dried under a stream of nitrogen. Thereafter, 20 µl of 1 % Triton X-100, 20 µl of 1 M Tris-HCl (pH 8.6) and 80 µl ddH_2O were added and the mixture was sonicated 3 times for 1 min each, on ice. Then, 40 µl heat-inactivated human serum containing ApoC-II as activator (pooled human serum, heated at 50°C for 1 h and stored at -20°C) and 40 µl of 10 % FA-free BSA were added and vortexed.

Two hundred µl of the substrate were incubated with 10 µl of heparinized plasma in a water bath for 1 h at 37°C under continuous shaking. The tubes were transferred onto ice and 3.25 ml stop solution (n-heptane:chloroform:methanol, 7:9:10) and 1 ml of 0.1 M potassium carbonate (pH 10.5) were added. Tubes were vortexed for 10-15 s and centrifuged at 4,000 rpm for 15 min at 4°C. One ml of the upper layer was transferred in tubes containing 3 ml scintillation cocktail and vortexed. The radioactivity was determined by liquid scintillation counting and normalized to protein concentrations.

3.19. Tissue lipid content

Tissue lipid content was determined by Folch method. Briefly, approximately 30 mg of tissue was homogenized in lysis buffer (pH7). Lysates containing 500 µg protein were normalized with the appropriate amount of lysis buffer to the same volume. A chloroform:methanol (2:1) solution was added to the tissue lysates in 20-fold excess and rotated for 2 h at RT. Thereafter, extracts were mixed with 1.2 ml PBS, centrifuged at 4,000 rpm for 15 min at 4°C and the organic phase was transferred to a fresh vial. Two hundred 2 % Triton X-100 in chloroform was added to the extracts, vortexed, and dried under a stream of nitrogen. Thereafter, the samples were redissolved in 100 µl of ddH_2O and TG, TC, and FC concentrations were measured enzymatically according to manufacturers' instructions. CE concentrations were calculated by subtracting FC from TC concentrations.

3.20. Very low-density lipoprotein (VLDL) secretion

Twelve hour-fasted mice were injected intraperitoneally with 500 mg/kg body weight of tyloxapol in PBS. Blood was drawn from *v. facialis* every h post-injection and plasma was separated by centrifugation at 7,000 rpm for 7 min at 4°C. TG content were determined enzymatically, as described above.

3.21. Fecal lipid content

Fecal samples were collected from mice fed WTD, lyophilized, and pulverized using mortar and pestle. Lipids from 100 µg of feces were extracted by rotating for 2 h at RT with hexane:isopropanol (3:2) solution in 80-fold excess. Thereafter, extracts were centrifuged at 4,000 rpm for 15 min at 4°C and the organic phase was decanted to a fresh vial. One hundred 2 % Triton X-100 in chloroform was added to the extracts, vortexed, and dried under a stream of nitrogen. Thereafter, the samples were redissolved in 100 µl of ddH_2O and TG and TC concentrations were measured enzymatically from 20 and 5 µl of extracts, respectively, according to manufacturers' instructions.

3.22. Gut transit time

Mice were fasted for 12 h, after which the animals were gavaged with 200 µl Evans blue suspension (5% Evans blue, 5% gum Arabic in PBS). Afterwards, mice had free access to water and the time until the detection of Evans blue in the feces was recorded.

3.23. Acute intestinal cholesterol and FA uptake

Chow diet-fed mice were fasted for 4 h, after which the animals were gavaged with 200 µl of corn oil containing 2 µCi [^{3}H]cholesterol and 500 µg cholesterol for cholesterol uptake, or 100 µl of corn oil containing 2 µCi [3H]oleic acid for FA uptake study. Every h post-gavaging, blood was collected and plasma isolated as described above. Four h post-gavaging, animals were sacrificed and gastrum, duodenum, jejunum, ileum, and liver were isolated. Tissues were lyophilized for 18 h and dry weight was measured. For cholesterol uptake study, tissues were digested in 1 M

NaOH for 6 h at 65°C and radioactivity was determined by liquid scintillation counting. For FA uptake study, tissues were pulverized with mortar and pestle and lipids extracted by Folch method. Thereafter, extracts were dried under a stream of N_2, dried lipids were redissolved in 100 µl of chloroform and used for thin layer chromatography (TLC) (n-hexane:diethylether:acetic acid (70:30:1, v:v:v)). Phospholipid, FC, FA, TG, and CE-corresponding bands were cut out and radioactivity was determined by liquid scintillation counting.

3.24. Fractional cholesterol absorption

Fractional cholesterol absorption was measured by using the fecal dual-isotope ratio method (222). Chow diet-fed mice were fasted for 4 h and then gavaged with 100 µl of corn oil containing 0.2 µCi $[^3H]$sitostanol and 0.1 µCi $[^{14}C]$cholesterol. Feces were collected daily for 3 consecutive days, lyophilized, and pulverized using mortar and pestle. Fecal lipids were extracted from approximately 180 mg pulverized sample by rotation for 2 h at RT using hexane:isopropanol (3:2) in 40-fold excess. Thereafter, extracts were centrifuged at 4,000 rpm for 15 min at 4°C and the organic phase was decanted to a fresh vial. One hundred 2% Triton X-100 in chloroform was added to the extracts, vortexed, and dried under a stream of N_2. Thereafter, the samples were redissolved in 100 µl of ddH2O and radioactivity in the extracts was determined by liquid scintillation counting. Fractional cholesterol absorption was calculated by the following formula:

% absorption = ((dose $[^{14}C]$:$[^3H]$-fecal $[^{14}C]$:$[^3H]$)/dose $[^{14}C]$:$[^3H]$)*100

3.25. Hepatic fatty acid and cholesterol biosynthesis

Animals were fasted for 12 h and re-fed for 3 h, and then intraperitoneally injected with $[1\text{-}^{14}C]$acetate (5 µCi in 200 µl PBS). One h post-injection, animals were sacrificed and liver was isolated and lyophilized for 48 h. tissues were pulverized with mortar and pestle and lipids extracted by Folch method. Thereafter, extracts were dried under a stream of N_2, dried lipids were redissolved in 100 µl of chloroform and used for thin layer chromatography (TLC) (n-hexane:diethylether:acetic acid (70:30:1, v:v:v)). Phospholipid (PL) , FC, FA, TG, and CE-corresponding bands were cut out and radioactivity was determined by liquid scintillation counting.

3.26. Chylomicron secretion

Mice were fasted for 4 h and then injected intraperitoneally with tyloxapol (500 mg/kg body weight). Thirty min post-injection, animals were gavaged with 200 µl corn oil containing 2 µCi [^{3}H]triolein and 0.5 µCi [^{14}C]cholesterol. Blood was taken hourly, up to 4 h post-gavaging, and radioactivity was determined from isolated plasma by liquid scintillation counting.

3.27. Electron microscopy

Liver tissue was dissected in small tissue fragments and fixed in 2.5 % (w/v) glutaraldehyde and 2 % paraformaldehyde in 0.1 M phosphate buffer (pH 7.4) for 2 h, postfixed in 2 % osmium tetroxide for 2 h at RT, dehydrated in graded series of ethanol, and embedded in a TAAB epoxy resin. Sections (70-nm thick) were contrasted with uranyl acetate and lead citrate. Images were taken using an FEI Techai G^2 20 transmission electron microscope (FEI Eindhoven, Eindhoven, The Netherlands) with a Gatan ultrascan 1000 CCD camera. Acceleration voltage was set to 120 kV.

3.28. Glucose tolerance test

Six h-fasted mice were injected intraperitoneally with 2 g/kg body weight of glucose in PBS. Blood glucose levels were measured 0, 15, 30, 60, 90, 120, 150, and 180 min post-injection using Accu-Chek® Active glucometer and glucose strips (Roche Diagnostics GmbH, Mannheim, Germany).

3.29. Insulin tolerance test

Four h-fasted mice were injected intraperitoneally with 0.75 IU/kg body weight of insulin in PBS (Actrapid Novo Nordisk, 100 IU/ml stock). Blood glucose levels were measured 0, 15, 30, 60, 90, 120, 150, and 180 min post-injection using Accu-Chek® Active glucometer and glucose strips (Roche Diagnostics GmbH, Mannheim, Germany).

3.30. Glucagon tolerance test

Mice in the fed state were injected intraperitoneally with 140 µg/kg body weight of glucagon (GlucaGen® HypoKit 1 mg, Novo Nordisk) in PBS. Blood glucose levels were measured 0, 15, 30, 60, 90, and 120 min post-injection using Accu-Chek®

Active glucometer and glucose strips (Roche Diagnostics GmbH, Mannheim, Germany).

3.31. Pyruvate tolerance test

Twelve h-fasted mice were injected intraperitoneally with 2 g/kg body weight of sodium-pyruvate in PBS. Blood glucose levels were measured 0, 15, 30, 60, 90, and 120 min post-injection using Accu-Chek® Active glucometer and glucose strips (Roche Diagnostics GmbH, Mannheim, Germany).

3.32. Glycerol tolerance test

Twelve h-fasted mice were injected intraperitoneally with 2 g/kg body weight of glycerol in PBS. Blood glucose levels were measured 0, 15, 30, 60, 90, 120, 150, and 180 min post-injection using Accu-Chek® Active glucometer and glucose strips (Roche Diagnostics GmbH, Mannheim, Germany).

3.33. Hepatic glycogen concentrations

Fifty mg of liver was digested in 500 µl of 30 % KOH for 30 min at 95°C. Afterwards, 100 µl of 20 % Na_2SO_4 was added to the digest and vortexed. One ml of 100 % ethanol was added to the tube and thoroughly vortexed, after which the samples were left to precipitate at -20°C for 30 min. Samples were then centrifuged at 6,500 rpm for 10 min at 4°C and the supernatant was discarded. The pellet was washed with 1.5 ml of 70 % ethanol and then the samples were centrifuged once again at 6,500 rpm for 10 min at 4°C. The supernatant was discarded and pellets were dried under a stream of air. Pellets were then dissolved in 500 or 1000 µl ddH_2O.Thereafter, 20 µl of fed state and 150 µl of fasted state liver samples, respectively, were mixed with water to a volume of 270 µl and 280 µl of 5 % phenol solution was added. After vortexing, 1.4 ml of concentrated H_2SO_4 was added, samples were vortexed and kept on ice for 30 min. Glycogen concentrations were measured spectrophotometrically at 490 nm wavelength.

3.34. Complete blood cell count

One hundred µl of blood was taken from *v. facialis* in EDTA-coated tubes (Kabe Labortechnik GmbH, Nuembrecht-Eisenroth, Germany). Complete blood cell count was performed on a Cell Counter Analyzer MS9-5V (Melet Schloesing Laboratories GmbH, Maria Enzersdorf, Austria).

3.35. Immunophenotyping of peripheral blood

Peripheral blood cells were collected by retro-bulbar puncture from isoflurane anesthetized mice. After red blood cell lysis in ACK lysis buffer, cells were incubated in PBS containing 10 % FCS for 10 min at 4°C. After incubation, the cells were washed, centrifuged (1,400 rpm, 5 min, 4°C), and stained in PBS containing 3 % FCS for 20 min at 4°C with the following antibodies against specific surface markers: CD11b (M1/90), SiglecF (E50-2440), Gr-1 (RB6-8C5) (all purchased from BD Biotechnologies, San Jose, CA), CD115 (AFS98), CD19 (1D3), and CD3 (145-2C11) (purchased from eBioscience, San Diego, CA) for peripheral blood cells. All antibodies were titrated prior to use. Data were acquired on a LSR II flow cytometer with DIVA 6.1.2 software (BD Biosciences) and the analysis was performed using Flowjo (Treestar Inc, San Carlos, CA). The frequencies of specific cell types were calculated as the percentage of living cells.

3.36. Immunophenotyping of BM

For BM analysis, both femurs and tibias were collected and the marrow was flushed out of the bones with HBSS-EDTA using a needle and syringe. Washed cell pellets were resuspended in 200 µl antibody cocktail and incubated at RT for 10 min. Finally, cells were washed in buffer and analyzed immediately. A forward-side scatter gate excluded cell debris and remaining red blood cells and dead cells were excluded by 7-aminoactinomycin D (7-AAD; BD Biosciences) uptake. LSK populations were defined as Lin$^-$Sca-1$^+$c-Kit$^+$ and myeloid progenitors were defined as Lin$^-$c-Kit$^+$Flt3$^+$FcγRII/III^{hi} (GMP) and Lin$^-$c-Kit$^+$CD115$^+$Flt3$^+$ (MDP). Lymphoid progenitors were identified as Lin$^-$c-Kit$^+$IL7Rα$^+$ (CLP). CD115-PE, CD117(c-Kit)-PE-Cy7, CD16/32(FcγRII/III)-eFluor450, Ly-6A/E(Sca-1)-PE-Cy7 were purchased from eBioscience. IL7Rα(CD127)-brilliant violet and Flt3(CD135)-APC were purchased from BioLegend (San Diego, CA) and CD117(c-Kit)-APC from BD Biosciences. Data were acquired on a LSR II flow cytometer with DIVA 6.1.2 software (BD Biosciences) and the analysis was performed using Flowjo (Treestar Inc, San Carlos, CA). The frequencies of specific cell types were calculated as the percentage of living cells.

3.37. White blood cell (WBC) half-life

Each mouse was injected with 3 mg EZ-Link Sulfo-NHS-Biotin (Pierce Biotechnology, Rockford, IL) via tail vein. Two and a half hours, 1, 3, 5, and 7 days post-injection, blood was drawn from *v. facialis.* Red blood cells were lysed with ACK lysis buffer. Remaining WBCs were washed with PBS/EDTA (1,400 rpm, 5 min, 4°C). Cells were then fixed with 4 % neutralized buffered paraformaldehyde (4 % PFA) for 10 min at 4°C, washed once again with PBS/EDTA, and stained with Streptavidin-PE (eBioscience Inc, San Diego, CA) antibody in PBS containing 3% fetal calf serum (FCS) for 20 min at 4°C. Data were acquired on a LSR II flow cytometer using DIVA 6.1.2 software (BD Biosciences, San Jose, CA) and the analysis was performed using Flowjo (Treestar Inc, San Carlos, CA). The frequencies of specific cell types were calculated as the percentage of living cells.

3.38. Cell culture

3.38.1. Mouse peritoneal macrophages (MPMs)

MPMs were collected by injecting 3 ml of 3 % thioglycolate intraperitoneally. Seventytwo h post-injection, MPMs were collected by flushing the peritoneum with 9 ml EDTA-PBS (1 mM EDTA in PBS). Cells were centrifuged at 850 rpm at 4°C for 5 min and then resuspended in the appropriate amount of Dulbecco’s Modified Eagle Medium (DMEM) containing high-glucose (25 mM), 4 mM glutamine, 1 mM pyruvate, 10 % lipoprotein-deficient serum (LPDS), and 1 % penicillin/1 % streptomycin (1 % P/S) and cultured for at least 2 h. Thereafter, the cells were washed 3 times with pre-warmed PBS and cultured for additional 24 h either in the absence or presence of VLDL or acetylated (ac)LDL (100 µg protein/ml medium).

3.38.2. Mouse peritoneal neutrophils (MPNs)

MPNs were collected by injecting 3 ml of 3 % thioglycolate intraperitoneally. Sixteen h post-injection, MPNs were collected by flushing the peritoneum with 9 ml EDTA-PBS (1 mM EDTA in PBS). Cells were centrifuged at 850 rpm at 4°C for 5 min, after which they were resuspended in the appropriate amount of DMEM containing high-glucose (25 mM), 4 mM glutamine, 1 mM pyruvate, 10 % lipoprotein-deficient serum (LPDS) and 1 % penicillin/1 % streptomycin (1 % P/S).

3.39. RNA isolation from MPM and tissues

Primary macrophages were isolated and cultured for at least 24 h. Total RNA was isolated with PerfectPure RNA Cultured Cell Kit (5 Prime GmbH, Hilden, Germany) according to manufacturer’s protocol. Briefly, 400 µl Lysis Solution (with freshly added 1 % β-mercaptoethanol) was added per well. The cells were incubated at RT for 10 min, scraped, and sheared by pressing the lysate through a 25 gauge needle for at least 10 times. These lysates were transferred onto purification columns and centrifuged for 1 min at 14,000 rpm at RT. Four hundred µl of Wash 1 Solution was added to the column and centrifuged again for 1 min at 14,000 rpm at RT. Thereafter, 50 µl of DNase was added. After 15 min at RT, columns were treated twice with 200 µl of Wash 2 Solution and centrifuged at 14,000 rpm at RT for 1 and 2 min, respectively. Finally, the column was transferred to a fresh tube, 30 – 50 µl of Elution solution was added per column and centrifuged at 14,000 rpm at RT for 1 minute.

Total RNA from tissues was isolated using TriFast reagent according to the manufacturer’s protocol (Peqlab, Erlangen, Germany). Briefly, tissues were homogenized in 1 ml of TriFast reagent using Precellys 24 beed homogenizer (Bertin technologies, Siege, France). 200 µl of chloroform was added per ml TriFast reagent, vortexed, and centrifuged at 8,500 rpm at 4°C for 15 min. Supernatant was transferred to a fresh tube, mixed with 2µl of glycogen solution (20 mg/ml, Santa Cruz, Heidelberg, Germany) and 500 µl of isopropanol, vortexed, and centrifuged at 8,500 rpm at 4°C for 10 min. Thereafter, supernatant was discarded, pellets were washed with 75 % ethanol and centrifuged again at 8,500 rpm at 4°C for 5 min. Supernatant was discarded, pellets were air-dried, and resuspended in 30-50 µl DEPC water.

RNA concentrations were measured at 260 nm using NanoDrop (Thermo scientific, Wilmington, USA). Two µl RNA were used for concentration determination using the following equation:

$$c_{(\text{ngRNA/µl})} = \lambda\ 260\text{nm} \times 40$$

RNA integrity was determined by gel electrophoresis. Gels were prepared by boiling 1.1g agarose, 11 ml 10x 3-(N-morpholino)propanesulfonic acid buffer (MOPS) (200 mM MOPS, 80 mM sodium-acetate, 10 mM EDTA, pH7) and 88.8 ml DEPC-water in a microwave. After cooling down to approximately 50°C, 18.7 ml of formalin solution was added to the solution, casted into gel molds, and left to solidify at RT. Two µg of RNA were mixed with 4 µl of RNA Loading buffer and ran at 70 V for 45 min. RNA was identified as non-degraded if clear 28S rRNA band at 4.7 kb and 18S rRNA band at 1.9 kb size could be defined.

3.40. cDNA preparation

cDNA was prepared from RNA by reverse transcription. One or two µg RNA in 10 µl (adjusted with nuclease-free ddH2O) were reversely transcribed by using High-Capacity DNA Reverse Transcription kit (Applied Biosystems, Foster City, CA).

High-Capacity cDNA Reverse Transcription master mix composition

Component	Volume (µl) / reaction
10 x RT Buffer	2
25 x dNTP Mix (100 mM)	0.8
10 x RT Random Primers	2
Multiscribe Reverse Transcriptase	1
RNase Inhibitor	0.7
Nuclease-free H_2O	3.5
1 or 2 µg RNA/10 µl ddH_2O	10
Total volume per reaction	**20**

Reverse transcription thermal cycling conditions were as follows:

	Step 1	Step 2	Step 3	Step 4
Temperature	25°C	37°C	85°C	4°C
Time	10 min	120 min	5 s	∞

3.41. Real time PCR

cDNA was diluted 1:50 in nuclease-free ddH_2O if 2 µg or 1:25 if 1 µg of RNA was used for reverse transcription. Three µl of diluted cDNA, 1 µl of forward and reverse primer (stock solution, 100 µM, diluted 1:10 with nuclease-free ddH_2O), and 5µl QuantiFastTM SYBR® Green were pipetted into a LightCycler 480 white Multiwell plate. The plate was centrifuged for 1 min at 800 rpm and loaded on a RocheLight Cycler 480 instrument.

Real-time PCR program conditions were as follows:

	Temperature	Time	Cycles
Denaturation	95°C	5 min	1
Amplification	95°C 60°C	10 s 30 s	40
Melting Curve	95°C 60°C 95°C	10 s 20 s continuous	1 1
Cool Down	40°C	20 s	1

Cyclophilin A or hypoxanthine-guanine phophoribosyl transferase (HPRT), were used as house-keeping genes for relative gene expressions. Relative expression of gene of interest to housekeeping gene was calculated using the $2^{-\Delta\Delta CT}$ method. Primer sequences which were used are listed in the Table 1.

Table 1. Primer sequences

Gene	Forward primer (5'-3')	Reverse primer (5'-3')
Cyclophilin A	CCATCCAGCCATTCAGTCTT	TTCCAGGATTCATGTGCCAG
Hprt	TCAGTCAACGGGGGACATAAA	GGGGCTGTACTGCTTAACCAG
Atgl	GCCACTCACATCTACGGAGC	GACAGCCACGGATGGTGTTC
Hsl	GCTGGTGACACTCGCAGAAG	TGGCTGGTGTCTCTGTGTCC
Mgl	GCAGCCACTAGGATGGAGATG	GCAATGTAGAACCCCAGAACAC
Lal	CGGCTTGCTGGCAGATTCTA	GTGCAGCCTTGAGAATGACC
Abhd6	TATTGGTACTGGCGGAGGAC	AAGGATGGATGGCTTGTGTC
Abhd12	GTCACCTTGGAGCATGAGC	GCAATGTAGAACCCCAGAACAC
Daglα	GTCCTGCCAGCTATCTTCCTC	CGTGTGGGTTATAGACCAAGC
Daglβ	AGCGACGACTTGGTGTTCC	GCGTGAGATACAACGTCAGACT
Faah	ATTGTGCATGAAAGCCCTACTT	GGGGTCGAGAACTTCTGTAGA
Abca1	CTCTTCATGACTCTAGCCTGGA	ACACAGACAGGAAGACGAACAC
Abcg1	GACGCTGACTATAAGAGAGACC	GGAGTTGCTCAGGACCTTCTTG
Abcg5	AGAGGGCCTCACATCAACAGA	CTGACGCTGTAGGACACATGC
Sr-bl	TTTGGAGTGGTAGTAAAAAGGGC	TGACATCAGGGACTCAGAGTAG

Lrp1	CCACTATGGATGCCCCTAAAAC	GCAATCTCTTTCACCGTCACA
Vldlr	GAGTCTGACTTCGTGTGCAAA	GAACCGTCTTCGCAATCAGGA
Ldlr	CATGTCTGTCACCTGTCAGTCC	CTTGTCCAAGCTGATGCACTCC
Fabp1	ATGAACTTCTCCGGCAAGTACC	GGTCCTCGGGCAGACCTAT
Cd36	GCAGGTCTATCTACGCTGTG	GGTTGTCTGGATTCTGGAGG
Bsep	GAACATGACAAACGGAACAAGC	CCCAGTGATTACCCACAACCTT
Cyp7a1	GGGCATCTCAAGCAAACACCATTC	CGGGACTGATCTAGAGGGGGACAC
HmgCoAr	CTATTGCACCGACAAGAAGCCT	GCCATCACAGTGCCACATACAA
Cpta1	CTCCGCCTGAGCCATGAAG	CACCAGTGATGATGCCATTCT
Fas	GAAGCCGAACACCTCTGTGCAGT	CTCCTTGCTGCCATCTGTATTG
Acc1	GGACTTGGAGCAGAGAACCTTCG	CAAGCTGGTTGTTGGAGGTGTA
Acc2	CGCTCACCAACAGTAAGGTGG	GCTTGGCAGGGAGTTCCTC
Scd1	TTCTTGCGATACACTCTGGTGC	CGGGATTGAATGTTCTTGTCGT
Msr1	TGGAGGAGAGAATCGAAAGCA	CTGGACTGACGAAATCAAGGAA
P-selectin	CATCTGGTTCAGTGCTTTGATCT	ACCCGTGAGTTATTCCATGAGT
E-selectin	TACTGTCAGCGGGACTACACA	CCACCCAGATCCATACGTTATTG
L-selectin	TACATTGCCCAAAAGCCCTTAT	CCTCCTTGGACTTCTTGTTGTT
Icam1	GTGATGCTCAGGTATCCATCCA	CACAGTTCTCAAAGCACAGCG
Vcam1	TGCACAGTCCCTAATGTGTATCC	GACTTTATGCCCATTTCCTCCA
Mmp2	ACCTGAACACTTTCTATGGCTG	CTTCCGCATGGTCTCGATG
Mmp9	GGACCCGAAGCGGACATTG	CGTCGTCGAAATGGGCATCT
Timp1	TCCTCTTGTTGCTATCACTGATAGCTT	CGGTGGTATAAGGTGGTCTCGTT
Timp2	TCAGAGCCAAAGCAGTGAGC	GCCGTGTAGATAAACTCGATGTC
Timp3	CTTCTGCAACTCCGACATCGT	GGGGCATCTTACTGAAGCCTC
Timp4	CACTCGGCTCTAGTGATACGG	CTTGGCCTTCTCGAACCCTTT
Cb1r	AAGTCGATCTTAGACGGCCTT	TCCTAATTTGGATGCCATGTCTC
Cb2r	ACGGTGGCTTGGAGTTCAAC	GCCGGGAGGACAGGATAAT
Vla4	AAAATGGCTCTATC	CAGAAGGCATGACGTAGCAAAT
Lfa1	TGCACCAAGTACAAAGTCAGC	GCGCAAGGAGTCAGGTTCT
Selplg	CCCTGGCAACAGCCTTCAG	GGGTCCTCAAAATCGTCATCC
Arg1	TGGCTTGCGAGACGTAGAC	GCTCAGGTGAATCGGCCTTTT
Mrc-1	GCTGAATCCCAGAAATTCCGC	ATCACAGGCATACAGGGTGAC
Mrc-2	TCTCCCGGAACCGACTCTTC	AACTGGTCCCCTAGTGTACGA
Mgl-2	CAATGTGCTTAGCTGGATGGG	CCATGCCAGTTATCCGGCTG
Chi3l3	CAGGTCTGGCAATTCTTCTGAA	GTCTTGCTCATGTGTGTAAGTGA
Itgax	CTGGATAGCCTTTCTTCTGCTG	GCACACTGTGTCCGAACTCA
Ccl5	GCTGCTTTGCCTACCTCTCC	TCGAGTGACAAACACGACTGC

Gro-1	CTGGGATTCACCTCAAGAACATC	CAGGGTCAAGGCAAGCCTC
Cxcl2	AGTGAACTGCGCTGTCAATG	GCCCTTGAGAGTGGCTATGA

3.42. Western blotting

Macrophages were lysed in RIPA buffer and protein concentrations from cell lysates were determined (Bio-Rad DC protein assay; Bio-Rad Laboratories, Hercules, CA). One hundred µg protein/lane were separated by SDS-PAGE (15%). Proteins were transferred to nitrocellulose membranes (Hybond-C Extra; Amersham Biosciences, Piscataway, NJ). Non-specific binding sites were blocked by incubating the membrane with 5% non-fat dry milk in 1x TBS-T buffer (150 mM NaCl, 10 mM Tris, 0.1% Tween 20, pH 8) for 2 h at RT. Blots were incubated with rabbit polyclonal antibodies against CB2R (1:1,000) (Abcam, Cambridge, UK) and mouse monoclonal antibody against β-actin (1:20,000) (Santa Cruz, Heidelberg, Germany). HRP-conjugated goat anti-rabbit (1:2,500) and rabbit anti-mouse antibodies (1:500) (Dako, Glostrup, Denmark) were visualized by enhanced chemiluminescence detection (Clarity^{TM} Western ECL substrate; Bio-Rad) using a ChemiDoc^{TM} MP imaging system (Bio-Rad).

3.43. MG hydrolase activity assay

Macrophages were lysed in MG hydrolase lysis buffer (250 mM sucrose, 1 mM EDTA, 0.1 % Triton X-100, 20 µM DTT, pH 7.0). Thereafter, 120 µg protein were incubated with 100 µl substrate (2 mM *rac*-1(3)-oleoyl glycerol bound to FA-free BSA in equimolar ratio in 50 mM potassium phosphate buffer, pH 7.0) for 30 min at 37°C. The reaction was stopped by adding 200 µl chloroform, samples were vortexed vigorously and centrifuged at 10,000 x *g* for 5 min at 4ºC. Free glycerol was estimated in 50 µl of the aqueous phage (Sigma-Aldrich, St. Louis, MO) according to manufacturer's instructions.

3.44. Cytosolic Ca^{2+} imaging using Fura-2/AM

Macrophages of ApoE-/- and DKO mice were plated on 30 mm glass coverslips. Prior to experiments, cells were incubated for 40 min with 2 µM Fura-2/AM (TEFLabs; Austin, TX) and maintained in HEPES buffer (138 mM NaCl, 5 mM KCl, 2 mM $CaCl_2$, 1 mM $MgCl_2$, 1 mM HEPES, 2.6 mM $NaHCO_3$, 0.44 mM KH_2PO_4, 0.34 mM Na_2HPO_4, 1 mM glucose, 0.1 % vitamins, 0.2 % essential amino acids, 1% P/S, pH 7.4). During experiments, cells were perfused with HEPES buffer (145 mM NaCl, 5 mM KCl, 2 mM $CaCl_2$, 1 mM $MgCl_2$, 10 mM glucose, 10 mM HEPES, pH 7.4) and stimulated with 20 µM 2-AG followed by 200 µM ATP (final concentrations). All solutions were supplemented with 250 µM sulfinpyrazone to prevent Fura-2 efflux from macrophages. Single cell measurements were performed on a Zeiss AxioVert inverted microscope (Zeiss; Goettingen, Germany) equipped with a polychromator illumination system (VisiChrome, Visitron Systems; Puchheim, Germany) and a thermoelectric-cooled CCD camera (Photometrics CoolSNAP HQ, Visitron Systems). Macrophages were imaged with a 40X oil-immersion objective (Zeiss). Cells were alternately illuminated at 340 and 380 nm (340HT15, 380HT15, Omega Optical; Brattleborough, VT), while fluorescence emission was recorded at 510 nm (510WB40, Omega Optical). Data were acquired by VisiView 2.0.3 (Visitron Systems) software. Results of Fura-2/AM measurements are shown as normalized ratios $(F_{380}/F_{340})/R_0$ to correct for photobleaching.

3.45. VLDL, LDL, HDL, and acetylated LDL preparation

Gradient ultracentrifugation was used to isolate VLDL, LDL, and HDL from human plasma. The plasma density was adjusted to 1.06 g/l with ~10 g NaCl/200 ml plasma. Thereafter, EDTA (1 g/l) and sodium azide (1 g /l) were added. Forty ml of this mixture was transferred to the centrifugation tubes and centrifuged at 48,000 rpm at 15°C for 24 h in an ultracentrifuge.

After centrifugation, two phases were separated; the upper phase contained VLDL/LDL, the lower phase Lp(a) and HDL. These two phases were collected separately and dialyzed with distilled water for 30 min. The upper phase density was adjusted to 1.027 g/l with NaCl and again centrifuged at 48,000 rpm at 15°C for 24 h. After centrifugation, VLDL and LDL were in the upper and lower phase, respectively. The lower phase (LDL) was collected (up to 18 ml) and the density was adjusted to 1.063 g/l with NaCl and centrifuged in 3 ml tubes at 48,000 rpm. After centrifugation, the yellow-colored LDL band (approximately 5 mm), which appeared in the middle of the centrifugation tube, was collected in a sterile tube.

From the lower phase of the first centrifugation step, HDL was separated by adjusting the density to 1.063 g/l and centrifuged at 48,000 rpm. The density was adjusted to 1.21 g/l with NaBr. After centrifugation, HDL_3 in the upper layer was collected and dialyzed for 48 h with PBS. LDL and VLDL were sterilized by passing through 0.2 µm and 0.8 µm filters, respectively, and protein, TG and TC concentrations were measured enzymatically.

For acetylated (ac)LDL preparation, the native LDL fraction (3.2 ml) was mixed with an equal volume of saturated NaCl. This mixture was kept on ice under continuous stirring and 5.4 µl of diethyl ether was added very slowly after every 3 min until a total of 57.76 µl was added. When diethyl ether was added the third time, 100 µl of 10x PBS was added to avoid precipitation. Once 57.76 µl of diethyl ether was added, this mixture was kept stirring on ice for 45 min. Thereafter, acLDL was dialyzed for 2-3 h with sterile PBS at 4°C. TC concentration was measured enzymatically.

3.46. Cholesterol efflux

MPMs were cultured in 12-well plates for 24 h. Per sample, 50 µg [^{3}H]acLDL (preloaded with 0.5 µCi/ml [^{3}H]cholesterol), 1 ml DMEM medium (0.2 % FA-free BSA, 1 % P/S) were prepared. Thereafter, 1 ml of medium was added to each well and incubated for 32 h. Then, the cells were washed with warmed PBS (37°C) and incubated with equilibration medium (DMEM, 0.2 % FA-free BSA, 1 % P/S) for 16 h. After washing, 3 wells were kept for zero time point and other wells for different cholesterol acceptors and time points. As cholesterol acceptors we used control (0.2 % FA-free BSA), 15 µg/ml apoAI or 100 µg/ml HDL$_3$. One ml of cholesterol acceptor medium was added into the respective well and 100 µl medium/well were collected after 1, 3, 6, 9, and 12 h. Hundred µl fresh acceptor medium was added per well at each time point, respectively. The collected 100 µl medium was mixed with 2 ml scintillation cocktail and incubated overnight at 4°C. Radioactivity in the medium was measured by scintillation counting and normalized on protein concentrations. Cholesterol efflux is expressed as the percentage of total cellular [^{3}H]cholesterol present in the medium after 1, 3, 6, 9, and 12 h. Basal efflux in the absence of ApoA-I and HDL$_3$ was subtracted from the data shown.

3.47. Nile red staining and fluorescence microscopy

MPMs were plated in 6-well plates on chamber slides for 24 h in DMEM/10% LPDS/1% P/S. Cells were washed twice with pre-warmed PBS and cultured for additional 24 h in the absence or presence of VLDL or acetylated LDL (100 µg protein/ml medium). Thereafter, cells were washed twice with pre-warmed PBS and fixed with 4% PFA for 10 min. LDs were visualized after Nile red staining (2.5 µg/ml) by confocal laser scanning microscopy using an LSM 510 META microscope system (Carl Zeiss GmbH, Vienna, Austria). Images (x63) were taken at excitation 543 nm and signals were recorded using a 560 nm long pass filter.

3.48. Lipid parameters in macrophages

MPMs were cultured in DMEM, 10 % LPDS, 1 % P/S, washed with pre-warmed PBS after 2 h, and incubated in DMEM, 10% LPDS, 1% P/S for 24 h. Thereafter cells were washed 3x with pre-warmed PBS and incubated in DMEM, 10% LPDS, 1% P/S with or without 100 µg acLDL or VLDL for additional 24 h. Lipids were extracted from the cells after adding 2 ml hexane:isopropanol (3:2, v:v) for 2 h at 4°C under constant shaking. The extract was collected in separate glass tubes and 100 µl of freshly prepared 2 % Triton-X100 in chloroform was added to each tube and dried under N_2. Dried samples were dissolved in 100 µl ddH_2O for 15 min at 37°C in a water bath. TG, TC, and FC concentrations were measured enzymatically from 40, 20, and 20 µl of the extract, respectively, using commercially available kits (Diagnostic Systems, Holzheim, Germany). The absorbance was normalized to protein concentrations.

3.49. Phagocytosis of fluorescein-labeled *E. coli* particles

Mice were injected intraperitoneally with 200 µl of fluorescein-labeled *E. coli* BioParticles® (Molecular Probes®, Life Technologies, Carlsbad, CA) suspended in Hanks' balanced salt solution. After 2 h, macrophages were collected by flushing the peritoneal cavity with 10 ml of PBS/EDTA and incubated in DMEM containing 25 mM glucose, 10% LPDS, and 1% P/S for 150 min. Cells were washed 3 times with PBS, and the fluorescence was determined prior and after addition of trypan blue to quench the extracellular probe. After aspiration of trypan blue, the fluorescence was measured at 484 (excitation) and 535 nm (emission) on a Victor 1420 multilabel counter (PerkinElmer Life Sciences, Waltham, MA). Experimental readings were normalized to protein content.

3.50. Gelatine zymography

Conditioned media collected from neutrophils after 6 h of incubation were seeded at a density of $5x10^6$ cells/ml of medium. Twenty five to 50 µl of conditioned medium was mixed with zymography loading dye (1:3) and proteins were separated by size using gel electrophoresis at 120 V for 1.5 h. Thereafter, SDS was removed from the gel by washing with 500 ml renaturation buffer for 40 min at RT with constant rocking. The gel was then incubated with 500 ml of incubation buffer at 37°C for 20 h with constant rocking. Then, the gel was stained with Coomassie brilliant blue solution and the excessive dye was removed with destaining solution. Gel images were taken after placing the gel on the bright surface illuminated from below and the density of the digested bands were measured on the inverted field by ImageJ software.

3.51. Preparation of histological sections for atheroassays

Mice were anesthetized by intraperitoneal injections of sodium-pentobarbital (50 mg/kg body weight). Mice were perfused with PBS/EDTA for 10-15 min. The abdominal part of the aorta was removed and frozen in liquid N_2 for RNA isolation. Animals were then perfused with 10% neutral buffered formalin (methanol-free) for 15 min. Adventitial adipose tissue was carefully removed from the upper part of the aorta, which was then excised from the thoracic cavity, cut open in a Y-formation, and stored in formalin until staining. Upper two thirds of the heart and a piece of liver were fixed with formalin for 24 h. Fixed tissues were stored in 30% sucrose. One day before sectioning, hearts and livers were transferred into Neg-50™ frozen section medium (Richard-Allan Scientific, Kalamazoo, MI). Serial sections (7-8 µm) of aortic root or liver tissue were cut at -20°C using a cryostat-microtome (HM 560 Cryo-Star; Microm International GmbH, Walldorf, Germany).

3.52. ORO staining of aortae

Aortae were washed with PBS for 1 min and then placed in 70% isopropanol for 5 min. Thereafter, aortae were stained with ORO working solution for 20 min and then dipped into 70% isopropanol to remove excessive ORO. Aortae were pinned on black dissecting wax and images were taken using a stereo zoom microscope (Olympus SZX12).

3.53. ORO staining of aortic valve and liver sections

Aortic root and livers sections were fixed in 10% methanol-free neutral-buffered formalin for 10 min. Sections were incubated in 70% isopropanol for 5 min, ORO for 15 min, dipped into 70% isopropanol, counterstained with hematoxylin for 5 min, and washed in 0.1% $NaHCO_3$. Sections were air dried and mounted with Kaiser's glycerol mounting medium (Merck, Darmstadt, Germany). Mean lesion area in the aortic root (mm^2) was calculated from 14-15 consecutive ORO-stained sections per mouse. Images were taken with ScanScope T3 whole slide scanner (Aperio Technologies, Bristol, UK). Plaque areas were quantitated with ImageJ software.

3.54. Monoclonal antibody to macrophages-2 (MoMa-2) immunostaining

The sections were fixed for 15 min in formalin and washed three times with PBS. Sections were blocked for 30 min with peroxidase blocking solution (Lab Vision, Fremont, CA) and washed 2 times with PBS. Thereafter, Ultra V block (Lab Vision, Fremont, CA) was added for 7 min. Sections were incubated with primary monoclonal antibody against macrophages-2 (MoMa-2, 1:600; Acris, Hiddenhausen, Germany) for 1 h at RT and then at 4°C overnight. Sections were washed two times with PBS, incubated for 3 h at RT with polyclonal rabbit anti-rat secondary antibody coupled to horseradish peroxidase (1:100, Dako Denmark A/S, Glostrup, Denmark), and washed once with PBS. AEC substrate (Vector Laboratories, Burlingame, CA) was added to the sections for 20 min and then sections were washed 3 times with dH_2O. The sections were stained with hematoxylin for 5 min, washed in 0.1% $NaHCO_3$, and fixed with Kaiser's glycerol mounting medium (Merck, Darmstadt, Germany). Images were taken with ScanScope T3 whole slide scanner (Aperio Technologies, Bristol, UK). Quantification of MoMa-2-stained sections was performed with ImageJ software.

3.55. Monoclonal antibody to alpha-smooth muscle actin (α-SMA) immunostaining

Antigen retrieval was performed with 10 mM sodium-citrate buffer (pH6) in a pressure chamber (Pascal, Dako Denmark A/S, Glostrup, Denmark) at 120°C for 170 seconds. Thereafter, slides were blocked with 1% H_2O_2 in methanol for 15 min and washed 3 times with PBS. The sections were then treated with primary antibody against alpha smooth muscle actin (1:25, ab5694, Abcam) in Dako REAL™ antibody diluent (Dako Denmark A/S, Glostrup, Denmark) for 1 h at RT. Slides were washed 5 times with PBS and treated with secondary antibody Dako REAL™ EnVision™ HRP Rabbit/Mouse (Dako Denmark A/S, Glostrup, Denmark) for 30 min at RT. After washing with PBS, AEC substrate was added to the sections

(DakoCytomation AEC Substrate Chromogen Ready-to-Use), incubated for 7 min, and the reaction was stopped with PBS. Slides were counterstained with Mayer's hematoxylin, washed under running tap water, and fixed with Aquatex mounting medium (Merck, Darmstadt, Germany). Images were taken with ScanScope T3 whole slide scanner (Aperio Technologies, Bristol, UK). Quantification of α-SMA stained sections was performed with ImageJ software.

3.56. Masson's Trichrome staining

Slides were incubated in Bouin's solution (Sigma-Aldrich, St. Louis, MO) overnight at RT, washed under running tap water until the sections were clear from yellow color, and then washed with dH_2O for 1 min. Working Accustain® Wigert's Iron Hematoxylin solution (Sigma-Aldrich, St. Louis, MO) was freshly prepared and sections were stained for 3 min, washed with running tap water for 5 min and dH_2O for 1 min. The sections were then stained with Masson's Trichrome stain (Sigma-Aldrich, St. Louis, MO) according to manufacturer's instructions, washed with dH_2O, and dehydrated (90, 95, and 100% of ethanol and xylene). The sections were fixed with Cytoseal™-60 mounting medium (Thermo Scientific, Kalamazoo, MI). Images were taken with ScanScope T3 whole slide scanner (Aperio Technologies, Bristol, UK). Collagen in Trichrome-stained sections (blue) and necrotic core (acellular area within the plaque) were quantitated with ImageJ software.

3.57. Statistics

Statistical analyses were performed using GraphPad Prism 5.04 software (GraphPad Software Inc, San Diego, CA). The significance was determined by Student's unpaired *t*-test and Welch t-test (in case of unequal variances) for two group comparison and ANOVA followed by Bonferroni correction for multiple group comparison. Data are presented as mean values ± SD. Significance levels were set at $p < 0.05$ (*), $p \leq 0.01$ (**) and $p \leq 0.001$ (***).

4. Results

4.1. Increased plasma 2-AG concentrations in DKO mice

We generated DKO mice by crossing MGL-/- animals with ApoE-/- mice. Since the animals are fertile, we used homozygous breeding to generate ApoE-/- or DKO mice. Starting from the 7th week of age, mice were fed WTD. Since MGL is the main degrading enzyme for 2-AG, we wanted to determine circulating concentrations of this endocannabinoid in DKO animals. Therefore, plasma samples from fed state were taken from these mice after 9 weeks of WTD feeding and 2-AG content was analyzed using mass spectrometry (in collaboration with Thomas Eichmann, University of Graz). We found concentrations of 0.3 mmol/l of 2-AG in the plasma of DKO mice, whereas 2-AG was below detection limit in ApoE-/- samples, indicating systemically elevated 2-AG concentrations in DKO mice compared to the controls (Figure 8).

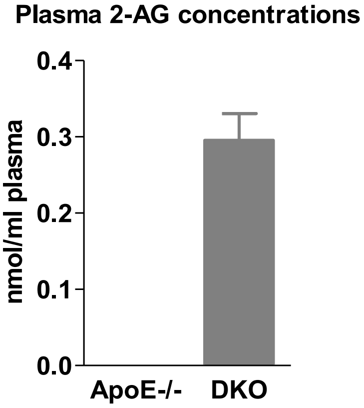

Figure 8. Increased 2-AG concentrations in DKO mice. (A) Plasma 2-AG concentrations in ApoE-/- and DKO mice after 9 weeks of WTD feeding, measured on an ACQUITY UPLC System. Data are presented as mean (n=5) + SD

4.2. DKO mice have normal body weights, food consumption, fecal production, and body adiposity

During WTD feeding, body weight was measured weekly in a fed state. We found comparable body weights between both female and male ApoE-/- and DKO mice throughout the feeding period (Figure 9).

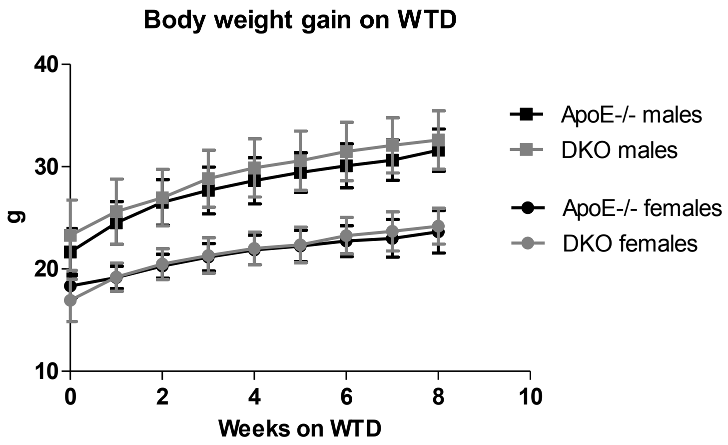

Figure 9. Body weight of ApoE-/- and DKO male (n=24-34) and female mice (n=22) during WTD feeding. Data are presented as mean ± SD.

Food and water consumption, and locomotor activity were determined in chow and WTD-fed mice during the period of 3 consecutive days. We found comparable amounts of ingested food (Figure 10A, B) and water (Figure 10C, D), and locomotor activities (Figure 10E, F) between these two genotypes. Fecal production was determined by measuring feces weight on a fasting grid during the period of 3 days of WTD feeding. We found comparable daily fecal production per the amount of ingested food between ApoE-/- and DKO mice (Figure 10G).

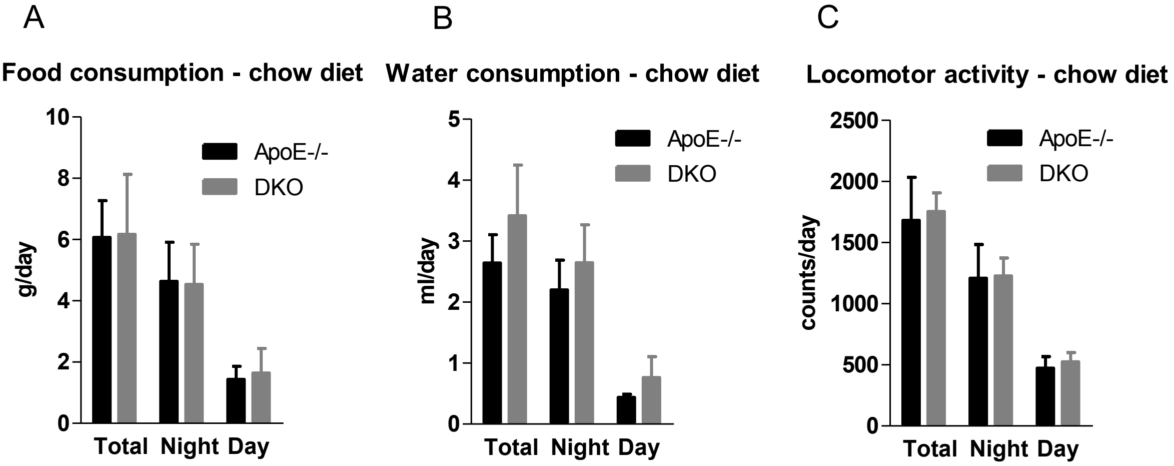

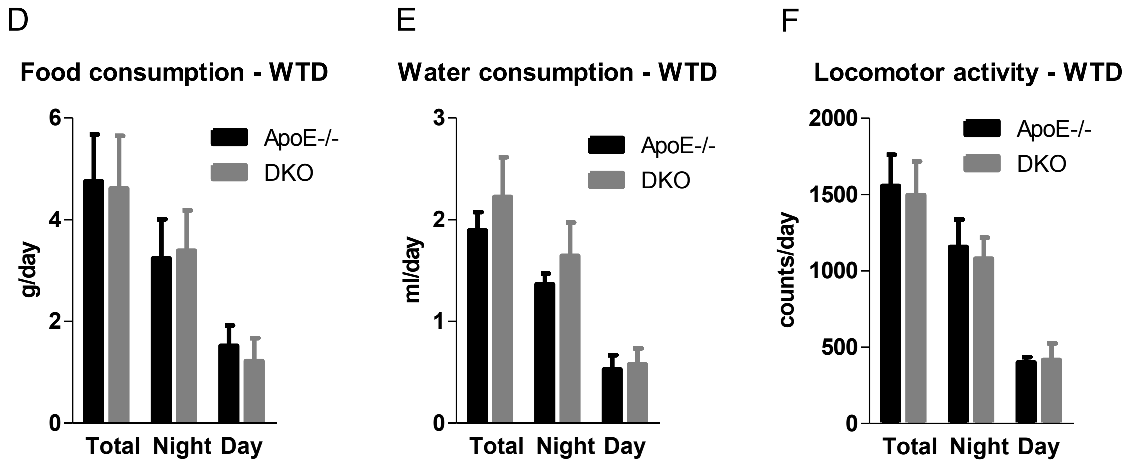

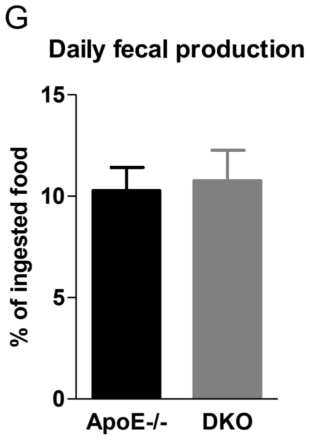

Figure 10. Comparable food and water consumption and locomotor activity between ApoE-/- and DKO mice. (A) Food and (B) water consumption, and (C) activity in chow diet-fed and (D) food, and (E) water consumption and (F) activity in WTD-fed mice during 3 consecutive days. Data are presented as mean values (n=5) + SD. (G) Fecal production was measured during 3 consecutive days of WTD feeding. Data are presented as mean (n=8-9) + SD.

Moreover, body adiposity as determined by NMR scanning (in collaboration with Clemens Diwoky, Graz University of Technology) was comparable between both genotypes. (Figures 11A,B).

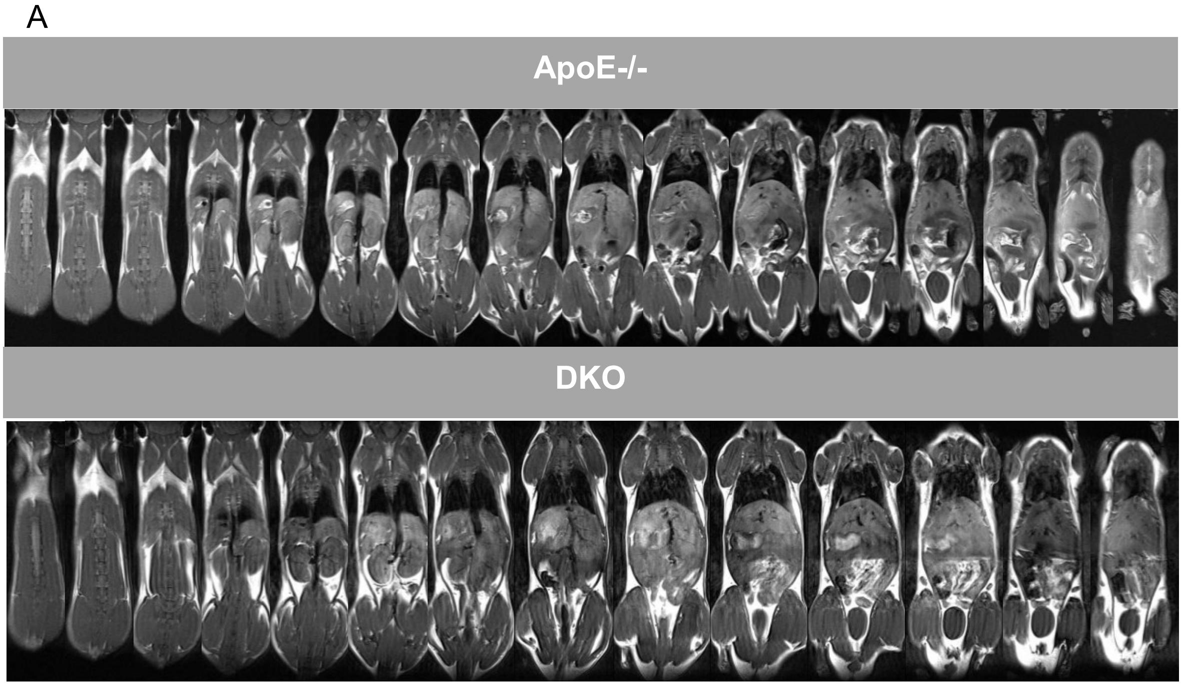

B

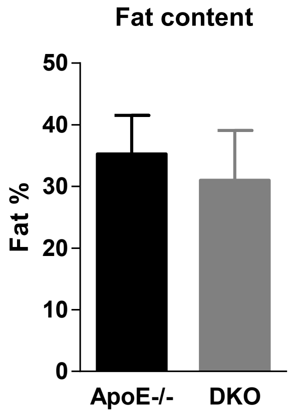

Figure 11. Comparable body adiposity between ApoE-/- and DKO mice. (A) Representative NMR images of ApoE-/- and DKO mice after 9 weeks of WTD feeding. (B) Quantification of total body fat content in ApoE-/- and DKO mice after 9 weeks of WTD feeding. Data are presented as means (n=5) + SD.

4.3. Fasted DKO mice have reduced plasma FFA and free glycerol concentrations compared to ApoE-/- animals

Plasma parameters were determined in *ad libitum* fed (8 am), 12 h fasted (from 8 pm to 8 am) as well as re-fed state (12 h of overnight fasting and 2 h re-feeding *ad libitum*) on chow and after 8 weeks of WTD. We found comparable plasma TG, TC, FC, and CE concentrations in all conditions in ApoE-/- and DKO mice. However, fasting plasma concentrations of FG and NEFA were significantly reduced in DKO compared to ApoE-/- animals on both chow (Table 2) and WTD (Table 3). Interestingly, when measured in a re-fed state, DKO plasma free glycerol (FG) on chow diet and FG and NEFA levels on WTD were elevated compared to ApoE-/- mice, maintaining levels similar to those found in the fasted state. In contrast, WTD fasted glucose levels were lower in DKO compared to ApoE-/- mice. These data may indicate delayed chylomicron assembly/secretion and thereby delayed repression of lipolysis which would lead to similar plasma FG and NEFA levels as in the fasted state.

Table 2. Reduced fasting FG and FFA concentrations in DKO mice. Plasma parameters in chow diet-fed mice aged 6-8 weeks were determined in fed, fasted, and re-fed conditions. Data are represented as mean (n=7-9) ± SD. *, $p < 0.05$; **, $p \leq 0.01$.

Chow diet						
Feeding state	**Fed state (*ad libitum*)**		**Fasted state (12 h fasting)**		**Re-fed state (2 h feeding after 12 h fasting)**	
Genotype	**ApoE-/-**	**DKO**	**ApoE-/-**	**DKO**	**ApoE-/-**	**DKO**
TG (mg/dl)	56.96 ± 14.93	44.39 ± 9.71	90.25 ± 42.83	64.07 ± 19.50	74.57 ± 11.49	69.85 ± 19.56
TC (mg/dl)	181.20 ± 43.53	178.75 ± 48.20	281.58 ± 40.84	250.84 ± 41.62	252.68 ± 40.35	261.05 ± 33.77
FC (mg/dl)	67.82 ± 14.09	68.53 ± 7.94	81.36 ± 14.83	74.03 ± 13.94	90.98 ± 11.93	91.69 ± 10.87
CE (mg/dl)	113.39 ± 30.59	110.22 ± 43.19	200.22 ± 27.77	176.81 ± 28.80	161.70 ± 32.14	169.36 ± 26.28
FG (mg/dl)	2.92 ± 0.95	2.83 ± 0.89	3.73 ± 0.74	2.54 ± 0.72**	1.77 ± 0.48	2.75 ± 0.94*
FFA (mmol/l)	0.50 ± 0.18	0.47 ± 0.15	0.92 ± 0.20	0.70 ± 0.23*	0.24 ± 0.03	0.28 ± 0.05
Glu (mg/dl)	183.0 ± 22.25	191.57 ± 28.56	108.38 ± 13.35	102.22 ± 14.41	185.86 ± 17.37	182.57 ± 18.46

Table 3**.** Reduced fasting FG, FFA, and glucose concentrations in DKO mice. Plasma parameters in mice aged 13-15 weeks and fed WTD for 6-8 weeks were determined in fed, fasted, and re-fed conditions. Data are represented as mean (n=7-9) ± SD. *, p < 0.05; ***, p ≤ 0.001.

Western-type diet						
Feeding state	**Fed state (*ad libitum*)**		**Fasted state (12 h fasting)**		**Re-fed state (2 h feeding after 12 h fasting)**	
Genotype	**ApoE-/-**	**DKO**	**ApoE-/-**	**DKO**	**ApoE-/-**	**DKO**
TG (mg/dl)	58.99 ± 21.97	47.31 ± 22.83	53.39 ± 14.89	47.29 ± 16.50	78.61 ± 25.27	106.42 ± 38.52
TC (mg/dl)	536.97 ± 80.02	587.02 ± 153.43	787.50 ± 178.33	646.07 ± 259.00	525.53 ± 63.84	600.48 ± 113.11
FC (mg/dl)	210.30 ± 17.82	235.36 ± 35.24	263.66 ± 60.99	235.56 ± 75.18	183.44 ± 19.64	210.73 ± 22.25
CE (mg/dl)	326.66 ± 67.85	351.66 ± 122.20	523.84 ± 119.48	410.52 ± 185.08	342.09 ± 52.68	389.74 ± 111.02
FG (mg/dl)	2.64 ± 0.48	2.17 ± 0.78	4.75 ± 0.79	3.13 ± 0.46***	2.53 ± 0.37	3.18 ± 0.57*
FFA (mmol/l)	0.61 ± 0.13	0.49 ± 0.23	0.88 ± 0.16	0.70 ± 0.15*	0.36 ± 0.08	0.50 ± 0.11*
Glu (mg/dl)	157.14 ± 15.59	155.16 ± 28.83	114.88 ± 16.37	93.25 ± 30.75*	168.20 ± 10.31	172.00 ± 10.42

To determine lipoprotein profiles of these mice, we performed FPLC separation of plasma samples in the fasted state after WTD feeding. We found comparable lipoprotein particle sizes, determined as the position of the TG (Figure 12A) and TC (Figure 12B) peaks, as well as lipoprotein particle compositions, determined as the peak surface in VLDL, LDL, and HDL fractions. The only observed difference was reduction in free glycerol content in the plasma of fasted DKO compared to ApoE-/- mice, shown in Table 3.

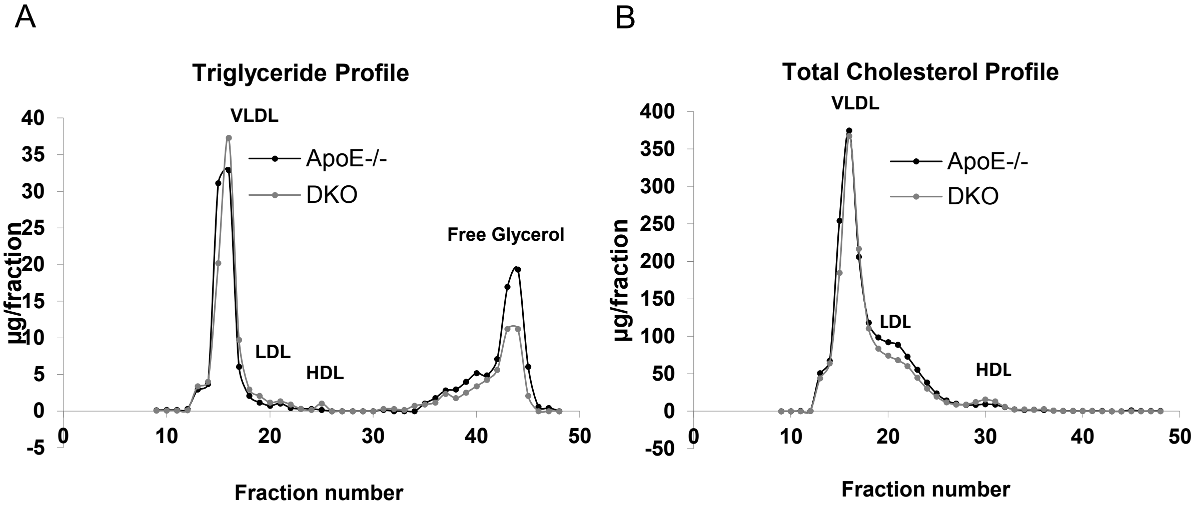

Figure 12. Unaltered plasma lipoprotein profiles between ApoE-/- and DKO mice. (A) Plasma lipoprotein profiles from ApoE-/- and DKO mice fed WTD. Plasma samples from each genotype (n=5) were pooled and 200 µl were subjected to FPLC separation using a Superose 6 column. (A) TG and (B) TC concentrations in each fraction were determined using enzymatic assays.

4.4. Reduced plasma concentrations of pro-inflammatory cytokines

Plasma interleukin 6 (IL-6) levels were at comparable and low levels in both genotypes, whereas MCP-1 concentrations were reduced in DKO mice (Figure 13). These data indicate that MGL deficiency on the ApoE-/- background results in systemic accumulation of 2-AG, which may affect endocannabinoid signaling and might lead to reduced systemic inflammation.

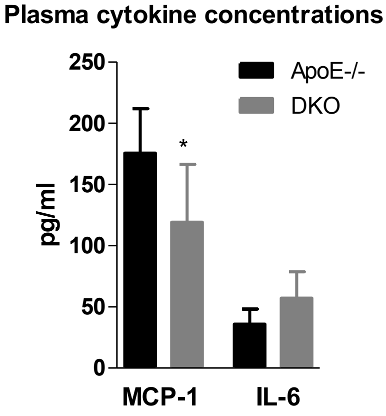

Figure 13. Reduced systemic inflammation in DKO mice. Serum MCP-1 and IL-6 concentrations were determined by ELISA. Data represent mean (n=8) + SD. *, $p < 0.05$.

4.5. Hepatic LD size, TG and CE content as well as VLDL production are reduced in DKO mice

Since lipid and carbohydrate metabolism are tightly regulated by liver homeostasis, we determined hepatic lipid levels. We found significantly reduced TG concentrations in livers of DKO mice compared to ApoE-/- mice in the fasted state after 16 weeks of WTD feeding (Figure 14A). Hepatic TC levels were even more reduced, whereas hepatic FC concentrations were comparable between both genotypes (Figure 14A). ORO staining of liver cryosections confirmed reduced accumulation of neutral lipids in livers of DKO mice (Figure 14B).

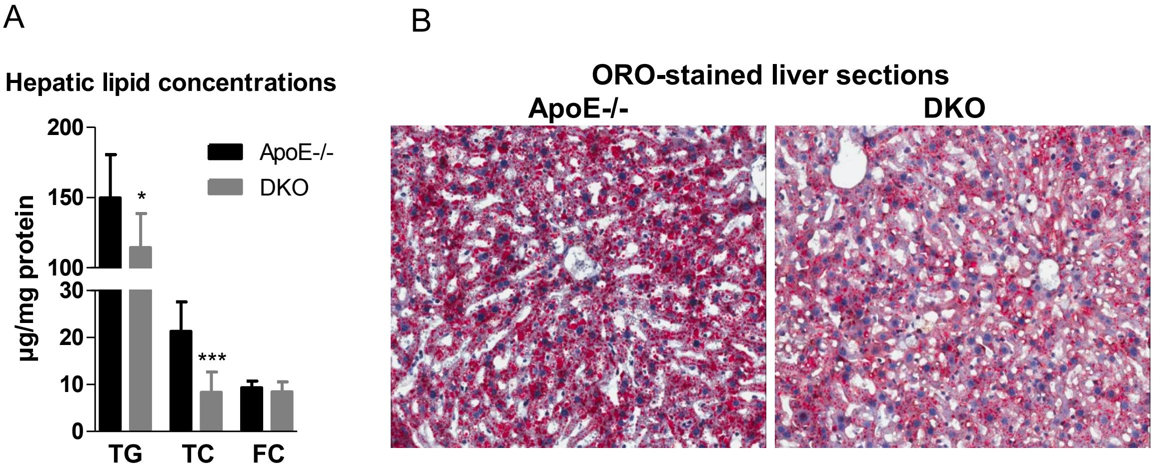

Figure 14. Reduced hepatic TG and TC concentrations in DKO mice. (A) Mice were fasted for 12 h and lipids were extracted from liver samples by Folch extraction. Data represent mean (n=6-9) + SD. (B) Representative images of ORO-stained liver cryosections. *, $p < 0.05$; ***, $p \leq 0.001$.

To further visualize and investigate LDs, we performed electron micrographs of fasted liver samples (in collaboration with Dr. Dagmar Kolb-Lenz) (Figure 15A). We found increased LD numbers (Figure 15B) but reduced relative diameter of LDs in the hepatocytes (Figure 15C). Almost 60% of all LDs in DKO mice were smaller than 1 µm and as much as 95% were smaller than 2.5 µm, compared to 25% and 60% in ApoE-/- livers, respectively.

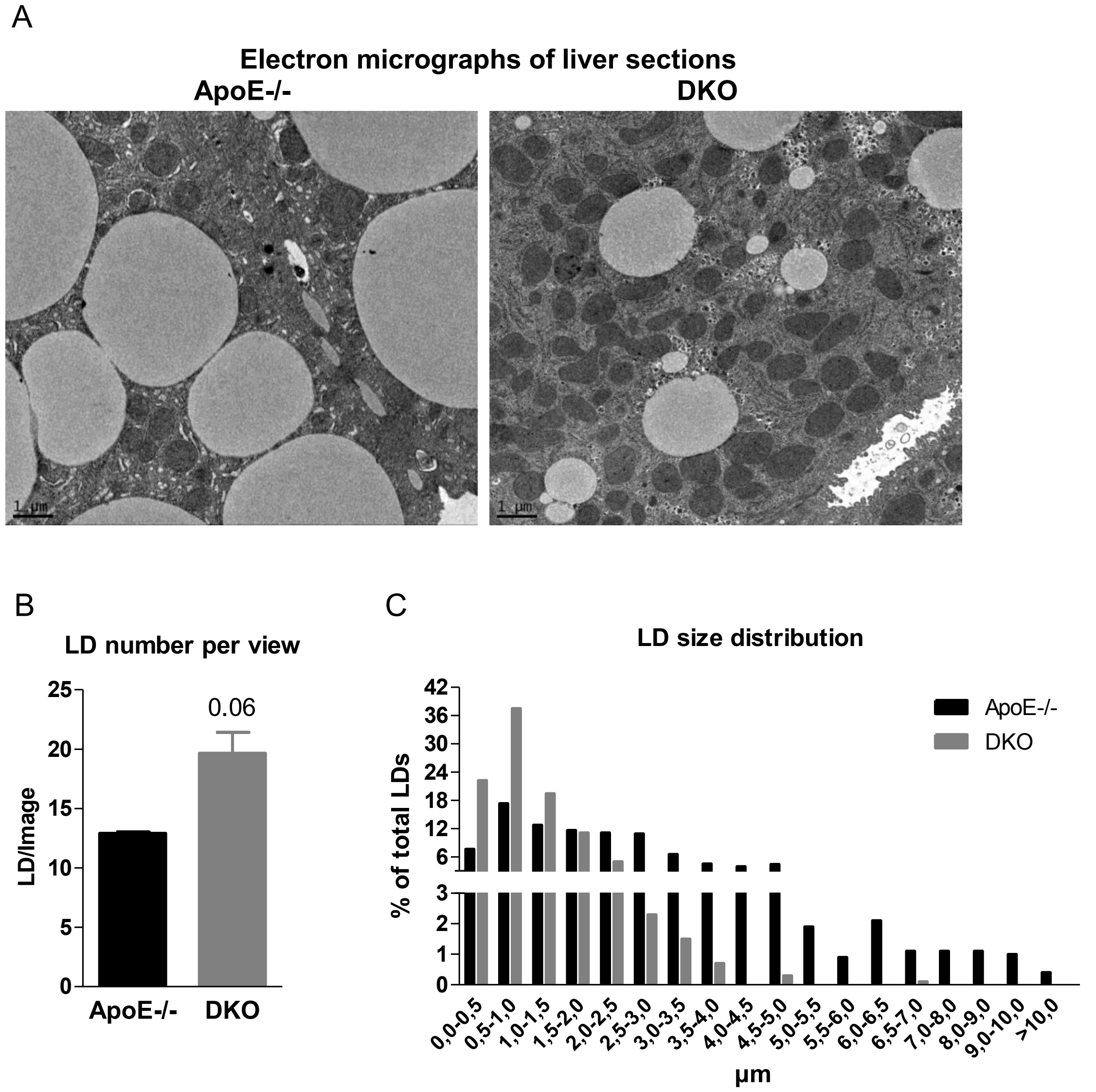

Figure 15. Reduced hepatic LD size but increased abundance in DKO mice. (A) Representative electron micrographs of livers from 12 h fasted mice. (B) Number of LDs per electron micrograph. Data represent mean values (n=3) + SD. (C) Size distribution of LDs according to the average diameter.

Since reductions in neutral lipid content affected liver TG levels and fasting FFA concentrations were reduced in DKO mice, we determined VLDL secretion capacities in WTD-fed DKO mice after pharmacological inhibition of lipoprotein lipase (LPL) by tyloxapol. We found significantly reduced VLDL secretion in DKO mice compared to the control animals 3 and 4 h post-tyloxapol injections (Figure 16A). Fasting plasma TG levels showed a slight but non-significant trend towards reduced concentrations (see also Table 2). In addition, post-heparin plasma samples showed comparable LPL activities in both genotypes (Figure 16B).

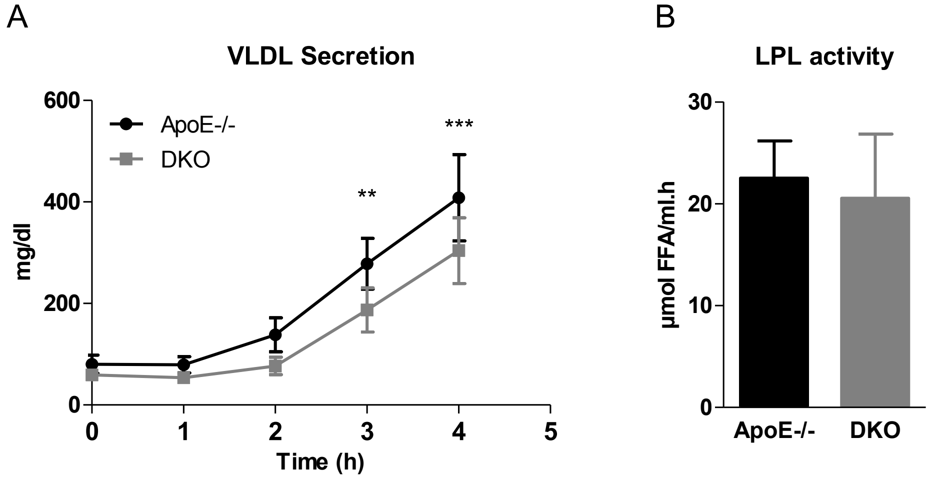

Figure 16. Reduced VLDL secretion in DKO mice. (A) VLDL was determined by plasma TG measurements in 12 h fasted mice upon LPL inhibition with tyloxapol (500mg/kg body weight). Data represent mean (n=5-6) ± SD. (B) LPL activity was determined in post-heparinized plasma 10 min after i.p. heparin injection. Data represent mean (n=7-8) + SD. **, $p \leq 0.01$; ***, $p \leq 0.001$.

EC signaling in DKO mice is likely altered at the hepatic level as well, due to elevated 2-AG concentrations in these animals (measured in collaboration with Thomas Eichmann, University of Graz) (Figure 17A). However, Cb1r mRNA expression was completely absent and Cb2r mRNA unchanged between both genotypes, respectively (Figure 8B). Hepatic mRNA expression of genes involved in lipid uptake was changed in fasted DKO compared to ApoE-/- mice with an increased expression of Srb-1 (cholesterol uptake) and reduction of Cd36 (FFA uptake). Moreover, expression levels of the rate limiting enzymes for cholesterol biosynthesis (HmgCoAr) and bile acid biosynthesis (Cyp7a1) were elevated in DKO mice (Figure 17B). In the fed state, transcription levels of lipogenic genes such as Acc1, Fas, and Scd1 were unaltered between genotypes with the exception of reduced expression of Acc2 (31 %) in DKO mice (Figure 17C).

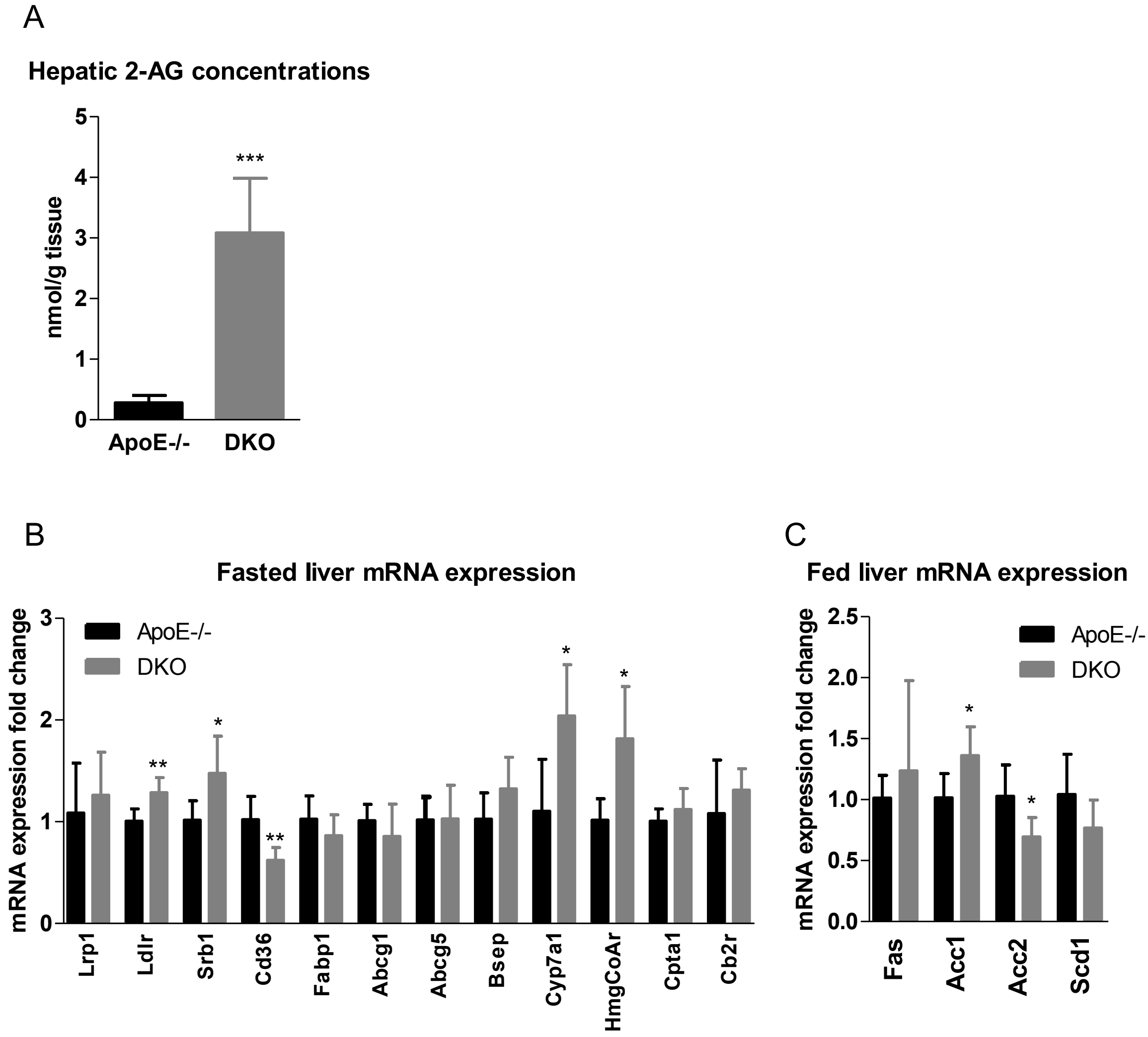

Figure 17. Changes in hepatic EC and mRNA expression of lipid metabolism genes in DKO mice. (A) 2-AG concentrations in the livers of ApoE-/- and DKO mice. Data are presented as means (n=7) + SD. Hepatic mRNA expression of target genes in (B) fasted and (C) fed states were analyzed in duplicate by real-time PCR and normalized to the expression of Cyclophilin A as reference gene. Data represent means (n=4-5) + SD. *, $p < 0.05$; **, $p \leq 0.01$; ***, $p \leq 0.001$.

4.6. Reduced hepatic cholesterol concentrations are likely due to increased cholesterol elimination via feces in DKO mice

Severe reduction in hepatic cholesterol concentrations can be either due to reduced cholesterol dietary uptake, reduced *de novo* lipogenesis, or increased elimination via bile. To investigate lipid uptake in the small intestine as well as consequences of MGL deficiency on the intestinal function, we first measured gut transit time in ApoE-/- and DKO mice fed chow diet. We found significantly increased gut transit time in DKO compared to ApoE-/- mice, indicating reduced gut motility in these animals (Figure 18A). An acute cholesterol absorption experiment revealed [^{3}H]cholesterol retention in the gastrum, reduced cholesterol uptake in the duodenum and jejunum, a trend towards reduction in liver (Figure 18B) as well as decreased plasma cholesterol concentrations of DKO mice compared to ApoE-/- animals (Figure 18B).

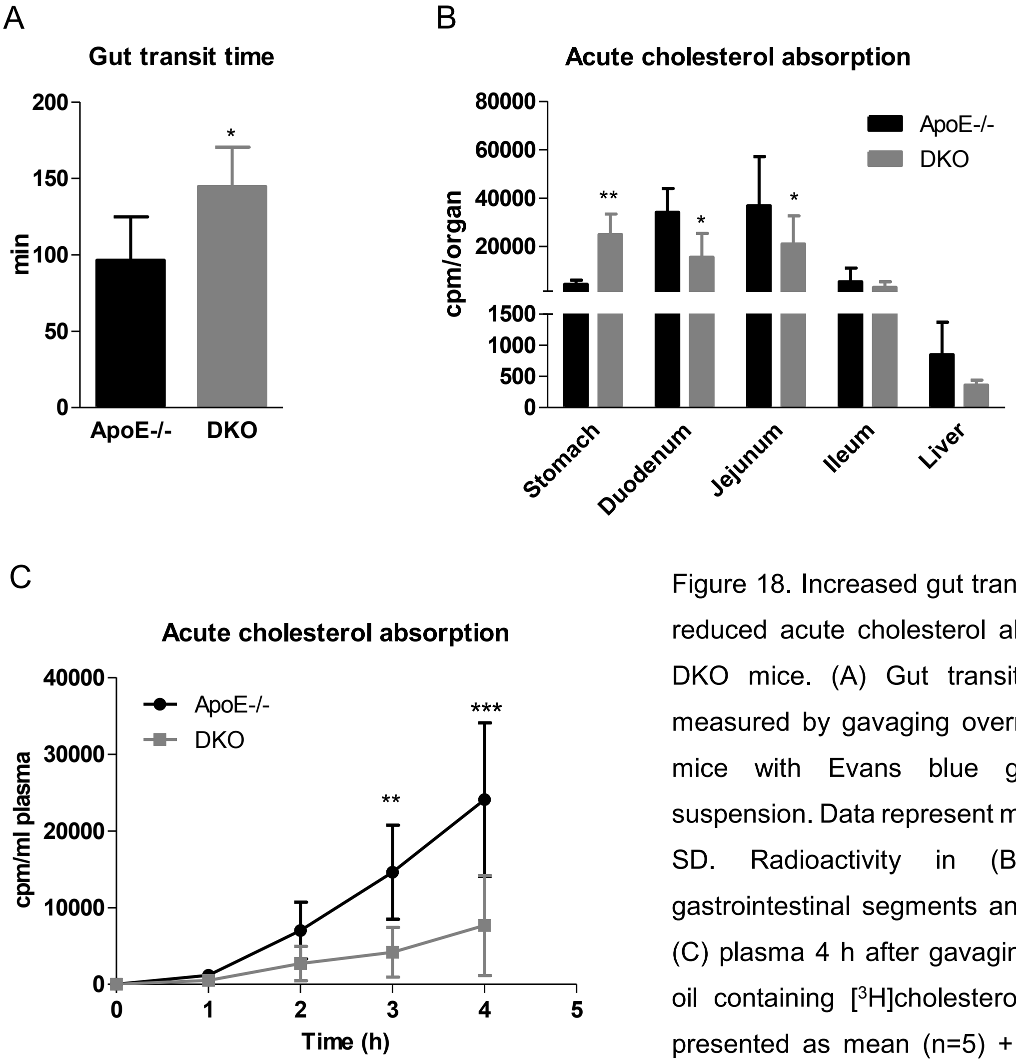

Figure 18. Increased gut transit time and reduced acute cholesterol absorption in DKO mice. (A) Gut transit time was measured by gavaging overnight fasted mice with Evans blue gum arabic suspension. Data represent mean (n=5) + SD. Radioactivity in (B) different gastrointestinal segments and liver, and (C) plasma 4 h after gavaging with corn oil containing [^{3}H]cholesterol. Data are presented as mean (n=5) + SD. *, $p < 0.05$; **, $p \leq 0.01$; ***, $p \leq 0.001$.

Similarly, a FA absorption experiment revealed [^{3}H]oleic acid retention in gastrum of DKO mice (Figure 19A), although without changes in FA incorporation in specific lipid species (PL, FC, FFA, TG, and CE) in duodenum, jejunum, and liver (Figure 19B-D). Plasma radioactivity was reduced during the first 2 h post-gavage (Figure 19E).

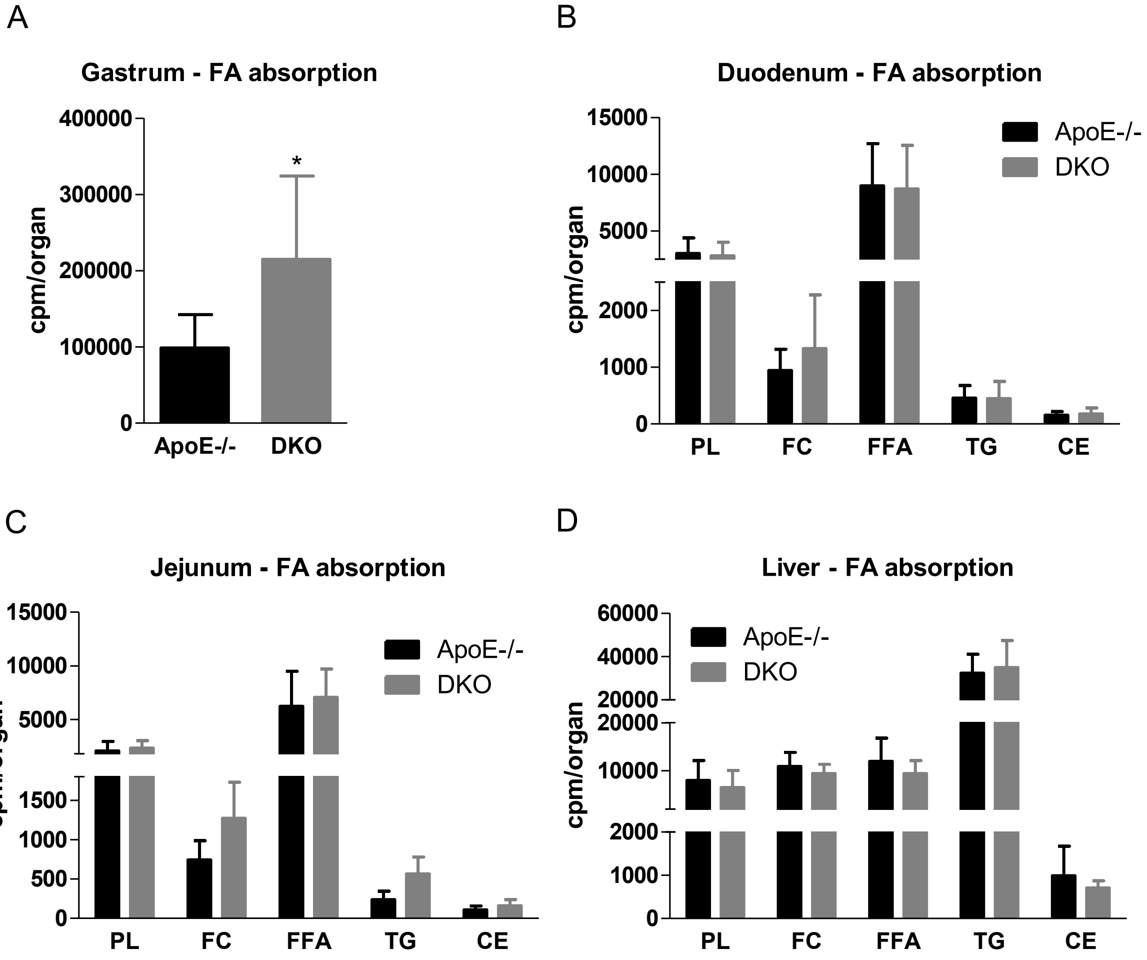

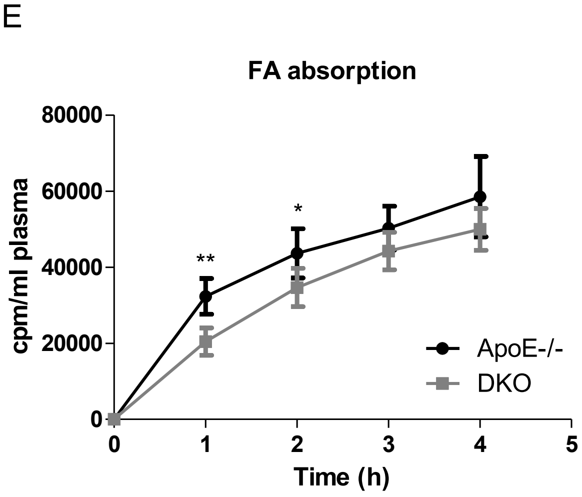

Figure 19. Increased gastric lipid retention but unchanged FA absorption in DKO mice. (A) Total radioactivity in gastrum and radioactivity in PL, FC, FFA, TG, and CE in (B) duodenum, (C) jejunum, and (D) liver. Total plasma radioactivity during 4 h post-gavaging with corn oil containing [^{3}H]oleic acid. Data are presented as mean (n=5) + SD. *, $p < 0.05$; **, $p \leq 0.01$.

To determine chylomicron production from the small intestine and the ability of enterocytes to pack both TG and CE into lipoprotein particles, we gavaged chow diet-fed mice with corn oil containing [^{3}H]triolein and [^{14}C]cholesterol. After tyloxapol injection and inhibition of LPL, DKO mice had reduced [^{3}H] and [^{14}C] in the plasma indicating increased gut retention of lipids, potential accumulation in the small intestine, and delayed chylomicron production (Figure 20).

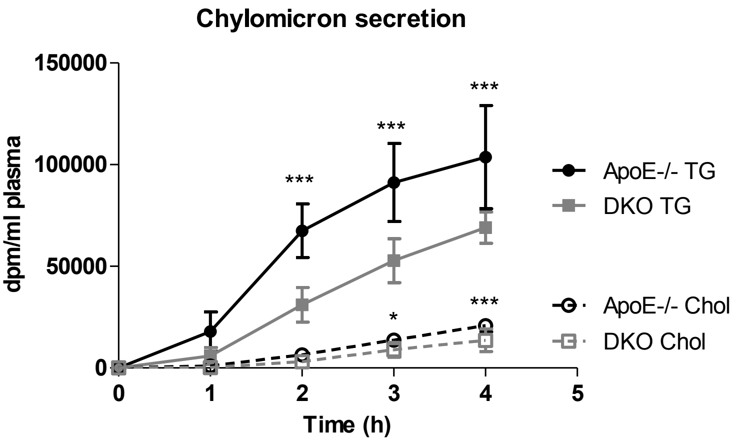

Figure 20. Delayed chylomicron secretion in DKO mice. Animals were i.p. injected with 500mg/kg tyloxapol and 30 min post-injection, mice were gavaged with corn oil containing [^{3}H]triolein and [^{14}C]cholesterol. Plasma radioactivity was measured periodically up to 4 h after gavage. Data represent mean (n=5) ± SD. *, $p < 0.05$; ***, $p \leq 0.001$.

To determine whether changes in the cholesterol uptake are the consequence of increased gastric retention of lipids or alterations in the uptake and lipid accumulation within enterocytes, we measured fractional cholesterol absorption utilizing the fecal dual-isotope ratio method. We found that comparable amounts of radioactively labeled cholesterol are taken up from the intestines of DKO and ApoE-/- mice during the period of 3 days after [^{14}C] cholesterol gavaging and use of [^{3}H] sitostanol as non-absorptive standard (Figure 21). These data indicate that timing, rather than quantitative lipid absorption, is altered in DKO mice. Delayed lipid delivery to the small intestine, probably due to increased gastric retention cause the later onset of absorption and chylomicron appearance in the systemic circulation, whereas on a long run cholesterol gets as efficiently absorbed as in ApoE-/- animals.

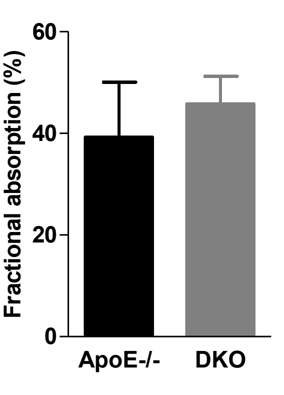

Figure 21. Unaltered fractional cholesterol absorption in DKO mice measured using fecal dual-isotope ratio method. Fractional cholesterol absorption was determined in stool pools 72 h after gavaging mice with corn oil containing [^{14}C] cholesterol and [^{3}H] sitostanol. Results are expressed as a ratio of absorbed to the total given dose. Data represent mean (n=4-6) + SD.

Furthermore, we explored whether reduced hepatic cholesterol concentreations are the consequence of reduced *de novo* cholesterol synthesis. Therefore, we injected mice with [^{14}C]acetic acid and determined its incorporation in specific lipid classes (PL, FC, FFA, TG, and CE) in livers of DKO and ApoE-/- mice one hour post-injection. We found similar incorporation of [^{14}C]acetic acid in all lipid classes with the exception of increased *de novo* TG synthesis (Figure 22).

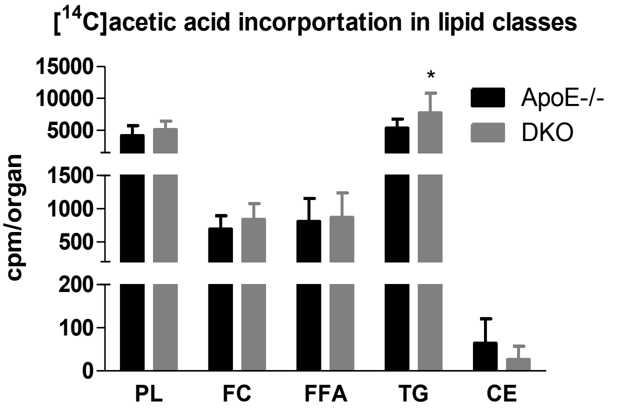

Figure 22. Increased TG and unchanged *de novo* cholesterol production in DKO mice. Mice in a refed state were injected with 5 µCi [^{14}C]acetic acid. One hour post-injections, animals were sacrificed, liver lipids extracted according to Folch method, separated by TLC and radioactivity was measured in corresponding lipid fractions. Data represent mean (n=5-6) + SD. *, $p < 0.05$.

Cholesterol excretion, however, is likely to be the determining factor for reduced hepatic cholesterol concentrations, since we found significantly increased fecal cholesterol content in the mice fed WTD during a 3 days collection period (Figure 23A). Although TC in the bile was similar between ApoE-/- and DKO mice (Figure 23 B), we cannot exclude that either increased bile acid production or daily amount of produced bile are higher, or that transintestinal cholesterol excretion is increased in DKO mice.

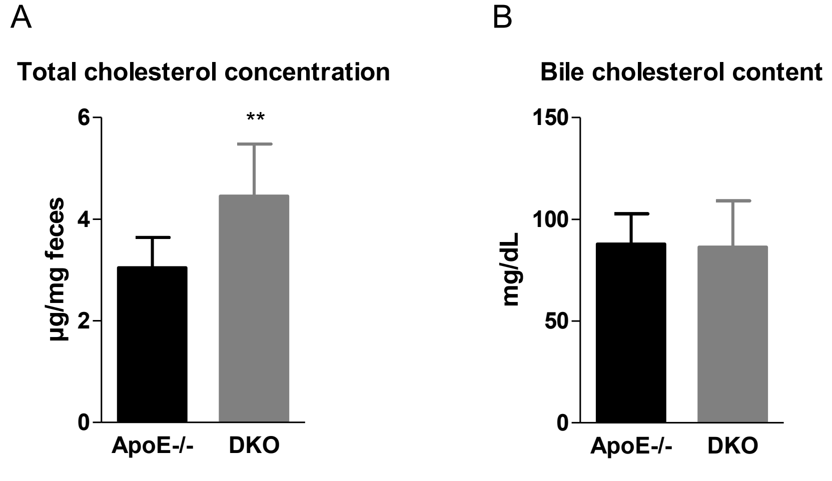

Figure 23. Increased fecal cholesterol content in DKO mice. (A) Stool samples were collected from WTD-fed mice during a period of 72 h after which lipids were extracted and measured

spectrophotometrically. Data represent mean (n=8-9) + SD. (B) Bile cholesterol content was measured in gall bladder bile obtained upon 12 h fasting. Data represent mean (n=5-9) + SD. **, p ≤ 0.01.

4.7. DKO mice show improved carbohydrate metabolism

Another important contributor for the development of atherosclerosis is deregulated carbohydrate metabolism. Therefore, we performed a series of tests to investigate consequences of MGL deficiency on carbohydrate homeostasis. We found reduced fasting glucose concentrations in DKO mice compared to the controls on WTD but not on chow diet (Tables 2 and 3). Moreover, intraperitoneal glucose tolerance test after WTD feeding revealed improved glucose utilization in DKO compared to ApoE-/- mice (Figure 24A). The improved glucose tolerance is likely not mediated through enhanced insulin activity since plasma insulin concentrations were at comparable levels in both fed and fasted ApoE-/- and DKO mice (Figure 24B). Moreover, insulin sensitivity was similar between ApoE-/- and DKO mice (Figure 24C), although the baseline plasma glucose concentrations were strongly reduced in DKO mice. Peripheral insulin action is largely associated with the adipokine secretion and action. Therefore, we assessed plasma leptin and adiponectin concentrations, which were, however, unaltered in DKO mice (Figure 24D).

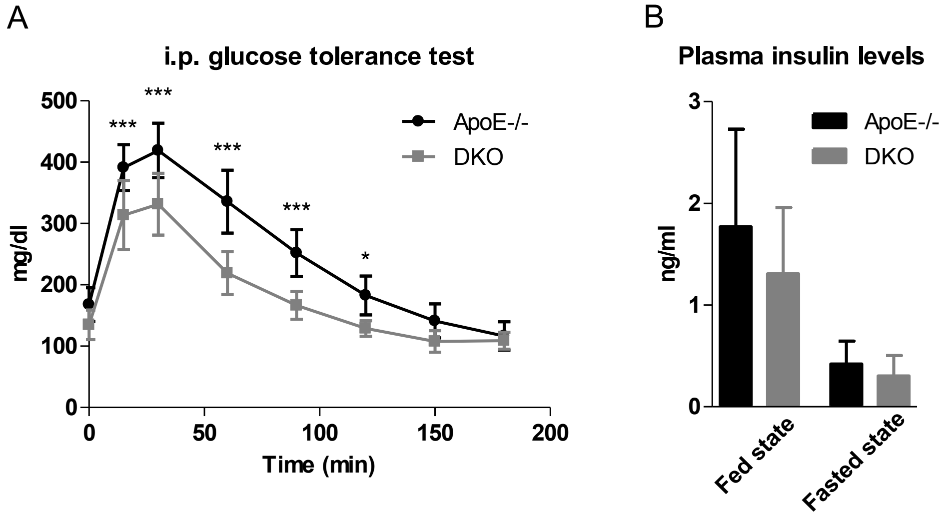

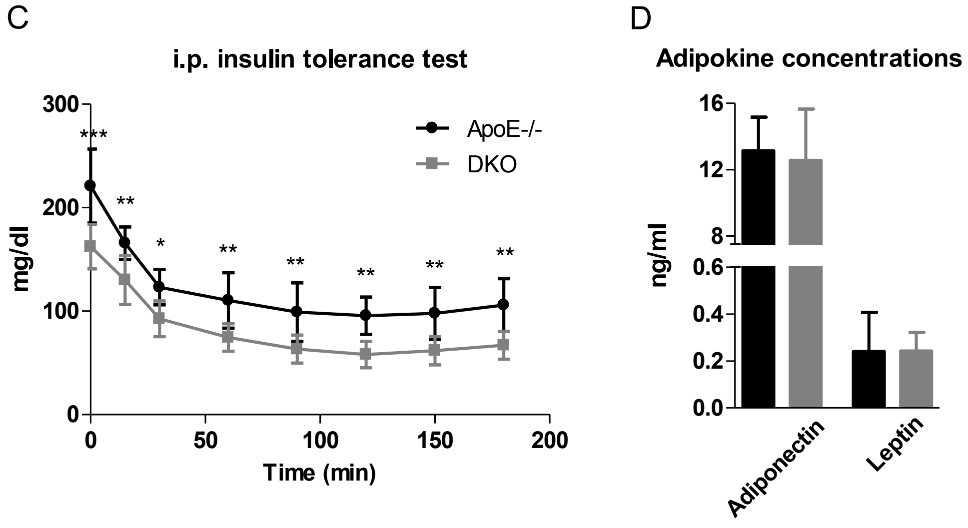

Figure 24. Improved glucose tolerance in DKO mice. (A) Intraperitoneal glucose tolerance test was performed after 6 h of fasting and injection of 2g/kg glucose. Data represent mean (n=9) ± SD. (B) Plasma insulin values measured by ELISA in fed and 12 h fasted mice (n=6-7) + SD. (C) Insulin tolerance test was performed after 4 h of fasting and i.p. injection of 0.75 IU/kg insulin. Data represent mean (n=9) ± SD. (D) Plasma adiponectin and leptin concentrations were measured in fed animals by ELISA according to manufacturers' instructions. Data represent mean (n=5-8) + SD. *, $p < 0.05$; **, $p \leq 0.01$; ***, $p \leq 0.001$.

Fasting hepatic glucose metabolism is likely not changed since gluconeogenesis from pyruvate (Figure 25A) or glycerol (Figure 25B) as substrates were unaltered in DKO mice. It seems, however, that livers of DKO animals are capable to store more glucose, as seen by a trend towards increased hepatic glycogen concentrations in the fed state (Figure 25C). Moreover, livers of DKO mice responded to glucagon more prominently since glucagon tolerance test showed increased release of glucose from the liver of DKO mice (Figure 25D). In accordance, fasting hepatic glycogen concentrations were reduced in the livers of DKO mice compared to the controls (Figure 25C).

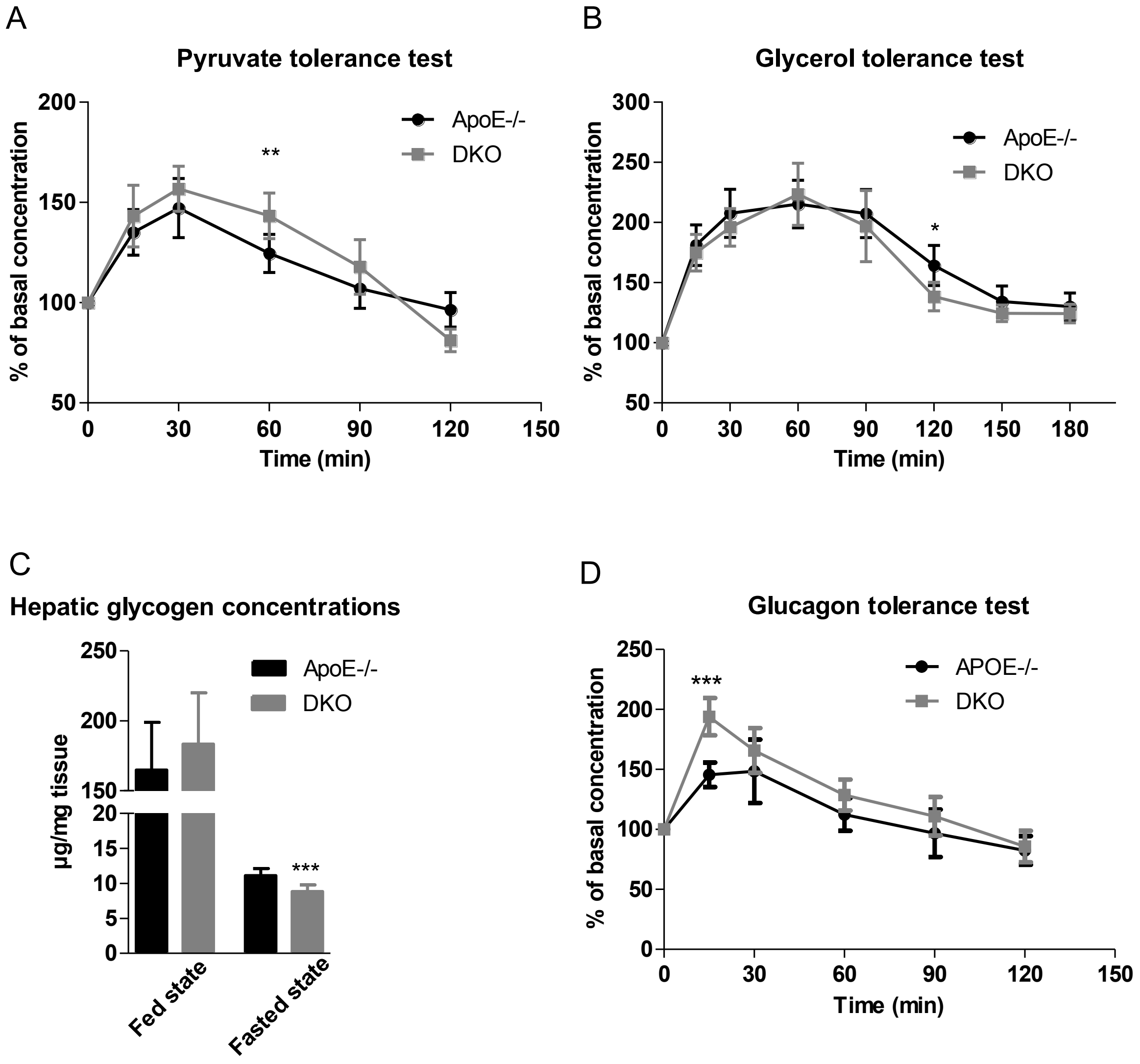

Figure 25. Increased glycogen depletion in DKO mice. Plasma glucose concentrations were measured after i.p. injection of 2 g/kg (A) pyruvate and (B) glycerol in 12 h-fasted mice. Data represent mean (n=7) ± SD. (C) Hepatic glycogen concentrations measured in fed and 12 h-fasted animals. Data represent mean (n=6-8) + SD. (D) Plasma glucose concentrations was determined after i.p. injection of 140 µg/kg glucagon in fed mice. Data represent mean (n=6) ± SD. *, $p < 0.05$; **, $p \leq 0.01$; ***, $p \leq 0.001$.

4.8. Comparable energy substrate utilization in ApoE-/- and DKO mice measured by indirect calorimetry

To determine energy substrate utilization used to sustain metabolic functions, we utilized indirect calorimetry to measure respiratory exchange ratio (RER) of ApoE-/- and DKO mice fed chow or WTD during 3 consecutive days of *ad libitum* feeding and during 12 h-fasting. We found similar RER in both genotypes fed chow (Figure 26A, B) and WTD (Figure 26C, D).

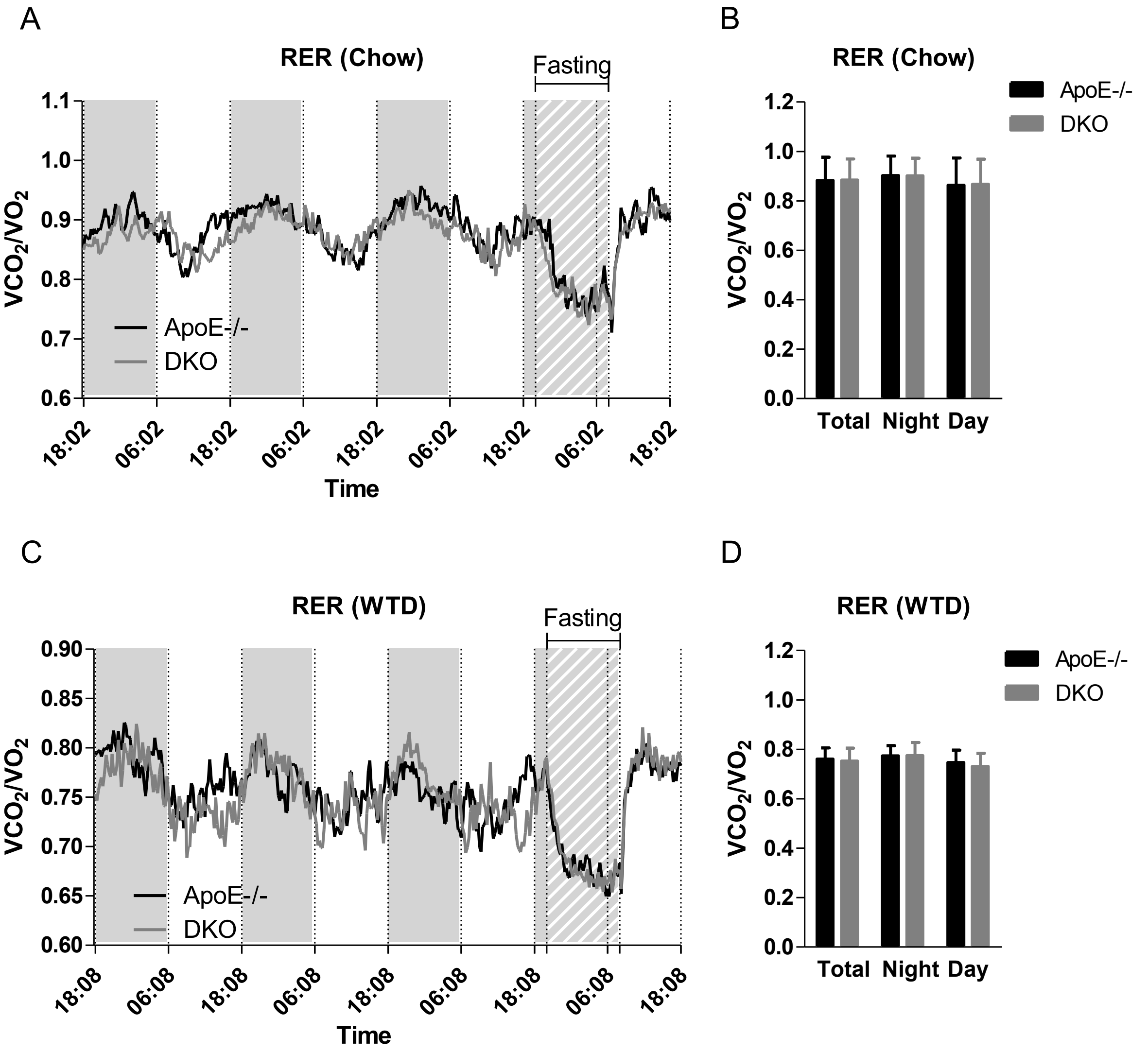

Figure 26. Comparable RER between ApoE-/- and DKO mice. RER was measured in (A, B) chow- and (C, D) WTD-fed mice during 3 consecutive days of *ad libitum* feeding and during 12 h-fasting. Data represent means (n=5) + SD.

4.9. DKO mice have increased lymphocytes and monocytes after WTD due to increased WBC production and survival

Since EC signaling can influence immune responses and leukocyte functions, we determined peripheral white blood cell (WBC) counts in ApoE-/- and DKO mice fed chow and 9 weeks of WTD. We did not observe significant changes in the total WBC counts nor specific subpopulation numbers (Figure 27A) between these two genotypes on chow diet. However, upon WTD feeding, the total number of WBCs was increased due to higher numbers of lymphocytes, monocytes, and basophils, whereas the levels of neutrophils and eosinophils were unaltered (Figure 27B). The relative abundance of specific WBC subpopulations revealed a relative increase in

T-lymphocytes without effects on B-lymphocyte counts, and unaltered abundance of Ly6C^{high} and Ly6C^{low} monocytes (Figure 27C).

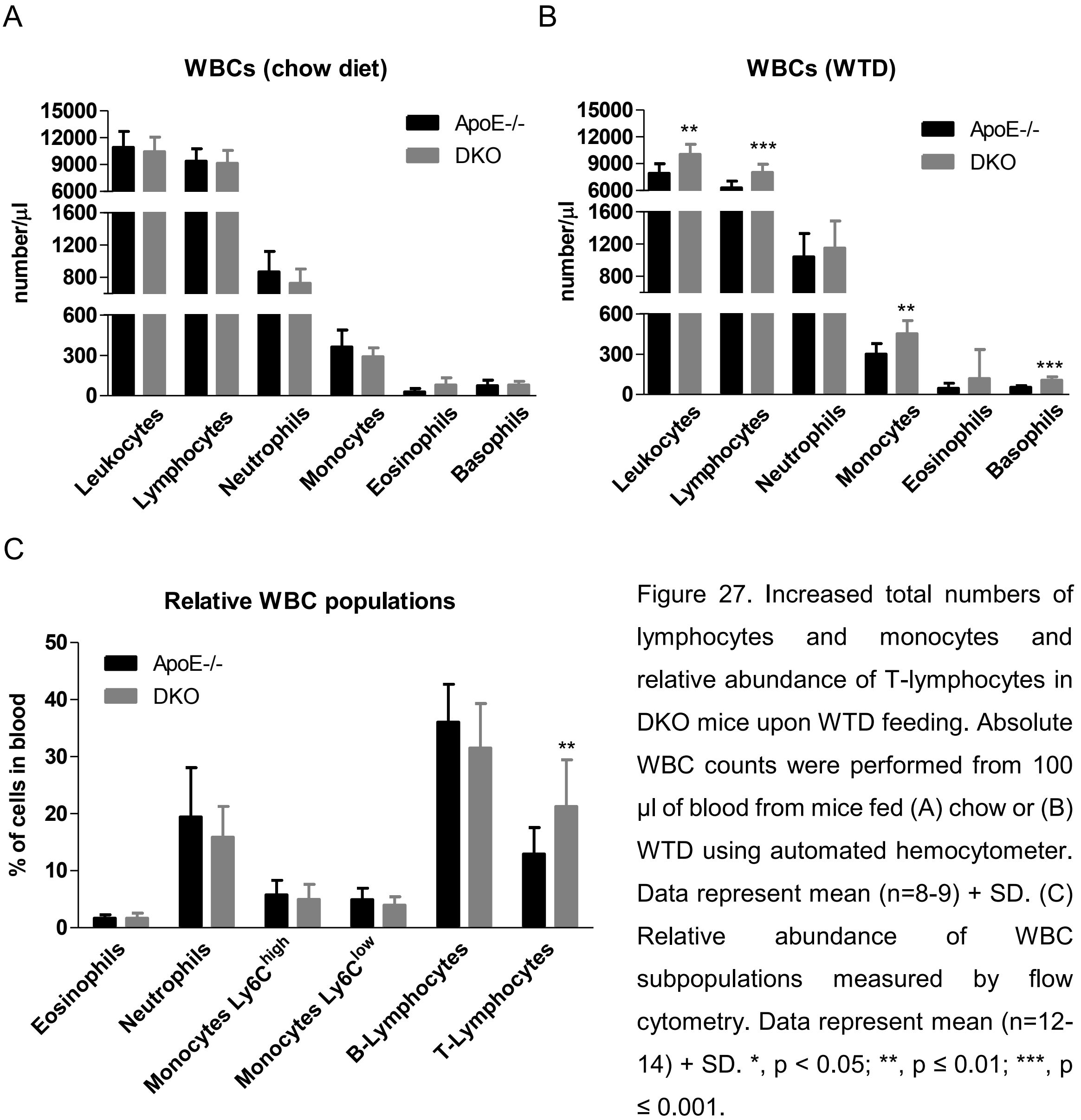

Figure 27. Increased total numbers of lymphocytes and monocytes and relative abundance of T-lymphocytes in DKO mice upon WTD feeding. Absolute WBC counts were performed from 100 µl of blood from mice fed (A) chow or (B) WTD using automated hemocytometer. Data represent mean (n=8-9) + SD. (C) Relative abundance of WBC subpopulations measured by flow cytometry. Data represent mean (n=12-14) + SD. *, $p < 0.05$; **, $p \leq 0.01$; ***, $p \leq 0.001$.

The increase in WBC numbers can be either due to their increased production, or prolonged lifespan within the circulation. BM immunophenotyping (done in collaboration with Albert Woelfler, Medical University of Graz) revealed increased relative abundance of hematopoietic Lin$^-$Sca-1$^+$c-Kit$^+$ (LSK) cells in DKO mice, which represent the progenitor cells for WBC production (Figure 28A). Moreover, we observed extended circulating WBC half-life indicating that increased cell survival contributes to the increased numbers of circulating WBCs in DKO mice (Figure 28B).

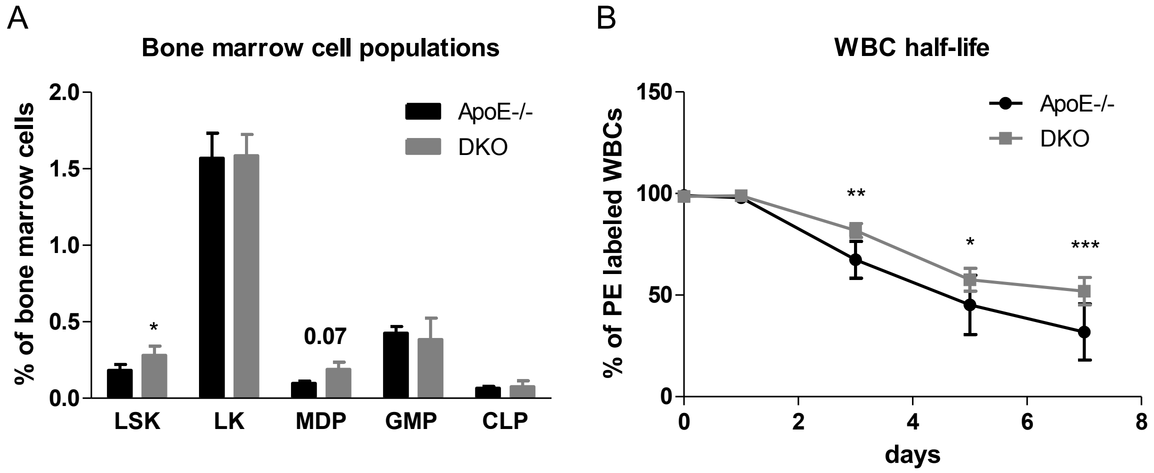

Figure 28. Increased WBC production and survival in DKO mice. BM analysis by flow cytometry: LSK populations (Lin$^-$Sca-1$^+$c-Kit$^+$), myeloid progenitor LK cells (Lin$^-$Sca-1$^-$c-Kit$^+$), granulocyte/monocyte progenitors (GMP; Lin$^-$c-Kit$^+$CD34$^+$FcγRII/III$^+$), monocyte/dendritic cell progenitors (MDP; Lin$^-$c-Kit$^{+/Int}$CD115$^+$Fit3$^+$), common lymphoid progenitors (CLP; Lin$^-$c-Kit^{lo}Sca-1^{lo}IL7Rα$^+$). Data represent means (n=6-7) + SD. (C) Half-life of WBCs as means (n=7) ± SD. *, $p < 0.05$; **, $p \leq 0.01$; ***, $p \leq 0.001$.

4.10. CB2R is not desensitized in macrophages from DKO mice

Macrophages originate from monocytes and represent the most dominant cell type in the atheroma. Thus, we explored consequences of MGL deficiency in these cells. We found comparable expression levels of lipases (Atgl, Hsl, Lal), enzymes capable to degrade MGs (Abhd6, Abhd12) and generate 2-AG (Daglα, Daglβ). The only observed difference was complete absence of Mgl mRNA in DKO cells, whereas Faah mRNA expression was absent in macrophages from both genotypes (Figure 29A). Western blot analysis of macrophage lysates revealed complete absence of MGL protein in DKO compared to ApoE-/- cells (Figure 29B).

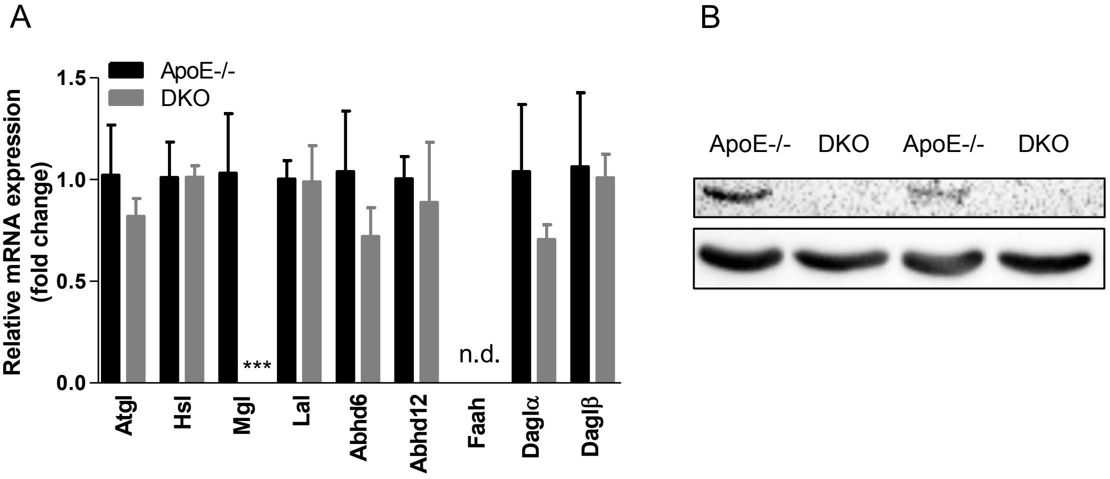

Figure 29. Comparable mRNA expression of lipases, 2-AG degrading and generating enzymes. (A) Macrophage mRNA expression of target genes was analyzed in duplicate by real-time PCR and normalized to the expression of Hprt as reference gene. Data represent means (n=4-5) + SD. (B) Western blot analysis of MGL protein expression in macrophages. ***, $p \leq 0.001$.

As expected, due to the absence of the main enzyme responsible for MG degradation, MG hydrolase activity was markedly reduced in DKO compared to ApoE-/- macrophages (Figure 30A). The reduction in MG hydrolytic activity led to intracellular accumulation of 2-AG in DKO compared to ApoE-/- macrophages (measured in collaboration with Thomas Eichmann, Universiy of Graz) (Figure 30B), indicating that MGL is the key enzyme in macrophage 2-AG homeostasis.

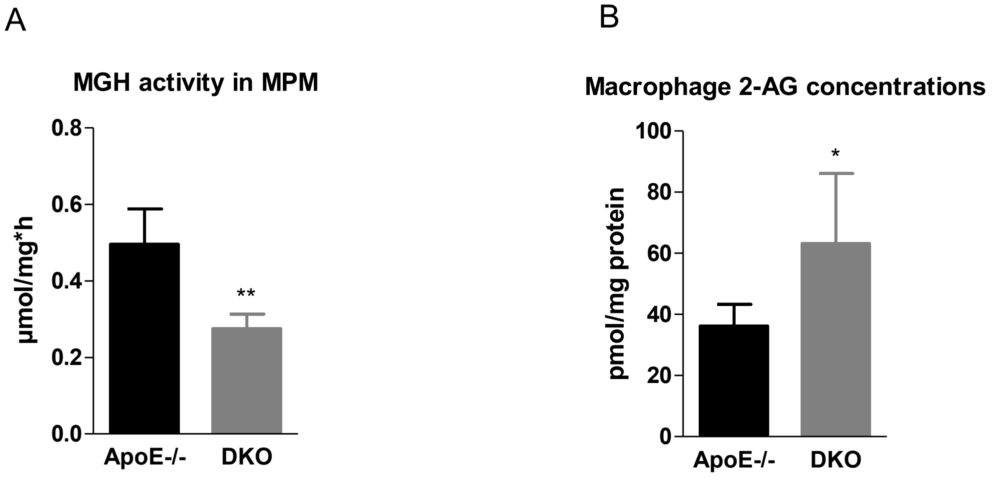

Figure 30. Reduced MGH activity and concomitant increase in cellular 2-AG concentrations in DKO macrophages. (A) MG hydrolase activity presented as means (n=6) + SD. (B) Macrophage 2-AG concentrations represented as means (n=5) + SD. *, $p < 0.05$; **, $p \leq 0.01$.

Next, we determined mRNA expression of Cb2r and Cb1r in ApoE-/- and DKO macrophages and found comparable Cb2r transcript levels in DKO and ApoE-/- cells, whereas Cb1r was undetectable (Figure 31A). In accordance, CB2R protein expression was unaltered Western blot and found comparable protein expression levels in DKO and ApoE-/- macrophages (Figure 31B).

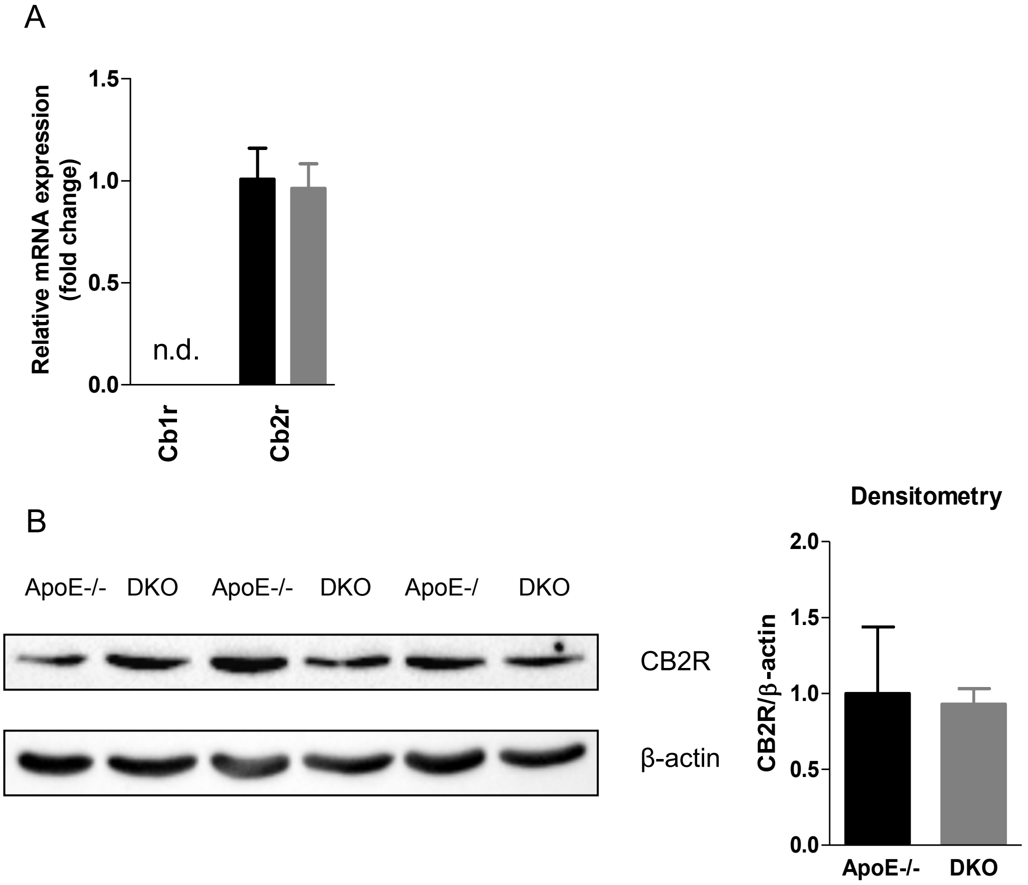

Figure 31. Unchanged CB2R mRNA and protein expression in DKO macrophages. (A) Real-time PCR and (B) Western blot analysis of CB2R expression in macrophages. Densitometric quantification of CB2R/β-actin (loading control) represent means (n=3) + SD.

Total cellular protein, however, does not indicate possible desensitization which occurs at least in brain of DKO mice, where the receptor is downregulated, internalized and rendered unavailable for ligand binding. Thus, we performed a functional assay (in collaboration with Corina Madreiter-Sokolowski, Medical University of Graz), where we measured macrophage Ca^{2+}-flux as a response to externally applied 2-AG, mimicking physiological conditions of elevated 2-AG in DKO animals. Comparable cytosolic Ca^{2+} responses to 2-AG treatment and an only slightly lower relative response of DKO cells to the maximal, ATP-provoked Ca^{2+}

flux (Figures 32A-C) indicate that although DKO macrophages are unable to clear 2-AG as efficiently as ApoE-/- cells, their EC system remains fully responsive to elevated 2-AG concentrations. Therefore, although CB1R in DKO animals is desensitized, CB2R downregulation is unlikely to occur, rendering CB2R-expressing cells sensitive to elevated 2-AG levels and potentiated EC signaling.

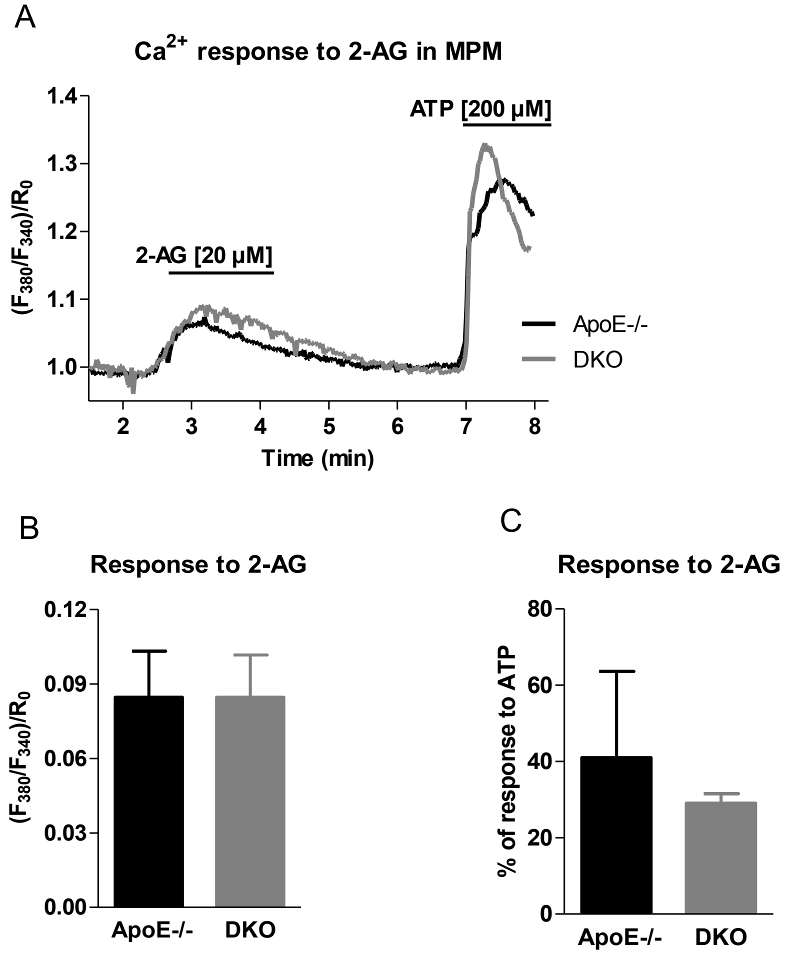

Figure 32. EC signaling is intact in DKO macrophages. (A) Representative traces of cytosolic Ca^{2+} signals in macrophages upon stimulation with 20 µM 2-AG and 200 µM ATP shown as normalized ratio $(F_{380}/F_{340})/R_0$. (B) Statistical evaluation of Ca^{2+} signals in macrophages in response to 2-AG; n=4-6 + SD. (C) Cytosolic Ca^{2+} response of macrophages to 2-AG calculated as percentage of response to ATP; n=4-6 + SD.

4.11. DKO macrophages show reduced foam cell formation due to reduced lipid uptake

Due to the importance of macrophage-derived foam cells in atherogenesis, we analyzed macrophage lipid parameters. Thioglycolate-elicited peritoneal macrophages isolated from DKO mice showed unaltered TG and reduced TC and FC concentrations under non-loaded conditions (Figures 33A, B). Upon loading with

VLDL or acLDL, macrophages from DKO mice displayed significant reductions in TG and cholesterol concentrations (Figures 33A-D). Nile red staining of LDs confirmed our observation of reduced foam cell formation upon lipoprotein loading of DKO macrophages (Figure 33E).

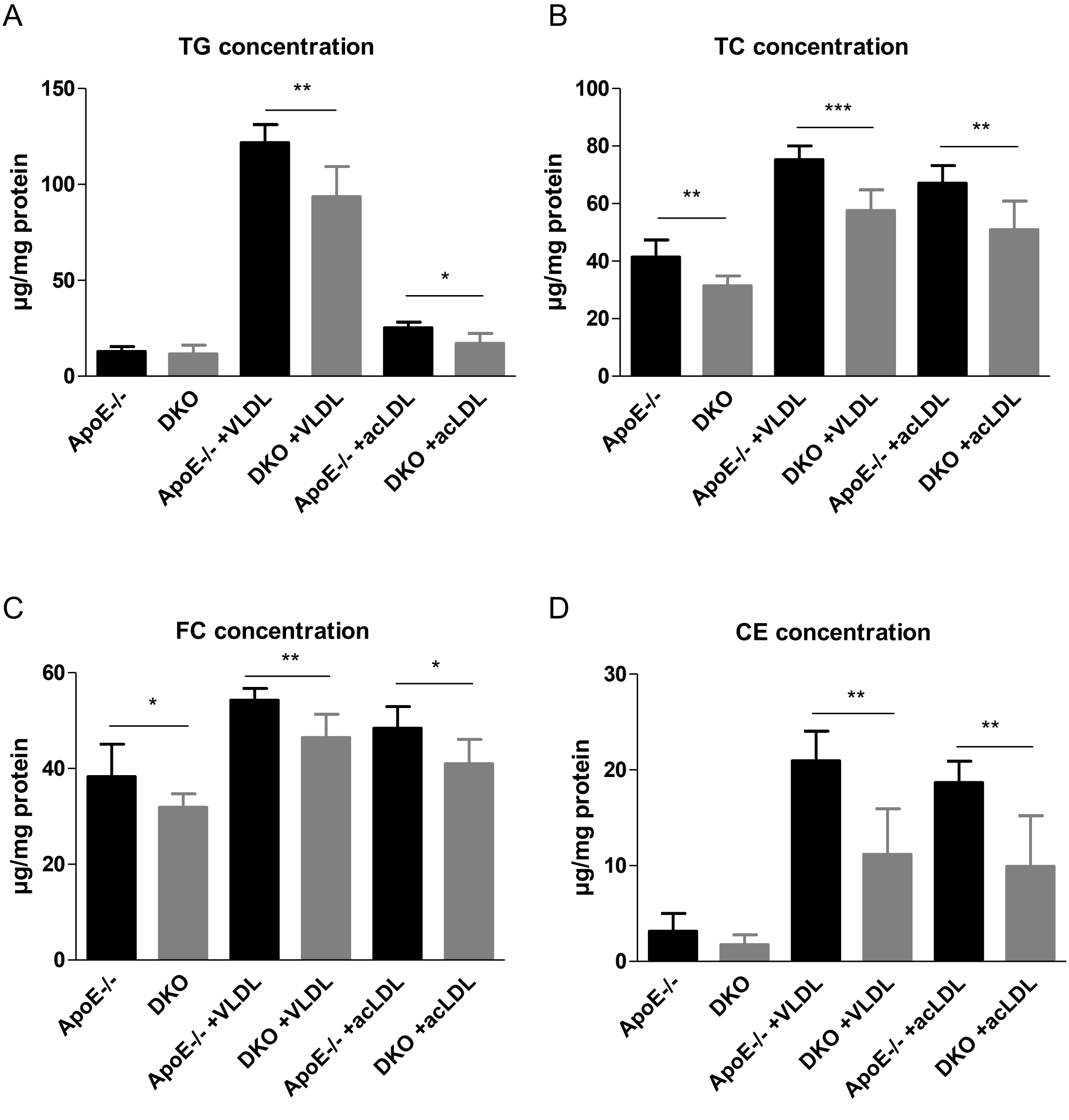

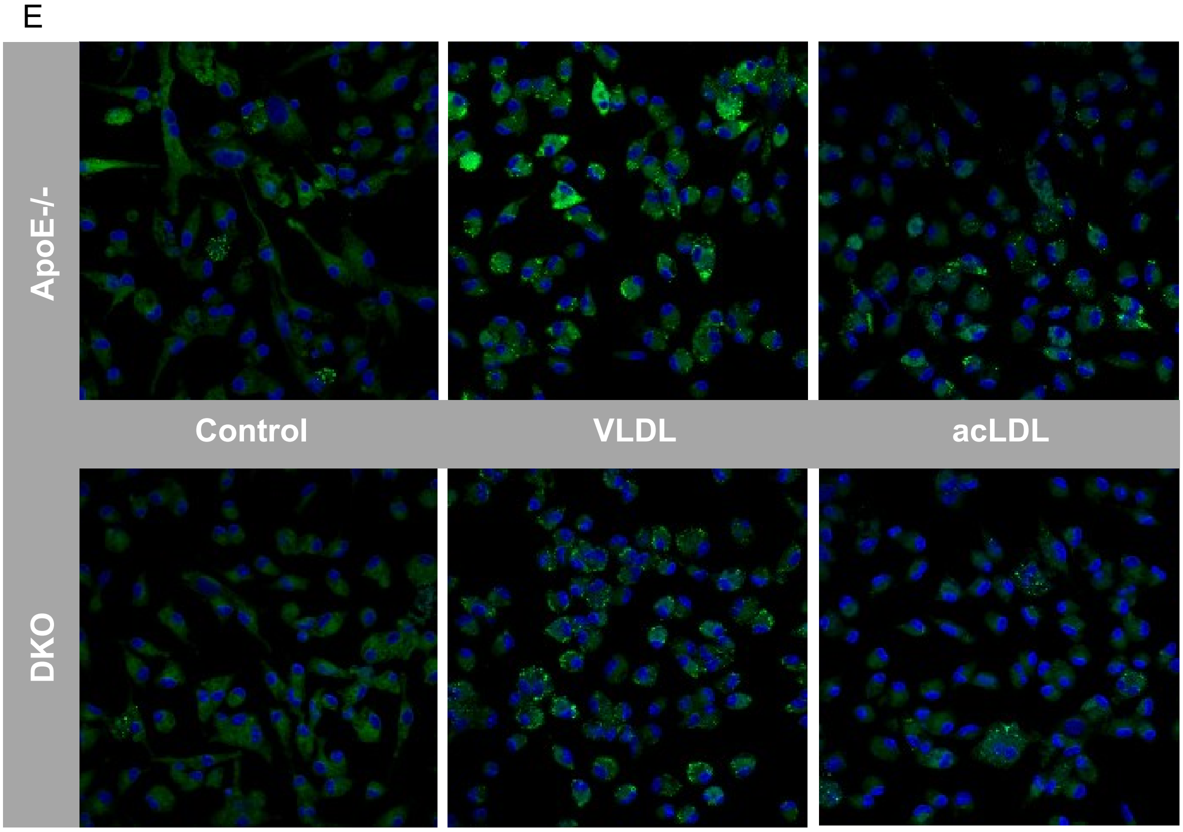

Figure 33. Reduced foam cell formation in DKO macrophages. Peritoneal macrophages were plated in 6-well plates for 24 h ± VLDL or acLDL (100 µg protein/ml medium). After lipid extraction, (A) TG, (B) TC, and (C) FC concentrations were measured spectrophotometrically, and (D) CE concentrations were calculated as TC minus FC. Data represent means (n=5-7) + SD. € LDs were visualized after Nile red staining (2.5 µg/ml) by confocal laser scanning microscopy. *, $p < 0.05$; **, $p \leq 0.01$, ***, $p \leq 0.001$.

The reduction in LD formation can be associated either with reduced lipid uptake, increased cholesterol efflux or increased FA oxidation. To address this question, we measured mRNA expression levels of Msr1 and Cd36, which are responsible for LDL, FA, and modified LDL uptake in macrophages, respectively. We found significantly reduced expression of Cd36 and unchanged expression of Msr1 compared to control cells. Other transporters associated with lipoprotein uptake (Vldlr, Ldlr, Lrp1) were unaltered. In addition, we assessed mRNA expression levels of Sr-b1 and Abc transporters (Abca1, Abcg1), which are responsible for cholesterol efflux from the cells. We found comparable expression levels of all cholesterol efflux transporters (Figure 34A). In accordance, macrophage efflux of radiolabeled cholesterol towards Apo-AI and HDL_3 was unaltered between these two genotypes (Figure 34B).

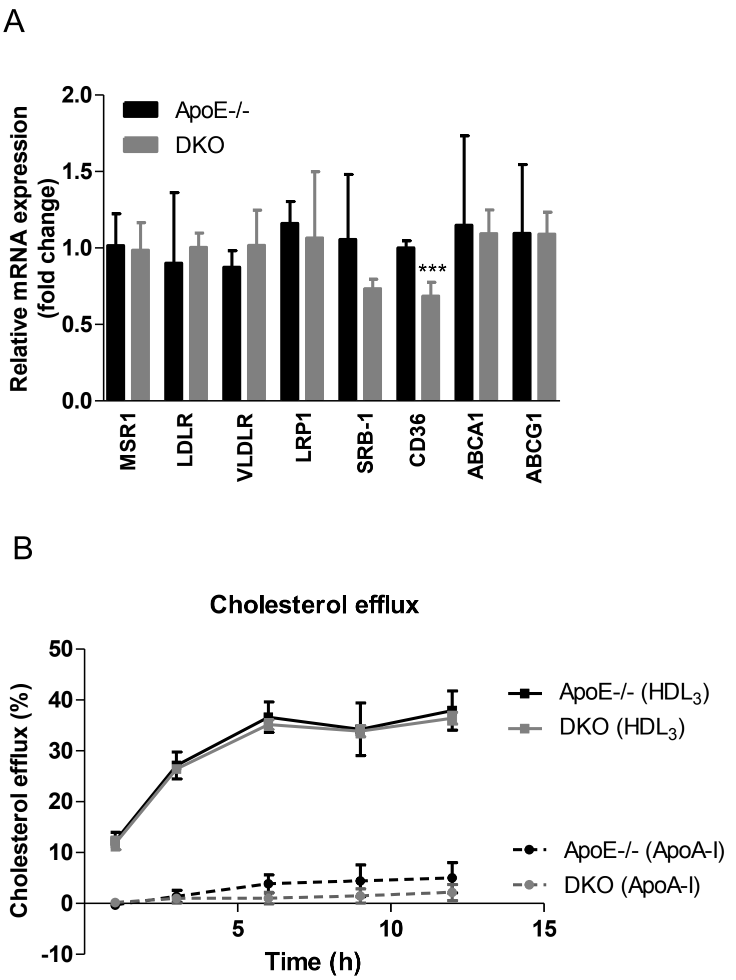

Figure 34. Reduction in foam cell formation of DKO macrophages is likely due to reduced lipid uptake rather than cholesterol efflux. (A) mRNA expression of target genes analyzed in duplicate by real-time PCR and normalized to the expression of Hprt as reference gene. Data represent means (n=4-5) + SD. Relative mRNA expression and associated statistical parameters were determined by the $2^{-\Delta\Delta CT}$ method. (B) Cholesterol efflux to ApoA-I and HDL_3 expressed as the percentage of [^{3}H]cholesterol transferred from cells to the medium. Data shown (n=3) ± SD of triplicate repeats. ***, $p \leq 0.001$.

4.12. DKO macrophages functionally phenocopy ApoE-/- cells

An increased area of advanced apoptosis is usually associated with enlarged necrotic core formation due to enhanced lesional cell apoptosis. Therefore, we investigated apoptosis in thioglycolate-elicited peritoneal macrophages in the absence and presence of VLDL and acLDL. We found comparable apoptosis and necrosis between the two genotypes (Figure 35A-C).

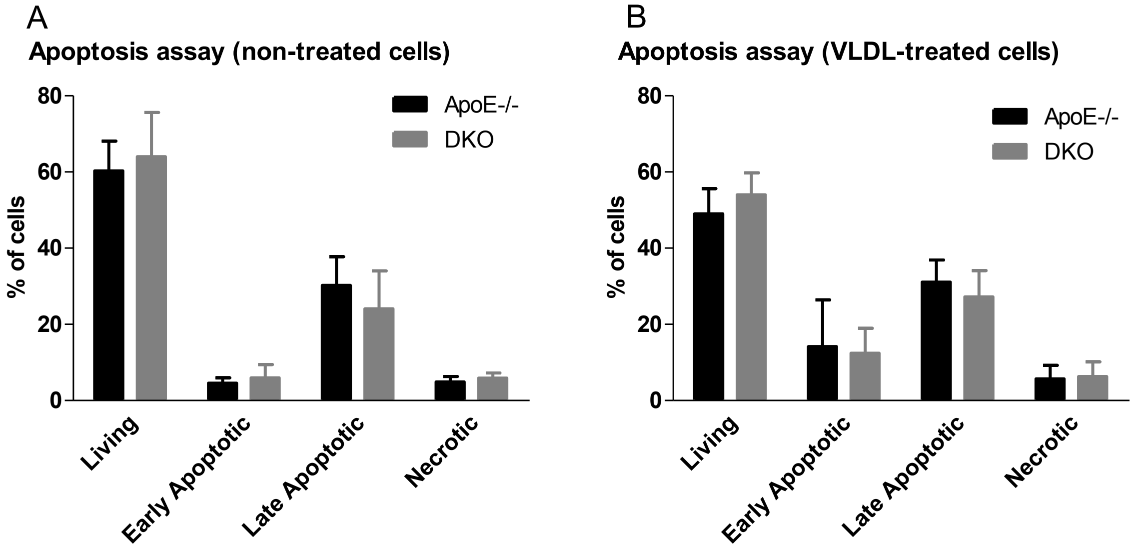

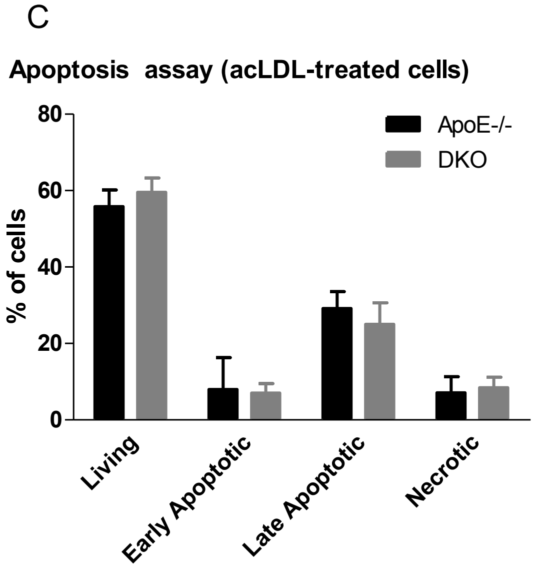

Figure 35. Comparable cell viability between ApoE-/- and DKO mice. (A-C) Apoptosis of macrophages was determined using Annexin V/PI staining. After isolation, MPMs were cultured for 24 h, after which cells were incubated for 24 h (A) without or with (B) VLDL (100 µg protein/ml medium) and (C) acLDL (100 µg protein/ml medium). Analysis was performed by flow cytometry. Data represent mean (n=6-7) + SD.

An M1 macrophage phenotype is often associated with increased propensity of cells to potentiate inflammatory process, whereas M2 macrophages are associated with a resolution of inflammation. To further characterize macrophage phenotype and function, we analyzed mRNA expression levels of M1 (Ccr5, Gro-1, Cxcl2, Itgax) and M2 (Arg1, Mrc1, Mrc2, Mgl2, Chi3l3) polarization markers, which were unaffected by MGL deficiency (Figure 36A). Since macrophage adhesion to endothelial cells is an important factor in the pathogenesis of atherosclerosis, we investigated mRNA expression levels of ligands for adhesion molecules which were comparable between the two genotypes (Figure 36B). To functionally characterize macrophages from DKO mice, we investigated *in vivo* phagocytic activity against fluorescently labeled *E. coli* particles. We found comparable phagocytic capacities between DKO and ApoE-/- macrophages (Figure 36C). All these data argue against profound changes in macrophage phenotype and function caused by alterations in 2-AG concentrations in macrophages and circulation.

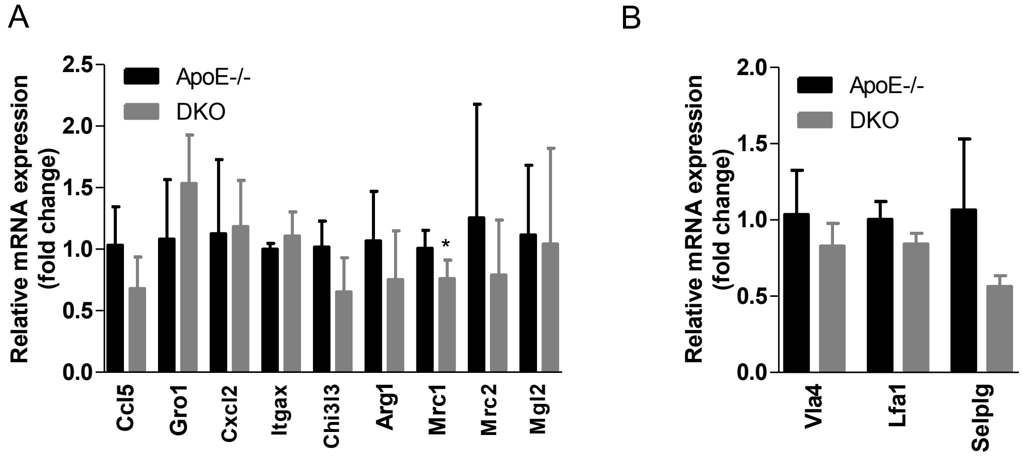

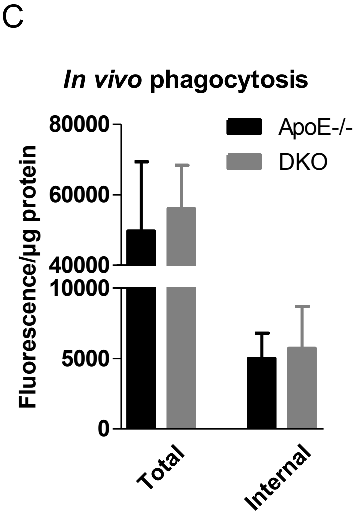

Figure 36. Total RNA was isolated from macrophages and subjected to real-time PCR analysis. (A, B) mRNA expression of target genes analyzed in duplicate by real-time PCR and normalized to the expression of Hprt as reference gene. Relative mRNA expression and associated statistical parameters were determined by the $2^{-\Delta\Delta CT}$ method. Data represent means (n=4-5) + SD. *, $p < 0.05$. (C) Fluorescein-labeled *E. coli* particles (200 µl) were injected into ApoE-/- and DKO mice. After 2 h, the peritoneum was flushed with 10 ml PBS/EDTA, macrophages were isolated and assayed for internalized fluorescence after quenching of extracellular fluorescence by trypan blue.

4.13. Aortic 2-AG increase is paralleled by the reduction in Cbr mRNA and the increase in Timps mRNA expression in DKO mice

Being the largest artery in the mouse exposed to the highest physical stress, aorta represents the predicted site for atherosclerosis lesion development. Thus, we investigated 2-AG levels (in collaboration with Thomas Eichmann, University of Graz) and expression of target genes in the aortic tissue. In the aorta, 2-AG concentrations were 3.5-fold increased in DKO compared to ApoE-/- mice (Figure 37A). Quantitative real-time PCR analyses revealed reduced expression of Cb1r and Cb2r in abdominal aortae of DKO compared to ApoE-/- mice after 9 weeks of WTD feeding. These data indicate that EC signaling is not only altered systemically and in the hepatic tissue but in the aortic tissue as well. Adhesion molecules are important mediators of leukocyte retention at the surface of the activated endothelium. Therefore, we assessed expression of integrins in the aortic tissue. Expression levels of adhesion molecules such as P-selectin, E-selectin, L-selectin, vascular cell adhesion molecule-1 (Vcam1), and intracellular adhesion molecule-1 (Icam1) were not markedly changed (Figure 37B), indicating that WBC arrest on the endothelial surface is likely not altered. Important for plaque stability is the balance between collagen degrading enzymes (Mmp-2 and -9) and tissue inhibitors of these enzymes (Timp-1, -2, -3, and -4). Although we did not observe any changes in Mmps expression, we found increased expression of Timp-1 and -2, which can lead to a net effect of reduced collagen degradation and improved plaque stabilization.

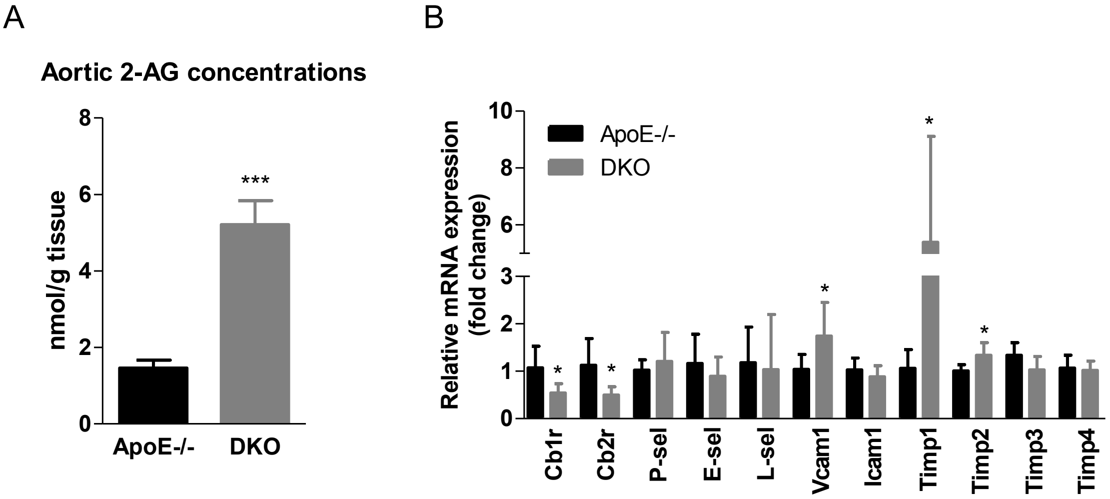

Figure 37. Increased 2-AG concentrations in aortae of DKO mice. (A) Aortic 2-AG concentrations after 9 weeks of WTD feeding presented as means (n=5) + SD. (B) mRNA expression of target genes analyzed in duplicate by real-time PCR and normalized to the expression of cyclophilin A as reference gene. Expression profiles and associated statistical parameters were determined by the 2-ΔΔCT method. Data represent means (n=8) + SD. *, $p < 0.05$; **, $p \leq 0.001$.

4.14. DKO mice show enlarged plaques due to collagen accumulation leading to plaque stabilization

To analyze atherosclerotic plaque formation, we sacrificed the animals after 9 weeks of WTD feeding, isolated thoracic aortae and stained them with ORO for plaque size measurements. Surprisingly, we found increased plaque size in *en face* aortae of DKO compared to ApoE-/- mice in total thoracic aorta (Figure 38A) and arch area (Figures 38B, C).

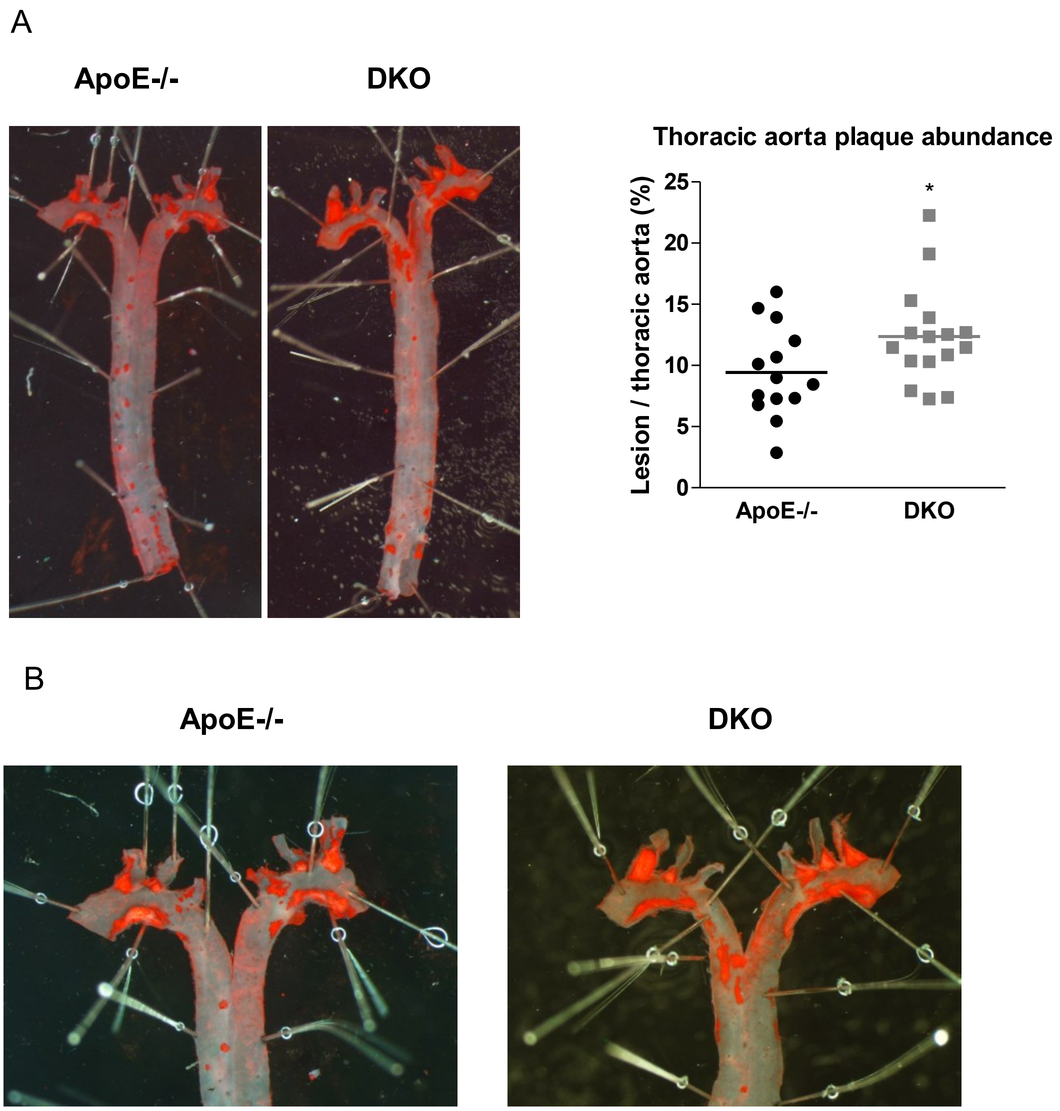

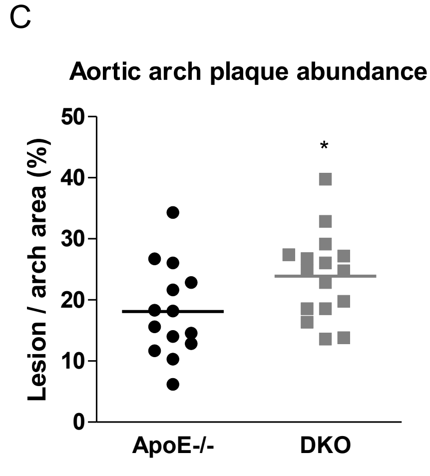

Figure 38. Increased plaque abundance in aortae of DKO mice. (A) Quantification of lesion sizes in total thoracic aortae and (B, C) arch area after 9 weeks of WTD feeding. Data represent mean (n=14-15). *, $p < 0.05$.

The increase in plaque burden was even more pronounced in aortic valve sections of DKO mice (Figure 39A, B). Interestingly, we also found reduced neutral lipid plaque content in DKO lesions compared to ApoE-/- mice, as manifested by reduced ORO-positive areas within the lesions (Figure 39A,C).

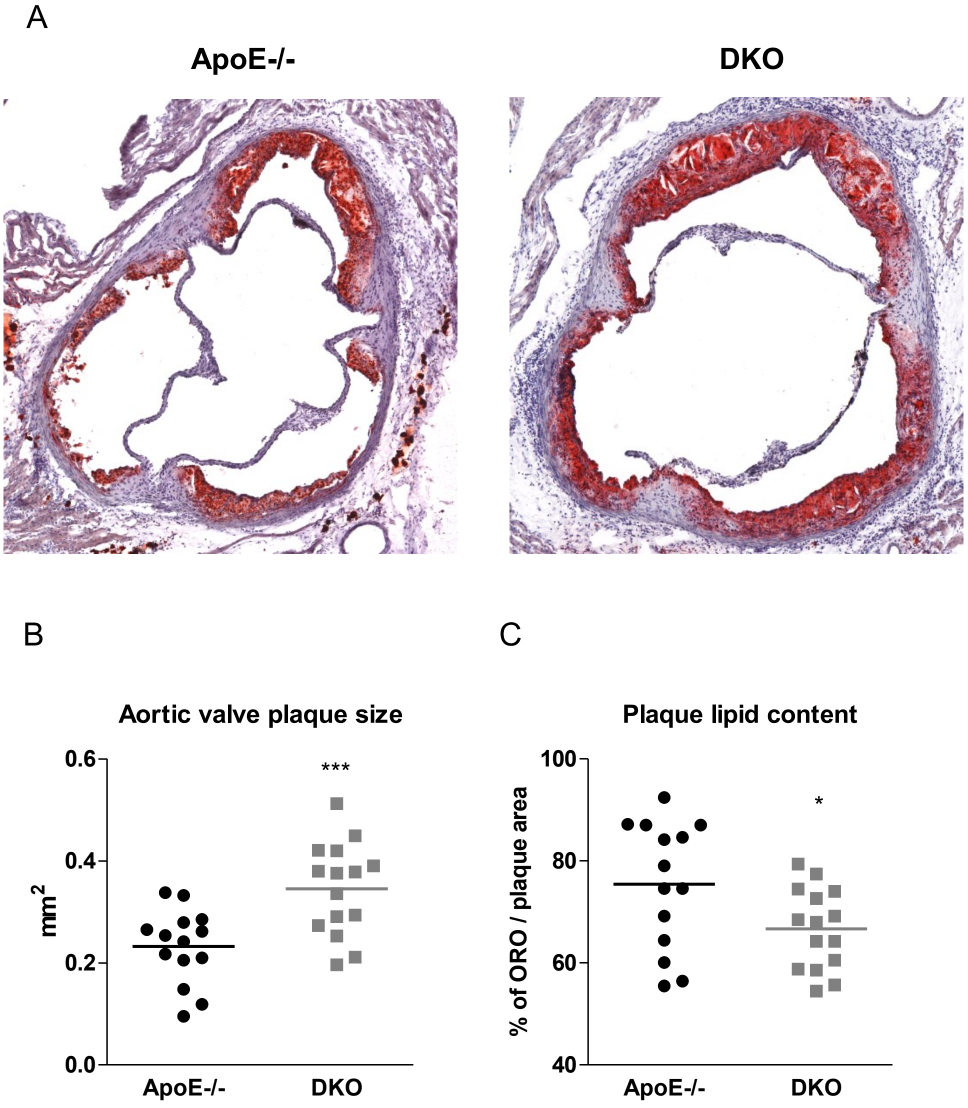

Figure 39. Increased plaque size but reduced lipid content in aortic valve lesions of DKO mice. (A, B) Total lesion size measurements and (A, C) ORO staining for lipids. Data represent mean values of 15 aortic valve sections for lesion size measurements and 3 aortic valve sections in the area of maximal plaque size for ORO (n=14-15). *, $p < 0.05$; ***, $p \leq 0.001$.

Since foam cells represent the main compartment of intraplaque lipid storage, we performed immunohistochemistry against MoMa-2, a marker for monocytes and macrophages. MoMa-2 staining revealed a trend towards reduced relative abundance of macrophages in the atheroma of DKO animals (Figure 40A, B). These data phenocopy *in vitro* results with reduced foam cell formation in DKO macrophages.

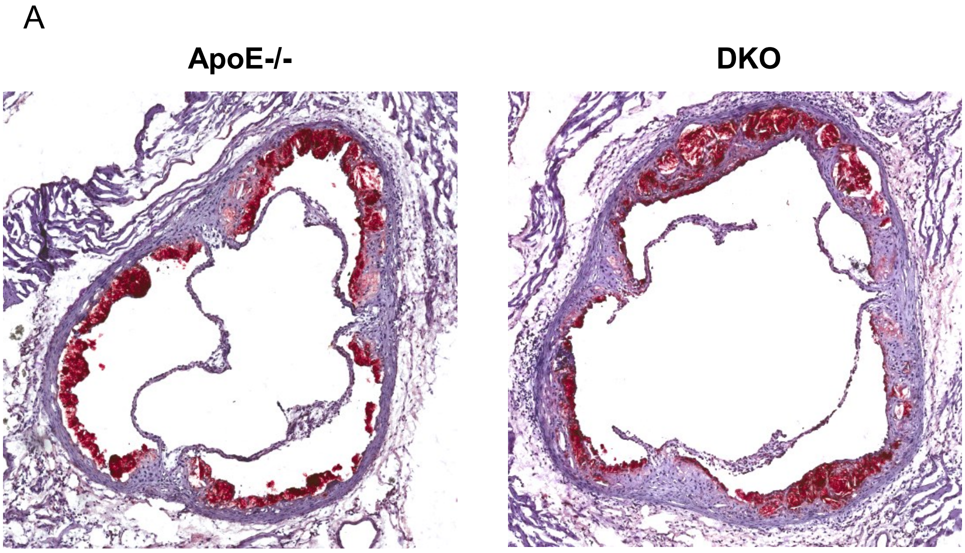

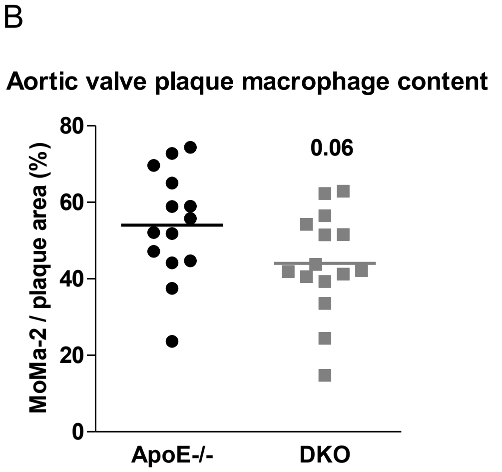

Figure 40. Reduced relative macrophage abundance in the atherosclerotic lesions of DKO mice. MoMa-2 immunohistochemical staining for macrophages (red). Data represent mean (n=14-15) values of 3 aortic valve sections in the area of maximal plaque size.

Increased plaque size, despite reduced macrophage and lipid content, indicate that another plaque component crucially determines relative plaque composition and size in DKO mice. Indeed, collagen content, measured by Masson's trichrome staining, was markedly increased in DKO plaques, comprising almost 40% of the total lesion area (Figure 41A, B). Additionally, necrotic core size, defined as the acellular compartment of Trichrome-stained sections, was reduced in DKO compared to ApoE-/- mice (Figure 41A, C).

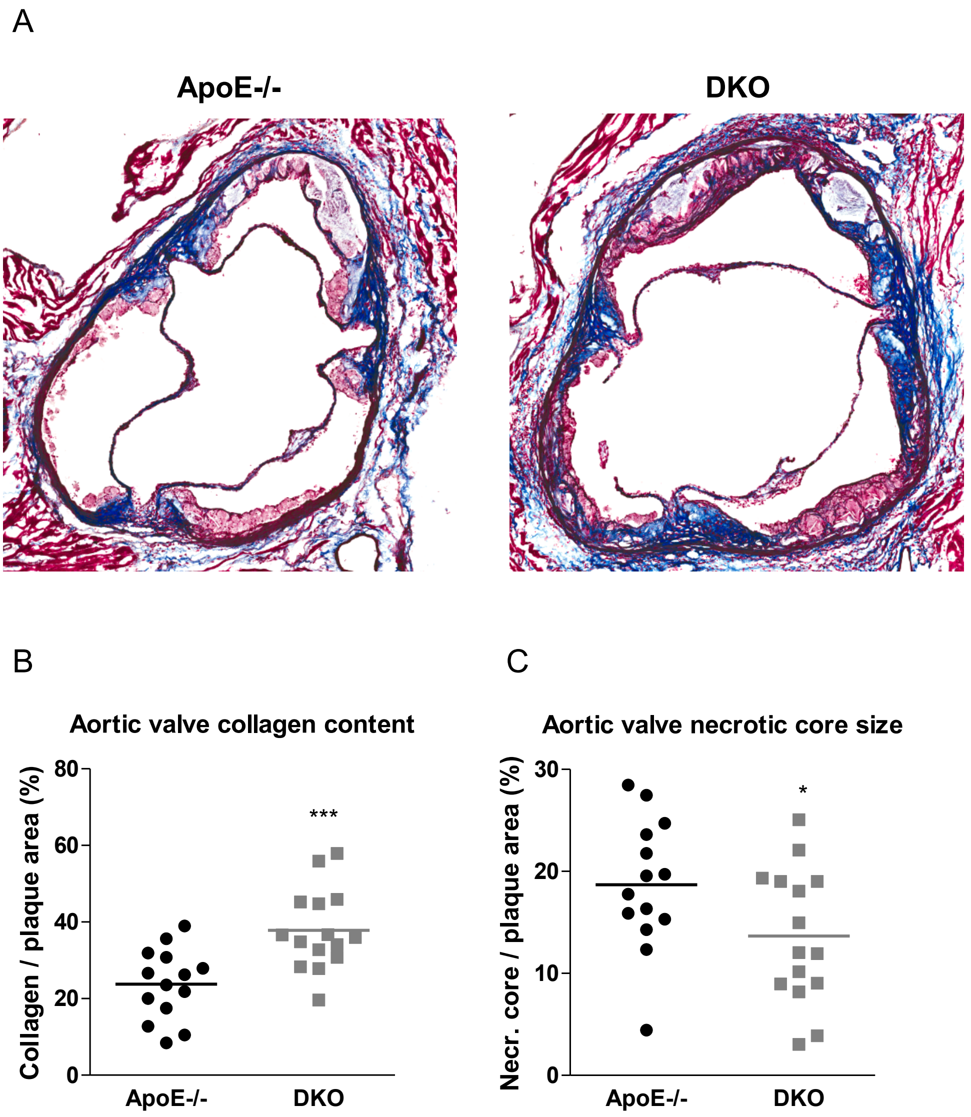

Figure 41. Increased collagen content and reduced necrotic core size in plaques of DKO mice. (A, B) Masson's Trichrome staining for collagen (blue), (A, C) necrotic core (acellular compartments). Data represent mean (n=14-15) values of 3 aortic valve sections in the area of maximal plaque size. *, $p < 0.05$; ***, $p \leq 0.001$.

Due to the importance of collagen in the pathophysiology of atherosclerosis, which leads to plaque stability and prevents acute cardiovascular events associated with plaque rupture and intravascular thrombosis, we focused our research to plaque composition and stability. An important characteristic of stabilized lesions is the minimal thickness of fibrous caps overlaying the unstable necrotic core and preventing lesion plaque rupture. Importantly, a lesion phenotype is largely characterized by the ratio of the highly stabilizing collagen compartment and the largely destabilizing necrotic core abundancies within the plaque. Both of these plaque stability determinants were significantly improved in DKO lesions (Figures 42A-C) leading to the conclusion that, although DKO plaques are enlarged, the increase in size is largely attributed to the high production of collagen content and thus lesion stabilization.

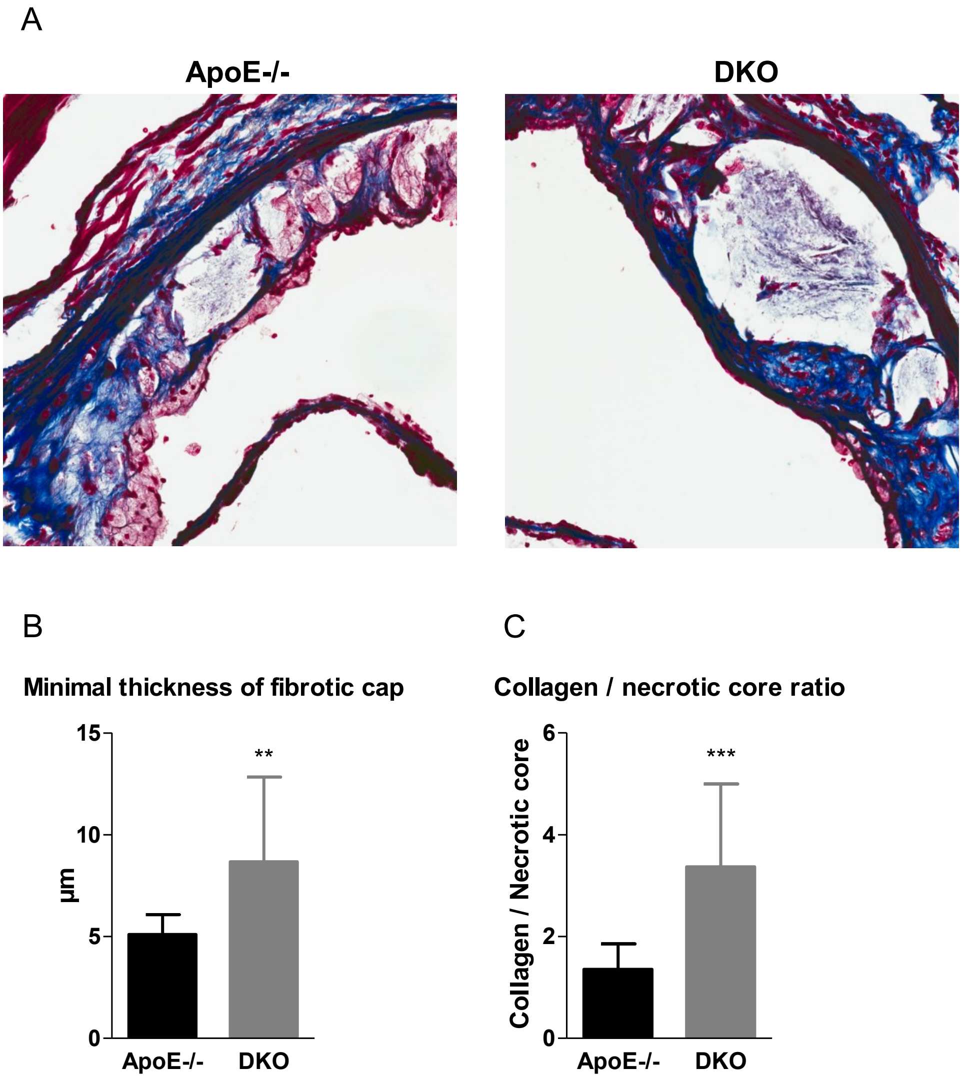

Figure 42. Increased minimal thickness of fibrotic cap and ratio of collagen to necrotic core in the lesions of DKO mice. (A, B) Minimal thickness of fibrotic cap, (C) collagen-to-necrotic core ratio. Data represent mean (n=14-15) + SD. **, $p \leq 0.01$; ***, $p \leq 0.001$.

Increased lesional collagen content can be either due to increased collagen production or reduced proteolytic intraplaque degradation of the connective tissue. Smooth muscle cells are the main source of newly generated collagen within the plaques and the observed elevated amount of intraplaque collagen buildup was likely caused by the increased abundance of smooth muscle cells within the plaque as determined by the relative increase in alpha smooth muscle actin (α-SMA)-positive areas (in collaboration with Silvia Schauer, Medical University of Graz) (Figure 43A, B). Additionally, the ratio of necrotic core to α-SMA as an indicator of plaque vulnerability was reduced in DKO mice (Figure 43C).

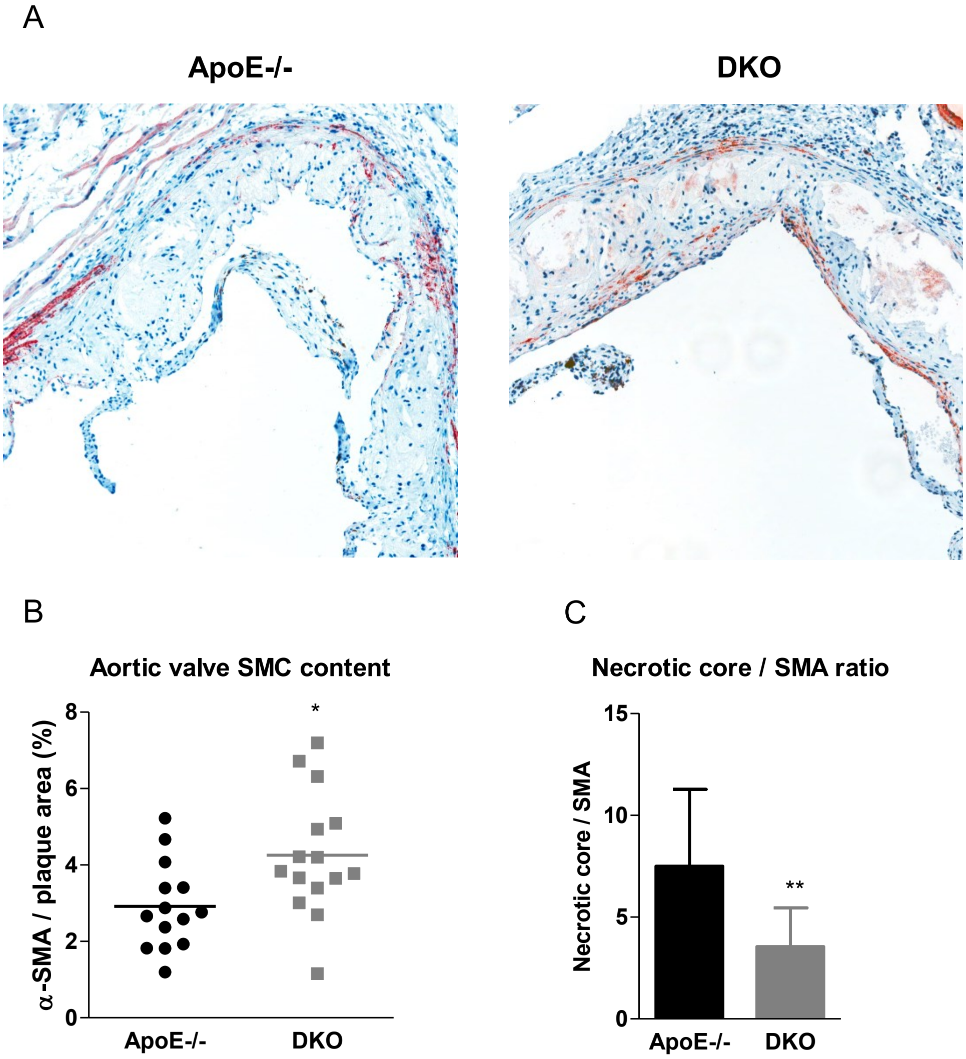

Figure 43. Increased relative abundance of smooth muscle cells in lesions of DKO mice. (A,B) α-smooth muscle actin immunohistochemical staining for smooth muscle cells (red). Data represent mean values (n=14-15) of 3 aortic valve sections in the area of maximal plaque size. Data represent mean. (C) Necrotic core-to-SMA ratio. Data are presented as mean (n=14-15) + SD. *, $p < 0.05$, ** $p \leq 0.01$.

Alternatively, changes in the plaque stability can be associated with neutrophil-mediated protease activity and degradation of collagen within the plaques. The effect of proteolytic activity itself is reflected in a net effect of produced MMPs and the activity of locally produced TIMPs, which inhibit collagen degrading functions of these enzymes. For these reasons, we used conditioned media from cultivated peritoneal neutrophils to perform gel zymographic analyses of pro-MMP-9, MMP-9, pro-MMP-2, and MMP-2. Comparable aortic expressions and gelatinolytic activities of neutrophil-produced MMPs (Figure 44A, B) and increased mRNA expression of aortic Timps indicate that collagen degradation is rather decreased than increased in DKO mice.

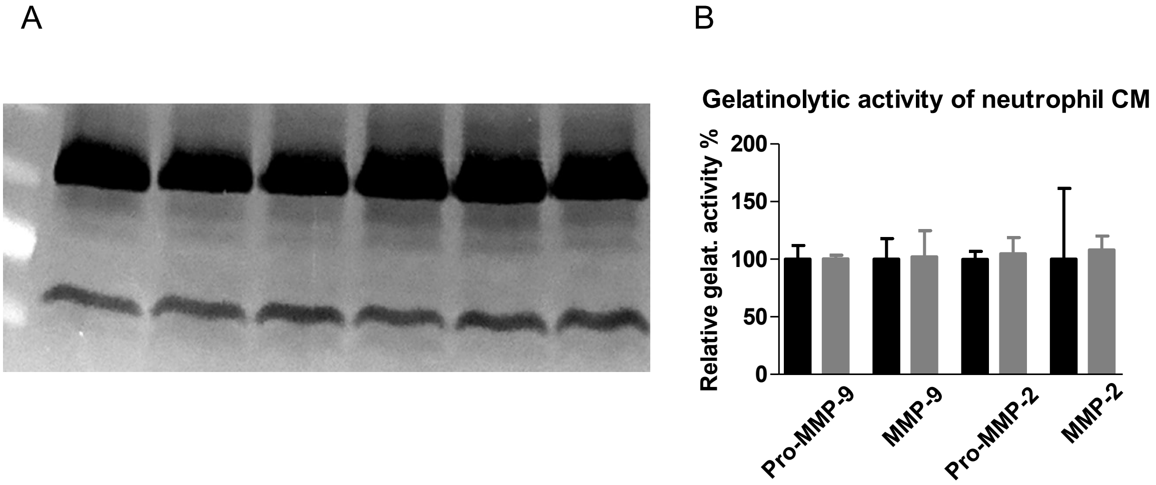

Figure 44. Comparable gelatinolytic activities of neutrophil conditioned media from ApoE-/- and DKO mice. (A, B) Relative gelatinolytic activity of neutrophil conditioned media from ApoE-/- and DKO mice (n=3). Data are presented as mean + SD.

Taken together, these results indicate that although DKO mice exhibit larger lesion size the atheroma composition is drastically changed to a more stable plaque phenotype with reduced destabilizing compartments of necrotic core and macrophages and increased content of smooth muscle cells and collagen, which stabilize atherosclerotic lesions (Figure 45).

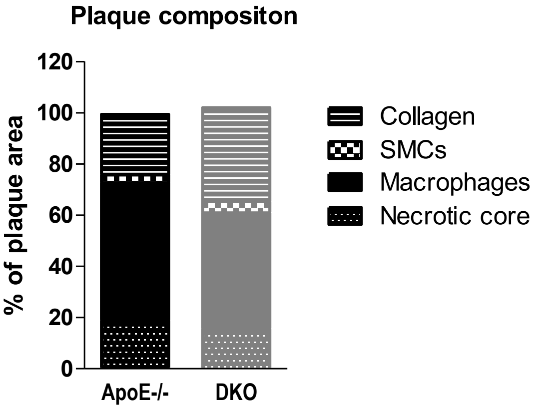

Figure 45. Atherosclerotic plaques are more stable in DKO mice. Bars represent the mean of 14-15 mice per group. Distribution of necrotic core, macrophages, smooth muscle cells, and collagen within the plaque.

5. Discussion

Intracellular lipolysis requires three consecutive steps, mediated by ATGL, HSL, and MGL, respectively. Thus, MGL catalyzes the final and rate-limiting step in TG hydrolysis by cleaving MGs to glycerol and FFA (45). Among the MG substrates hydrolyzed by MGL is 2-AG, the most abundant EC in mammals, which acts as full agonist on CB1R and CB2R (127, 128). Therefore, MGL is at a crossroad of lipid and energy metabolism on one hand, and 2-AG turnover and signaling on the other. EC signaling affects a wide plethora of homeostatic functions, ranging from energy homeostasis to immune response. Thus, we speculated that the lack of MGL may also affect the pathogenesis of atherosclerosis. To investigate the consequences of MGL deficiency on atherosclerosis development, we generated MGL-/- mice on the atherosclerotic ApoE-/- background and challenged them with WTD.

We found systemically increased 2-AG concentrations in DKO mice, indicating that MGL is capable to efficiently regulate 2-AG degradation and homeostasis. However, expected cannabimimetic effects mediated by CB1R such as increased food intake, potentiated body weight gain, lipogenesis, and adiposity were absent in DKO animals. These results phenocopy the state of MGL-/- mice, in which increased brain 2-AG levels do not promote CB1R-mediated signaling, due to receptor desensitization via receptor downregulation and blunting of cannabimimetic signaling (86). Current knowledge is limited to brain (84-86) and intestinal (223) CB1R desensitization, although it is highly unlikely that other organs and tissues expressing CB1R do not undergo desensitization as well.

Plasma lipid parameters in DKO animals remained at comparable levels to ApoE-/- mice on chow and WTD in fed states. In the fasted state, DKO mice showed reduced FG and FFA concentrations. This reduction is due to the pivotal role of MGL in lipolysis, defective TG hydrolysis and reduced release of lipolytic endproducts from WAT during fasting. It is interesting that, although FG and FFA concentrations were reduced, fasting TG concentrations showed just a non-significant trend towards reduction in DKO animals. This result differs from MGL-/- mice, in which fasting plasma TGs were reduced (86). It is important to mention, however, that ApoE-deficiency causes suppression of normal VLDL secretion (224, 225), thereby possibly hindering the effect of MGL deficiency on VLDL output in our animal model.

Hepatic lipid metabolism was altered in DKO mice as well. Fasting liver TG and in particular CE concentrations were strongly reduced in DKO mice, whereas FC concentrations remained at the same level compared to ApoE-/- animals. Reduced hepatic TG is a result of reduced liver supply with FFA from WAT as their main source during fasting. In addition, Cd36 mRNA expression was reduced in livers of DKO animals, indicating reduced FFA uptake from the plasma. This consequently leads to reduced availability of FFA for TG re-synthesis in the liver. Concomitantly, liver TG concentrations as well as TG output via VLDL secretion were reduced in DKO animals. Interestingly, in the fed state we observed increased hepatic mRNA expression of Acc1 and reduced expression of Acc2. Indeed, after refeeding, DKO mice showed increased incorporation of [^{14}C]acetate into TG, presumably due to elevated Acc1 expression and activity. In contrast, genetic deficiency of Acc2 in mice leads to a lean phenotype with increased FFA oxidation in liver (226). We, however, failed to observe any difference between DKO and ApoE-/- mice in energy substrate utilization as measured by indirect calorimetry. In addition to 25 % reduction in fasting hepatic TG levels and plasma TG levels being significantly reduced 3 and 4 h post-LPL inhibition with tyloxapol injection, these data imply that the observed effects are minor and thus do not largely impact global energy homeostasis in DKO mice.

Hepatic cholesterol content was also significantly altered in DKO mice with reduction in CE but not FC levels. Reduced cholesterol can be a consequence of reduced dietary cholesterol uptake, reduced *de novo* cholesterol synthesis, increased intraconvesion of cholesterol into bile acids and elimination via bile, or trans-intestinal cholesterol excretion (TICE) (227). We found comparable *de novo* cholesterol synthesis and [^{14}C]acetate incorporation into FC and CE in DKO and ApoE-/- mice. To determine cholesterol uptake, we performed acute cholesterol absorption as well as prolonged cholesterol absorption study using the fecal dual-isotope ratio method (222). To our surprise, we observed prolonged gastric retention of the cholesterol bolus with a consequent reduction in cholesterol accumulation in duodenum and jejunum and delayed appearance of cholesterol in the circulation. Similarly, increased gastric retention of the [3H]oleic acid was observed after intragastric oil gavage, with the delayed appearance of radioactivity in circulation, although without effect on duodenal or jejunal FA retention. Indeed, when we performed a gut transit time measurement, total gut transit was reduced in DKO animals compared to controls. The delayed gut transit influences chylomicron production and release, evidenced by delayed appearance of radiolabeled triolein and cholesterol in the circulation of DKO mice. Current knowledge in this field is somewhat conflicting. Although Taschler *et al.* found CB1R desensitization in the intestine of MGL-/- mice with the concomitant lack of reduction in gut motility (223), another study shows that MGL-/- mice indeed suffer from delayed lipid absorption (87). A proposed mechanism for this discrepancy is that the effect on lipid absorption may be independent of CBRs since it has been shown that the MG 2-oleoylglycerol can act on GRP119 to stimulate GLP-1 production and concomitantly reduce gastric motility (228). Increased gut transit time may also be the reason for the observed elevation in postprandial FFA and FG concentrations in DKO mice compared to ApoE-/- animals. A concomitant delay in chylomicron-mediated delivery of FAs to peripheral tissues would also delay the suppression of lipolysis and thus the release of lipolytic endproducts into the circulation. Total lipid absorption in DKO mice is likely not affected since fractional cholesterol absorption after 3 days of measurement showed comparable results in both genotypes. Similar data with delayed lipid appearance in the circulation have recently been published in MGL-/- compared to WT mice (87). Important to mention is that fecal cholesterol concentrations were increased in DKO mice fed WTD. Taking into account that total cholesterol uptake is unaltered, the source of increased fecal cholesterol must be either bile secretion or TICE. In addition, we observed increased mRNA expression of Cyp7a1 in the livers of DKO animals, which may be a contributing factor for the reduced hepatic cholesterol levels, due to interconversion of cholesterol into bile acids. Moreover, expression levels of Ldlr, Srb1, and HmgCoAr were increased, probably as a compensatory response to the absence of hepatic CE stores. Moreover, it has been shown previously that MGL-deficiency protects mice from hepatic ischemia/reperfusion injury by limiting liver inflammation and oxidative stress. This process is partly mediated by CB2R through elevated 2-AG levels and partly by reduced eicosanoid production (218). These results clearly indicate that MGL, although acting as an MG hydrolyzing enzyme, strongly affects the homeostasis of both TG and cholesterol in a direct and indirect manner via MG species serving as signaling molecules.

In the process of atherogenesis, hyperglycemia *per se* is not considered as a causative factor for atherosclerosis development. However, altered glycemic control as a comorbidity to hyperlipidemia strongly accelerates the process of atherogenesis (229). Due to close association of lipid and carbohydrate metabolism as well as the influence of hyperglycemia on atherogenesis, we explored glucose metabolism in DKO animals. We found improved glucose tolerance in DKO animals, which is unlikely the consequence of increased insulin sensitivity. Circulating insulin levels were similar between DKO and ApoE-/- mice either in fed or fasted states. In addition, reduced blood glucose levels in DKO mice during insulin tolerance test reflect only the basal reduction and not increased relative reduction in plasma glucose of DKO mice. Moreover, a potentiated insulin action would diminish gluconeogenesis, which remained unchanged between both genotypes with either pyruvate or glycerol used as a source for *de novo* synthesis of glucose. It is plausible, however, that the reduced abundance of FFAs during fasting shifts energy substrate utilization from lipids to glucose. This notion is supported by the fact that plasma glucose levels were reduced in DKO animals only upon fasting but not in fed state. Moreover, enhanced glucose release upon glucagon stimulation, together with reduced fasting hepatic glycogen concentrations, argue in favor of increased glucose utilization during fasting due to reduced FFA availability.

As mentioned before, CBRs have biphasic distribution, with CB1R being expressed in metabolic tissues and CB2R in immune cells. Little is, however, known regarding CB2R activity during chronic 2-AG elevation. Chanda *et al.* state that CB2R expression and activity remain unchanged in spleens of MGL-/- compared to WT animals (84). To date, no functional assay investigated the influence of systemically increased 2-AG levels on CB2R-expressing cells. In our model, mRNA expression of cytosolic (Atgl, Hsl) and lysosomal lipases (Lal), enzymes capable to degrade MGs (Abhd6, Abhd12), and enzymes responsible for 2-AG generation (Daglα, Daglβ), remained unaltered in the absence of MGL. Thereafter, we measured macrophage MG hydrolase activity *in vitro* to determine to which extent MGL influences MG degradation. We found ~44 % reduced MG hydrolase activity in DKO compared to ApoE-/- macrophages. Moreover, MGL deficiency caused ~75 % increased 2-AG concentrations in DKO macrophages. These results together indicate that MGL represents the key enzyme responsible for 2-AG homeostasis in macrophages. Since chronically elevated levels of 2-AG lead to CB1R desensitization, we assessed whether CB2R desensitization occurs as well. mRNA and protein expression of CB2R in macrophages were identical between ApoE-/-

and DKO macrophages. However, total cellular protein abundance does not indicate receptor downregulation and internalization. Next, we tried to determine macrophage cell-surface *versus* cytosolic CB2R localization, and thus possible desensitization, by using either immunofluorescence or flow cytometry, but failed due to unspecificity of all tested CB2R antibodies (data not shown). Thus, we performed a functional assay of CB2R activity by stimulating macrophages with 2-AG and measuring cytosolic Ca^{2+} levels. We found unchanged cellular Ca^{2+} response to 2-AG treatment, indicating that DKO macrophages retain their full CB2R capacity in response to 2-AG stimulation with no evidence of receptor desensitization. Although DKO mice have systemically increased 2-AG levels, CB2R-mediated signaling remains fully functional. Thus, systemically and locally elevated 2-AG concentrations can potentiate cannabimimetic effects on CB2R-expressing immune cells in DKO animals. As previously proposed by Lichtman *et al*, CB1R may be more prone to desensitization compared to CB2R (230).

Activation of CB2R on immune cells would was expected to alter immune response and inflammation. Indeed, elevated leukocyte numbers in DKO mice upon WTD feeding indicate that MGL deficiency affects the hematopoietic system *in vivo*, likely via altered EC signaling. Interestingly, not all cells were affected by the increase in cell numbers, but the effect was most pronounced in lymphocytes and monocytes, suggesting that not all WBCs express the same sensitivity to alterations in 2-AG concentrations, which may be associated with different expression levels of MGL and CB2R in various types of WBCs. An estimation of the relative abundance of specific WBC populations revealed comparable amounts of $Ly6C^{high}$ and $Ly6C^{low}$ monocytes and an increase in T lymphocyte counts in DKO compared to ApoE-/- mice. Due to the importance of T lymphocytes in the pathogenesis of atherosclerosis, it is likely that elevation of circulating lymphocytes may affect atherogenesis or plaque structure. The increase in leukocyte numbers may originate either from potentiated hematopoiesis in the BM or extended WBC half-life. Indeed, we found an increased relative abundance of LSK cells, which carry most of the hematopoietic stem cell activity in the BM. In accordance, a recent publication from Jiang *et al.* clearly demonstrates implication of EC system in hematopoiesis, where potentiated CB2R activity in the BM stimulates stress-induced hematopoiesis by increasing the marrow cellularity, LSK numbers, and BM cell survival (231).

Likewise, extended *in vivo* WBC half-life in the peripheral circulation of DKO animals may be another potent contributor to increased WBC counts.

Detectable plasma 2-AG levels and significantly elevated 2-AG concentrations in the aortae of DKO mice suggest systemic and local changes in the aortic EC signaling. However, mRNA expression levels of Cb1r and Cb2r in aortae of DKO mice were decreased, indicating a down-regulation of both CBRs and local dampening of CBR-mediated signaling as a compensatory consequence of increased 2-AG concentrations. Expression levels of adhesion molecules in the aortae as well as their ligands in macrophages were comparable between DKO and ApoE-/- mice, implying that leukocyte adhesion and endothelial transmigration are likely not affected by the perturbations in EC system.

En face and aortic valve section analyses demonstrated increased plaque formation in DKO compared to ApoE-/- mice. However, the plaque lipid content differed significantly between ApoE-/- and DKO mice with reduction in neutral lipid accumulation in DKO lesions. Foam cell formation is considered to be a hallmark of atherosclerosis due to subintimal macrophage accumulation and uptake of modified lipoprotein particles in an uncontrolled manner. Thus, we performed MoMa-2 immunostaining to determine the relative abundance of macrophages in the lesions. We found a trend towards a reduced intraplaque macrophage amount in DKO compared to ApoE-/- mice. In line with these results, *ex vivo* assays in DKO macrophages revealed reduced intracellular TG and CE concentrations upon VLDL and acLDL loading and decreased TC and FC content in both loaded and non-loaded conditions. Unchanged mRNA expression of ABCA1 and ABCG1 as well as cholesterol efflux efficiencies towards ApoA1 and HDL_3 between macrophages of both genotypes argue against increased cholesterol removal as the mechanism for attenuated foam cell formation in DKO cells. Instead, Cd36 transcript reduction in DKO macrophages indicates that lipid uptake, rather than efflux, is likely responsible for the reduced susceptibility of DKO cells to foam cell formation. In line with decreased Cd36 mRNA expression in DKO macrophages, Chiurchiu *et al*. have recently demonstrated that CB2R activation in human macrophages leads to downregulation of CD36, causing reduced foam cell formation (220). Changes in intracellular lipid homeostasis substantially alter functions of macrophages as important members of the innate immunity. Macrophage FC accumulation triggers cellular apoptosis (232), which in turn affects the fate of atherosclerotic plaques, leading to necrotic core formation and reduction in efferocytosis efficiency (18). In thioglycolate-elicited DKO and ApoE-/- macrophages, we observed comparable apoptotic and necrotic cells after *ex vivo* loading with VLDL and acLDL. In accordance to our findings, CB2R activation (231) and increased 2-AG concentrations (233) do not affect apoptosis rates. However, changes in MCP-1 concentrations (and possibly other cytokines as well) could lead to increased macrophage survival within atherosclerotic plaques *in vivo.* Beside reduced foam cell formation, macrophage phenotype and functions remained unaltered between DKO and ApoE-/- cells, as evidenced by comparable M1/M2 polarization markers and integrin expression and *in vivo* phagocytic activity.

Formation of fibrous a cap represents the key event in atherosclerosis pathogenesis and lesion stability. Vulnerable plaques are characterized by decreasing amounts of fibrous cap collagen, increase in neutral lipid accumulation and foam cell formation, and build-up of the necrotic core. A thick fibrous cap protects the necrotic core from rupture into the luminal part of the artery and thus prevents cardiovascular events. A thinning fibrous cap decreases lesion stability, rendering atherosclerotic plaques susceptible to rupture and thrombus formation (12). Moreover, reducing collagen to necrotic core ratio as well as increasing necrotic core to smooth muscle cell ratio are the indicators of decreased plaque stability (234). It is therefore important to point out that the necrotic core area, which contributes to inflammation, proteolytic plaque breakdown, and physical stress on the fibrous cap (12), was reduced in plaques of DKO mice, rendering reduced inflammatory properties of the lesion. The amount of intraplaque collagen content as a stabilizing component in the plaque structure is defined by the net effects of collagen production (caused by infiltrating smooth muscle cells) and degradation (mediated by neutrophil-produced matrix metalloproteinases). Importantly, we found markedly increased collagen content in lesions of DKO mice, with a relative collagen amount comprising as much as 40% of the total lesion area and indicating profound lesion stabilization. On the one hand, the origin of increased plaque fibrosis is likely not due to reduced production of proteolytic enzymes. Comparable mRNA expression levels of Mmp-2 and -9 in aortae and unchanged gelatinolytic capacities of (pro-)MMP-2 and -9 from DKO neutrophil-conditioned media argue against the direct involvement of MMP production in the observed effect. Increased mRNA expression of aortic Timp-1 and Timp-2 may, however, be a contributing factor for hindered matrix degradation via *in vivo* inhibition of gelatinolytic enzymes. On the other hand, the increase in collagen plaque content of DKO mice is most likely attributable to the increased abundance of smooth muscle cells, indicating either increased migration of smooth muscle cells from the media into subintimal areas or their prolonged survival within the lesions. Interestingly, the observed plaque phenotype in DKO mice phenocopies the plaque size and structure in an atherosclerotic model of dietary switch where Ldlr-/- mice were challenged with WTD for 5 or 9 weeks and subsequently switched back to chow diet for 3 weeks. This resulted in complete plasma lipid normalization, the main goal of contemporary CVD therapy (234).

Recent work by Steffens *et al.* reported an opposite plaque phenotype in ApoE-/-FAAH-/- mice (135). FAAH efficiently degrades anandamide, the second molecule identified as a potential EC. The authors found reduced plaque size with comparable amount of macrophages and decreased plaque stability in ApoE-/-FAAH-/- compared to ApoE-/- mice. Surprisingly, the expected elevation in plasma anandamide concentrations in ApoE-/-FAAH-/- mice was accompanied by a reduction in 2-AG concentrations (135). It is therefore tempting to speculate that the plaque phenotype in ApoE-/-FAAH-/- mice may be an indirect consequence of decreased 2-AG levels and blunted 2-AG-mediated CB2R signaling, instead of increased anandamide concentrations *per se*, since (i) tissue 2-AG levels are by far more abundant than anandamide with nanomolar *versus* picomolar concentrations (reviewed in (90)), (ii) 2-AG is a full whereas anandamide is a partial CBR agonist, which is also capable to attenuate the effectiveness of 2-AG to activate CB2R (147), and (iii) structure-activity relationship studies suggested that 2-AG rather than anandamide is the true natural ligand for both CB1R and CB2R (128, 129). Thus, it may be plausible that MGL and 2-AG are the key regulators of EC homeostasis in atherosclerosis, whereas FAAH and anandamide may act indirectly, mediating its effects on atherogenesis via modulations in 2-AG signaling.

In summary, our data provide evidence that genetic ablation of MGL causes alterations in both lipolysis and EC signaling, thereby indirectly affecting lipid and carbohydrate metabolism, inflammatory response, and concomitantly atherogenesis. Elevated 2-AG concentrations cause CB1R desensitization and blunting of CB1R-mediated signaling. However, CB2R-mediated signaling remains fully functional, arguing against CB2R desensitization, at least in macrophages. Therefore, lack of MGL modulates EC signaling in CB2R-expressing cells and influences (patho)physiological processes, which concomitantly affect the pathogenesis of atherosclerosis. Additionally, defective lipolysis as a consequence of MGL deficiency mildly resembles beneficial effects of reduced circulating FFAs on overall lipid and carbohydrate metabolism as observed in ATGL-/- mice (50). Naïve translation of the lessons learned from MGL-/- mice or *in vitro* pharmacological inhibition of MGL might give an explanation for lacking records of enzyme mutation(s) in humans. Results from our and other groups demonstrate that MGL-/- mice show a trend towards resistance to diet-induced obesity (84, 87), ameliorated fasting lipemia (86) and delayed postprandial TG excursions (87), improved liver steatosis, glucose metabolism (86), and a beneficial atherosclerotic phenotype. Observed leukocytosis after WTD in DKO mice was not associated with increased systemic inflammation, possibly causing a more alert immune system and thereby being capable to respond to pathogens and/or recognition of tumor cells more promptly. Atherosclerotic lesions, though enlarged (and considering the fact that arterial occlusion carries much lower mortality rates), show a phenotype resistant to rupture which is the leading cause of CVD mortality. Moreover, recent findings demonstrate that MGL overactivity may be implicated in promoting the aggressive properties of malignant cancer cells, in which the enzyme regulates a FA network that feeds into a number of pro-tumorigenic signaling pathways (235). Taken all into account, it is probable that human MGL mutations remain undiagnosed merely because possible patients encounter less health issues compared to the general population. Due to multiple beneficial effects of MGL deficiency on hepatic steatosis, glucose metabolism and plaque stabilization, chronic MGL inhibition might be a novel therapeutic intervention in treatment of the metabolic syndrome and atherosclerosis, leading to the formation of less vulnerable atherosclerotic plaques and reduced CVD mortality.

PART II: Relative contribution of hematopoietic DGAT1 deficiency on atherosclerosis development in LDLR-/- mice

1. Introduction

1.1. Triglyceride biosynthesis

FAs have multiple functions in mammalian organism. They are utilized as fuel in the process of β-oxidation, particularly because they are the most energy dense substrates. They also serve as building blocks for phospholipid and ceramide biogenesis. Additionally, poly-unsaturated FAs are precursors for eicosanoid synthesis and act as ligands for PPARs. However, excessive FA concentrations have detrimental effect on cell survival, causing membrane and mitochondrial dysfunction, ER stress, inflammation, and cellular apoptosis. Therefore, these molecules have to be sequestered in their inert pools of neutral lipids, mostly TGs, which are intracellularly localized in special organelles called lipid droplets (LDs). Thus, the process of TG synthesis is of essential importance for cellular homeostasis and survival (45).

Two major pathways for TG biosynthesis are known (Figure 1): the glycerol phosphate or Kennedy pathway, which is ubiquitously present in most cells and tissues, and the monoacylglycerol (MG) pathway, dominant in small intestine and to a lesser extent in adipocytes which is responsible for the assimilation of dietary derived MGs and FAs taken up from the luminal side of the enterocytes. Both pathways utilize “activated” form of FAs, acyl-CoAs. In the Kennedy pathway, acyl-CoAs are transferred to glycerol-3-phospahte to form lysophosphatidic acid mediated by glycerol-3-phosphate acyltransferases (GPATs). 1-acylglycerol-3-phosphate acyltransferases (AGPAT) catalyze esterification of newly generated lysophosphatidic acid with another acyl-CoA molecule to form phosphatidic acid. Finally, lipins, enzymes which carry phosphatidate phosphatase activity, cleave phosphatidic acid to form DGs, which are at the crossroad of the two pathways of TG biosynthesis (236). Alternatively, MGs absorbed in the small intestine are esterified with FAs to DGs mediated by acyl-CoA:monoacylglycerol acyltransferases

(MGATs. The last, rate-limiting step in TG biosynthesis is committed by acyl-CoA:diacylglycerol acyltransferase (DGAT) enzymes (237).

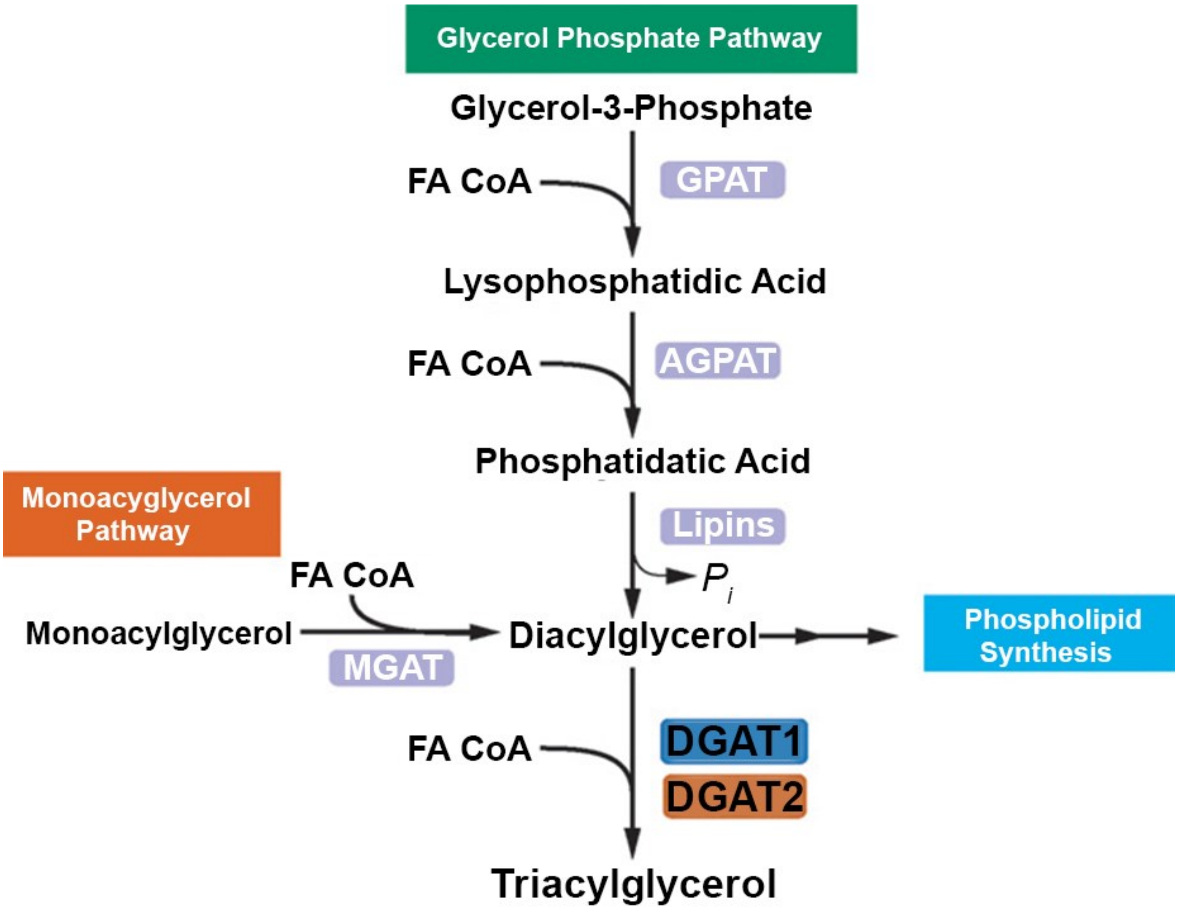

Figure 1. TG biosynthesis. The Kennedy or glycerol phosphate pathway is the dominant pathway of TG biosynthesis. GPAT catalyzes transfer of acyl-CoA to glycerol-3-phosphate to form lysophosphatidic acid. AGPAT transferres another acyl-CoA to lysophosphatidic acid, generating phosphatidic acid. Lipins remove a phosphate group from lysophosphatidic acid to form DGs. In intestine and adipocytes, MGs are esterified with acyl-CoA via MGATs to form DGs. Finally, the process of TG biosynthesis is ended by the action of DGAT1 or DGAT2 enzyme. Adapted from Yen CL *et al*, Thematic review series: glycerolipids. DGAT enzymes and triacylglycerol biosynthesis (238).

1.2. DGAT1 enzyme functions

There are two genetically unrelated DGAT enzymes which share the same function, DGAT1 and DGAT2. DGAT1 belongs to a large family of membrane-bound O-acyltransferases (MBOAT). In humans, its gene is located on chromosome 8 and encodes a 500 amino acids long protein with the size of 50 kDa (238). Enzyme topology presumably largely determines its function. It is considered that ER-bound enzymes are involved in the production of cellular proteins in the cytosolic (overt) compartment or of proteins destined to secretion if they are located on the luminal (latent) compartment of the ER. DGAT1 is bound to the ER and is expressed in both luminal and cytosolic compartments, thereby affecting TG synthesis for either secretion or intracellular storage (Figure 2) (239). In humans, DGAT1 is ubiquitously expressed with highest mRNA levels found in small intestine, WAT, mammary glands, skeletal muscle, heart, spleen, pancreas, and liver. In mice, hepatic DGAT1 expression is much lower compared to humans (240).

Besides acyl-CoA:diacylglycerol acyltransferase activity, DGAT1 also carries out acyl-CoA:monoacylglycerol acyltransferase, acyl-CoA:retinol acyltransferase as well as mono- and diester wax synthesizing activities (241). Preferred substrates for DGAT1 activity are monounsaturated *versus* saturated FAs and its enzymatic activity is more pronounced in mid-to-high substrate range of ≥ 100 µM oleoyl-CoA (242). DGAT1 expression and activity regulations are not yet quite well understood. PPARγ activation (243), glucose stimulation (in the presence or absence of insulin) and fasting (244), increase, whereas obesity decreases DGAT1 mRNA levels (245). Moreover, enzymatic activity of DGATs is promoted with glucose and FA (246), but negatively regulated by potentiated cellular proliferation (247), glucagon (248), and adrenaline (249).

DGAT1-/- mice were generated in 2000. The animals are viable and fertile, but female mice have impaired mammary gland development and cannot produce milk (250, 251). The animals also suffer from sebaceous gland and fur atrophy as well as alopecia. (252). DGAT1-/- mice are resistant to diet-induced obesity, have reduced adiposity and ectopic lipid deposition, increased energy expenditure, physical activity, thermogenesis (251, 253), and extended life span (254). Interestingly, reduced TG levels in tissues are not followed by compensatory increase in the DGAT1 substrates DGs and FAs, which have detrimental effects on cell survival and metabolic functions. It is likely that DGs' fate is directed towards phospholipid synthesis, whereas potentiated β-oxidation may reduce cellular FA levels. DGAT1-/- mice also have increased leptin and insulin sensitivity and improved glucose tolerance (253). The effect, however, may be an indirect consequence of tissue-specific deletion of the enzyme in WAT, since WT mice transplanted with WAT from DGAT1-/- donors have improved glucose tolerance, increased adiponectin, and reduced leptin levels (255). On the contrary, *ex vivo* experimentation on isolated murine soleus muscle imply involvement of DGAT1 enzyme overexpression in athlete's paradox, where increased skeletal muscle TG deposition increases insulin sensitivity and glucose uptake. DGAT1 deficiency causes the opposite effect in the isolated muscles, with the compensatory increase in intracellular DG and ceramide levels (256). Similarly, cardiac-specific DGAT1 overexpression increased TG levels in cardiomyocytes and reduced ceramide, DG, and FA levels with a concomitant improvement of lipotoxic parameters (257). Overexpression of DGAT1 in macrophages, however, has similar effects on carbohydrate metabolism like whole body deficiency. The reason for this may be sequestering of lipotoxic FAs and/or DGs in DGAT1 overexpressing macrophages, which in turn causes reduced inflammation of WAT and diminished production of pro-inflammatory cytokines. Additionally, there is an implication that macrophages from DGAT1-/- mice may have an M1 phenotype (258).

The role of DGAT1 in liver function remains unclear. Although DGAT1-/- mice have reduced hepatic lipid accumulation (251) and are resistant to diet- and fasting-induced hepatic steatosis (259), Dgat1-ASO treatment in rats failed to decrease liver lipid concentrations (260) and even increased hepatic TG levels in *db/db* mice (261). On the contrary, transgenic mice overexpressing DGAT1 in liver show modest increase in hepatic TG levels (262), similar to adenoviral-mediated DGAT1 overexpression with (263) or without (264) concomitant increase in VLDL secretion. Some evidence indicate that DGAT1 in liver probably regulates assimilation of exogenous FAs, mediating their re-esterification, rather than generating TGs from *de novo* synthetized FAs (259, 265).

DGAT1 activity is extremely important in the process of dietary TG assimilation and chylomicron assembly. Although DGAT1 deficiency in mice does not cause TG malabsorption (251), dynamics of TG assimilation is largely altered. DGAT1-/- animals can efficiently produce chylomicrons, however, plasma TG excursions upon intragastric fat bolus are diminished in these mice (266). Moreover, fat load (acute and chronic) cause transitory accumulation of lipids in enterocytes of DGAT1-/- mice, indicating that dietary fat challenge may empty into the circulation at a decreased but more sustained rate (266, 267). An important contributor to the alterations in intestinal chylomicron production rates in DGAT1-/- mice is reduced gastric emptying due to elevated circulating levels of glucagon-like peptide 1 (GLP-1). The increase in GLP-1, however, is not the sole cause of this effect, since the rates of chylomicron production remain unaltered in intestinal DGAT1-/- mice with or without treatment with GLP-1 receptor antagonist. However, GLP-1 receptor antagonism causes loss of dietary fat via stool in intestinal DGAT1-/- mice (267). Thus, it is likely that reduced gastric emptying coupled with DGAT1 deficiency represents a metabolic adaptation in order to preserve normal dietary uptake of TGs and to prevent the loss of energy from dietary sources. Interestingly, pharmacological inhibition of DGAT1 in rats leads to increased FA oxidation and reduced energy intake (268). To emphasize the importance of DGAT1 in normal function of the small intestine, it is worth to mention that resistance to diet-induced obesity, reduced hepatic steatosis, and delayed chylomicron secretion are abolished after re-expression of DGAT1 in the intestine of DGAT1-/- mice (269). Surprisingly, not only TG, buy also intestinal cholesterol metabolism is altered in DGAT1-/- mice on an ApoE-/- background (270). These mice have reduced dietary cholesterol and TG uptake, reduced plasma lipid concentrations, and show reduced atherosclerotic propensity with decreased amount of macrophages within the lesions. Macrophages from ApoE-/-DGAT1-/- mice have reduced capacity to generate foam cells due to reduced LDL uptake and increased cholesterol efflux, and they show reduced migratory capacity towards MCP-1 (270). Therefore, the causal factor for the ameliorated atherosclerosis in these mice remained unclear. Whether altered intestinal and hepatic lipid metabolism, which consequently affect entire lipid homeostasis, or whether macrophage resistance to foam cell formation, differential handling of lipoproteins and reduced inflammatory propensity of these cells, remains to be determined.

To date, only two cases of DGAT1 mutation in humans have been reported, one with fatal outcome (271). The main clinical manifestation of the disease is congenital diarrheal disorder followed by growth retardation, hyperlipidemia, protein loss, and malnutrition. The lessons from mice, thus, cannot be directly translated to humans. The main reason for this is the differential DGAT enzyme expression pattern between the two species. Mice express both DGAT1 and 2 in the small intestine, whereas humans lack intestinal DGAT2 expression. The deficiency of DGAT1 in murine intestine is not lethal due to the capability of DGAT2 to compensate for the TG synthesizing activity, which is not the case in human intestine. It is highly likely that in humans with DGAT1 mutations, rapid build-up of TG precursors, which cause lipotoxic effects, severely damages enterocytes, leading to protein-losing enteropathy, inability to assimilate dietary lipids, and malnutrition (271). Therefore, pharmacological intervention tackling DGAT1 would have a severe adverse effect in humans, which opens a question of DGAT1 as a potential target in the treatment of metabolic disorders.

1.3. DGAT2 enzyme functions

DGAT2 belongs to a larger gene family of DAGAT enzymes, which in addition consists of acyl-CoA:monoacylglycerol acyltransferase (MGAT) -1, -2, and -3, and wax monoester synthases. In humans, the DGAT2 gene is located on chromosome 11 and encodes 388 amino acids long protein with the size of 44 kDa (238). Enzyme topology studies revealed that DGAT2 is bound to the ER with the expression on cytosolic compartment, thus presumably affecting TG synthesis destined to cytosolic storage in LDs (Figure 2) (272). Indeed, it has been shown that the enzyme is responsible for incorporation of *de novo* synthesized FAs in the cellular TG pool (265). DGAT2 is ubiquitously expressed in humans with highest mRNA levels found in liver, WAT, mammary gland, testis, leukocytes, and heart. In mice, the expression pattern is similar, though it is likely not as highly expressed in immune cells as in humans (242).

In contrast to DGAT1, which shows a range of catalytic activities towards different substrates, DGAT2 catalyzes only TG synthesis. Preferred substrates for DGAT2 activity are medium-chain *versus* long-chain FAs and DGs containing short-to-medium chain FAs (273). It seems that the enzyme is more active compared to DGAT1 in low-to-mid substrate range of ≤ 100 μM oleoyl-CoA. Additionally, Mg^{2+} concentrations strongly regulate DGAT activities with concentrations ≤ 20 mM suppressing DGAT1 and ≥ 50 mM suppressing DGAT2 activity (242). Little is known about DGAT2 expression and activity regulation. Insulin stimulation (in the presence or absence of glucose), genetic and diet-induced obesity, and re-feeding increase, whereas leptin and fasting reduce DGAT2 mRNA expression (244, 245).

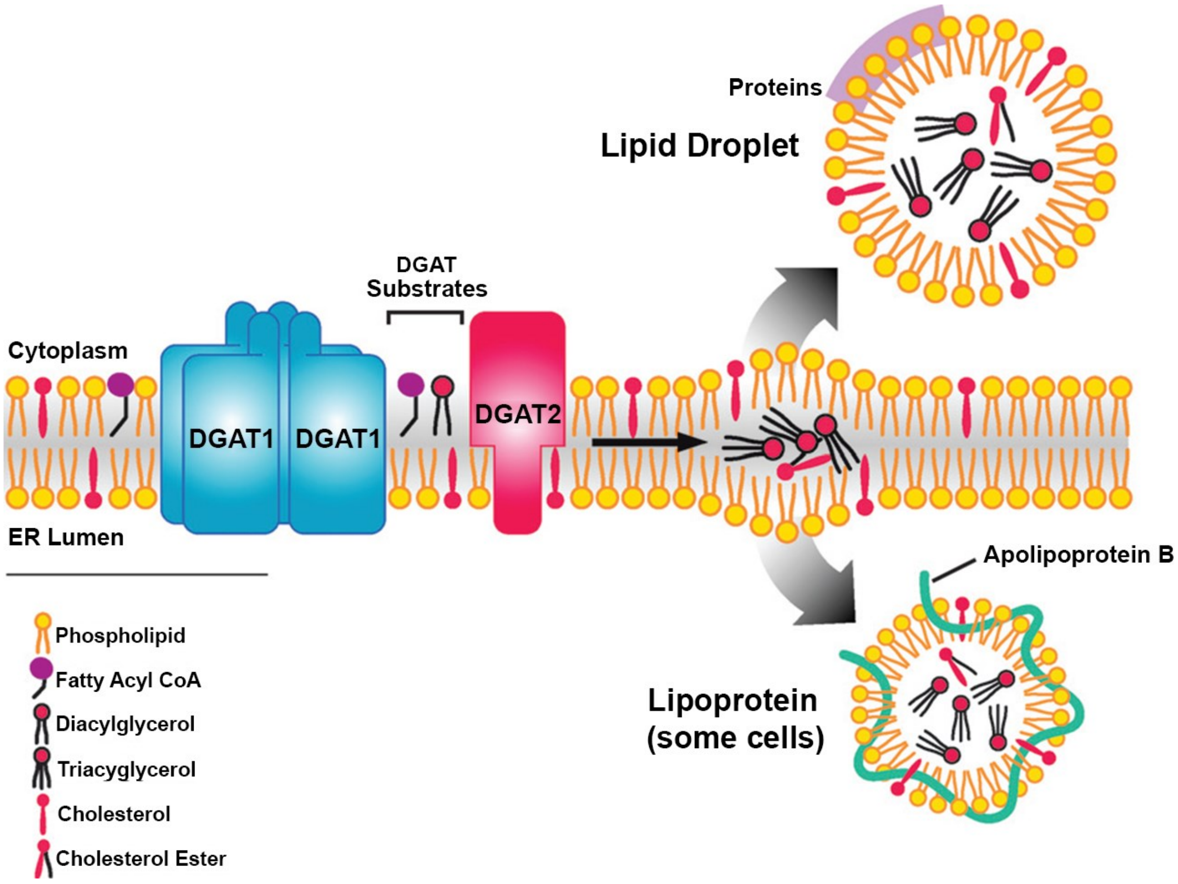

Figure 2. Membrane topology of DGAT enzymes. Membrane topology of ER-associated enzymes largely determines the fate of catalytic products. Enzymes found in the cytosolic (overt) compartment produce molecules directed towards cytosol, whereas enzymes in the luminal (latent) compartment produce molecules destined to secretion. DGAT1 is bound to the ER and expressed in both luminal and cytosolic compartments, thereby affecting TG synthesis for either secretion in form of ApoB-containing lipoproteins or intracellular storage in LDs. DGAT2 is predominantly oriented towards cytosol, therefore largely contributing to the production of TGs stored in cytosolic LDs. Adapted from Yen CL *et al*, Thematic review series: glycerolipids. DGAT enzymes and triacylglycerol biosynthesis (238).

In vivo effects of DGAT2 deficiency remain largely unexplored due to its incompatibility with life. DGAT2-/- pups die within several hours after birth due to severe reduction in TGs as energy substrates as well as defective skin barrier function and rapid dehydration (274). Thus, available *in vivo* data are so far limited to either ASO-treated animals or transgenic mice overexpressing DGAT2 in a specific tissue. DGAT2 ASO treatment in mice leads to reduced hepatic steatosis, downregulated expression of lipogenic genes, reduced VLDL production, but did not affect glucose metabolism (275). Another study in mice phenocopied reduced hepatic steatosis but also found improved glycemia, and surprisingly, increased liver damage and fibrosis (276). In rats, ASO treatment caused reduced TG and DG concentrations in liver, increased FA oxidation, and increased hepatic and peripheral insulin sensitivity (260). On the other hand, transgenic overexpression of DGAT2 in murine liver concomitantly led to hepatic steatosis, which was dissociated from insulin resistance and associated with increased hepatic FA oxidation (262). Additionally, adenovirus-mediated DGAT2 overexpression in mice caused a similar increase in liver lipid concentrations, but failed to affect VLDL production (263, 264). *In vitro* experimentation focused on pharmacological DGAT1 and DGAT2 functions in primary murine hepatocytes led to somewhat conflicting data compared to *in vivo* studies. DGAT enzymes are compensating for each other to produce TGs, however, TGs produced by DGAT1 are preferentially used for FA oxidation, while TGs produces by DGAT2 are destined for VLDL production (277).

1.4. Murine models in atherosclerosis research – of mice and men

Application of murine models in atherosclerosis research has been indespensible, particularly due to possibilities of genetic manipulation in mice and targeted research of specific proteins. Additional advantages of mice as an *in vivo* model in atherosclerosis research include short generation time and sizable litters, atherosclerotic plaque development in reasonable time frame, relatively low costs of maintenance and space requirements, and reduced resources required for studies involving pharmacological interventions due to small animal size (278).

However, there are certain drawbacks, particularly in translation of the data obtained from the murine models to human biology. WT mice are resistant to atherosclerosis development due to different lipoprotein profile in mice compared to humans. Plasma cholesterol levels in WT animals on chow diet do not rise above 80 mg/dl and the majority is carried within atheroprotective HDL particles (279). Moreover, mice do not have cholesterol ester transfer protein (CETP) which is involved in HDL clearance (280). Lesion development is different in mice than in humans as well. Most murine models do not develop unstable plaques and rupture is rarely evidenced in these animals and also seldom develop complicated, fibrotic lesions, which are common in human atherosclerosis. Due to their hemodynamic characteristics, mice hardly develop any plaque in coronary arteries, but the predicted sites for plaque formation in these animals is aortic sinus, aortic arch, and the descending part of thoracic aorta.

For all these reasons, genetically altered mice, which are more susceptible to atherogenesis as compared to their WT counterparts, are an extremely valuable tool to investigate such a complex disease in *in vivo* conditions. To date, two most widely used strains are apolipoprotein E (ApoE) and LDL receptor (LDLR) knockout mice.

1.4.1. ApoE -/- mice

Since their generation in 1992, ApoE-/- mice have been the most extensively used murine model in atherosclerosis research. The animals are resistant to diet-induced obesity (281) and have increased hepatic steatosis (282), but improved glucose tolerance compared to WT mice (283). The major effect of ApoE deficiency is manifested in lipid homeostasis with cholesterol rich ApoB48-containing remnant particles accumulating in the circulation, thereby potentiating atherogenic properties (278). Moreover, HDL plasma concentrations are low in these mice, causing detrimental ApoB-containing lipoprotein to HDL ratio. Due to implication of ApoE in the process of VLDL secretion, these mice also have impaired VLDL secretion rates compared to WT animals (224, 282). ApoE-/- mice develop atherosclerotic lesions already on chow diet due to high plasma cholesterol levels reaching as much as 500 mg/dl (284). In this model, fatty streaks appear at 10 weeks of age, proceeding to intermediate lesions at 5 months and fibrous plaques developing at the age of 10 months (285). Dietary intervention rich in cholesterol and TGs leads to high elevation in plasma cholesterol levels and increases the pace of atherosclerosis progression (286). Moreover, VCAM-1 is constitutively expressed at the endothelial surface in ApoE-/- mice (287). Atherosclerotic lesion structure in these mice resembles plaques found in humans. The greatest disadvantage of this model is the fact that ApoE is also expressed in BM-derived cells, predominantly in the monocyte/macrophage compartment. Therefore, adoptive transfer of the BM from a donor mouse expressing ApoE to a recipient ApoE-/- mouse would lead to amelioration of atherosclerosis due to ApoE secretion by hematopoietic cells (288).

1.4.2. LDLR-/- mice

LDLR-/- is another widely used mouse model in atherosclerosis research. In contrast to ApoE-/- mice, to date there was no report of any difference between LDLR-/- and

WT mice in the onset of diet-induced obesity. Changes in the lipid profile are associated with elevated cholesterol levels mostly in the LDL and intermediate-density lipoprotein (IDL) fractions (289) and therefore the lipoprotein profile resembles the human phenotype of patients suffering from familial hypercholesterolemia. The effect of LDLR deficiency on the lipid profile is not of as striking as compared to ApoE-/- animals. Cholesterol levels are doubled on chow diet compared to WT mice (289), but still below threshold of 300 mg/dl required for atherosclerosis development (290). Thus, these mice do not develop atherosclerotic lesions spontaneously and dietary intervention is required for the initiation of atherogenesis. On the other hand, this is a valuable model for investigation of the effects of lipid lowering treatments on atherosclerosis development, due to its ability to return to basal cholesterol levels upon return from high fat to chow diet. The structure of atherosclerotic lesions in LDLR-/- mice has not been as extensively studied as in ApoE-/- mice, but there are some implications that LDLR-/- mice represent a milder atherosclerotic model, generating less complex plaques with higher abundance of foam cells and reduced fibrotic capacity compared to ApoE-/- mice (291). However, the most important feature of this model is the independence of LDLR expression in the BM on atherosclerosis development. Therefore, LDLR-/- mice represent the most extensively used model for BM transplantation studies, used to determine the relative contribution of a specific gene in the hematopoietic compartment on atherosclerosis development (292).

2. Aim

DGAT1 enzyme serves a key function in the process of TG biosynthesis. Previous research showed improved atherogenesis in whole body DGAT1-/- mice on ApoE-/- background. The effect may have at least two different causes. Firstly, macrophage function was dramatically improved in this model, along with systemic inflammation. Secondly, these mice exhibited ameliorated lipid metabolism and reduced hyperlipidemia in ApoE-/-DGAT1-/- mice. To differentiate between these two separated pathways and investigate the effect of DGAT1 deficiency in macrophages in the context of atherogenesis, we utilized adoptive transfer of the BM from either WT or DGAT1-/- mice to LDLR-/- recipients and investigated atherosclerosis development.

3. Materials and methods

3.1. Animals and diets

For BM transplantations, we used WT C57BL/6J and DGAT1-/- as donor and LDLR-/- as recipient mice. LDLR-/- (purchased from Jackson Laboratory, Bar Harbor, ME) and DGAT1-/- mice were on a C57BL/6J background (backcrossed for more than 10 generations). Animals were maintained in a clean environment with unlimited access to a standard 5053 PicoLab chow diet (Purina, St. Louis, MO) and water in a regular light-dark cycle (12h light, 12h dark). 16-week-old mice were fed a Western-type diet (WTD) containing 21.2% fat, and 0.2% cholesterol by weight (TD 88137; Harlan-Teklad, IN). Female mice were fed WTD for 13 weeks, whereas male mice received WTD for 19 weeks. All procedures were approved by the UCSF Animal Research Committee and followed NIH guidelines.

3.2. BM transplantation

BM cells harvested from 8-week-old WT or DGAT1-/- donor mice were resuspended in PBS with 0.1% FA-free BSA, and 10^6 donor cells were injected into age- and sex-matched recipient LDLR-/- mice via tail vein. Recipient mice were irradiated in two 5-Gy doses spaced 3 h apart 1 day before tail vein injection of isolated BM cells. After BM injections, recipient mice were placed in their home cages with antibiotic water for 4 weeks, after which genotyping from blood was performed to confirm BM transplantation efficiency. The mice then recovered under usual care until they were 16 weeks old, at which time they were placed on WTD for additional 13 or 19 weeks.

3.3. Genotyping from blood

One hundred µl of blood was lysed with ACK buffer and centrifuged at 850 rpm at 4°C for 5 min. Thereafter, pellet was washed with PBS and centrifuged again at 1200 rpm at 4°C for 5 min. DNA was isolated by digesting cells in 100 µl Direct PCR-lysis cocktail for cells (Viagen Biotech Inc., Los Angeles, CA) and 10 µl proteinase K (10 mg/ml) (Viagen Biotech Inc., Los Angeles, CA) for 2 h at 56°C and vigorous shaking. To deactivate proteinase K, samples were incubated at 85°C for 45 min.

For LDLR genotyping, the following primers were used:

LDLR-forward: 5’-ACCCCAAGACGTGCTCCCAGGATGA-3´;

LDLR-reverse-: 5’-CGCAGTGCTCCTCATCTGACTTGT-3´;

LDLR-ko-forward: 5’-AGGTGAGATGACAGGAGA-3´.

The reaction mix contained ~100-200 ng of template DNA, 1 mM $MgCl_2$, 0.2 µM of each dNTP, 0.5 µM of each primer, 0.75 U GoTaq Hot Start Polymerase (Promega, Madison, WI).

For DGAT1 genotyping, the following primers were used:

DGAT1-forward: 5’-TGTGCACGGGGATATTCCAG-3´;

DGAT1-reverse-: 5’-ACTCCTGTCTCAATGCTGTGG-3´;

DGAT1-neo: 5’-TACCGGTGGATGTGGAATGTGTGCG-3´.

The reaction mix contained ~100-200 ng of template DNA, 0.2 µM of each dNTP, 0.5 µM of each primer, 1 U HotStarTaq DNA Polymerase (Qiagen, Venlo, The Netherlands).

The following cycle conditions were used for the amplification of the specific DNA products:

	LDLR		DGAT1	
Initial denaturation	95°C – 3 min		95°C – 5 min	
Denaturation	95°C – 20 sec	10 x	94°C – 30 sec	35 x
Annealing	64°C – 30 sec		60°C – 30 sec	
Elongation	72°C – 50 sec		72°C – 45 sec	
Denaturation	95°C – 20 sec	30 x		
Annealing	58°C – 30 sec			
Elongation	72°C – 50 sec			
Final elongation	72°C – 5 min		72°C – 5 min	
Cool down	4°C – ∞		4°C – ∞	

3.4. Cell culture

MPMs were collected by injecting 3 ml of 3 % thioglycolate intraperitoneally. Seventy two h post-injection, MPMs were collected by flushing the peritoneum with 9 ml EDTA-PBS (1 mM EDTA in PBS). Cells were centrifuged at 850 rpm at 4°C for 5 min and then resuspended in the appropriate amount of Dulbecco’s Modified Eagle Medium (DMEM) containing high-glucose (25 mM), 4 mM glutamine, 1 mM pyruvate, 10 % lipoprotein-deficient serum (LPDS), and 1 % penicillin/1 % streptomycin (1 % P/S) and cultured for at least 2 h. Thereafter, the cells were washed 3 times with pre-warmed PBS and cultured for additional 24 h either in the absence or presence of VLDL or acLDL (100 µg protein/ml medium), or LPS (100 ng/ml).

3.5. RNA isolation from MPM

Primary macrophages were isolated and cultured for at least 24 h. Total RNA from tissues was isolated using TriFast reagent according to the manufacturer's protocol (Peqlab, Erlangen, Germany). Briefly, cells were homogenized in 500 µl/well of TriFast reagent. 200 µl of chloroform was added per ml TriFast reagent, vortexed, and centrifuged at 8,500 rpm at 4°C for 15 min. Supernatant was transferred to a fresh tube, mixed with 2µl of glycogen solution (20 mg/ml, Santa Cruz, Heidelberg, Germany) and 500 µl of isopropanol, vortexed, and centrifuged at 8,500 rpm at 4°C for 10 min. Thereafter, supernatant was discarded, pellets were washed with 75 % ethanol and centrifuged again at 8,500 rpm at 4°C for 5 min. Supernatant was discarded, pellets were air-dried, and resuspended in 30-50 µl DEPC water.

RNA concentrations were measured at 260 nm using NanoDrop (Thermo scientific, Wilmington, USA). Two µl RNA were used for concentration determination using the following equation:

$$c_{(ngRNA/\mu l)} = \lambda\ 260nm \times 40$$

3.6. cDNA preparation

cDNA was prepared from RNA by reverse transcription. One or two µg RNA in 10 µl (adjusted with nuclease-free ddH_2O) were reversely transcribed by using High-Capacity DNA Reverse Transcription kit (Applied Biosystems, Foster City, CA).

High-Capacity cDNA Reverse Transcription master mix composition

Component	Volume (µl) / reaction
10 x RT Buffer	2
25 x dNTP Mix (100 mM)	0.8
10 x RT Random Primers	2
Multiscribe Reverse Transcriptase	1

RNase Inhibitor	0.7
Nuclease-free H_2O	3.5
1 or 2 µg RNA/10 µl ddH$_2$O	10
Total volume per reaction	**20**

Reverse transcription thermal cycling conditions were as follows:

	Step 1	Step 2	Step 3	Step 4
Temperature	25°C	37°C	85°C	4°C
Time	10 min	120 min	5 s	∞

3.7. Real time PCR

cDNA was diluted 1:50 in nuclease-free ddH$_2$O. Three µl of diluted cDNA, 1 µl of forward and reverse primer (stock solution, 100 µM, diluted 1:10 with nuclease-free ddH$_2$O), and 5 µl QuantiFastTM SYBR® Green were pipetted into a LightCycler 480 white Multiwell plate. The plate was centrifuged for 1 min at 800 rpm and loaded on a Roche LightCycler 480 instrument.

Real-time PCR program conditions:

	Temperature	Time	Cycles
Denaturation	95°C	5 min	1
Amplification	95°C	10 s	40
	60°C	30 s	
Melting Curve	95°C	10 s	1
	60°C	20 s	1
	95°C	continuous	
Cool Down	40°C	20 s	1

Hypoxanthine-guanine phosphoribosyl transferase (Hprt) was used as house-keeping genes for relative gene expressions. Relative expression of gene of interest to housekeeping gene was calculated using the $2^{-\Delta\Delta CT}$ method. Primers which were used are listed in the table 1.

Table 1. Primer sequences:

Gene	Forward primer (5’-3’)	Reverse primer (5’-3’)
Hprt	TCAGTCAACGGGGGACATAAA	GGGGCTGTACTGCTTAACCAG
Ccl5	GCTGCTTTGCCTACCTCTCC	TCGAGTGACAAACACGACTGC
Itgax	CTGGATAGCCTTTCTTCTGCTG	GCACACTGTGTCCGAACTCA
Tnfα	CCACCACGCTCTTCTGTCTAC	AGGGTCTGGGCCATAGAACT
iNos	GTTCTCAGCCCAACAATACAAGA	GTGGACGGGTCGATGTCAC
Gro-1	CTGGGATTCACCTCAAGAACATC	CAGGGTCAAGGCAAGCCTC
Arg1	TGGCTTGCGAGACGTAGAC	GCTCAGGTGAATCGGCCTTTT
Mrc-1	GCTGAATCCCAGAAATTCCGC	ATCACAGGCATACAGGGTGAC

3.8. Body composition analysis

Body composition in mice was analyzed under isoflurane anesthesia by dual energy X-ray absorptiometry (DEXA) with a PIXImus2 scanner (GE Healthcare Lunar, WI).

3.9. Complete blood cell count

One undred μl of blood were taken from *v. facialis* in tri-K-EDTA coated tubes (Sarstedt AG, Nuembrecht, Germany) and complete blood cell count was performed with Hemavet 850 (Drew Scientific Group, Waterbury, CT).

3.10. Plasma lipid parameters

Three hundred μl of blood were drawn into EDTA coated tubes from *v. facialis* after 10-h of fasting. Plasma was separated (7000 rpm at 4°C for 7 min) and TG concentrations were measured with Infinity Triglycerides kit (Thermo Scientific, Middletown, VA). Total cholesterol (TC) and free cholesterol (FC) concentrations were determined using Cholesterol E and Free Cholesterol E kits (WAKO Chemicals, Richmond, VA), whereas cholesterol ester (CE) concentrations were calculated as the difference between TC and FC.

3.11. Preparation of histological sections for atheroassays

Mice were anesthetized by intraperitoneal injections of sodium-pentobarbital (50 mg/kg body weight). Mice were perfused with PBS/EDTA for 10-15 min. The abdominal part of the aorta was removed and frozen in liquid N_2 for RNA isolation. Animals were then perfused with 10% neutral buffered formalin (methanol-free) for 15 min. Adventitial adipose tissue was carefully removed from the upper part of the aorta, which was then excised from the thoracic cavity, cut open in a Y-formation, and stored in formalin until staining. Upper two thirds of the heart were fixed with formalin for 24 h. Fixed tissues were stored in 30% sucrose. One day before sectioning, hearts were transferred into Tissue-Tek® O.C.T.™ section medium (Sakura Finetek, Leiden, The Netherlands). Serial sections (7-8 µm) of aortic root were cut at -20°C using a cryostat-microtome.

3.12. ORO staining of aortae

Aortae were washed with PBS for 1 min and then placed in 70% isopropanol for 5 min. Thereafter, aortae were stained with ORO working solution for 20 min and then dipped into 70% isopropanol to remove excessive ORO. Aortas were pinned on black dissecting wax and images were taken using a stereo zoom microscope.

3.13. ORO staining of aortic valve sections

Aortic root sections were fixed in 10% methanol-free neutral buffered formalin for 10 min. Sections were incubated in 70% isopropanol for 5 min, ORO for 15 min, dipped into 70% isopropanol, counterstained with hematoxylin for 5 min, and washed in 0.1% $NaHCO_3$. Sections were air dried and mounted with glycerol gelatin mounting medium (Sigma-Aldrich, St. Louis, MO). Mean lesion area (mm^2) was calculated from 14-15 consecutive ORO-stained sections per mouse. After imaging, plaque areas were quantitated with ImageJ software.

3.14. Monoclonal antibody to macrophages-2 (MoMa-2) immunostaining

Sections were fixed for 15 min in formalin and washed three times with PBS. Sections were blocked for 30 min with peroxidase blocking solution (Signet Covance, Princeton, NJ) and washed two times with PBS. Thereafter, Ultra V block (Lab Vision, Fremont, CA) was added for 7 min. Sections were incubated with primary monoclonal antibody against macrophages-2 (MoMa-2, 1:600; Acris, Hiddenhausen, Germany) for 1 h at RT and then at 4°C overnight. Sections were washed two times with PBS, incubated for 3 h at RT with polyclonal rabbit anti-rat secondary antibody coupled to horseradish peroxidase (1:100, Dako Denmark A/S, Glostrup, Denmark), and washed once with PBS. AEC substrate (Vector Laboratories, Burlingame, CA) was added to the sections for 20 min and then sections were washed 3 times with dH_2O. The sections were stained with hematoxylin for 5 min, washed in 0.1% $NaHCO_3$, and fixed with glycerol gelatin mounting medium (Sigma-Aldrich, St. Louis, MO). After imaging, quantification of MoMa-2-stained sections was performed with ImageJ software.

3.15. Masson’s Trichrome staining

Slides were incubated in Bouin’s solution (Sigma-Aldrich, St. Louis, MO) overnight at RT, washed under running tap water until the sections were clear from yellow color, and then washed with dH_2O for 1 min. Working Accustain® Wigert’s Iron Hematoxylin solution (Sigma-Aldrich, St. Louis, MO) was freshly prepared and sections were stained for 3 min, washed with running tap water for 5 min and dH_2O for 1 min. The sections were then stained with Masson’s Trichrome stain (Sigma-Aldrich, St. Louis, MO) according to manufacturer’s instructions, washed with dH_2O, and dehydrated (90, 95, and 100% of ethanol and xylene). The sections were fixed with Cytoseal™-60 mounting medium (Thermo Scientific, Kalamazoo, MI). After imaging, collagen in Trichrome-stained sections (blue) were quantitated with ImageJ software.

3.16. Statistics

Statistical analyses were performed using GraphPad Prism 5.04 software (GraphPad Software Inc, San Diego, CA). The significance was determined by Student’s unpaired *t*-test and Welch t-test (in case of unequal variances) for two group comparison and ANOVA followed by Bonferroni correction for multiple group comparison. Data are presented as mean values ± SD. Significance levels were set at $p < 0.05$ (*), $p \leq 0.01$ (**) and $p \leq 0.001$ (***).

4. Results

4.1. Comparable body weight gain between WT:LDLR-/- and DGAT1-/-:LDLR-/- mice

In order to investigate effects of hematopoietic cell DGAT1 deficiency on atherosclerosis development, we transplanted LDLR-/- recipient mice with BM from age and sex matching WT and DGAT1-/- donor animals. Four weeks post-transplantation, we performed PCR from genomic DNA isolated from WBCs of transplanted mice to confirm successful irradiation and adoptive transplant by the presence of LDLR in all samples (Figure 3A), and presence or absence of DGAT1 gene (Figure 3B), depending on the donor genotype.

A

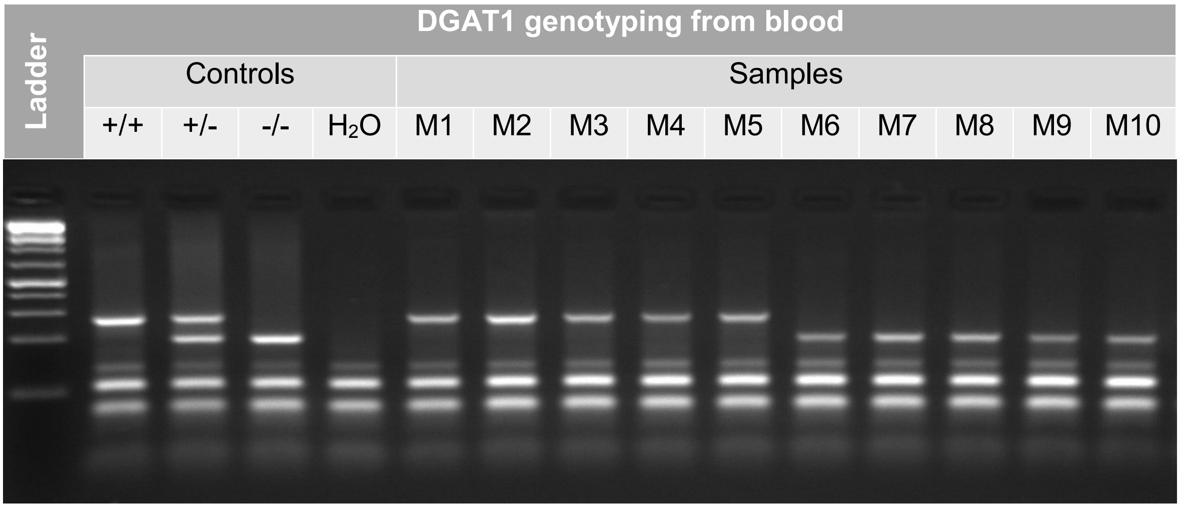

B

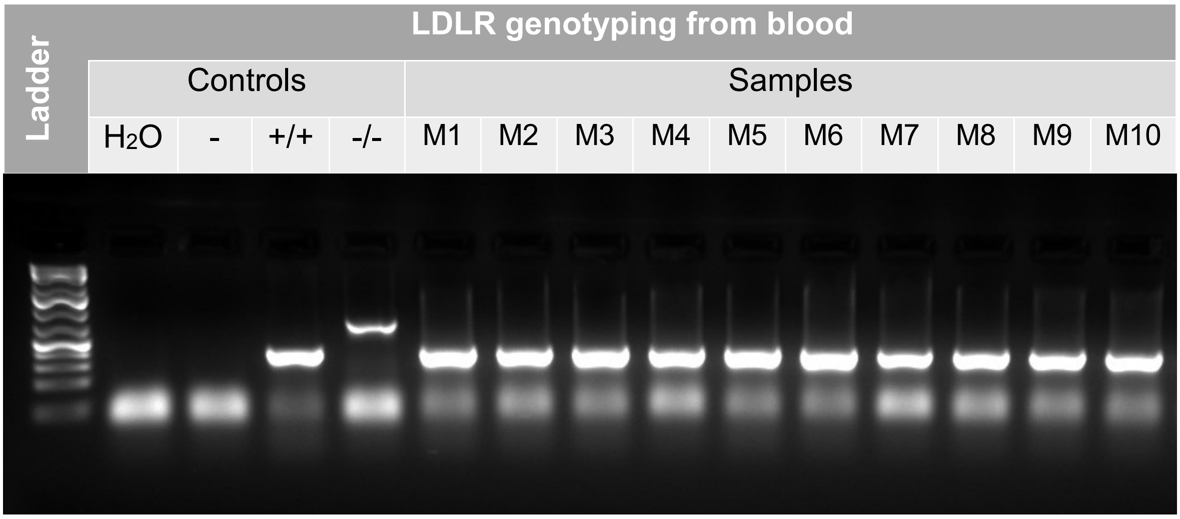

Figure 3. Successful BM transplantation from WT and DGAT1-/- donors to LDLR-/- recipient mice. Four weeks post-transplantation, peripheral blood samples were used for (A) DGAT1 and (B) LDLR genotyping. PCR products were analyzed by agarose gel electrophoresis. Images show representative gels for mice transplanted with WT or DGAT1-/- BM, respectively (n=5).

To investigate stage- and sex-dependent changes in atherosclerosis development, we fed female mice for 13 and male mice for 19 weeks with WTD and performed atheroassays. Male cohort was fed longer to female mice due to increased rate of atherosclerosis progression in female mice (293). We found similar body weight gain in DGAT1-/-:LDLR-/- mice compared to the controls in either 13 weeks (Figure 4A), and 19 weeks WTD fed group (Figure 4B).

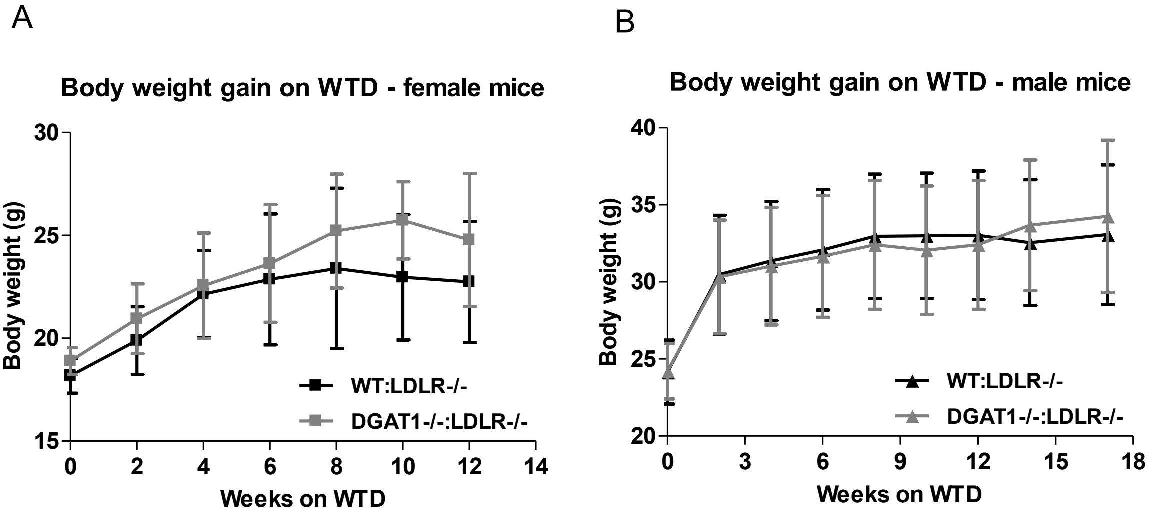

Figure 4. Comparable body weight gains between WT:LDLR-/- and DGAT1-/-:LDLR-/- mice. Weight gain of (C) female mice after 13 weeks (n=6-8), and (D) male mice after 18 weeks of WTD feeding (n=11-12). Data are presented as mean ± SD.

4.2. Comparable body composition between WT:LDLR-/- and DGAT1-/-:LDLR-/- mice

Possible effects of BM transplantation on body composition were determined using dual energy X-ray absorptiometry. We found comparable amounts of total body fat (Figure 5A), relative fat content (Figure 5B), and lean mass (Figure 5C) between DGAT1-/-:LDLR-/- and WT:LDLR-/- mice. Additionally, gonadal fat (Figure 5D) and liver size (Figure 5E) were at comparable levels in both genotypes.

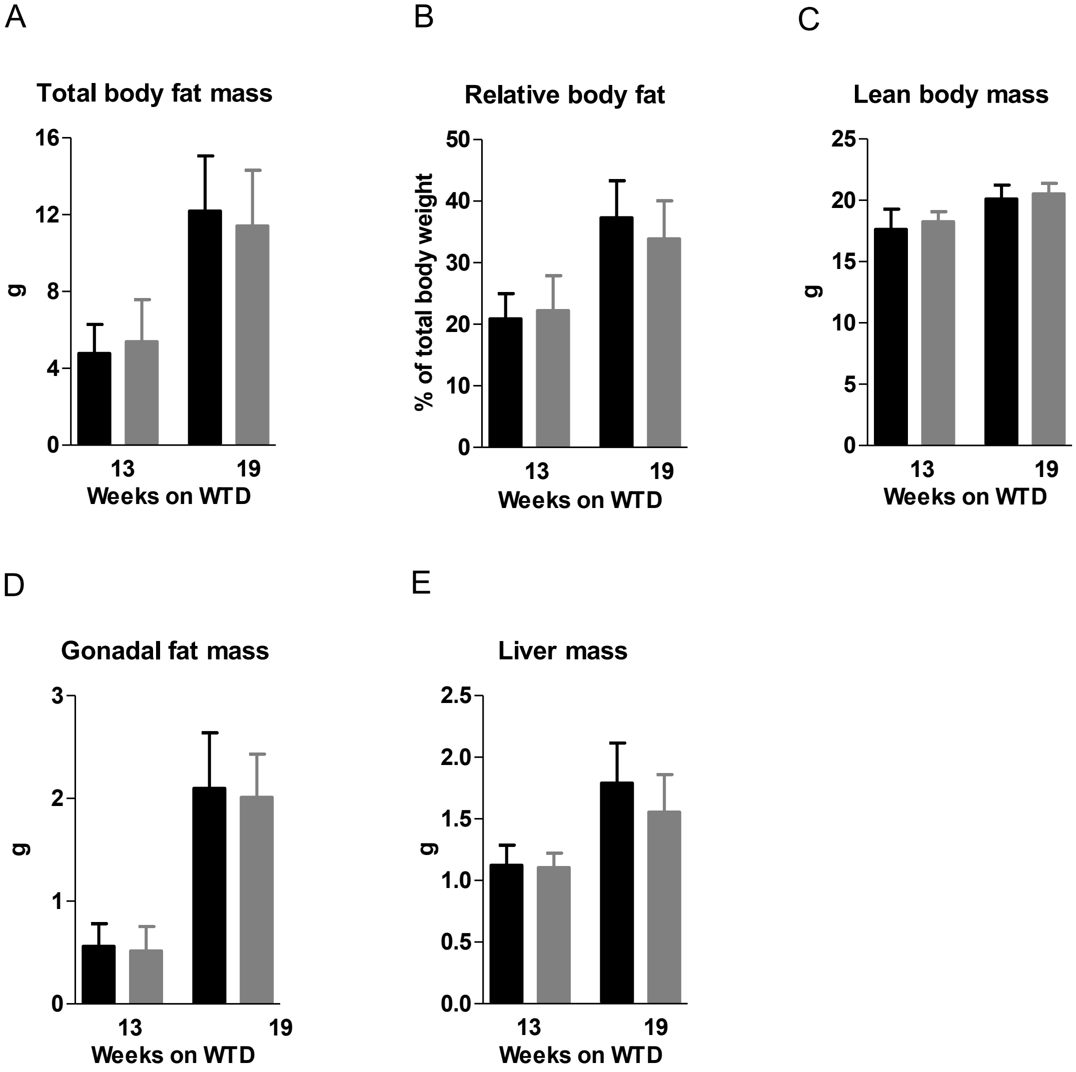

Figure 5. Unchanged adiposity in DGAT1-/-:LDLR-/- mice. (A) Total body fat mass, (B) relative adiposity, (C) lean body mass, (D) gonadal fat mass, and (E) liver mass in WT:LDLR-/- (black bar) and DGAT1-/-:LDLR-/- mice (gray bar) after 13 (n=6-8) and 19 weeks (n=9-10) of WTD feeding. Data are presented as mean + SD.

4.3. Cholesterol homeostasis is differentially regulated in male and female DGAT1-/-:LDLR-/- mice upon WTD feeding

WTD feeding failed to affect plasma TG concentrations in WT:LDLR-/- and DGAT1-/-LDLR-/- mice in any gender or time point of feeding (Table 2). However, total cholesterol concentrations were reduced in female mice after 13 weeks of WTD feeding. In contrast, male DGAT1-/-:LDLR-/- mice after 19 weeks of diet had increased cholesterol concentrations compared to WT:LDLR-/- animals.

Table 2. WT:LDLR-/- and DGAT1-/-:LDLR-/- mice were fasted for 10 h and plasma parameters after feeding Western-type diet for 13 or 19 weeks were determined. Data are mean (n=5-10) ± SD. *, p< 0.05; **, p ≤ 0.01; ***, p ≤ 0.001.

	13 weeks		19 weeks	
Genotype	**WT:LDLR-/-**	**DGAT1-/-:LDLR-/-**	**WT:LDLR-/-**	**DGAT1-/-:LDLR-/-**
TG (mg/dl)	328 ± 124	261 ± 81.6	308 ± 68.4	312 ± 80.1
TC (mg/dl)	1098 ± 202	894 ± 88.4*	1438 ± 209	1692 ± 109**
FC (mg/dl)	269 ± 40.0	248 ± 34.0	491 ± 97.9	522 ± 95.9
CE (mg/dl)	859 ± 170	646 ± 65.6*	947 ± 126	1170 ± 32.3***

4.4. White blood cell counts are unaltered between WT:LDLR-/- and DGAT1-/-:LDLR-/- animals

BM transplantations severely affect hematopoietic system of recipient animals. Therefore, one week prior to atheroassays, we estimated the number of WBCs as well as specific subpopulations in the blood of WT:LDLR-/- and DGAT1-/-:LDLR-/- mice. We did not observe any differences in total WBC numbers in female DGAT1-/-:LDLR-/- mice compared to WT:LDLR-/- animals after 13 weeks of WTD feeding (Figure 6A). Additionally, the relative abundance of WBC subpopulations remained unchanged between both genotypes (Figures 6B-F). Male mice fed WTD for 19 weeks showed comparable numbers of WBCs (Figure 6A) but with a reduced relative abundance of lymphocytes (Figure 6B) and increased numbers of neutrophils (Figure 6C) in the peripheral circulation.

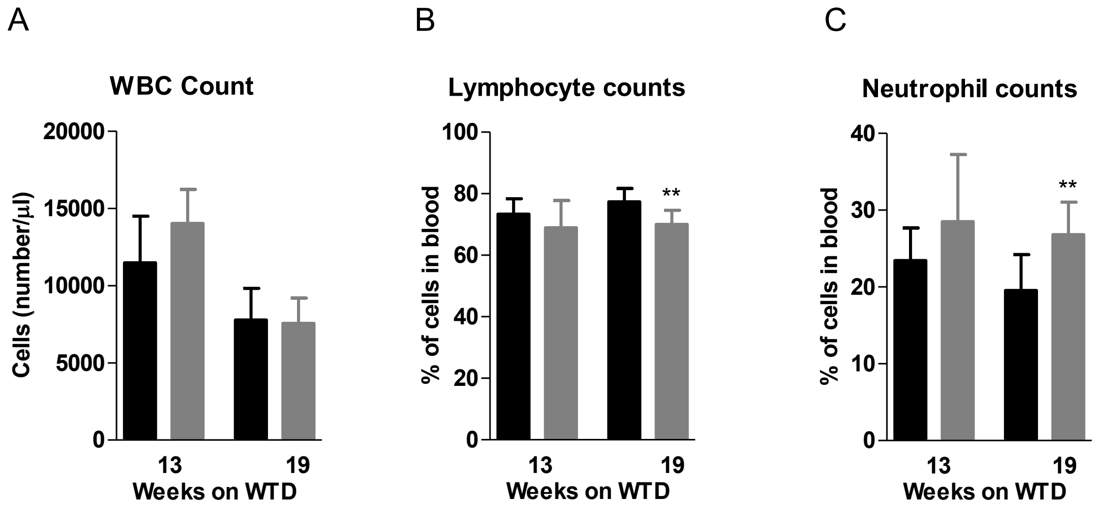

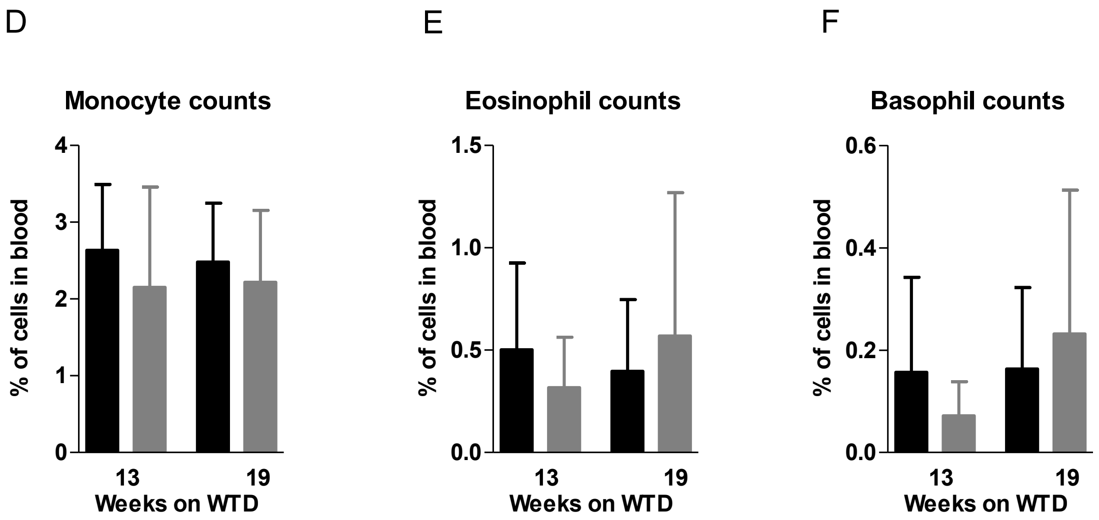

Figure 6. Reduced relative lymphocyte and increased neutrophil numbers in male DGAT1:LDLR-/- mice after 19 weeks of WTD. (A) Total leukocyte counts, (B) relative lymphocyte, (C) neutrophil, (D) monocyte, (E) eosinophil and (F) basophil abundance in WT:LDLR-/- (black bar) and DGAT1-/-:LDLR-/- (gray bar) after 13 (n=6-8, females) and 19 weeks (n=9-10, males) of WTD feeding, determined by automated hemocytometer counting. Data are presented as mean + SD. **, p ≤ 0.01

4.5. DGAT1-/-:LDLR-/- mice develop pro-inflammatory atherosclerotic plaques

Atherosclerotic plaque formation was analyzed in aortas and aortic valve sections of transplanted animals. ORO-stained aortas showed comparable plaque formation in both transplanted genotypes, irrespective of sex or feeding duration in either aortic arches (Figure 7A, B) or thoracic aortae (Figure 7A, C).

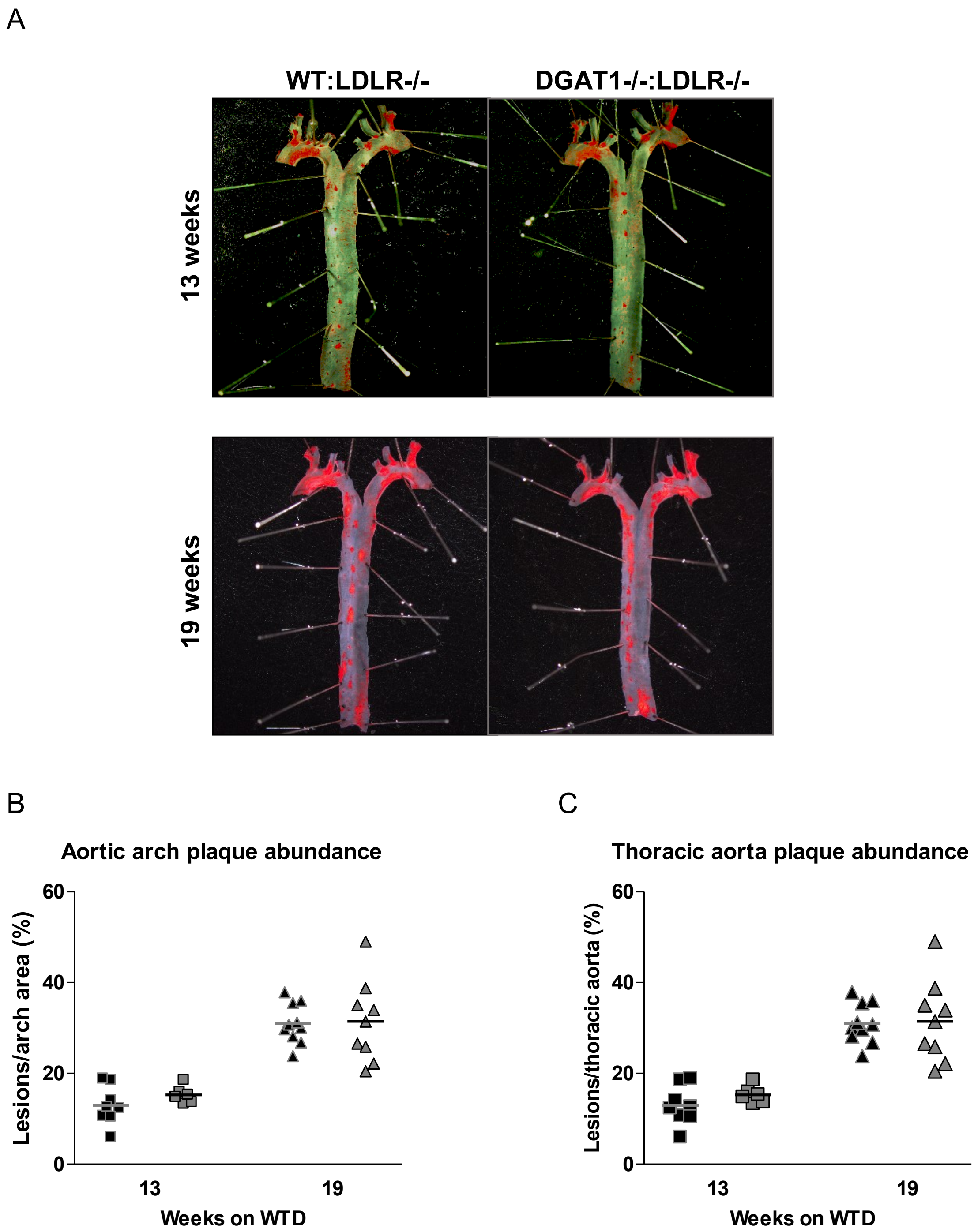

Figure 7. Comparable atherosclerotic plaque size in the *en face* aortae of WT:LDLR-/- and DGAT1-/-:LDLR-/- mice. (A) ORO-stained aortae after 13 and 19 weeks of WTD feeding. (B) Quantification of plaque size in thoracic aortae and (C) aortic arches of WT:LDLR-/- (black lined with gray) and DGAT1-/-:LDLR-/- mice (gray lined with black) after 13 (n=6-8, females) and 19 (n=9-10, males) weeks of WTD feeding. Bars represent mean values.

Aortic valve section analyses revealed comparable plaque size between DGAT1-/-:LDLR-/- and WT:LDLR-/- mice upon 13 and 19 weeks of WTD feeding (Figure 8B).

Interestingly, plaque structure was severely changed, by the development of more pro-inflammatory, rupture prone plaques characterized with the relative increase in macrophage content and a reduction in collagen amount in both male and female DGAT1-/-LDLR-/- mice compared to WT:LDLR-/- animals (Figures 8A-D). These data indicate that irrespective of sex and plasma lipid concentrations, hematopoietic DGAT1 deficiency causes aggravation of atherogenesis by generating pro-inflammatory lesion phenotype, which is detrimental to plaque stability and causes formation of rupture-prone lesions in DGAT1-/-:LDLR-/- mice.

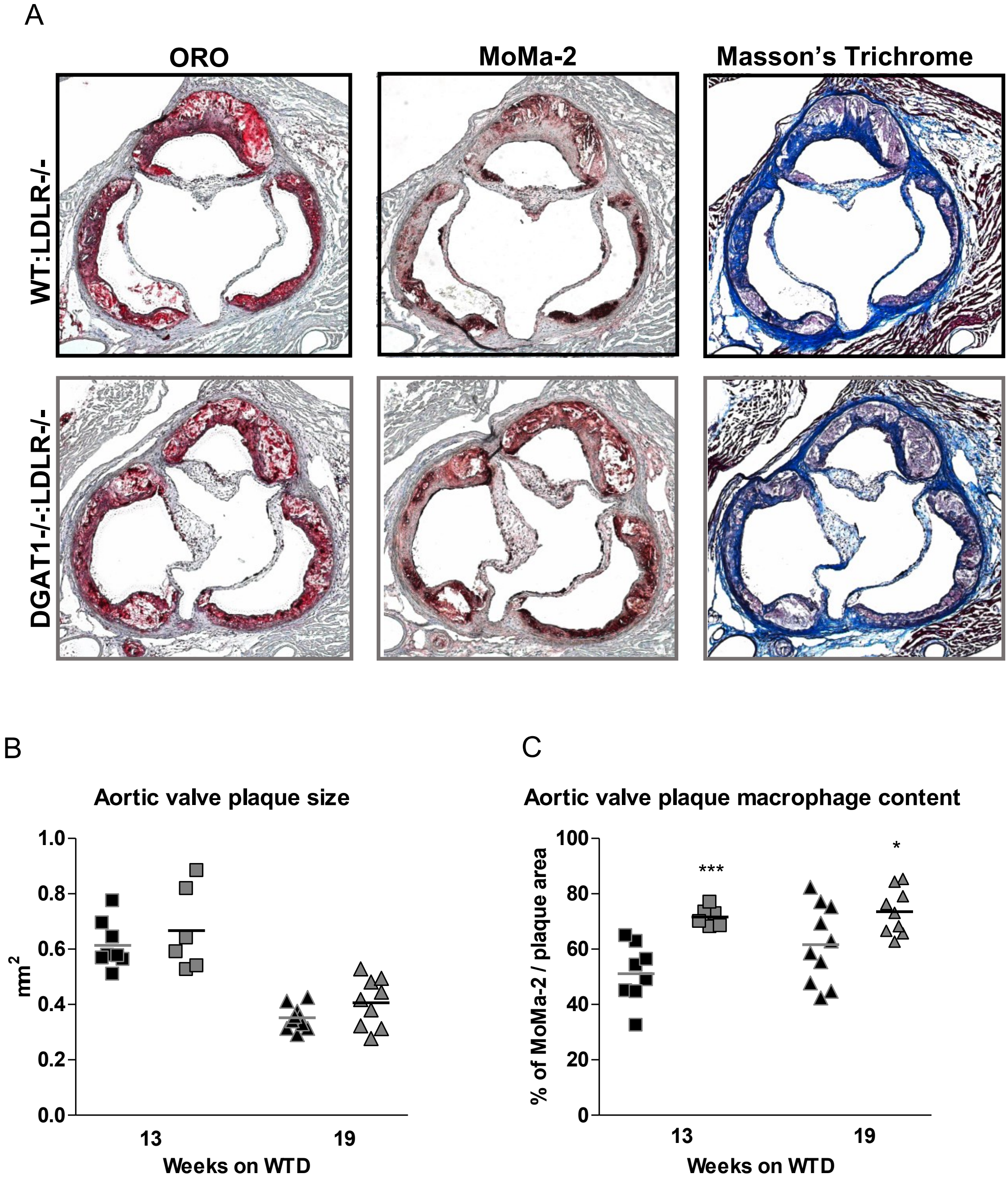

D

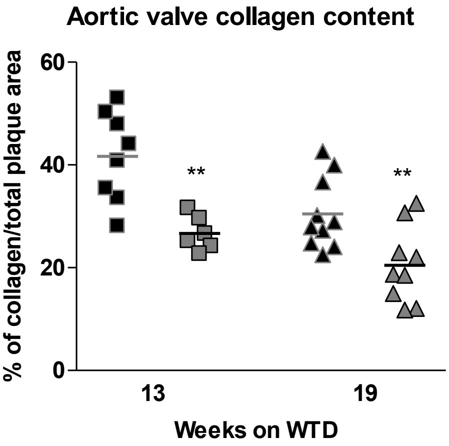

Figure 8. Destabilized plaque phenotype in DGAT1-/-:LDLR-/- mice. (A) Representative images of ORO, MoMa-2, and Masson's Trichrome for staining of lipids, macrophages, and collagen, respectively, in mice fed WTD for 13 weeks. Quantification of (B) plaque size, (C) MoMa-2 positive, and (D) collagen content per plaque area. Data represent mean values of 12 aortic valve sections for ORO and 3 aortic valve sections in the area of maximal plaque size for MoMa-2 and Trichrome stain per mouse after 13 (n=6-8, females), and 19 weeks (n=9-10, males) of WTD feeding. *, $p < 0.05$; **, $p \leq 0.01$; ***, $p \leq 0.001$.

4.6. Comparable macrophage polarization between WT and DGAT1-/- cells

To determine a possible effect of lipoproteins exposure on macrophage phenotype, we loaded peritoneal macrophages from WT and DGAT1-/- cells with VLDL and acLDL for 24 h. Macrophages exposed to LPS for 24 h were used as positive control. We found comparable mRNA expression levels of genes associated with M1 (Ccl5, Itgax, Tnfα, Mcp-1, iNos, and Gro1) (Figure 9A) and M2 (Arg1 and Mrc1) (Figure 9B) polarization in cells without any treatment, or upon exposure to either treatments, indicating that macrophages from DGAT1-/- mice differ little compared to control cells in terms of inflammatory response.

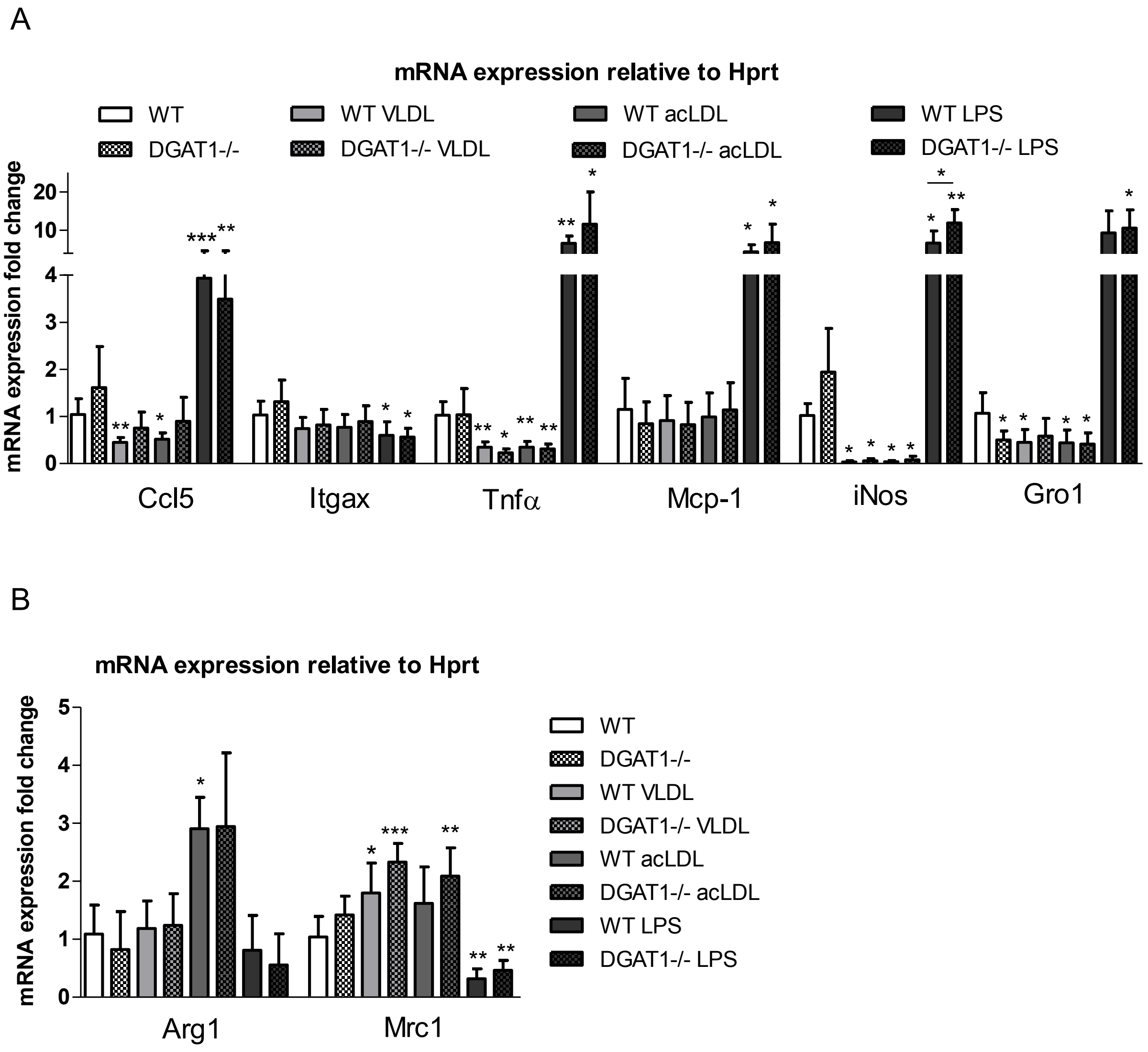

Figure 9. Total RNA was isolated from macrophages with or without treatment with 100 μg/ml VLDL, acLDL or 100 ng/ml LPS and subjested to real-time PCR analysis. mRNA expression of (A) M1 phenotype and (B) M2 phenotype target genes was analyzed in duplicate and normalized to the expression of hypoxanthine-guanine phosphoribosyl transferase as reference gene. mRNA expression and associated statistical parameters were determined using $2^{-\Delta\Delta CT}$ method. Expression of target genes in untreated WT cells was arbitrarily set to 1. Data represent mean (n=3-6) + SD. *, $p < 0.05$; **, $p \le 0.01$; ***, $p \le 0.001$.

5. Discussion

DGAT enzymes catalyze the central reaction in the process of FA detoxification and TG biosynthesis (238). Although DGAT2 deficiency is incompatible with the post-natal survival in the murine model, multiple beneficial effects of DGAT1 deficiency in mice have been well documented. They are ranging from resistance to diet-induced obesity (251), ameliorated postprandial hyperlipidemia (266, 267), improved glucose metabolism (253, 255) to increased longevity (254). However, in certain cells and tissues, DGAT1 deficiency caused detrimental effects on cellular functions, and thus cell-specific effects can largely contribute to the pathogenesis of the disease (256). Although improved atherogenesis has been described before in whole body DGAT1-/- mice on an ApoE-/- background, the cause for this effect remained largely unexplored due to two possible reasons for the reduced plaque formation in these animals. On the one hand, systemic inflammation and macrophage functions were significantly improved in this model. ApoE-/-DGAT1-/- cells were resistant to foam cell formation due to reduced lipid uptake and had potentiated efflux due to upregulated ABC transporters. Moreover, macrophages had reduced migratory propensity towards MCP-1. Aortic adhesion molecule expression as well as plasma MCP-1 levels were reduced in ApoE-/-DGAT1-/- mice, indicating reduced inflammation. On the other hand, general lipid metabolism was ameliorated and hyperlipidemia diminished in ApoE-/-DGAT1-/- mice. This effect is most probably related to reduced cholesterol uptake and absorption in the small intestine and thus reduced influence of dietary-derived cholesterol to the process of atherogenesis (270). Thus, to explore *in vivo* the consequences of DGAT1 deficiency solely in hematopoietic cells on the process of atherosclerosis development, we transplanted LDLR-/- mice with BM of WT and DGAT1-/- donor animals.

Four weeks post-transplantation, we utilized PCR from genomic DNA from WBCs to verify successful adoption of the transplanted BM. We confirmed successful irradiation and transplantation by being able to detect complete absence of LDLR-deficiency in the WBCs of transplanted mice. Furthermore, correct transplantation was verified by genotyping for WT or DGAT1 transcripts, respectively. Confirmation of successful transplantation allowed us to induce atherogenesis with dietary intervention. Thus, we fed female mice with WTD for 13 and male mice for 19 weeks.

Due to ubiquitously present of macrophages and their pleiotropic effects on tissues they are invading, we determined the effect of the transplantation on body composition of recipient mice. We failed to observe any changes in body weight gain, adiposity, or liver size in the recipient mice transplanted with BM from either genotype. Interestingly, we observed a change in circulating cholesterol levels in DGAT1:LDLR-/- mice compared to control animals. The intriguing fact is that the opposite effect is seen between male and female mice. Whether the difference arises from the sex-specific effects or whether the length of feeding affects cholesterol homeostasis remains unclear. It is important, however, to point out that alterations of DGAT1 in hematopoietic compartment solely had the capacity to alter whole body cholesterol homeostasis.

Since BM transplantation can largely affect hematopoiesis, we measured blood counts one week before we performed atheroassays. We found comparable total WBC numbers between the recipient mice. However, the relative abundance of specific WBC populations revealed elevated neutrophils, followed by reduced neutrophils in the blood of DGAT1-/-:LDLR-/- mice fed WTD for 19 weeks compared to control mice. Similar trends were observed in female mice fed WTD for 13 weeks. Due to the importance of neutrophils in the process of atherogenesis and plaque stabilization (27, 28), it is reasonable to speculate that this effect may be responsible for the observed plaque structure in DGAT1-/-:LDLR-/- animals.

We found comparable plaque size between WT:LDLR-/- and DGAT1-/-:LDR-/- mice in either sex or feeding period. However, plaque structure was significantly changed in both conditions with an increased relative abundance of macrophages and thinning fibrous caps in DGAT1-/-:LDLR-/- animals.

To get a deeper insight into macrophage function, we treated cells with VLDL, acLDL or LPS and determined mRNA expression of macrophage polarization and inflammatory markers. We failed to observe any change in the macrophage phenotype in DGAT1-/- compared to WT cells in any treatment condition, indicating that the change in the plaque phenotype in DGAT1-/-LDLR-/- compared to WT:LDLR-/- mice results in altered behavior of some other cell type rather than macrophages. Due to the change in neutrophil counts in peripheral blood, it is plausible to believe that these cells may play an important role in lesion structure alteration. Interestingly, it has been shown previously that saturated FA treatment of DGAT1-/- macrophages triggers an M1-like phenotype of cells (258). Taking into account our data, it seems that the observed effect of FAs is independent of macrophage exposure to lipids *per se*, but may be associated with FAs function as ligands for specific inflammation-associated receptors, such as toll-like receptors (TLRs).

The detrimental effect of DGAT1-deficiency in the hematopoietic compartment on plaque development is contrasting the previously seen effect in DGAT1-/-ApoE-/- mice (270). It is important to mention that ApoE deficiency affects multiple metabolic functions without limitation strictly on cholesterol homeostasis, which contrasts the LDLR-/- model mainly characterized by hypercholesterolemia. Together with the strong influence of global DGAT1 deficiency on lipid homeostasis, coupled with ApoE deficiency in macrophages of DGAT1-/-ApoE-/- mice, the macrophage function may be severely altered compared to DGAT1-/- cells. Additionally, strongly ameliorated lipid metabolism in DGAT1-/-ApoE-/- mice may postpone atherosclerosis development in these animals or slow down the pace of plaque formation, thereby improving atherogenesis compared to ApoE-/- mice. Intestinal specific DGAT1-/- mice on ApoE-/- background would be a valuable tool to further describe the role of DGAT1 in atherosclerotic development. It is plausible that due to reductions in cholesterol uptake and absorption, this model would phenocopy the atherosclerosis development observed in DGAT1-/-ApoE-/- mice. There is no information available, however, regarding collagen content and plaque stability in DGAT1-/-ApoE-/- animals.

Finally, it is important to mention that irradiation itself tremendously affects vascular pathophysiology. Irradiated ApoE-/- mice, although with unchanged plasma cholesterol and inflammatory cytokine concentrations, develop accelerated atherogenesis with pro-inflammatory, macrophage-rich lesions, prone to intraplaque hemorrhage (294, 295). Moreover, the phenotype of existing plaques was severely aggravated upon ionizing irradiation by increasing M1 macrophage polarization, intraplaque apoptosis, and reducing efferocytosis (296). It is, thus, important to take into account possible irradiation effects on DGAT1-/- BM engraftment, vascular responses of LDLR-/- recipient mice, and concomitant effects on atherosclerosis development.

6. References

1. Ross R. Mechanisms of disease - Atherosclerosis - An inflammatory disease. New England Journal of Medicine. 1999 Jan 14;340(2):115-26. PubMed PMID: ISI:000078016200007. English.

2. Allam AH, Thompson RC, Wann LS, Miyamoto MI, Nur El-Din Ael H, El-Maksoud GA, et al. Atherosclerosis in ancient Egyptian mummies: the Horus study. JACC Cardiovasc Imaging. 2011 Apr;4(4):315-27. PubMed PMID: 21466986. Epub 2011/04/07. eng.

3. Lozano R, Naghavi M, Foreman K, Lim S, Shibuya K, Aboyans V, et al. Global and regional mortality from 235 causes of death for 20 age groups in 1990 and 2010: a systematic analysis for the Global Burden of Disease Study 2010. Lancet. 2012 Dec 15;380(9859):2095-128. PubMed PMID: 23245604. Epub 2012/12/19. eng.

4. Nichols M, Townsend N, Scarborough P, Rayner M. Cardiovascular disease in Europe 2014: epidemiological update. Eur Heart J. 2014 Nov 7;35(42):2950-9. PubMed PMID: 25139896. Epub 2014/08/21. eng.

5. Ross R. The pathogenesis of atherosclerosis: a perspective for the 1990s. Nature. 1993 Apr 29;362(6423):801-9. PubMed PMID: 8479518. Epub 1993/04/29. eng.

6. Chiu JJ, Chien S. Effects of disturbed flow on vascular endothelium: pathophysiological basis and clinical perspectives. Physiol Rev. 2011 Jan;91(1):327-87. PubMed PMID: 21248169. Pubmed Central PMCID: 3844671. Epub 2011/01/21. eng.

7. Weber C, Noels H. Atherosclerosis: current pathogenesis and therapeutic options. Nat Med. 2011;17(11):1410-22. PubMed PMID: 22064431. Epub 2011/11/09. eng.

8. Glass CK, Witztum JL. Atherosclerosis. the road ahead. Cell. 2001 Feb 23;104(4):503-16. PubMed PMID: 11239408. Epub 2001/03/10. eng.

9. Ley K, Miller YI, Hedrick CC. Monocyte and macrophage dynamics during atherogenesis. Arteriosclerosis, thrombosis, and vascular biology. 2011 Jul;31(7):1506-16. PubMed PMID: 21677293. Pubmed Central PMCID: 3133596. Epub 2011/06/17. eng.

10. Huo Y, Ley K. Adhesion molecules and atherogenesis. Acta Physiol Scand. 2001 Sep;173(1):35-43. PubMed PMID: 11678724. Epub 2001/10/27. eng.

11. Lessner SM, Prado HL, Waller EK, Galis ZS. Atherosclerotic lesions grow through recruitment and proliferation of circulating monocytes in a murine model. American Journal of Pathology. 2002 Jun;160(6):2145-55. PubMed PMID: ISI:000176056900025. English.

12. Moore KJ, Tabas I. Macrophages in the pathogenesis of atherosclerosis. Cell. 2011 Apr 29;145(3):341-55. PubMed PMID: 21529710. Pubmed Central PMCID: 3111065. Epub 2011/05/03. eng.

13. Moore KJ, Freeman MW. Scavenger receptors in atherosclerosis: beyond lipid uptake. Arteriosclerosis, thrombosis, and vascular biology. 2006 Aug;26(8):1702-11. PubMed PMID: 16728653. Epub 2006/05/27. eng.

14. Kzhyshkowska J, Neyen C, Gordon S. Role of macrophage scavenger receptors in atherosclerosis. Immunobiology. 2012 May;217(5):492-502. PubMed PMID: 22437077. Epub 2012/03/23. eng.

15. Libby P. Inflammation in atherosclerosis. Nature. 2002 Dec 19-26;420(6917):868-74. PubMed PMID: 12490960.

16. Llodra J, Angeli V, Liu J, Trogan E, Fisher EA, Randolph GJ. Emigration of monocyte-derived cells from atherosclerotic lesions characterizes regressive, but not progressive, plaques. Proceedings of the National Academy of Sciences of the United States of America. 2004 Aug 10;101(32):11779-84. PubMed PMID: 15280540. Pubmed Central PMCID: 511052. Epub 2004/07/29. eng.

17. Cuchel M, Rader DJ. Macrophage reverse cholesterol transport: key to the regression of atherosclerosis? Circulation. 2006 May 30;113(21):2548-55. PubMed PMID: 16735689. Epub 2006/06/01. eng.

18. Thorp E, Tabas I. Mechanisms and consequences of efferocytosis in advanced atherosclerosis. J Leukoc Biol. 2009 Nov;86(5):1089-95. PubMed PMID: 19414539. Pubmed Central PMCID: 2774877. Epub 2009/05/06. eng.

19. Seimon T, Tabas I. Mechanisms and consequences of macrophage apoptosis in atherosclerosis. Journal of lipid research. 2009 Apr;50 Suppl:S382-7. PubMed PMID: 18953058. Pubmed Central PMCID: 2674693. Epub 2008/10/28. eng.

20. Rudijanto A. The role of vascular smooth muscle cells on the pathogenesis of atherosclerosis. Acta Med Indones. 2007 Apr-Jun;39(2):86-93. PubMed PMID: 17933075. Epub 2007/10/16. eng.

21. Faxon DP, Fuster V, Libby P, Beckman JA, Hiatt WR, Thompson RW, et al. Atherosclerotic Vascular Disease Conference: Writing Group III: pathophysiology. Circulation. 2004 Jun 1;109(21):2617-25. PubMed PMID: 15173044. Epub 2004/06/03. eng.

22. Khokha R, Murthy A, Weiss A. Metalloproteinases and their natural inhibitors in inflammation and immunity. Nat Rev Immunol. 2013 Sep;13(9):649-65. PubMed PMID: 23969736. Epub 2013/08/24. eng.

23. Libby P, Ridker PM, Hansson GK. Progress and challenges in translating the biology of atherosclerosis. Nature. 2011 May 19;473(7347):317-25. PubMed PMID: 21593864.

24. Simon SI, Kim MH. A day (or 5) in a neutrophil's life. Blood. 2010 Jul 29;116(4):511-2. PubMed PMID: 20671133.

25. Amulic B, Cazalet C, Hayes GL, Metzler KD, Zychlinsky A. Neutrophil function: from mechanisms to disease. Annu Rev Immunol. 2012;30:459-89. PubMed PMID: 22224774. Epub 2012/01/10. eng.

26. Zernecke A, Bot I, Djalali-Talab Y, Shagdarsuren E, Bidzhekov K, Meiler S, et al. Protective role of CXC receptor 4/CXC ligand 12 unveils the importance of neutrophils in atherosclerosis. Circulation research. 2008 Feb 1;102(2):209-17. PubMed PMID: 17991882. Epub 2007/11/10. eng.

27. van Leeuwen M, Gijbels MJ, Duijvestijn A, Smook M, van de Gaar MJ, Heeringa P, et al. Accumulation of myeloperoxidase-positive neutrophils in atherosclerotic lesions in LDLR-/- mice. Arteriosclerosis, thrombosis, and vascular biology. 2008 Jan;28(1):84-9. PubMed PMID: 17991873. Epub 2007/11/10. eng.

28. Rotzius P, Thams S, Soehnlein O, Kenne E, Tseng CN, Bjorkstrom NK, et al. Distinct infiltration of neutrophils in lesion shoulders in ApoE-/- mice. American Journal of Pathology.

2010 Jul;177(1):493-500. PubMed PMID: 20472897. Pubmed Central PMCID: 2893691. Epub 2010/05/18. eng.

29. Soehnlein O. Multiple roles for neutrophils in atherosclerosis. Circulation research. 2012 Mar 16;110(6):875-88. PubMed PMID: 22427325. Epub 2012/03/20. eng.

30. Swirski FK, Pittet MJ, Kircher MF, Aikawa E, Jaffer FA, Libby P, et al. Monocyte accumulation in mouse atherogenesis is progressive and proportional to extent of disease. Proceedings of the National Academy of Sciences of the United States of America. 2006 Jul 5;103(27):10340-5. PubMed PMID: 16801531. Pubmed Central PMCID: 1502459. Epub 2006/06/28. eng.

31. Galkina E, Ley K. Immune and inflammatory mechanisms of atherosclerosis (*). Annu Rev Immunol. 2009;27:165-97. PubMed PMID: 19302038. Pubmed Central PMCID: 2734407. Epub 2009/03/24. eng.

32. Swirski FK, Libby P, Aikawa E, Alcaide P, Luscinskas FW, Weissleder R, et al. Ly-6Chi monocytes dominate hypercholesterolemia-associated monocytosis and give rise to macrophages in atheromata. The Journal of clinical investigation. 2007 Jan;117(1):195-205. PubMed PMID: 17200719. Pubmed Central PMCID: 1716211. Epub 2007/01/04. eng.

33. Tacke F, Alvarez D, Kaplan TJ, Jakubzick C, Spanbroek R, Llodra J, et al. Monocyte subsets differentially employ CCR2, CCR5, and CX3CR1 to accumulate within atherosclerotic plaques. The Journal of clinical investigation. 2007 Jan;117(1):185-94. PubMed PMID: 17200718. Pubmed Central PMCID: 1716202. Epub 2007/01/04. eng.

34. Martinez FO, Gordon S. The M1 and M2 paradigm of macrophage activation: time for reassessment. F1000Prime Rep. 2014;6:13. PubMed PMID: 24669294. Pubmed Central PMCID: 3944738. Epub 2014/03/29. eng.

35. Stoger JL, Gijbels MJ, van der Velden S, Manca M, van der Loos CM, Biessen EA, et al. Distribution of macrophage polarization markers in human atherosclerosis. Atherosclerosis. 2012 Dec;225(2):461-8. PubMed PMID: 23078881. Epub 2012/10/20. eng.

36. Chinetti-Gbaguidi G, Baron M, Bouhlel MA, Vanhoutte J, Copin C, Sebti Y, et al. Human atherosclerotic plaque alternative macrophages display low cholesterol handling but high phagocytosis because of distinct activities of the PPARgamma and LXRalpha pathways. Circulation research. 2011 Apr 15;108(8):985-95. PubMed PMID: 21350215. Pubmed Central PMCID: 3319502. Epub 2011/02/26. eng.

37. Colin S, Chinetti-Gbaguidi G, Staels B. Macrophage phenotypes in atherosclerosis. Immunological reviews. 2014 Nov;262(1):153-66. PubMed PMID: 25319333.

38. Chinetti-Gbaguidi G, Colin S, Staels B. Macrophage subsets in atherosclerosis. Nature reviews Cardiology. 2015 Jan;12(1):10-7. PubMed PMID: 25367649.

39. Roselaar SE, Kakkanathu PX, Daugherty A. Lymphocyte populations in atherosclerotic lesions of apoE -/- and LDL receptor -/- mice. Decreasing density with disease progression. Arteriosclerosis, thrombosis, and vascular biology. 1996 Aug;16(8):1013-8. PubMed PMID: 8696940. Epub 1996/08/01. eng.

40. Tedgui A, Mallat Z. Cytokines in atherosclerosis: pathogenic and regulatory pathways. Physiol Rev. 2006 Apr;86(2):515-81. PubMed PMID: 16601268. Epub 2006/04/08. eng.

41. Hansson GK, Holm J, Jonasson L. Detection of activated T lymphocytes in the human atherosclerotic plaque. American Journal of Pathology. 1989 Jul;135(1):169-75. PubMed PMID: 2505620. Pubmed Central PMCID: 1880219. Epub 1989/07/01. eng.

42. Frostegard J, Ulfgren AK, Nyberg P, Hedin U, Swedenborg J, Andersson U, et al. Cytokine expression in advanced human atherosclerotic plaques: dominance of pro-inflammatory (Th1) and macrophage-stimulating cytokines. Atherosclerosis. 1999 Jul;145(1):33-43. PubMed PMID: 10428293. Epub 1999/07/31. eng.

43. Feng J, Zhang Z, Kong W, Liu B, Xu Q, Wang X. Regulatory T cells ameliorate hyperhomocysteinaemia-accelerated atherosclerosis in apoE-/- mice. Cardiovasc Res. 2009 Oct 1;84(1):155-63. PubMed PMID: 19502284. Epub 2009/06/09. eng.

44. Kita T, Yamashita T, Sasaki N, Kasahara K, Sasaki Y, Yodoi K, et al. Regression of atherosclerosis with anti-CD3 antibody via augmenting a regulatory T-cell response in mice. Cardiovasc Res. 2014 Apr 1;102(1):107-17. PubMed PMID: 24403315. Epub 2014/01/10. eng.

45. Zechner R, Zimmermann R, Eichmann TO, Kohlwein SD, Haemmerle G, Lass A, et al. FAT SIGNALS--lipases and lipolysis in lipid metabolism and signaling. Cell metabolism. 2012 Mar 7;15(3):279-91. PubMed PMID: 22405066. Pubmed Central PMCID: 3314979. Epub 2012/03/13. eng.

46. Zimmermann R, Strauss JG, Haemmerle G, Schoiswohl G, Birner-Gruenberger R, Riederer M, et al. Fat mobilization in adipose tissue is promoted by adipose triglyceride lipase. Science. 2004 Nov 19;306(5700):1383-6. PubMed PMID: 15550674. Epub 2004/11/20. eng.

47. Lass A, Zimmermann R, Haemmerle G, Riederer M, Schoiswohl G, Schweiger M, et al. Adipose triglyceride lipase-mediated lipolysis of cellular fat stores is activated by CGI-58 and defective in Chanarin-Dorfman Syndrome. Cell metabolism. 2006 May;3(5):309-19. PubMed PMID: 16679289. Epub 2006/05/09. eng.

48. Jenkins CM, Mancuso DJ, Yan W, Sims HF, Gibson B, Gross RW. Identification, cloning, expression, and purification of three novel human calcium-independent phospholipase A2 family members possessing triacylglycerol lipase and acylglycerol transacylase activities. The Journal of biological chemistry. 2004 Nov 19;279(47):48968-75. PubMed PMID: 15364929. Epub 2004/09/15. eng.

49. Yang X, Lu X, Lombes M, Rha GB, Chi YI, Guerin TM, et al. The G(0)/G(1) switch gene 2 regulates adipose lipolysis through association with adipose triglyceride lipase. Cell metabolism. 2010 Mar 3;11(3):194-205. PubMed PMID: 20197052. Pubmed Central PMCID: 3658843.

50. Haemmerle G, Lass A, Zimmermann R, Gorkiewicz G, Meyer C, Rozman J, et al. Defective lipolysis and altered energy metabolism in mice lacking adipose triglyceride lipase. Science. 2006 May 5;312(5774):734-7. PubMed PMID: 16675698. Epub 2006/05/06. eng.

51. Fischer J, Lefevre C, Morava E, Mussini JM, Laforet P, Negre-Salvayre A, et al. The gene encoding adipose triglyceride lipase (PNPLA2) is mutated in neutral lipid storage disease with myopathy. Nature genetics. 2007 Jan;39(1):28-30. PubMed PMID: 17187067. Epub 2006/12/26. eng.

52. Campagna F, Nanni L, Quagliarini F, Pennisi E, Michailidis C, Pierelli F, et al. Novel mutations in the adipose triglyceride lipase gene causing neutral lipid storage disease with myopathy. Biochemical and biophysical research communications. 2008 Dec 19;377(3):843-6. PubMed PMID: 18952067. Epub 2008/10/28. eng.

53. Lefevre C, Jobard F, Caux F, Bouadjar B, Karaduman A, Heilig R, et al. Mutations in CGI-58, the gene encoding a new protein of the esterase/lipase/thioesterase subfamily, in Chanarin-Dorfman syndrome. Am J Hum Genet. 2001 Nov;69(5):1002-12. PubMed PMID: 11590543. Pubmed Central PMCID: 1274347. Epub 2001/10/09. eng.

54. Carr PD, Ollis DL. Alpha/beta hydrolase fold: an update. Protein Pept Lett. 2009;16(10):1137-48. PubMed PMID: 19508187. Epub 2009/06/11. eng.

55. Yeaman SJ, Smith GM, Jepson CA, Wood SL, Emmison N. The multifunctional role of hormone-sensitive lipase in lipid metabolism. Adv Enzyme Regul. 1994;34:355-70. PubMed PMID: 7942281. Epub 1994/01/01. eng.

56. Fredrikson G, Stralfors P, Nilsson NO, Belfrage P. Hormone-sensitive lipase of rat adipose tissue. Purification and some properties. The Journal of biological chemistry. 1981 Jun 25;256(12):6311-20. PubMed PMID: 7240206. Epub 1981/06/25. eng.

57. Haemmerle G, Zimmermann R, Hayn M, Theussl C, Waeg G, Wagner E, et al. Hormone-sensitive lipase deficiency in mice causes diglyceride accumulation in adipose tissue, muscle, and testis. The Journal of biological chemistry. 2002 Feb 15;277(7):4806-15. PubMed PMID: 11717312. Epub 2001/11/22. eng.

58. Buchebner M, Pfeifer T, Rathke N, Chandak PG, Lass A, Schreiber R, et al. Cholesteryl ester hydrolase activity is abolished in HSL-/- macrophages but unchanged in macrophages lacking KIAA1363. Journal of lipid research. 2010 Oct;51(10):2896-908. PubMed PMID: 20625037. Pubmed Central PMCID: 2936755. Epub 2010/07/14. eng.

59. Park SY, Kim HJ, Wang S, Higashimori T, Dong J, Kim YJ, et al. Hormone-sensitive lipase knockout mice have increased hepatic insulin sensitivity and are protected from short-term diet-induced insulin resistance in skeletal muscle and heart. American journal of physiology Endocrinology and metabolism. 2005 Jul;289(1):E30-9. PubMed PMID: 15701680. Epub 2005/02/11. eng.

60. Voshol PJ, Haemmerle G, Ouwens DM, Zimmermann R, Zechner R, Teusink B, et al. Increased hepatic insulin sensitivity together with decreased hepatic triglyceride stores in hormone-sensitive lipase-deficient mice. Endocrinology. 2003 Aug;144(8):3456-62. PubMed PMID: 12865325. Epub 2003/07/17. eng.

61. Osuga J, Ishibashi S, Oka T, Yagyu H, Tozawa R, Fujimoto A, et al. Targeted disruption of hormone-sensitive lipase results in male sterility and adipocyte hypertrophy, but not in obesity. Proceedings of the National Academy of Sciences of the United States of America. 2000 Jan 18;97(2):787-92. PubMed PMID: 10639158. Pubmed Central PMCID: 15409. Epub 2000/01/19. eng.

62. Albert JS, Yerges-Armstrong LM, Horenstein RB, Pollin TI, Sreenivasan UT, Chai S, et al. Null mutation in hormone-sensitive lipase gene and risk of type 2 diabetes. N Engl J Med. 2014 Jun 12;370(24):2307-15. PubMed PMID: 24848981. Pubmed Central PMCID: 4096982. Epub 2014/05/23. eng.

63. Schweiger M, Eichmann TO, Taschler U, Zimmermann R, Zechner R, Lass A. Measurement of lipolysis. Methods in enzymology. 2014;538:171-93. PubMed PMID: 24529439. Pubmed Central PMCID: 4018506.

64. Vaughan M, Berger JE, Steinberg D. Hormone-Sensitive Lipase and Monoglyceride Lipase Activities in Adipose Tissue. The Journal of biological chemistry. 1964 Feb;239:401-9. PubMed PMID: 14169138. Epub 1964/02/01. eng.

65. Kupiecki FP. Partial purification of monoglyceride lipase from adipose tissue. Journal of lipid research. 1966 Mar;7(2):230-5. PubMed PMID: 5947037. Epub 1966/03/01. eng.

66. Karlsson M, Contreras JA, Hellman U, Tornqvist H, Holm C. cDNA cloning, tissue distribution, and identification of the catalytic triad of monoglyceride lipase. Evolutionary relationship to esterases, lysophospholipases, and haloperoxidases. The Journal of biological chemistry. 1997 Oct 24;272(43):27218-23. PubMed PMID: 9341166. Epub 1997/10/27. eng.

67. Karlsson M, Reue K, Xia YR, Lusis AJ, Langin D, Tornqvist H, et al. Exon-intron organization and chromosomal localization of the mouse monoglyceride lipase gene. Gene. 2001 Jul 11;272(1-2):11-8. PubMed PMID: 11470505. Epub 2001/07/27. eng.

68. Ollis DL, Cheah E, Cygler M, Dijkstra B, Frolow F, Franken SM, et al. The alpha/beta hydrolase fold. Protein Eng. 1992 Apr;5(3):197-211. PubMed PMID: 1409539. Epub 1992/04/01. eng.

69. Bertrand T, Auge F, Houtmann J, Rak A, Vallee F, Mikol V, et al. Structural basis for human monoglyceride lipase inhibition. J Mol Biol. 2010 Feb 26;396(3):663-73. PubMed PMID: 19962385. Epub 2009/12/08. eng.

70. Labar G, Bauvois C, Borel F, Ferrer JL, Wouters J, Lambert DM. Crystal structure of the human monoacylglycerol lipase, a key actor in endocannabinoid signaling. Chembiochem. 2010 Jan 25;11(2):218-27. PubMed PMID: 19957260. Epub 2009/12/04. eng.

71. Tornqvist H, Belfrage P. Purification and some properties of a monoacylglycerol-hydrolyzing enzyme of rat adipose tissue. The Journal of biological chemistry. 1976 Feb 10;251(3):813-9. PubMed PMID: 1249056. Epub 1976/02/10. eng.

72. Berglund L, Khoo JC, Jensen D, Steinberg D. Resolution of hormone-sensitive triglyceride/diglyceride lipase from monoglyceride lipase of chicken adipose tissue. The Journal of biological chemistry. 1980 Jun 10;255(11):5420-8. PubMed PMID: 6246107. Epub 1980/06/10. eng.

73. Karlsson M, Tornqvist H, Holm C. Expression, purification, and characterization of histidine-tagged mouse monoglyceride lipase from baculovirus-infected insect cells. Protein Expr Purif. 2000 Apr;18(3):286-92. PubMed PMID: 10733881. Epub 2000/03/29. eng.

74. Vila A, Rosengarth A, Piomelli D, Cravatt B, Marnett LJ. Hydrolysis of prostaglandin glycerol esters by the endocannabinoid-hydrolyzing enzymes, monoacylglycerol lipase and fatty acid amide hydrolase. Biochemistry. 2007 Aug 21;46(33):9578-85. PubMed PMID: 17649977. Epub 2007/07/26. eng.

75. Vandevoorde S, Saha B, Mahadevan A, Razdan RK, Pertwee RG, Martin BR, et al. Influence of the degree of unsaturation of the acyl side chain upon the interaction of analogues of 1-arachidonoylglycerol with monoacylglycerol lipase and fatty acid amide

hydrolase. Biochemical and biophysical research communications. 2005 Nov 11;337(1):104-9. PubMed PMID: 16181610. Epub 2005/09/27. eng.

76. Ghafouri N, Tiger G, Razdan RK, Mahadevan A, Pertwee RG, Martin BR, et al. Inhibition of monoacylglycerol lipase and fatty acid amide hydrolase by analogues of 2-arachidonoylglycerol. British journal of pharmacology. 2004 Nov;143(6):774-84. PubMed PMID: 15492019. Pubmed Central PMCID: 1575926. Epub 2004/10/20. eng.

77. Dinh TP, Carpenter D, Leslie FM, Freund TF, Katona I, Sensi SL, et al. Brain monoglyceride lipase participating in endocannabinoid inactivation. Proceedings of the National Academy of Sciences of the United States of America. 2002 Aug 6;99(16):10819-24. PubMed PMID: 12136125. Pubmed Central PMCID: 125056. Epub 2002/07/24. eng.

78. Dinh TP, Kathuria S, Piomelli D. RNA interference suggests a primary role for monoacylglycerol lipase in the degradation of the endocannabinoid 2-arachidonoylglycerol. Mol Pharmacol. 2004 Nov;66(5):1260-4. PubMed PMID: 15272052. Epub 2004/07/24. eng.

79. Vandevoorde S, Jonsson KO, Labar G, Persson E, Lambert DM, Fowler CJ. Lack of selectivity of URB602 for 2-oleoylglycerol compared to anandamide hydrolysis in vitro. British journal of pharmacology. 2007 Jan;150(2):186-91. PubMed PMID: 17143303. Pubmed Central PMCID: 2042901. Epub 2006/12/05. eng.

80. Sakurada T, Noma A. Subcellular localization and some properties of monoacylglycerol lipase in rat adipocytes. J Biochem. 1981 Nov;90(5):1413-9. PubMed PMID: 7338512. Epub 1981/11/01. eng.

81. Blankman JL, Simon GM, Cravatt BF. A comprehensive profile of brain enzymes that hydrolyze the endocannabinoid 2-arachidonoylglycerol. Chemistry & biology. 2007 Dec;14(12):1347-56. PubMed PMID: 18096503. Pubmed Central PMCID: 2692834. Epub 2007/12/22. eng.

82. Long JZ, Nomura DK, Cravatt BF. Characterization of monoacylglycerol lipase inhibition reveals differences in central and peripheral endocannabinoid metabolism. Chemistry & biology. 2009 Jul 31;16(7):744-53. PubMed PMID: 19635411. Pubmed Central PMCID: 2867454. Epub 2009/07/29. eng.

83. Rakhshandehroo M, Sanderson LM, Matilainen M, Stienstra R, Carlberg C, de Groot PJ, et al. Comprehensive analysis of PPARalpha-dependent regulation of hepatic lipid metabolism by expression profiling. PPAR Res. 2007;2007:26839. PubMed PMID: 18288265. Pubmed Central PMCID: 2233741. Epub 2008/02/22. eng.

84. Chanda PK, Gao Y, Mark L, Btesh J, Strassle BW, Lu P, et al. Monoacylglycerol lipase activity is a critical modulator of the tone and integrity of the endocannabinoid system. Mol Pharmacol. 2010 Dec;78(6):996-1003. PubMed PMID: 20855465. Epub 2010/09/22. eng.

85. Schlosburg JE, Blankman JL, Long JZ, Nomura DK, Pan B, Kinsey SG, et al. Chronic monoacylglycerol lipase blockade causes functional antagonism of the endocannabinoid system. Nature neuroscience. 2010 Sep;13(9):1113-9. PubMed PMID: 20729846. Pubmed Central PMCID: 2928870. Epub 2010/08/24. eng.

86. Taschler U, Radner FP, Heier C, Schreiber R, Schweiger M, Schoiswohl G, et al. Monoglyceride lipase deficiency in mice impairs lipolysis and attenuates diet-induced insulin resistance. The Journal of biological chemistry. 2011 May 20;286(20):17467-77. PubMed PMID: 21454566. Pubmed Central PMCID: 3093820. Epub 2011/04/02. eng.

87. Douglass JD, Zhou YX, Wu A, Zadrogra JA, Gajda AM, Lackey AI, et al. Global deletion of MGL in mice delays lipid absorption and alters energy homeostasis and diet-induced obesity. Journal of lipid research. 2015 Jun;56(6):1153-71. PubMed PMID: 25842377. Pubmed Central PMCID: 4442873.

88. Long JZ, Li W, Booker L, Burston JJ, Kinsey SG, Schlosburg JE, et al. Selective blockade of 2-arachidonoylglycerol hydrolysis produces cannabinoid behavioral effects. Nat Chem Biol. 2009 Jan;5(1):37-44. PubMed PMID: 19029917. Pubmed Central PMCID: 2605181. Epub 2008/11/26. eng.

89. Gaoni Y, Mechoulam R. Isolation, Structure, and Partial Synthesis of an Active Constituent of Hashish. Journal of the American Chemical Society. 1964;86(8):1646-+. PubMed PMID: ISI:A19643141B00015. English.

90. Sugiura T, Kishimoto S, Oka S, Gokoh M. Biochemistry, pharmacology and physiology of 2-arachidonoylglycerol, an endogenous cannabinoid receptor ligand. Prog Lipid Res. 2006 Sep;45(5):405-46. PubMed PMID: 16678907. Epub 2006/05/09. eng.

91. Matsuda LA, Lolait SJ, Brownstein MJ, Young AC, Bonner TI. Structure of a cannabinoid receptor and functional expression of the cloned cDNA. Nature. 1990 Aug 9;346(6284):561-4. PubMed PMID: 2165569. Epub 1990/08/09. eng.

92. Munro S, Thomas KL, Abu-Shaar M. Molecular characterization of a peripheral receptor for cannabinoids. Nature. 1993 Sep 2;365(6441):61-5. PubMed PMID: 7689702. Epub 1993/09/02. eng.

93. Devane WA, Hanus L, Breuer A, Pertwee RG, Stevenson LA, Griffin G, et al. Isolation and structure of a brain constituent that binds to the cannabinoid receptor. Science. 1992 Dec 18;258(5090):1946-9. PubMed PMID: 1470919.

94. Sugiura T, Kondo S, Sukagawa A, Nakane S, Shinoda A, Itoh K, et al. 2-Arachidonoylglycerol: a possible endogenous cannabinoid receptor ligand in brain. Biochemical and biophysical research communications. 1995 Oct 4;215(1):89-97. PubMed PMID: 7575630. Epub 1995/10/04. eng.

95. Mechoulam R, Ben-Shabat S, Hanus L, Ligumsky M, Kaminski NE, Schatz AR, et al. Identification of an endogenous 2-monoglyceride, present in canine gut, that binds to cannabinoid receptors. Biochem Pharmacol. 1995 Jun 29;50(1):83-90. PubMed PMID: 7605349. Epub 1995/06/29. eng.

96. Pertwee RG. The pharmacology of cannabinoid receptors and their ligands: an overview. International Journal of Obesity. 2006 Apr;30:S13-S8. PubMed PMID: ISI:000236709500004. English.

97. Ong WY, Mackie K. A light and electron microscopic study of the CB1 cannabinoid receptor in primate brain. Neuroscience. 1999;92(4):1177-91. PubMed PMID: 10426477. Epub 1999/07/30. eng.

98. Pagotto U, Marsicano G, Cota D, Lutz B, Pasquali R. The emerging role of the endocannabinoid system in endocrine regulation and energy balance. Endocr Rev. 2006 Feb;27(1):73-100. PubMed PMID: 16306385. Epub 2005/11/25. eng.

99. Galiegue S, Mary S, Marchand J, Dussossoy D, Carriere D, Carayon P, et al. Expression of central and peripheral cannabinoid receptors in human immune tissues and leukocyte subpopulations. Eur J Biochem. 1995 Aug 15;232(1):54-61. PubMed PMID: 7556170. Epub 1995/08/15. eng.

100. Ledent C, Valverde O, Cossu G, Petitet F, Aubert JF, Beslot F, et al. Unresponsiveness to cannabinoids and reduced addictive effects of opiates in CB1 receptor knockout mice. Science. 1999 Jan 15;283(5400):401-4. PubMed PMID: 9888857. Epub 1999/01/15. eng.

101. Zimmer A, Zimmer AM, Hohmann AG, Herkenham M, Bonner TI. Increased mortality, hypoactivity, and hypoalgesia in cannabinoid CB1 receptor knockout mice. Proceedings of the National Academy of Sciences of the United States of America. 1999 May 11;96(10):5780-5. PubMed PMID: 10318961. Pubmed Central PMCID: 21937. Epub 1999/05/13. eng.

102. Ravinet Trillou C, Delgorge C, Menet C, Arnone M, Soubrie P. CB1 cannabinoid receptor knockout in mice leads to leanness, resistance to diet-induced obesity and enhanced leptin sensitivity. Int J Obes Relat Metab Disord. 2004 Apr;28(4):640-8. PubMed PMID: 14770190. Epub 2004/02/11. eng.

103. Osei-Hyiaman D, DePetrillo M, Pacher P, Liu J, Radaeva S, Batkai S, et al. Endocannabinoid activation at hepatic CB1 receptors stimulates fatty acid synthesis and contributes to diet-induced obesity. The Journal of clinical investigation. 2005 May;115(5):1298-305. PubMed PMID: 15864349. Pubmed Central PMCID: 1087161. Epub 2005/05/03. eng.

104. Tiyerili V, Zimmer S, Jung S, Wassmann K, Naehle CP, Lutjohann D, et al. CB1 receptor inhibition leads to decreased vascular AT1 receptor expression, inhibition of oxidative stress and improved endothelial function. Basic Res Cardiol. 2010 Jul;105(4):465-77. PubMed PMID: 20361197. Epub 2010/04/03. eng.

105. Dol-Gleizes F, Paumelle R, Visentin V, Mares AM, Desitter P, Hennuyer N, et al. Rimonabant, a selective cannabinoid CB1 receptor antagonist, inhibits atherosclerosis in LDL receptor-deficient mice. Arteriosclerosis, thrombosis, and vascular biology. 2009 Jan;29(1):12-8. PubMed PMID: 18845788. Epub 2008/10/11. eng.

106. Van Gaal LF, Rissanen AM, Scheen AJ, Ziegler O, Rossner S. Effects of the cannabinoid-1 receptor blocker rimonabant on weight reduction and cardiovascular risk factors in overweight patients: 1-year experience from the RIO-Europe study. Lancet. 2005 Apr 16-22;365(9468):1389-97. PubMed PMID: 15836887. Epub 2005/04/20. eng.

107. Pi-Sunyer FX, Aronne LJ, Heshmati HM, Devin J, Rosenstock J. Effect of rimonabant, a cannabinoid-1 receptor blocker, on weight and cardiometabolic risk factors in overweight or obese patients: RIO-North America: a randomized controlled trial. JAMA. 2006 Feb 15;295(7):761-75. PubMed PMID: 16478899. Epub 2006/02/16. eng.

108. Despres JP, Golay A, Sjostrom L. Effects of rimonabant on metabolic risk factors in overweight patients with dyslipidemia. N Engl J Med. 2005 Nov 17;353(20):2121-34. PubMed PMID: 16291982. Epub 2005/11/18. eng.

109. Scheen AJ, Finer N, Hollander P, Jensen MD, Van Gaal LF. Efficacy and tolerability of rimonabant in overweight or obese patients with type 2 diabetes: a randomised controlled study. Lancet. 2006 Nov 11;368(9548):1660-72. PubMed PMID: 17098084. Epub 2006/11/14. eng.

110. Rosenstock J, Hollander P, Chevalier S, Iranmanesh A. SERENADE: the Study Evaluating Rimonabant Efficacy in Drug-naive Diabetic Patients: effects of monotherapy with rimonabant, the first selective CB1 receptor antagonist, on glycemic control, body weight, and lipid profile in drug-naive type 2 diabetes. Diabetes Care. 2008

Nov;31(11):2169-76. PubMed PMID: 18678611. Pubmed Central PMCID: 2571069. Epub 2008/08/06. eng.

111. Christensen R, Kristensen PK, Bartels EM, Bliddal H, Astrup A. Efficacy and safety of the weight-loss drug rimonabant: a meta-analysis of randomised trials. Lancet. 2007 Nov 17;370(9600):1706-13. PubMed PMID: 18022033. Epub 2007/11/21. eng.

112. Sam AH, Salem V, Ghatei MA. Rimonabant: From RIO to Ban. J Obes. 2011;2011:432607. PubMed PMID: 21773005. Pubmed Central PMCID: 3136184. Epub 2011/07/21. eng.

113. Buckley NE, McCoy KL, Mezey E, Bonner T, Zimmer A, Felder CC, et al. Immunomodulation by cannabinoids is absent in mice deficient for the cannabinoid CB(2) receptor. Eur J Pharmacol. 2000 May 19;396(2-3):141-9. PubMed PMID: 10822068. Epub 2000/05/24. eng.

114. Ziring D, Wei B, Velazquez P, Schrage M, Buckley NE, Braun J. Formation of B and T cell subsets require the cannabinoid receptor CB2. Immunogenetics. 2006 Sep;58(9):714-25. PubMed PMID: 16924491. Epub 2006/08/23. eng.

115. Ofek O, Karsak M, Leclerc N, Fogel M, Frenkel B, Wright K, et al. Peripheral cannabinoid receptor, CB2, regulates bone mass. Proceedings of the National Academy of Sciences of the United States of America. 2006 Jan 17;103(3):696-701. PubMed PMID: 16407142. Pubmed Central PMCID: 1334629. Epub 2006/01/13. eng.

116. Julien B, Grenard P, Teixeira-Clerc F, Van Nhieu JT, Li L, Karsak M, et al. Antifibrogenic role of the cannabinoid receptor CB2 in the liver. Gastroenterology. 2005 Mar;128(3):742-55. PubMed PMID: 15765409. Epub 2005/03/15. eng.

117. Batkai S, Osei-Hyiaman D, Pan H, El-Assal O, Rajesh M, Mukhopadhyay P, et al. Cannabinoid-2 receptor mediates protection against hepatic ischemia/reperfusion injury. Faseb Journal. 2007 Jun;21(8):1788-800. PubMed PMID: 17327359. Pubmed Central PMCID: 2228252. Epub 2007/03/01. eng.

118. Steffens S, Veillard NR, Arnaud C, Pelli G, Burger F, Staub C, et al. Low dose oral cannabinoid therapy reduces progression of atherosclerosis in mice. Nature. 2005 Apr 7;434(7034):782-6. PubMed PMID: 15815632. Epub 2005/04/09. eng.

119. Zhao Y, Liu Y, Zhang W, Xue J, Wu YZ, Xu W, et al. WIN55212-2 ameliorates atherosclerosis associated with suppression of pro-inflammatory responses in ApoE-knockout mice. Eur J Pharmacol. 2010 Dec 15;649(1-3):285-92. PubMed PMID: 20868672. Epub 2010/09/28. eng.

120. Hoyer FF, Steinmetz M, Zimmer S, Becker A, Lutjohann D, Buchalla R, et al. Atheroprotection via cannabinoid receptor-2 is mediated by circulating and vascular cells in vivo. J Mol Cell Cardiol. 2011 Dec;51(6):1007-14. PubMed PMID: 21884703. Epub 2011/09/03. eng.

121. Willecke F, Zeschky K, Ortiz Rodriguez A, Colberg C, Auwarter V, Kneisel S, et al. Cannabinoid receptor 2 signaling does not modulate atherogenesis in mice. PloS one. 2011;6(4):e19405. PubMed PMID: 21541300. Pubmed Central PMCID: 3082575. Epub 2011/05/05. eng.

122. Delsing DJ, Leijten FP, Arts K, van Eenennaam H, Garritsen A, Gijbels MJ, et al. Cannabinoid Receptor 2 Deficiency in Haematopoietic cells Aggravates Early

Atherosclerosis in LDL Receptor Deficient Mice. Open Cardiovasc Med J. 2011;5:15-21. PubMed PMID: 21660251. Pubmed Central PMCID: 3109635. Epub 2011/06/11. eng.

123. Devane WA, Hanus L, Breuer A, Pertwee RG, Stevenson LA, Griffin G, et al. Isolation and Structure of a Brain Constituent That Binds to the Cannabinoid Receptor. Science. 1992 Dec 18;258(5090):1946-9. PubMed PMID: ISI:A1992KD08800035. English.

124. Mackie K, Devane WA, Hille B. Anandamide, an Endogenous Cannabinoid, Inhibits Calcium Currents as a Partial Agonist in N18 Neuroblastoma-Cells. Molecular Pharmacology. 1993 Sep;44(3):498-503. PubMed PMID: ISI:A1993LY91500002. English.

125. Burkey TH, Quock RM, Consroe P, Ehlert FJ, Hosohata Y, Roeske WR, et al. Relative efficacies of cannabinoid CB1 receptor agonists in the mouse brain. Eur J Pharmacol. 1997 Oct 8;336(2-3):295-8. PubMed PMID: 9384246. Epub 1998/01/24. eng.

126. Glass M, Northup JK. Agonist selective regulation of G proteins by cannabinoid CB(1) and CB(2) receptors. Mol Pharmacol. 1999 Dec;56(6):1362-9. PubMed PMID: 10570066. Epub 1999/11/26. eng.

127. Gonsiorek W, Lunn C, Fan X, Narula S, Lundell D, Hipkin RW. Endocannabinoid 2-arachidonyl glycerol is a full agonist through human type 2 cannabinoid receptor: antagonism by anandamide. Mol Pharmacol. 2000 May;57(5):1045-50. PubMed PMID: 10779390. Epub 2000/04/25. eng.

128. Sugiura T, Kodaka T, Nakane S, Miyashita T, Kondo S, Suhara Y, et al. Evidence that the cannabinoid CB1 receptor is a 2-arachidonoylglycerol receptor - Structure-activity relationship of 2-arachidonoylglycerol ether-linked analogues, and related compounds. Journal of Biological Chemistry. 1999 Jan 29;274(5):2794-801. PubMed PMID: ISI:000078319500030. English.

129. Sugiura T, Kondo S, Kishimoto S, Miyashita T, Nakane S, Kodaka T, et al. Evidence that 2-arachidonoylglycerol but not N-palmitoylethanolamine or anandamide is the physiological ligand for the cannabinoid CB2 receptor - Comparison of the agonistic activities of various cannabinoid receptor ligands in HL-60 cells. Journal of Biological Chemistry. 2000 Jan 7;275(1):605-12. PubMed PMID: ISI:000085951600081. English.

130. Ross RA, Gibson TM, Brockie HC, Leslie M, Pashmi G, Craib SJ, et al. Structure-activity relationship for the endogenous cannabinoid, anandamide, and certain of its analogues at vanilloid receptors in transfected cells and vas deferens. British journal of pharmacology. 2001 Feb;132(3):631-40. PubMed PMID: ISI:000166942600004. English.

131. Smart D, Gunthorpe MJ, Jerman JC, Nasir S, Gray J, Muir AI, et al. The endogenous lipid anandamide is a full agonist at the human vanilloid receptor (hVR1). British journal of pharmacology. 2000 Jan;129(2):227-30. PubMed PMID: ISI:000085046000001. English.

132. Ralevic V, Kendall DA, Jerman JC, Middlemiss DN, Smart D. Cannabinoid activation of recombinant and endogenous vanilloid receptors. Eur J Pharmacol. 2001 Jul 27;424(3):211-9. PubMed PMID: 11672565. Epub 2001/10/24. eng.

133. Cravatt BF, Demarest K, Patricelli MP, Bracey MH, Giang DK, Martin BR, et al. Supersensitivity to anandamide and enhanced endogenous cannabinoid signaling in mice lacking fatty acid amide hydrolase. Proceedings of the National Academy of Sciences of the United States of America. 2001 Jul 31;98(16):9371-6. PubMed PMID: 11470906. Pubmed Central PMCID: 55427. Epub 2001/07/27. eng.

134. Brown WH, Gillum MP, Lee HY, Camporez JP, Zhang XM, Jeong JK, et al. Fatty acid amide hydrolase ablation promotes ectopic lipid storage and insulin resistance due to centrally mediated hypothyroidism. Proceedings of the National Academy of Sciences of the United States of America. 2012 Sep 11;109(37):14966-71. PubMed PMID: 22912404. Pubmed Central PMCID: 3443187. Epub 2012/08/23. eng.

135. Lenglet S, Thomas A, Soehnlein O, Montecucco F, Burger F, Pelli G, et al. Fatty acid amide hydrolase deficiency enhances intraplaque neutrophil recruitment in atherosclerotic mice. Arteriosclerosis, thrombosis, and vascular biology. 2013 Feb;33(2):215-23. PubMed PMID: 23241405. Epub 2012/12/18. eng.

136. Molica F, Burger F, Thomas A, Staub C, Tailleux A, Staels B, et al. Endogenous cannabinoid receptor CB1 activation promotes vascular smooth-muscle cell proliferation and neointima formation. Journal of lipid research. 2013 May;54(5):1360-8. PubMed PMID: 23479425. Pubmed Central PMCID: 3622330. Epub 2013/03/13. eng.

137. Mechoulam R, Benshabat S, Hanus L, Ligumsky M, Kaminski NE, Schatz AR, et al. Identification of an Endogenous 2-Monoglyceride, Present in Canine Gut, That Binds to Cannabinoid Receptors. Biochemical Pharmacology. 1995 Jun 29;50(1):83-90. PubMed PMID: ISI:A1995RH27200012. English.

138. Savinainen JR, Jarvinen T, Laine K, Laitinen JT. Despite substantial degradation, 2-arachidonoylglycerol is a potent full efficacy agonist mediating CB1 receptor-dependent G-protein activation in rat cerebellar membranes. British journal of pharmacology. 2001 Oct;134(3):664-72. PubMed PMID: ISI:000171395000024. English.

139. Stella N, Schweitzer P, Piomelli D. A second endogenous cannabinoid that modulates long-term potentiation. Nature. 1997 Aug 21;388(6644):773-8. PubMed PMID: ISI:A1997XR66700051. English.

140. Ueda H, Kobayashi T, Kishimoto M, Tsutsumi T, Okuyama H. A possible pathway of phosphoinositide metabolism through EDTA-insensitive phospholipase A1 followed by lysophosphoinositide-specific phospholipase C in rat brain. J Neurochem. 1993 Nov;61(5):1874-81. PubMed PMID: 8229000. Epub 1993/11/01. eng.

141. Nakane S, Oka S, Arai S, Waku K, Ishima Y, Tokumura A, et al. 2-Arachidonoyl-sn-glycero-3-phosphate, an arachidonic acid-containing lysophosphatidic acid: occurrence and rapid enzymatic conversion to 2-arachidonoyl-sn-glycerol, a cannabinoid receptor ligand, in rat brain. Arch Biochem Biophys. 2002 Jun 1;402(1):51-8. PubMed PMID: 12051682. Epub 2002/06/08. eng.

142. Marsicano G, Goodenough S, Monory K, Hermann H, Eder M, Cannich A, et al. CB1 cannabinoid receptors and on-demand defense against excitotoxicity. Science. 2003 Oct 3;302(5642):84-8. PubMed PMID: 14526074. Epub 2003/10/04. eng.

143. Piomelli D. The molecular logic of endocannabinoid signalling. Nature Reviews Neuroscience. 2003 Nov;4(11):873-84. PubMed PMID: ISI:000186362300014. English.

144. Saario SM, Savinainen JR, Laitinen JT, Jarvinen T, Niemi R. Monoglyceride lipase-like enzymatic activity is responsible for hydrolysis of 2-arachidonoylglycerol in rat cerebellar membranes. Biochemical Pharmacology. 2004 Apr 1;67(7):1381-7. PubMed PMID: ISI:000220411700017. English.

145. Saario SM, Salo OM, Nevalainen T, Poso A, Laitinen JT, Jarvinen T, et al. Characterization of the sulfhydryl-sensitive site in the enzyme responsible for hydrolysis of

2-arachidonoyl-glycerol in rat cerebellar membranes. Chemistry & biology. 2005 Jun;12(6):649-56. PubMed PMID: 15975510. Epub 2005/06/25. eng.

146. Makara JK, Mor M, Fegley D, Szabo SI, Kathuria S, Astarita G, et al. Selective inhibition of 2-AG hydrolysis enhances endocannabinoid signaling in hippocampus. Nature neuroscience. 2005 Sep;8(9):1139-41. PubMed PMID: 16116451. Epub 2005/08/24. eng.

147. Goparaju SK, Ueda N, Yamaguchi H, Yamamoto S. Anandamide amidohydrolase reacting with 2-arachidonoylglycerol, another cannabinoid receptor ligand. FEBS letters. 1998 Jan 23;422(1):69-73. PubMed PMID: 9475172. Epub 1998/02/25. eng.

148. Pacher P, Batkai S, Osei-Hyiaman D, Offertaler L, Liu J, Harvey-White J, et al. Hemodynamic profile, responsiveness to anandamide, and baroreflex sensitivity of mice lacking fatty acid amide hydrolase. Am J Physiol Heart Circ Physiol. 2005 Aug;289(2):H533-41. PubMed PMID: 15821037. Pubmed Central PMCID: 2225481. Epub 2005/04/12. eng.

149. Lichtman AH, Hawkins EG, Griffin G, Cravatt BF. Pharmacological activity of fatty acid amides is regulated, but not mediated, by fatty acid amide hydrolase in vivo. Journal of Pharmacology and Experimental Therapeutics. 2002 Jul;302(1):73-9. PubMed PMID: ISI:000176183000010. English.

150. Thomas G, Betters JL, Lord CC, Brown AL, Marshall S, Ferguson D, et al. The Serine Hydrolase ABHD6 Is a Critical Regulator of the Metabolic Syndrome. Cell Reports. 2013 Oct;5(2):508-20. PubMed PMID: ISI:000328263000022. English.

151. Di Marzo V. Targeting the endocannabinoid system: to enhance or reduce? Nature reviews Drug discovery. 2008 May;7(5):438-55. PubMed PMID: 18446159.

152. Savinainen JR, Saario SM, Laitinen JT. The serine hydrolases MAGL, ABHD6 and ABHD12 as guardians of 2-arachidonoylglycerol signalling through cannabinoid receptors. Acta physiologica. 2012 Feb;204(2):267-76. PubMed PMID: 21418147. Pubmed Central PMCID: 3320662.

153. Panikashvili D, Simeonidou C, Ben-Shabat S, Hanus L, Breuer A, Mechoulam R, et al. An endogenous cannabinoid (2-AG) is neuroprotective after brain injury. Nature. 2001 Oct 4;413(6855):527-31. PubMed PMID: ISI:000171340500048. English.

154. Sinor AD, Irvin SM, Greenberg DA. Endocannabinoids protect cerebral cortical neurons from in vitro ischemia in rats. Neuroscience Letters. 2000 Jan 14;278(3):157-60. PubMed PMID: 10653017. Epub 2000/02/01. eng.

155. Baker D, Pryce G, Croxford JL, Brown P, Pertwee RG, Makriyannis A, et al. Endocannabinoids control spasticity in a multiple sclerosis model. Faseb Journal. 2001 Feb;15(2):300-2. PubMed PMID: 11156943. Epub 2001/02/07. eng.

156. Hohmann AG, Suplita RL, Bolton NM, Neely MH, Fegley D, Mangieri R, et al. An endocannabinoid mechanism for stress-induced analgesia. Nature. 2005 Jun 23;435(7045):1108-12. PubMed PMID: 15973410. Epub 2005/06/24. eng.

157. Connell K, Bolton N, Olsen D, Piomelli D, Hohmann AG. Role of the basolateral nucleus of the amygdala in endocannabinoid-mediated stress-induced analgesia. Neuroscience Letters. 2006 Apr 24;397(3):180-4. PubMed PMID: 16378681. Epub 2005/12/28. eng.

158. Patel S, Roelke CT, Rademacher DJ, Cullinan WE, Hillard CJ. Endocannabinoid signaling negatively modulates stress-induced activation of the hypothalamic-pituitary-

adrenal axis. Endocrinology. 2004 Dec;145(12):5431-8. PubMed PMID: 15331569. Epub 2004/08/28. eng.

159. Van Sickle MD, Duncan M, Kingsley PJ, Mouihate A, Urbani P, Mackie K, et al. Identification and functional characterization of brainstem cannabinoid CB2 receptors. Science. 2005 Oct 14;310(5746):329-32. PubMed PMID: 16224028. Epub 2005/10/15. eng.

160. Kirkham TC, Williams CM, Fezza F, Di Marzo V. Endocannabinoid levels in rat limbic forebrain and hypothalamus in relation to fasting, feeding and satiation: stimulation of eating by 2-arachidonoyl glycerol. British journal of pharmacology. 2002 Jun;136(4):550-7. PubMed PMID: 12055133. Pubmed Central PMCID: 1573386. Epub 2002/06/11. eng.

161. Di Marzo V, Goparaju SK, Wang L, Liu J, Batkai S, Jarai Z, et al. Leptin-regulated endocannabinoids are involved in maintaining food intake. Nature. 2001 Apr 12;410(6830):822-5. PubMed PMID: 11298451. Epub 2001/04/12. eng.

162. Matias I, Gonthier MP, Orlando P, Martiadis V, De Petrocellis L, Cervino C, et al. Regulation, function, and dysregulation of endocannabinoids in models of adipose and beta-pancreatic cells and in obesity and hyperglycemia. J Clin Endocrinol Metab. 2006 Aug;91(8):3171-80. PubMed PMID: 16684820. Epub 2006/05/11. eng.

163. Pagano C, Pilon C, Calcagno A, Urbanet R, Rossato M, Milan G, et al. The endogenous cannabinoid system stimulates glucose uptake in human fat cells via phosphatidylinositol 3-kinase and calcium-dependent mechanisms. J Clin Endocrinol Metab. 2007 Dec;92(12):4810-9. PubMed PMID: 17785353. Epub 2007/09/06. eng.

164. Cota D, Marsicano G, Tschop M, Grubler Y, Flachskamm C, Schubert M, et al. The endogenous cannabinoid system affects energy balance via central orexigenic drive and peripheral lipogenesis. The Journal of clinical investigation. 2003 Aug;112(3):423-31. PubMed PMID: 12897210. Pubmed Central PMCID: 166293. Epub 2003/08/05. eng.

165. Bartelt A, Orlando P, Mele C, Ligresti A, Toedter K, Scheja L, et al. Altered endocannabinoid signalling after a high-fat diet in Apoe(-/-) mice: relevance to adipose tissue inflammation, hepatic steatosis and insulin resistance. Diabetologia. 2011 Nov;54(11):2900-10. PubMed PMID: 21847582. Epub 2011/08/19. eng.

166. Bensaid M, Gary-Bobo M, Esclangon A, Maffrand JP, Le Fur G, Oury-Donat F, et al. The cannabinoid CB1 receptor antagonist SR141716 increases Acrp30 mRNA expression in adipose tissue of obese fa/fa rats and in cultured adipocyte cells. Mol Pharmacol. 2003 Apr;63(4):908-14. PubMed PMID: 12644592. Epub 2003/03/20. eng.

167. Liu YL, Connoley IP, Wilson CA, Stock MJ. Effects of the cannabinoid CB1 receptor antagonist SR141716 on oxygen consumption and soleus muscle glucose uptake in Lep(ob)/Lep(ob) mice. Int J Obes (Lond). 2005 Feb;29(2):183-7. PubMed PMID: 15558076. Epub 2004/11/24. eng.

168. Lofgren P, Sjolin E, Wahlen K, Hoffstedt J. Human adipose tissue cannabinoid receptor 1 gene expression is not related to fat cell function or adiponectin level. Journal of Clinical Endocrinology & Metabolism. 2007 Apr;92(4):1555-9. PubMed PMID: ISI:000245466600060. English.

169. Hezode C, Roudot-Thoraval F, Nguyen S, Grenard P, Julien B, Zafrani ES, et al. Daily cannabis smoking as a risk factor for progression of fibrosis in chronic hepatitis C. Hepatology. 2005 Jul;42(1):63-71. PubMed PMID: ISI:000230189200010. English.

170. Teixeira-Clerc F, Julien B, Grenard P, Tran Van Nhieu J, Deveaux V, Li L, et al. CB1 cannabinoid receptor antagonism: a new strategy for the treatment of liver fibrosis. Nat Med. 2006 Jun;12(6):671-6. PubMed PMID: 16715087. Epub 2006/05/23. eng.

171. Siegmund SV, Qian T, de Minicis S, Harvey-White J, Kunos G, Vinod KY, et al. The endocannabinoid 2-arachidonoyl glycerol induces death of hepatic stellate cells via mitochondrial reactive oxygen species. Faseb Journal. 2007 Sep;21(11):2798-806. PubMed PMID: 17440119. Epub 2007/04/19. eng.

172. Munoz-Luque J, Ros J, Fernandez-Varo G, Tugues S, Morales-Ruiz M, Alvarez CE, et al. Regression of fibrosis after chronic stimulation of cannabinoid CB2 receptor in cirrhotic rats. Journal of Pharmacology and Experimental Therapeutics. 2008 Feb;324(2):475-83. PubMed PMID: 18029545. Pubmed Central PMCID: 2887659. Epub 2007/11/22. eng.

173. Jourdan T, Djaouti L, Demizieux L, Gresti J, Verges B, Degrace P. CB1 antagonism exerts specific molecular effects on visceral and subcutaneous fat and reverses liver steatosis in diet-induced obese mice. Diabetes. 2010 Apr;59(4):926-34. PubMed PMID: 20110567. Pubmed Central PMCID: 2844840. Epub 2010/01/30. eng.

174. Osei-Hyiaman D, Liu J, Zhou L, Godlewski G, Harvey-White J, Jeong WI, et al. Hepatic CB1 receptor is required for development of diet-induced steatosis, dyslipidemia, and insulin and leptin resistance in mice. The Journal of clinical investigation. 2008 Sep;118(9):3160-9. PubMed PMID: 18677409. Pubmed Central PMCID: 2491458. Epub 2008/08/05. eng.

175. Tam J, Vemuri VK, Liu J, Batkai S, Mukhopadhyay B, Godlewski G, et al. Peripheral CB1 cannabinoid receptor blockade improves cardiometabolic risk in mouse models of obesity. The Journal of clinical investigation. 2010 Aug;120(8):2953-66. PubMed PMID: 20664173. Pubmed Central PMCID: 2912197. Epub 2010/07/29. eng.

176. Ruby MA, Nomura DK, Hudak CS, Mangravite LM, Chiu S, Casida JE, et al. Overactive endocannabinoid signaling impairs apolipoprotein E-mediated clearance of triglyceride-rich lipoproteins. Proceedings of the National Academy of Sciences of the United States of America. 2008 Sep 23;105(38):14561-6. PubMed PMID: 18794527. Pubmed Central PMCID: 2567196. Epub 2008/09/17. eng.

177. Eckardt K, Sell H, Taube A, Koenen M, Platzbecker B, Cramer A, et al. Cannabinoid type 1 receptors in human skeletal muscle cells participate in the negative crosstalk between fat and muscle. Diabetologia. 2009 Apr;52(4):664-74. PubMed PMID: 19089403. Epub 2008/12/18. eng.

178. Nogueiras R, Veyrat-Durebex C, Suchanek PM, Klein M, Tschop J, Caldwell C, et al. Peripheral, but not central, CB1 antagonism provides food intake-independent metabolic benefits in diet-induced obese rats. Diabetes. 2008 Nov;57(11):2977-91. PubMed PMID: 18716045. Pubmed Central PMCID: 2570394. Epub 2008/08/22. eng.

179. Cota D, Sandoval DA, Olivieri M, Prodi E, D'Alessio DA, Woods SC, et al. Food intake-independent effects of CB1 antagonism on glucose and lipid metabolism. Obesity (Silver Spring). 2009 Aug;17(8):1641-5. PubMed PMID: 19325539. Epub 2009/03/28. eng.

180. Ruby MA, Nomura DK, Hudak CS, Barber A, Casida JE, Krauss RM. Acute overactive endocannabinoid signaling induces glucose intolerance, hepatic steatosis, and novel cannabinoid receptor 1 responsive genes. PloS one. 2011;6(11):e26415. PubMed PMID: 22073164. Pubmed Central PMCID: 3208546. Epub 2011/11/11. eng.

181. Jourdan T, Godlewski G, Cinar R, Bertola A, Szanda G, Liu J, et al. Activation of the Nlrp3 inflammasome in infiltrating macrophages by endocannabinoids mediates beta cell loss in type 2 diabetes. Nat Med. 2013 Sep;19(9):1132-40. PubMed PMID: 23955712. Pubmed Central PMCID: 4050982. Epub 2013/08/21. eng.

182. Nahas GG, Suciu-Foca N, Armand JP, Morishima A. Inhibition of cellular mediated immunity in marihuana smokers. Science. 1974 Feb 1;183(4123):419-20. PubMed PMID: 4271816. Epub 1974/02/01. eng.

183. Nahas GG, Morishima A, Desoize B. Effects of cannabinoids on macromolecular synthesis and replication of cultured lymphocytes. Fed Proc. 1977 Apr;36(5):1748-52. PubMed PMID: 844617. Epub 1977/04/01. eng.

184. Klein TW, Newton CA, Widen R, Friedman H. The effect of delta-9-tetrahydrocannabinol and 11-hydroxy-delta-9-tetrahydrocannabinol on T-lymphocyte and B-lymphocyte mitogen responses. J Immunopharmacol. 1985;7(4):451-66. PubMed PMID: 3003204. Epub 1985/01/01. eng.

185. Specter S, Lancz G, Hazelden J. Marijuana and immunity: tetrahydrocannabinol mediated inhibition of lymphocyte blastogenesis. Int J Immunopharmacol. 1990;12(3):261-7. PubMed PMID: 2158486. Epub 1990/01/01. eng.

186. Yebra M, Klein TW, Friedman H. Delta 9-tetrahydrocannabinol suppresses concanavalin A induced increase in cytoplasmic free calcium in mouse thymocytes. Life Sci. 1992;51(2):151-60. PubMed PMID: 1319535. Epub 1992/01/01. eng.

187. Schatz AR, Kessler FK, Kaminski NE. Inhibition of adenylate cyclase by delta 9-tetrahydrocannabinol in mouse spleen cells: a potential mechanism for cannabinoid-mediated immunosuppression. Life Sci. 1992;51(6):PL25-30. PubMed PMID: 1321935. Epub 1992/01/01. eng.

188. Diaz S, Specter S, Coffey RG. Suppression of lymphocyte adenosine 3':5'-cyclic monophosphate (cAMP) by delta-9-tetrahydrocannabinol. Int J Immunopharmacol. 1993 May;15(4):523-32. PubMed PMID: 8396073. Epub 1993/05/01. eng.

189. Klein TW, Kawakami Y, Newton C, Friedman H. Marijuana components suppress induction and cytolytic function of murine cytotoxic T cells in vitro and in vivo. J Toxicol Environ Health. 1991 Apr;32(4):465-77. PubMed PMID: 1850002. Epub 1991/04/01. eng.

190. Fischer-Stenger K, Updegrove AW, Cabral GA. Delta 9-tetrahydrocannabinol decreases cytotoxic T lymphocyte activity to herpes simplex virus type 1-infected cells. Proc Soc Exp Biol Med. 1992 Jul;200(3):422-30. PubMed PMID: 1319584. Epub 1992/07/01. eng.

191. Nahas GG, Osserman EF. Altered serum immunoglobulin concentration in chronic marijuana smokers. Adv Exp Med Biol. 1991;288:25-32. PubMed PMID: 1950736. Epub 1991/01/01. eng.

192. Zimmerman S, Zimmerman AM, Cameron IL, Laurence HL. delta1-tetrahydrocannabinol, cannabidiol and cannabinol effects on the immune response of mice. Pharmacology. 1977;15(1):10-23. PubMed PMID: 320608. Epub 1977/01/01. eng.

193. Baczynsky WO, Zimmerman AM. Effects of delta 9-tetrahydrocannabinol, cannabinol and cannabidiol on the immune system in mice. I. In vivo investigation of the primary and secondary immune response. Pharmacology. 1983;26(1):1-11. PubMed PMID: 6298841. Epub 1983/01/01. eng.

194. Specter S, Lancz G, Goodfellow D. Suppression of human macrophage function in vitro by delta 9-tetrahydrocannabinol. J Leukoc Biol. 1991 Nov;50(5):423-6. PubMed PMID: 1660911. Epub 1991/11/01. eng.

195. Lopez-Cepero M, Friedman M, Klein T, Friedman H. Tetrahydrocannabinol-induced suppression of macrophage spreading and phagocytic activity in vitro. J Leukoc Biol. 1986 Jun;39(6):679-86. PubMed PMID: 3011935. Epub 1986/06/01. eng.

196. Drath DB, Shorey JM, Price L, Huber GL. Metabolic and functional characteristics of alveolar macrophages recovered from rats exposed to marijuana smoke. Infect Immun. 1979 Jul;25(1):268-72. PubMed PMID: 225274. Pubmed Central PMCID: 414447. Epub 1979/07/01. eng.

197. Lu T, Newton C, Perkins I, Friedman H, Klein TW. Cannabinoid treatment suppresses the T-helper cell-polarizing function of mouse dendritic cells stimulated with Legionella pneumophila infection. Journal of Pharmacology and Experimental Therapeutics. 2006 Oct;319(1):269-76. PubMed PMID: 16837556. Epub 2006/07/14. eng.

198. Sacerdote P, Massi P, Panerai AE, Parolaro D. In vivo and in vitro treatment with the synthetic cannabinoid CP55, 940 decreases the in vitro migration of macrophages in the rat: involvement of both CB1 and CB2 receptors. J Neuroimmunol. 2000 Sep 22;109(2):155-63. PubMed PMID: 10996217. Epub 2000/09/21. eng.

199. Klein TW, Newton C, Friedman H. Cannabinoid receptors and immunity. Immunol Today. 1998 Aug;19(8):373-81. PubMed PMID: 9709506. Epub 1998/08/26. eng.

200. Zhu WG, Friedman H, Klein TW. Delta(9)-Tetrahydrocannabinol induces apoptosis in macrophages and lymphocytes: Involvement of Bcl-2 and caspase-1. Journal of Pharmacology and Experimental Therapeutics. 1998 Aug;286(2):1103-9. PubMed PMID: ISI:000075359600068. English.

201. McKallip RJ, Lombard C, Martin BR, Nagarkatti M, Nagarkatti PS. Delta(9)-Tetrahydrocannabinol-induced apoptosis in the thymus and spleen as a mechanism of immunosuppression in vitro and in vivo. Journal of Pharmacology and Experimental Therapeutics. 2002 Aug;302(2):451-65. PubMed PMID: ISI:000176899200006. English.

202. Bayewitch M, Rhee MH, Avidor-Reiss T, Breuer A, Mechoulam R, Vogel Z. (-)-Delta9-tetrahydrocannabinol antagonizes the peripheral cannabinoid receptor-mediated inhibition of adenylyl cyclase. The Journal of biological chemistry. 1996 Apr 26;271(17):9902-5. PubMed PMID: 8626625. Epub 1996/04/26. eng.

203. Han KH, Lim S, Ryu J, Lee CW, Kim Y, Kang JH, et al. CB1 and CB2 cannabinoid receptors differentially regulate the production of reactive oxygen species by macrophages. Cardiovasc Res. 2009 Dec 1;84(3):378-86. PubMed PMID: 19596672. Epub 2009/07/15. eng.

204. Rockwell CE, Snider NT, Thompson JT, Heuvel JPV, Kaminski NE. Interleukin-2 suppression by 2-arachidonyl glycerol is mediated through peroxisome proliferator-activated receptor gamma independently of cannabinoid receptors 1 and 2. Molecular Pharmacology. 2006 Jul;70(1):101-11. PubMed PMID: ISI:000238438100013. English.

205. Gallily R, Breuer A, Mechoulam R. 2-Arachidonylglycerol, an endogenous cannabinoid, inhibits tumor necrosis factor-alpha production in murine macrophages, and in mice. Eur J Pharmacol. 2000 Oct 6;406(1):R5-7. PubMed PMID: 11011050. Epub 2000/09/30. eng.

206. Kaplan BL, Ouyang Y, Rockwell CE, Rao GK, Kaminski NE. 2-Arachidonoyl-glycerol suppresses interferon-gamma production in phorbol ester/ionomycin-activated mouse splenocytes independent of CB1 or CB2. J Leukoc Biol. 2005 Jun;77(6):966-74. PubMed PMID: 15774549. Epub 2005/03/19. eng.

207. Chang YH, Lee ST, Lin WW. Effects of cannabinoids on LPS-stimulated inflammatory mediator release from macrophages: involvement of eicosanoids. J Cell Biochem. 2001;81(4):715-23. PubMed PMID: 11329626. Epub 2001/05/01. eng.

208. Kishimoto S, Kobayashi Y, Oka S, Gokoh M, Waku K, Sugiura T. 2-Arachidonoylglycerol, an endogenous cannabinoid receptor ligand, induces accelerated production of chemokines in HL-60 cells. J Biochem. 2004 Apr;135(4):517-24. PubMed PMID: 15115777. Epub 2004/04/30. eng.

209. Jorda MA, Verbakel SE, Valk PJ, Vankan-Berkhoudt YV, Maccarrone M, Finazzi-Agro A, et al. Hematopoietic cells expressing the peripheral cannabinoid receptor migrate in response to the endocannabinoid 2-arachidonoylglycerol. Blood. 2002 Apr 15;99(8):2786-93. PubMed PMID: 11929767. Epub 2002/04/04. eng.

210. Montecucco F, Matias I, Lenglet S, Petrosino S, Burger F, Pelli G, et al. Regulation and possible role of endocannabinoids and related mediators in hypercholesterolemic mice with atherosclerosis. Atherosclerosis. 2009 Aug;205(2):433-41. PubMed PMID: 19187936. Epub 2009/02/04. eng.

211. Walter L, Franklin A, Witting A, Wade C, Xie Y, Kunos G, et al. Nonpsychotropic cannabinoid receptors regulate microglial cell migration. Journal of Neuroscience. 2003 Feb 15;23(4):1398-405. PubMed PMID: 12598628. Epub 2003/02/25. eng.

212. Oka S, Wakui J, Ikeda S, Yanagimoto S, Kishimoto S, Gokoh M, et al. Involvement of the cannabinoid CB2 receptor and its endogenous ligand 2-arachidonoylglycerol in oxazolone-induced contact dermatitis in mice. J Immunol. 2006 Dec 15;177(12):8796-805. PubMed PMID: 17142782. Epub 2006/12/05. eng.

213. Kishimoto S, Muramatsu M, Gokoh M, Oka S, Waku K, Sugiura T. Endogenous cannabinoid receptor ligand induces the migration of human natural killer cells. J Biochem. 2005 Feb;137(2):217-23. PubMed PMID: 15749836. Epub 2005/03/08. eng.

214. Kishimoto S, Gokoh M, Oka S, Muramatsu M, Kajiwara T, Waku K, et al. 2-Arachidonoylglycerol induces the migration of HL-60 cells differentiated into macrophage-like cells and human peripheral blood monocytes through the cannabinoid CB2 receptor-dependent mechanism. Journal of Biological Chemistry. 2003 Jul 4;278(27):24469-75. PubMed PMID: ISI:000183824800028. English.

215. Oka S, Ikeda S, Kishimoto S, Gokoh M, Yanagimoto S, Waku K, et al. 2-arachidonoylglycerol, an endogenous cannabinoid receptor ligand, induces the migration of EoL-1 human eosinophilic leukemia cells and human peripheral blood eosinophils. J Leukoc Biol. 2004 Nov;76(5):1002-9. PubMed PMID: 15316028. Epub 2004/08/19. eng.

216. Gokoh M, Kishimoto S, Oka S, Metani Y, Sugiura T. 2-Arachidonoylglycerol, an endogenous cannabinoid receptor ligand, enhances the adhesion of HL-60 cells differentiated into macrophage-like cells and human peripheral blood monocytes. FEBS letters. 2005 Nov 21;579(28):6473-8. PubMed PMID: ISI:000233520700029. English.

217. Shoemaker JL, Ruckle MB, Mayeux PR, Prather PL. Agonist-directed trafficking of response by endocannabinoids acting at CB2 receptors. Journal of Pharmacology and

Experimental Therapeutics. 2005 Nov;315(2):828-38. PubMed PMID: ISI:000232681300041. English.

218. Cao Z, Mulvihill MM, Mukhopadhyay P, Xu H, Erdelyi K, Hao E, et al. Monoacylglycerol lipase controls endocannabinoid and eicosanoid signaling and hepatic injury in mice. Gastroenterology. 2013 Apr;144(4):808-17 e15. PubMed PMID: 23295443. Pubmed Central PMCID: 3608818. Epub 2013/01/09. eng.

219. Gokoh M, Kishimoto S, Oka S, Sugiura T. 2-Arachidonoylglycerol enhances the phagocytosis of opsonized zymosan by HL-60 cells differentiated into macrophage-like cells. Biological & Pharmaceutical Bulletin. 2007 Jul;30(7):1199-205. PubMed PMID: ISI:000248712000003. English.

220. Chiurchiu V, Lanuti M, Catanzaro G, Fezza F, Rapino C, Maccarrone M. Detailed characterization of the endocannabinoid system in human macrophages and foam cells, and anti-inflammatory role of type-2 cannabinoid receptor. Atherosclerosis. 2014 Mar;233(1):55-63. PubMed PMID: 24529123. Epub 2014/02/18. eng.

221. Knittelfelder OL, Weberhofer BP, Eichmann TO, Kohlwein SD, Rechberger GN. A versatile ultra-high performance LC-MS method for lipid profiling. J Chromatogr B Analyt Technol Biomed Life Sci. 2014 Mar 1;951-952:119-28. PubMed PMID: 24548922. Pubmed Central PMCID: 3946075. Epub 2014/02/20. eng.

222. Wang DQ, Carey MC. Measurement of intestinal cholesterol absorption by plasma and fecal dual-isotope ratio, mass balance, and lymph fistula methods in the mouse: an analysis of direct versus indirect methodologies. Journal of lipid research. 2003 May;44(5):1042-59. PubMed PMID: 12588946.

223. Taschler U, Eichmann TO, Radner FP, Grabner GF, Wolinski H, Storr M, et al. Monoglyceride lipase-deficiency causes desensitization of intestinal cannabinoid receptor type 1 and increased colonic mu-opioid receptor sensitivity. British journal of pharmacology. 2015 Jun 15. PubMed PMID: 26075589.

224. Kuipers F, Jong MC, Lin Y, Eck M, Havinga R, Bloks V, et al. Impaired secretion of very low density lipoprotein-triglycerides by apolipoprotein E- deficient mouse hepatocytes. The Journal of clinical investigation. 1997 Dec 1;100(11):2915-22. PubMed PMID: 9389759. Pubmed Central PMCID: 508499.

225. Tsukamoto K, Maugeais C, Glick JM, Rader DJ. Markedly increased secretion of VLDL triglycerides induced by gene transfer of apolipoprotein E isoforms in apoE-deficient mice. Journal of lipid research. 2000 Feb;41(2):253-9. PubMed PMID: 10681409.

226. Choi CS, Savage DB, Abu-Elheiga L, Liu ZX, Kim S, Kulkarni A, et al. Continuous fat oxidation in acetyl-CoA carboxylase 2 knockout mice increases total energy expenditure, reduces fat mass, and improves insulin sensitivity. Proceedings of the National Academy of Sciences of the United States of America. 2007 Oct 16;104(42):16480-5. PubMed PMID: 17923673. Pubmed Central PMCID: 2034222.

227. van der Velde AE, Brufau G, Groen AK. Transintestinal cholesterol efflux. Current opinion in lipidology. 2010 Jun;21(3):167-71. PubMed PMID: 20410820.

228. Lan H, Lin HV, Wang CF, Wright MJ, Xu S, Kang L, et al. Agonists at GPR119 mediate secretion of GLP-1 from mouse enteroendocrine cells through glucose-independent pathways. British journal of pharmacology. 2012 Apr;165(8):2799-807. PubMed PMID: 22029751. Pubmed Central PMCID: 3423251.

229. Chait A, Bornfeldt KE. Diabetes and atherosclerosis: is there a role for hyperglycemia? Journal of lipid research. 2009 Apr;50 Suppl:S335-9. PubMed PMID: 19029122. Pubmed Central PMCID: 2674740.

230. Lichtman AH, Blankman JL, Cravatt BF. Endocannabinoid overload. Mol Pharmacol. 2010 Dec;78(6):993-5. PubMed PMID: 20952498. Pubmed Central PMCID: 2993463. Epub 2010/10/19. eng.

231. Jiang S, Fu Y, Avraham HK. Regulation of hematopoietic stem cell trafficking and mobilization by the endocannabinoid system. Transfusion. 2011 Nov;51 Suppl 4:65S-71S. PubMed PMID: 22074629. Epub 2011/12/07. eng.

232. Yao PM, Tabas I. Free cholesterol loading of macrophages induces apoptosis involving the fas pathway. J Biol Chem. 2000 Aug 4;275(31):23807-13. PubMed PMID: 10791964. Epub 2000/05/03. eng.

233. Maccarrone M, Finazzi-Agro A. The endocannabinoid system, anandamide and the regulation of mammalian cell apoptosis. Cell death and differentiation. 2003 Sep;10(9):946-55. PubMed PMID: 12934069.

234. Zhao Y, Ye D, Wang J, Calpe-Berdiel L, Azzis SB, Van Berkel TJ, et al. Stage-specific remodeling of atherosclerotic lesions upon cholesterol lowering in LDL receptor knockout mice. The American journal of pathology. 2011 Sep;179(3):1522-32. PubMed PMID: 21741939. Pubmed Central PMCID: 3157208.

235. Nomura DK, Long JZ, Niessen S, Hoover HS, Ng SW, Cravatt BF. Monoacylglycerol lipase regulates a fatty acid network that promotes cancer pathogenesis. Cell. 2010 Jan 8;140(1):49-61. PubMed PMID: 20079333. Pubmed Central PMCID: 2885975.

236. Takeuchi K, Reue K. Biochemistry, physiology, and genetics of GPAT, AGPAT, and lipin enzymes in triglyceride synthesis. American journal of physiology Endocrinology and metabolism. 2009 Jun;296(6):E1195-209. PubMed PMID: 19336658. Pubmed Central PMCID: 2692402.

237. Shi Y, Cheng D. Beyond triglyceride synthesis: the dynamic functional roles of MGAT and DGAT enzymes in energy metabolism. American journal of physiology Endocrinology and metabolism. 2009 Jul;297(1):E10-8. PubMed PMID: 19116371. Pubmed Central PMCID: 3735925.

238. Yen CL, Stone SJ, Koliwad S, Harris C, Farese RV, Jr. Thematic review series: glycerolipids. DGAT enzymes and triacylglycerol biosynthesis. Journal of lipid research. 2008 Nov;49(11):2283-301. PubMed PMID: 18757836. Pubmed Central PMCID: 3837458.

239. Wurie HR, Buckett L, Zammit VA. Evidence that diacylglycerol acyltransferase 1 (DGAT1) has dual membrane topology in the endoplasmic reticulum of HepG2 cells. The Journal of biological chemistry. 2011 Oct 21;286(42):36238-47. PubMed PMID: 21846726. Pubmed Central PMCID: 3196132.

240. Cases S, Smith SJ, Zheng YW, Myers HM, Lear SR, Sande E, et al. Identification of a gene encoding an acyl CoA:diacylglycerol acyltransferase, a key enzyme in triacylglycerol synthesis. Proceedings of the National Academy of Sciences of the United States of America. 1998 Oct 27;95(22):13018-23. PubMed PMID: 9789033. Pubmed Central PMCID: 23692.

241. Yen CL, Monetti M, Burri BJ, Farese RV, Jr. The triacylglycerol synthesis enzyme DGAT1 also catalyzes the synthesis of diacylglycerols, waxes, and retinyl esters. Journal of lipid research. 2005 Jul;46(7):1502-11. PubMed PMID: 15834126.

242. Cases S, Stone SJ, Zhou P, Yen E, Tow B, Lardizabal KD, et al. Cloning of DGAT2, a second mammalian diacylglycerol acyltransferase, and related family members. The Journal of biological chemistry. 2001 Oct 19;276(42):38870-6. PubMed PMID: 11481335.

243. Ranganathan G, Unal R, Pokrovskaya I, Yao-Borengasser A, Phanavanh B, Lecka-Czernik B, et al. The lipogenic enzymes DGAT1, FAS, and LPL in adipose tissue: effects of obesity, insulin resistance, and TZD treatment. Journal of lipid research. 2006 Nov;47(11):2444-50. PubMed PMID: 16894240. Pubmed Central PMCID: 1850099.

244. Meegalla RL, Billheimer JT, Cheng D. Concerted elevation of acyl-coenzyme A:diacylglycerol acyltransferase (DGAT) activity through independent stimulation of mRNA expression of DGAT1 and DGAT2 by carbohydrate and insulin. Biochemical and biophysical research communications. 2002 Nov 1;298(3):317-23. PubMed PMID: 12413942.

245. Suzuki R, Tobe K, Aoyama M, Sakamoto K, Ohsugi M, Kamei N, et al. Expression of DGAT2 in white adipose tissue is regulated by central leptin action. The Journal of biological chemistry. 2005 Feb 4;280(5):3331-7. PubMed PMID: 15550388.

246. Hillmar I, Henze K, Zollner N. Influence of fatty acids on microsomal diacylglycerol acyltransferase activity in primary cultures of hepatocytes. Hoppe-Seyler's Zeitschrift fur physiologische Chemie. 1983 Feb;364(2):173-8. PubMed PMID: 6840704.

247. Tsai J, Qiu W, Kohen-Avramoglu R, Adeli K. MEK-ERK inhibition corrects the defect in VLDL assembly in HepG2 cells: potential role of ERK in VLDL-ApoB100 particle assembly. Arteriosclerosis, thrombosis, and vascular biology. 2007 Jan;27(1):211-8. PubMed PMID: 17038630.

248. Haagsman HP, de Haas CG, Geelen MJ, van Golde LM. Regulation of triacylglycerol synthesis in the liver: a decrease in diacylglycerol acyltransferase activity after treatment of isolated rat hepatocytes with glucagon. Biochimica et biophysica acta. 1981 Apr 23;664(1):74-81. PubMed PMID: 6263342.

249. Sooranna SR, Saggerson ED. A decrease in diacylglycerol acyltransferase after treatment of rat adipocytes with adrenaline. FEBS letters. 1978 Nov 1;95(1):85-7. PubMed PMID: 720609.

250. Cases S, Zhou P, Shillingford JM, Wiseman BS, Fish JD, Angle CS, et al. Development of the mammary gland requires DGAT1 expression in stromal and epithelial tissues. Development. 2004 Jul;131(13):3047-55. PubMed PMID: 15163627. Pubmed Central PMCID: 2775443.

251. Smith SJ, Cases S, Jensen DR, Chen HC, Sande E, Tow B, et al. Obesity resistance and multiple mechanisms of triglyceride synthesis in mice lacking Dgat. Nature genetics. 2000 May;25(1):87-90. PubMed PMID: 10802663.

252. Shih MY, Kane MA, Zhou P, Yen CL, Streeper RS, Napoli JL, et al. Retinol Esterification by DGAT1 Is Essential for Retinoid Homeostasis in Murine Skin. The Journal of biological chemistry. 2009 Feb 13;284(7):4292-9. PubMed PMID: 19028692. Pubmed Central PMCID: 2640966.

253. Chen HC, Smith SJ, Ladha Z, Jensen DR, Ferreira LD, Pulawa LK, et al. Increased insulin and leptin sensitivity in mice lacking acyl CoA:diacylglycerol acyltransferase 1. The

Journal of clinical investigation. 2002 Apr;109(8):1049-55. PubMed PMID: 11956242. Pubmed Central PMCID: 150948.

254. Streeper RS, Grueter CA, Salomonis N, Cases S, Levin MC, Koliwad SK, et al. Deficiency of the lipid synthesis enzyme, DGAT1, extends longevity in mice. Aging. 2012 Jan;4(1):13-27. PubMed PMID: 22291164. Pubmed Central PMCID: 3292902.

255. Chen HC, Jensen DR, Myers HM, Eckel RH, Farese RV, Jr. Obesity resistance and enhanced glucose metabolism in mice transplanted with white adipose tissue lacking acyl CoA:diacylglycerol acyltransferase 1. The Journal of clinical investigation. 2003 Jun;111(11):1715-22. PubMed PMID: 12782674. Pubmed Central PMCID: 156099.

256. Liu L, Zhang Y, Chen N, Shi X, Tsang B, Yu YH. Upregulation of myocellular DGAT1 augments triglyceride synthesis in skeletal muscle and protects against fat-induced insulin resistance. The Journal of clinical investigation. 2007 Jun;117(6):1679-89. PubMed PMID: 17510710. Pubmed Central PMCID: 1866250.

257. Liu L, Shi X, Bharadwaj KG, Ikeda S, Yamashita H, Yagyu H, et al. DGAT1 expression increases heart triglyceride content but ameliorates lipotoxicity. The Journal of biological chemistry. 2009 Dec 25;284(52):36312-23. PubMed PMID: 19778901. Pubmed Central PMCID: 2794747.

258. Koliwad SK, Streeper RS, Monetti M, Cornelissen I, Chan L, Terayama K, et al. DGAT1-dependent triacylglycerol storage by macrophages protects mice from diet-induced insulin resistance and inflammation. The Journal of clinical investigation. 2010 Mar;120(3):756-67. PubMed PMID: 20124729. Pubmed Central PMCID: 2827941.

259. Villanueva CJ, Monetti M, Shih M, Zhou P, Watkins SM, Bhanot S, et al. Specific role for acyl CoA:Diacylglycerol acyltransferase 1 (Dgat1) in hepatic steatosis due to exogenous fatty acids. Hepatology. 2009 Aug;50(2):434-42. PubMed PMID: 19472314. Pubmed Central PMCID: 3097135.

260. Choi CS, Savage DB, Kulkarni A, Yu XX, Liu ZX, Morino K, et al. Suppression of diacylglycerol acyltransferase-2 (DGAT2), but not DGAT1, with antisense oligonucleotides reverses diet-induced hepatic steatosis and insulin resistance. The Journal of biological chemistry. 2007 Aug 3;282(31):22678-88. PubMed PMID: 17526931.

261. Yamaguchi K, Yang L, McCall S, Huang J, Yu XX, Pandey SK, et al. Diacylglycerol acyltranferase 1 anti-sense oligonucleotides reduce hepatic fibrosis in mice with nonalcoholic steatohepatitis. Hepatology. 2008 Feb;47(2):625-35. PubMed PMID: 18000880.

262. Monetti M, Levin MC, Watt MJ, Sajan MP, Marmor S, Hubbard BK, et al. Dissociation of hepatic steatosis and insulin resistance in mice overexpressing DGAT in the liver. Cell metabolism. 2007 Jul;6(1):69-78. PubMed PMID: 17618857.

263. Yamazaki T, Sasaki E, Kakinuma C, Yano T, Miura S, Ezaki O. Increased very low density lipoprotein secretion and gonadal fat mass in mice overexpressing liver DGAT1. The Journal of biological chemistry. 2005 Jun 3;280(22):21506-14. PubMed PMID: 15797871.

264. Millar JS, Stone SJ, Tietge UJ, Tow B, Billheimer JT, Wong JS, et al. Short-term overexpression of DGAT1 or DGAT2 increases hepatic triglyceride but not VLDL triglyceride or apoB production. Journal of lipid research. 2006 Oct;47(10):2297-305. PubMed PMID: 16877777.

265. Wurie HR, Buckett L, Zammit VA. Diacylglycerol acyltransferase 2 acts upstream of diacylglycerol acyltransferase 1 and utilizes nascent diglycerides and de novo synthesized fatty acids in HepG2 cells. The FEBS journal. 2012 Sep;279(17):3033-47. PubMed PMID: 22748069.

266. Buhman KK, Smith SJ, Stone SJ, Repa JJ, Wong JS, Knapp FF, Jr., et al. DGAT1 is not essential for intestinal triacylglycerol absorption or chylomicron synthesis. The Journal of biological chemistry. 2002 Jul 12;277(28):25474-9. PubMed PMID: 11959864.

267. Ables GP, Yang KJ, Vogel S, Hernandez-Ono A, Yu S, Yuen JJ, et al. Intestinal DGAT1 deficiency reduces postprandial triglyceride and retinyl ester excursions by inhibiting chylomicron secretion and delaying gastric emptying. Journal of lipid research. 2012 Nov;53(11):2364-79. PubMed PMID: 22911105. Pubmed Central PMCID: 3466005.

268. Schober G, Arnold M, Birtles S, Buckett LK, Pacheco-Lopez G, Turnbull AV, et al. Diacylglycerol acyltransferase-1 inhibition enhances intestinal fatty acid oxidation and reduces energy intake in rats. Journal of lipid research. 2013 May;54(5):1369-84. PubMed PMID: 23449193. Pubmed Central PMCID: 3622331.

269. Lee B, Fast AM, Zhu J, Cheng JX, Buhman KK. Intestine-specific expression of acyl CoA:diacylglycerol acyltransferase 1 reverses resistance to diet-induced hepatic steatosis and obesity in Dgat1-/- mice. Journal of lipid research. 2010 Jul;51(7):1770-80. PubMed PMID: 20147738. Pubmed Central PMCID: 2882751.

270. Chandak PG, Obrowsky S, Radovic B, Doddapattar P, Aflaki E, Kratzer A, et al. Lack of acyl-CoA:diacylglycerol acyltransferase 1 reduces intestinal cholesterol absorption and attenuates atherosclerosis in apolipoprotein E knockout mice. Biochimica et biophysica acta. 2011 Dec;1811(12):1011-20. PubMed PMID: 21924378. Pubmed Central PMCID: 3223411.

271. Haas JT, Winter HS, Lim E, Kirby A, Blumenstiel B, DeFelice M, et al. DGAT1 mutation is linked to a congenital diarrheal disorder. The Journal of clinical investigation. 2012 Dec;122(12):4680-4. PubMed PMID: 23114594. Pubmed Central PMCID: 3533555.

272. Stone SJ, Levin MC, Farese RV, Jr. Membrane topology and identification of key functional amino acid residues of murine acyl-CoA:diacylglycerol acyltransferase-2. The Journal of biological chemistry. 2006 Dec 29;281(52):40273-82. PubMed PMID: 17035227.

273. Lardizabal KD, Mai JT, Wagner NW, Wyrick A, Voelker T, Hawkins DJ. DGAT2 is a new diacylglycerol acyltransferase gene family: purification, cloning, and expression in insect cells of two polypeptides from Mortierella ramanniana with diacylglycerol acyltransferase activity. The Journal of biological chemistry. 2001 Oct 19;276(42):38862-9. PubMed PMID: 11481333.

274. Stone SJ, Myers HM, Watkins SM, Brown BE, Feingold KR, Elias PM, et al. Lipopenia and skin barrier abnormalities in DGAT2-deficient mice. The Journal of biological chemistry. 2004 Mar 19;279(12):11767-76. PubMed PMID: 14668353.

275. Yu XX, Murray SF, Pandey SK, Booten SL, Bao D, Song XZ, et al. Antisense oligonucleotide reduction of DGAT2 expression improves hepatic steatosis and hyperlipidemia in obese mice. Hepatology. 2005 Aug;42(2):362-71. PubMed PMID: 16001399.

276. Yamaguchi K, Yang L, McCall S, Huang J, Yu XX, Pandey SK, et al. Inhibiting triglyceride synthesis improves hepatic steatosis but exacerbates liver damage and fibrosis

in obese mice with nonalcoholic steatohepatitis. Hepatology. 2007 Jun;45(6):1366-74. PubMed PMID: 17476695.

277. Li C, Li L, Lian J, Watts R, Nelson R, Goodwin B, et al. Roles of Acyl-CoA:Diacylglycerol Acyltransferases 1 and 2 in Triacylglycerol Synthesis and Secretion in Primary Hepatocytes. Arteriosclerosis, thrombosis, and vascular biology. 2015 May;35(5):1080-91. PubMed PMID: 25792450.

278. Getz GS, Reardon CA. Animal models of atherosclerosis. Arteriosclerosis, thrombosis, and vascular biology. 2012 May;32(5):1104-15. PubMed PMID: 22383700. Pubmed Central PMCID: 3331926.

279. Pendse AA, Arbones-Mainar JM, Johnson LA, Altenburg MK, Maeda N. Apolipoprotein E knock-out and knock-in mice: atherosclerosis, metabolic syndrome, and beyond. Journal of lipid research. 2009 Apr;50 Suppl:S178-82. PubMed PMID: 19060252. Pubmed Central PMCID: 2674752.

280. Barter PJ, Brewer HB, Jr., Chapman MJ, Hennekens CH, Rader DJ, Tall AR. Cholesteryl ester transfer protein: a novel target for raising HDL and inhibiting atherosclerosis. Arteriosclerosis, thrombosis, and vascular biology. 2003 Feb 1;23(2):160-7. PubMed PMID: 12588754.

281. Bartelt A, Beil FT, Schinke T, Roeser K, Ruether W, Heeren J, et al. Apolipoprotein E-dependent inverse regulation of vertebral bone and adipose tissue mass in C57Bl/6 mice: modulation by diet-induced obesity. Bone. 2010 Oct;47(4):736-45. PubMed PMID: 20633710.

282. Mensenkamp AR, Jong MC, van Goor H, van Luyn MJ, Bloks V, Havinga R, et al. Apolipoprotein E participates in the regulation of very low density lipoprotein-triglyceride secretion by the liver. The Journal of biological chemistry. 1999 Dec 10;274(50):35711-8. PubMed PMID: 10585451.

283. Hofmann SM, Perez-Tilve D, Greer TM, Coburn BA, Grant E, Basford JE, et al. Defective lipid delivery modulates glucose tolerance and metabolic response to diet in apolipoprotein E-deficient mice. Diabetes. 2008 Jan;57(1):5-12. PubMed PMID: 17914034. Pubmed Central PMCID: 2830804.

284. Plump AS, Breslow JL. Apolipoprotein E and the apolipoprotein E-deficient mouse. Annual review of nutrition. 1995;15:495-518. PubMed PMID: 8527231.

285. Reddick RL, Zhang SH, Maeda N. Atherosclerosis in mice lacking apo E. Evaluation of lesional development and progression. Arteriosclerosis and thrombosis : a journal of vascular biology / American Heart Association. 1994 Jan;14(1):141-7. PubMed PMID: 8274470.

286. Jawien J, Nastalek P, Korbut R. Mouse models of experimental atherosclerosis. Journal of physiology and pharmacology : an official journal of the Polish Physiological Society. 2004 Sep;55(3):503-17. PubMed PMID: 15381823.

287. Nakashima Y, Raines EW, Plump AS, Breslow JL, Ross R. Upregulation of VCAM-1 and ICAM-1 at atherosclerosis-prone sites on the endothelium in the ApoE-deficient mouse. Arteriosclerosis, thrombosis, and vascular biology. 1998 May;18(5):842-51. PubMed PMID: 9598845.

288. Linton MF, Fazio S. Macrophages, lipoprotein metabolism, and atherosclerosis: insights from murine bone marrow transplantation studies. Current opinion in lipidology. 1999 Apr;10(2):97-105. PubMed PMID: 10327277.

289. Ishibashi S, Brown MS, Goldstein JL, Gerard RD, Hammer RE, Herz J. Hypercholesterolemia in low density lipoprotein receptor knockout mice and its reversal by adenovirus-mediated gene delivery. The Journal of clinical investigation. 1993 Aug;92(2):883-93. PubMed PMID: 8349823. Pubmed Central PMCID: 294927.

290. Getz GS, Reardon CA. Diet and murine atherosclerosis. Arteriosclerosis, thrombosis, and vascular biology. 2006 Feb;26(2):242-9. PubMed PMID: 16373607.

291. Ma Y, Wang W, Zhang J, Lu Y, Wu W, Yan H, et al. Hyperlipidemia and atherosclerotic lesion development in Ldlr-deficient mice on a long-term high-fat diet. PloS one. 2012;7(4):e35835. PubMed PMID: 22558236. Pubmed Central PMCID: 3338468.

292. Wouters K, Shiri-Sverdlov R, van Gorp PJ, van Bilsen M, Hofker MH. Understanding hyperlipidemia and atherosclerosis: lessons from genetically modified apoe and ldlr mice. Clinical chemistry and laboratory medicine : CCLM / FESCC. 2005;43(5):470-9. PubMed PMID: 15899668.

293. Paigen B, Holmes PA, Mitchell D, Albee D. Comparison of atherosclerotic lesions and HDL-lipid levels in male, female, and testosterone-treated female mice from strains C57BL/6, BALB/c, and C3H. Atherosclerosis. 1987 Apr;64(2-3):215-21. PubMed PMID: 3606719.

294. Stewart FA, Heeneman S, Te Poele J, Kruse J, Russell NS, Gijbels M, et al. Ionizing radiation accelerates the development of atherosclerotic lesions in ApoE-/- mice and predisposes to an inflammatory plaque phenotype prone to hemorrhage. The American journal of pathology. 2006 Feb;168(2):649-58. PubMed PMID: 16436678. Pubmed Central PMCID: 1606487.

295. Hoving S, Heeneman S, Gijbels MJ, te Poele JA, Russell NS, Daemen MJ, et al. Single-dose and fractionated irradiation promote initiation and progression of atherosclerosis and induce an inflammatory plaque phenotype in ApoE(-/-) mice. International journal of radiation oncology, biology, physics. 2008 Jul 1;71(3):848-57. PubMed PMID: 18514779.

296. Gabriels K, Hoving S, Gijbels MJ, Pol JF, te Poele JA, Biessen EA, et al. Irradiation of existing atherosclerotic lesions increased inflammation by favoring pro-inflammatory macrophages. Radiotherapy and oncology : journal of the European Society for Therapeutic Radiology and Oncology. 2014 Mar;110(3):455-60. PubMed PMID: 24630533.